

ELECTROKINETICS IN EARTH SCIENCES

GUEST EDITORS: LAURENCE JOUNIAUX AND TSUNEO ISHIDO





Electrokinetics in Earth Sciences

International Journal of Geophysics

Electrokinetics in Earth Sciences

Guest Editors: Laurence Jouniaux and Tsuneo Ishido



Copyright © 2013 Hindawi Publishing Corporation. All rights reserved.

This is a special issue published in "International Journal of Geophysics." All articles are open access articles distributed under the Creative Commons Attribution License, which permits unrestricted use, distribution, and reproduction in any medium, provided the original work is properly cited.

Editorial Board

José Badal, Spain
Andrea Bizzarri, Italy
Jean-Pierre Burg, Switzerland
John F. Cassidy, Canada
Ping Chang, USA
Yun-tai Chen, China
Gordon Cooper, South Africa
Robin Crockett, UK
Gary Egbert, USA
Semih Ergintav, Turkey
Fabrizio Galadini, Italy
Marek Grad, Poland
Hans-Gert Kahle, Switzerland

Masao Kanamitsu, USA
Honn Kao, Canada
Shuichi Kodaira, Japan
Libo Liu, China
Francisco Luzon Martinez, Spain
Zdenek Martinec, Czech Republic
Philip Meredith, UK
Steve Milan, UK
Marco Mucciarelli, Italy
Michael Nicolls, USA
Salvatore Piro, Italy
Ruey-Juin Rau, Taiwan
Wouter Schellart, Australia

Joerg Schleicher, Brazil
Sheng-Rong Song, Taiwan
Alexey Stovas, Norway
Sándor Szalai, Hungary
P. Talwani, USA
Robert Tenzer, New Zealand
Rudolf A. Treumann, Germany
Filippos Vallianatos, Greece
Petr Vaníček, Canada
Michael S. Zhdanov, USA
Sergej Zilitinkevich, Finland

Contents

Electrokinetics in Earth Sciences, Laurence Jouniaux and Tsuneo Ishido
Volume 2013, Article ID 419854, 1 page

Experimental Validation of the Electrokinetic Theory and Development of Seismoelectric Interferometry by Cross-Correlation, F. C. Schoemaker, N. Grobbe, M. D. Schakel, S. A. L. de Ridder, E. C. Slob, and D. M. J. Smeulders
Volume 2012, Article ID 514242, 23 pages

On the Validity of the “Thin” and “Thick” Double-Layer Assumptions When Calculating Streaming Currents in Porous Media, Matthew D. Jackson and Eli Leinov
Volume 2012, Article ID 897807, 12 pages

Frequency-Dependent Streaming Potential of Porous Media—Part 1: Experimental Approaches and Apparatus Design, P. W. J. Glover, J. Ruel, E. Tardif, and E. Walker
Volume 2012, Article ID 846204, 15 pages

Frequency-Dependent Streaming Potentials: A Review, L. Jouniaux and C. Bordes
Volume 2012, Article ID 648781, 11 pages

Implications of Self-Potential Distribution for Groundwater Flow System in a Nonvolcanic Mountain Slope, Tada-nori Goto, Kazuya Kondo, Rina Ito, Keisuke Esaki, Yasuo Oouchi, Yutaka Abe, and Maki Tsujimura
Volume 2012, Article ID 640250, 10 pages

Frequency-Dependent Streaming Potential of Porous Media—Part 2: Experimental Measurement of Unconsolidated Materials, P. W. J. Glover, E. Walker, J. Ruel, and E. Tardif
Volume 2012, Article ID 728495, 17 pages

Electrokinetics in Earth Sciences: A Tutorial, L. Jouniaux and T. Ishido
Volume 2012, Article ID 286107, 16 pages

Characterization of Fractured Reservoirs Using a Combination of Downhole Pressure and Self-Potential Transient Data, Yuji Nishi and Tsuneo Ishido
Volume 2012, Article ID 148919, 13 pages

Changes in Electrokinetic Coupling Coefficients of Granite under Triaxial Deformation, Osamu Kuwano and Shingo Yoshida
Volume 2012, Article ID 290915, 12 pages

Electric Signals on and under the Ground Surface Induced by Seismic Waves, Akihiro Takeuchi, Kan Okubo, and Nobunao Takeuchi
Volume 2012, Article ID 270809, 10 pages

The Self-Potential Anomaly Produced by a Subsurface Flow at the Contact of Two Horizontal Layers and Its Quantitative Interpretation, Georgios Aim. Skianis
Volume 2012, Article ID 483590, 8 pages

Editorial

Electrokinetics in Earth Sciences

Laurence Jouniaux,¹ and Tsuneo Ishido²

¹*Institut de Physique du Globe de Strasbourg, CNRS UMR7516 and Université de Strasbourg, 67084 Strasbourg Cedex, France*

²*Geological Survey of Japan, AIST, Central 7, Tsukuba 305-8567, Japan*

Correspondence should be addressed to Laurence Jouniaux; laurence.jouniaux@unistra.fr

Received 29 November 2012; Accepted 29 November 2012

Copyright © 2013 L. Jouniaux and T. Ishido. This is an open access article distributed under the Creative Commons Attribution License, which permits unrestricted use, distribution, and reproduction in any medium, provided the original work is properly cited.

Electrokinetics is used in earth sciences to provide insights concerning near-surface earth structures (from a few hundred meters up to several thousand meters depth) that host interstitial fluids (water, ice, oil, and gas). Electrokinetic phenomena are induced by the relative motion between the fluid and the rock matrix and, therefore, can provide information about the fluids within the earth. Self-potentials have been measured in hydrology, in active volcanic areas, and in polluted environments. Various methods based on electrokinetics, including self-potentials and seismoelectromagnetic conversion, have been applied to the management of hydraulic and hydrocarbon reservoirs, the resource prospecting in glaciated regions, the exploration for and monitoring of geothermal reservoirs, the characterization of fractured reservoirs, and so forth.

Electrokinetic phenomena have been known for more than two centuries (Reuss, 1809). Electrokinetic potential has been studied in relation to the field of colloid science and also in petroleum engineering research through its effects upon SP logging. Instrumentation improvements have resulted in an increased number of field observations, giving rise to new theoretical insights, specifically Pride's theory (1994) which combines Biot's equations and Maxwell's equations, and the developments by Garambois and Dietrich (2001) on the transfer functions between the electromagnetic field and the seismic field. This also arose new interest in modeling studies and led to numerous other publications in these fields during the past few decades.

This special issue addresses both self-potential and seismoelectrical conversions. The themes include field observations, modeling at small- and large-scale experimental developments, and theoretical analysis. From thirteen submissions, eleven papers were selected for publication in the

special issue. Two reviewers critiqued each paper, and the manuscripts were then revised appropriately. We also include a tutorial which presents the basic principles of the coupling between fluid and electrical flow under both steady and unsteady conditions as developed by Pride (1994), and a review of various applications such as geothermal reservoir characterization, as well as an explanation about the electric double layer, whose assumptions are discussed in the paper of M. D. Jackson and E. Leinov. Field observations of self-potential caused by flow in fractured reservoirs are described by Y. Nishi and T. Ishido; observed SP on mountain slopes is examined by T. N. Goto et al.; the self-potential induced by horizontal fluid flow is modeled by G. A. Skianis.

Seismic wave propagation induces a relative movement between the fluid and the rock matrix, leading to electrokinetic effects. Electrical signals that might arise due to earthquakes are described by A. Takeuchi et al. The seismoelectric method could be extended in future decades using interferometry by cross-correlation, as developed by F. C. Schoemaker et al.

To properly interpret observations of self-potential and seismoelectrical conversion, we need a better quantitative understanding of the electrokinetic coupling. The effect of deformation on this coupling is measured in granite by O. Kuwano and S. Yoshida. The frequency dependence of this coupling is reviewed by L. Jouniaux and C. Bordes, and new laboratory experiments are described by P. W. J. Glover et al. (part 1 and part 2).

Laurence Jouniaux
Tsuneo Ishido

Research Article

Experimental Validation of the Electrokinetic Theory and Development of Seismoelectric Interferometry by Cross-Correlation

F. C. Schoemaker,¹ N. Grobbe,¹ M. D. Schakel,^{1,2} S. A. L. de Ridder,³
E. C. Slob,¹ and D. M. J. Smeulders^{1,4}

¹ Department of Geotechnology, Delft University of Technology, Stevinweg 1, 2600 GA Delft, The Netherlands

² BP, BP Sunbury Business Park, Building H, Sunbury on Thames, Middlesex TW16 7LN, UK

³ Department of Geophysics, Stanford University, 397 Panama Mall, Stanford, CA 94305-2115, USA

⁴ Department of Mechanical Engineering, Eindhoven University of Technology, P.O. Box 513, 5600 MB Eindhoven, The Netherlands

Correspondence should be addressed to N. Grobbe, n.grobbe@tudelft.nl

Received 29 June 2011; Revised 30 November 2011; Accepted 10 February 2012

Academic Editor: Laurence Jouniaux

Copyright © 2012 F. C. Schoemaker et al. This is an open access article distributed under the Creative Commons Attribution License, which permits unrestricted use, distribution, and reproduction in any medium, provided the original work is properly cited.

We experimentally validate a relatively recent electrokinetic formulation of the streaming potential (SP) coefficient as developed by Pride (1994). The start of our investigation focuses on the streaming potential coefficient, which gives rise to the coupling of mechanical and electromagnetic fields. It is found that the theoretical amplitude values of this dynamic SP coefficient are in good agreement with the normalized experimental results over a wide frequency range, assuming no frequency dependence of the bulk conductivity. By adopting the full set of electrokinetic equations, a full-waveform wave propagation model is formulated. We compare the model predictions, neglecting the interface response and modeling only the coseismic fields, with laboratory measurements of a seismic wave of frequency 500 kHz that generates electromagnetic signals. Agreement is observed between measurement and electrokinetic theory regarding the coseismic electric field. The governing equations are subsequently adopted to study the applicability of seismoelectric interferometry. It is shown that seismic sources at a single boundary location are sufficient to retrieve the 1D seismoelectric responses, both for the coseismic and interface components, in a layered model.

1. Introduction

The first observation of coupling between electromagnetic and mechanical effects (also known as electroosmosis, which is one of the electrokinetic effects) dates back to the beginning of the 19th century. In 1809, Reuss [1] was the first to report on an experiment where a direct current was applied to a clay-sand-water mixture. The experiment was performed with a U-tube, filled with quartz at the bottom. Application of an electric current caused the water to rise in the leg containing the negative electrode [2].

The electrokinetic effect works as follows. In a fully fluid-saturated porous medium, a charged nanolayer at the solid-liquid interface is present (see Figure 1). The origin of this charged nanolayer lies in the presence of an aqueous

solution, typically a negatively charged silane grain surface. The resulting interface potential is called the zeta-potential, which is typically negative and on the order of a few tens of millivolts [9]. The counterions in the fluid reorganize in a layer that is bound to the surface by electrostatic forces (Stern layer) and a diffuse layer that is free to flow. In the diffuse layer two types of physical phenomena are competing, the electrostatic forces between the ions and the Brownian motion of the particles. This effectively results in an exponentially decreasing potential away from the solid-liquid interface towards the bulk of the pore (see Figure 1). The characteristic length over which the EDL exponentially decays, known as the Debye length, is of the order of a few tens of nanometers for typical reservoir rocks. The Stern layer and the diffuse layer together are usually called the electric

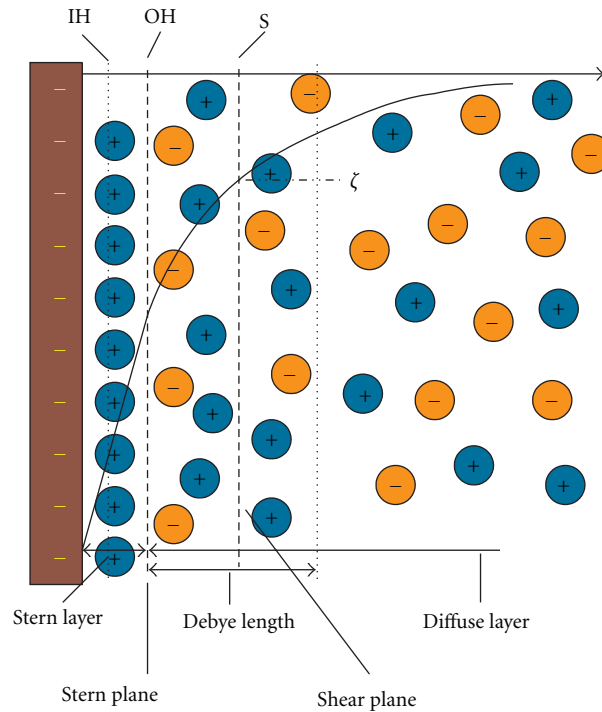


FIGURE 1: Electric double-layer according to the Stern model. The inner and outer Helmholtz planes are indicated as IH and OH, respectively. The slipping plane is denoted by S and its charge is characterized by the ζ -potential (modified from [2–8]).

double-layer (EDL), see Figure 1. The Debye length is considerably thinner than any viscous boundary layer that normally develops in pore fluid transport phenomena [3]. Quincke [10] performed electroosmosis experiments on glass capillaries. The simple geometry used, allowed for controlled experimental conditions. Linearity between the electroosmotic volume and the applied electric field was observed. Another electrokinetic effect, the physical phenomenon of electrophoretic mobility, where particles are mobilized by electrical fields, was described by Quincke [10] together with Reuss [1]. A mathematical description of both phenomena (electroosmotic and electrophoretic mobility) was later derived by Helmholtz [11]. However he did not consider the electric permittivity. Von Smoluchowski [12] derived the well-known Helmholtz-Smoluchowski equation, in which the electric permittivity is incorporated. Smoluchowski also recognized reciprocity between electroosmotic flow and streaming potential phenomena (mechanical to electromagnetic effect), later described by Onsager [13, 14].

Gouy [16] and Chapman [17] improved the theoretical model by including the diffuse layer of counterions in the model, thereby relating the thickness of the diffuse layer to the ionic strength of the solution [3]. To overcome limitations with highly charged electric double layers, Stern [18] added another layer to the model, see Figure 1. This theorem was some years later perfected by Derjaguin and Landau [19], and also by Verwey and Overbeek [4] in the “DLVO” theory, which describes in even more detail the forces between charged surfaces interacting through an electrolyte.

In 1936, Thompson [20] suggested that the electrokinetic effect could be used for geophysical prospecting. The Russian

physicist Yacov Il’ich Frenkel [21] developed a theory for wave propagation of electrokinetic phenomena in fluid-saturated porous media, in which he predicted the slow compressional wave and the seismoelectric effect (thereby he made a marginal error in the development of the Biot-Gassmann constants, he also only considered the electric effect and not the full Maxwell equations [22]). In 1959, Martner and Sparks [23] were the first to report that an electric potential difference generated in the subsurface by the passage of seismic waves could be detected by electrode pairs. Somewhat later, an experimental programme was undertaken to evaluate the electroseismic effect as a possible means for detecting underground nuclear tests. The goal was to develop long range systems for detection of nuclear blasts, see for example, Broding et al. [24] and Long and Rivers [25]. Due to insensitive technical equipment, lack of computing power, and the success of conventional seismic and electromagnetic methods, electrokinetics never gained much attention in geophysical exploration, at least until the 1990s. Moreover, the majority of field tests up to that time were concerned with the seismoelectric effect while the reciprocal electroseismic effect was underexposed. Extended field tests were only performed recently [26].

Regarding wave modeling, Neev and Yeatts [28] were the first in recent history (since Frenkel) to postulate a set of equations, which attempted to model the interaction between mechanical waves and electric fields due to electrokinetics. Their model did not include the Maxwell equations and frequency-dependence of the transport laws. A possible way to include all effects is by volume averaging the continuum equations for solid grains and electrolyte fluids.

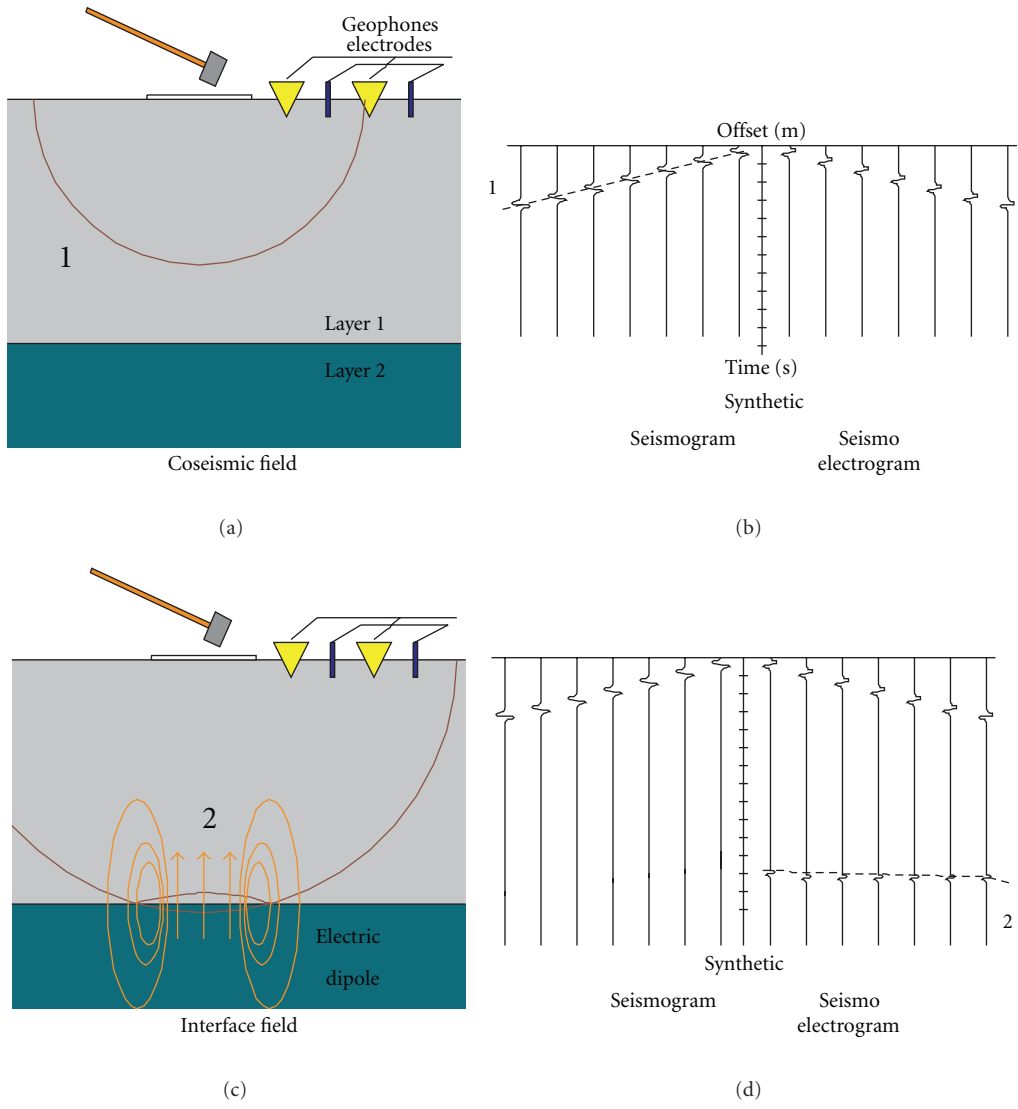


FIGURE 2: Schematic of a “standard” geometry for a seismoelectric survey (modified from Haines [5], Kroeger [6, 15]). One fluid-saturated porous layer (layer 1) overlies a porous half-space (layer 2), with contrasting medium parameters (panels (a) and (c)). The seismic source generates longitudinal wave (labelled 1) that is recorded by surface geophones (left part of panel (b)). This wave also creates a coseismic electric field that is registered by the surface electrodes (right part of panel (b)). When the longitudinal wave arrives at the interface between the porous layers, the interface field is generated (labelled 2), that is also recorded by the surface electrodes (right part of panel (d)).

Using this approach, Pride [29] obtained the governing equations for coupled electromagnetics and elastodynamics of porous media.

The governing equations of Pride describe coupled seismic and electromagnetic wave propagation effects. A schematic description of the coseismic and interface response effects is given in Figure 2. Figures 2(a) and 2(c) show a cross-section of the subsurface, with corresponding seismogram and seismo electrograms in Figures 2(b) and 2(d), respectively. The subsurface consists of two layers. Geophones and electrodes are positioned at the surface. In Figure 2(a), a local pressure disturbance is initiated at $t = 0$. Due to the mechanical pressure source, a longitudinal wave is created (labelled 1 in Figures 2(a)–2(d)). The seismic wave creates

a fluid pressure gradient within the pulse that induces pore fluid flow. Excess electrical charge in the double layer is transported by this flow. The net flow of charge relative to the grains is known as the streaming electric current. The induced conduction current leads to the electric field known as the “coseismic field” [5, 6, 30]. The coseismic field travels along with the seismic wave, giving it the same velocity as the compressional wave (compare the slope of event 1 in the left and right part of Figure 2(b)). When the pressure wave encounters the interface (with changing medium parameters) between porous layers 1 and 2, this results in a local asymmetry in the charge distribution. This will induce an oscillating electric dipole (Figure 2(c)). The associated independent electromagnetic field will travel almost

immediately to the receiver electrodes (Figure 2(d), right part). This seismoelectric effect is known as the “*interface response field*”. The coseismic and interface response fields were measured in the laboratory (e.g., [7, 31–34]) and in the field (e.g., [25, 35–40]). Zhu and Toksöz [41] and Bordes et al. [34, 42] reported on coseismic magnetic field measurements associated with a Stoneley wave and a shear wave, respectively. The dynamic *SP* coefficient, that links the mechanical and electromagnetic fields in Pride’s set of equations, was measured by Reppert et al. [8] and another validation is presented in this paper. Also, full-waveform seismoelectric models that adopt Pride’s theory were compared with measurements. Mikhailov et al. [36] and Haines et al. [39] compare seismoelectric synthetic sections with field measurements and find qualitative agreement. Zhu et al. [32] found kinematic agreement between full-waveform seismoelectric predictions and laboratory measurements. Block and Harris [7] compared amplitudes of coseismic wave fields in sands with numerically predicted amplitudes and fitted their measurements to Pride’s theory by incorporating an additional surface conductivity term. Charara et al. [43] found agreement between modeled and measured seismoelectric waveforms and amplitudes at a fluid/porous-medium interface in a laboratory setup. Schakel et al. [44, 45] found agreement between laboratory measurements of the coseismic and interface response fields and full-waveform and spatial seismoelectric predictions in terms of traveltime, waveform, and spatial amplitude pattern. Seismic waves can image to great depths but at the cost of resolution. Electromagnetic waves are sensitive to additional material properties and can therefore provide us with information about the pore fluid content. Seismoelectric conversion methods in field studies can combine seismic resolution and electromagnetic hydrocarbon sensitivity [39].

However, in seismoelectric surveys, the interface response is known to be very weak, that is, the response suffers from a very low signal-to-noise ratio. Therefore, the sources in classical seismoelectric surveys need to be strong. This is not always possible and therefore it is beneficial to be able to replace those strong sources by receivers: the principle of interferometry. In addition, by doing interferometry, stacking inherently takes place with a possible improvement of the signal-to-noise ratio as a result [46]. From an imaging point of view, the principle of interferometry has already been proven useful for a wide class of phenomena, for example in seismic and electromagnetic systems (e.g., Wapenaar et al. [47], Slob et al. [48]). Seismic interferometry is a seismological technique which makes use of the cross-correlation of responses at different receivers in order to obtain the Green’s function between these receivers [49]. It can include both passive and active sources. Due to the fact that the cross-correlation generates new data from measured data, it may allow for improved imaging compared to the situations where imaging algorithms are applied to the measured data only.

The foundations of the principle of interferometry were laid in 1968 by Claerbout who showed that by using the autocorrelation of the 1D transmission response of a horizontally layered medium (bounded by a free surface), the

reflection response of this medium can be obtained [50, 51]. Later, Claerbout conjectured that this relation could also be extended for 3D inhomogeneous situations, which was proven by Wapenaar [52]. By cross-correlating the recorded noise at two locations on the surface, it is possible to construct the wavefield that would be recorded at one of the locations as if there was a source at the other [53]. For a detailed overview of the theory of interferometry (e.g., stationary phase arguments, controlled-sources, interferometric imaging), the reader is referred to Wapenaar et al. [49, 54, 55] and Schuster [56]. Wapenaar et al. [57] showed the link between the principle of reciprocity and seismic interferometry. Using the reciprocity theorem of the correlation type, they generalized Claerbout’s relation between transmission and reflection responses to 3D inhomogeneous acoustic and elastic media. This theory was confirmed with numerically modeled seismic data in laterally varying media [58]. Wapenaar et al. [47] have shown that using cross-correlation to retrieve the Green’s function response between two stations is in principle not limited to seismic systems but holds for a wide class of phenomena, including seismoelectromagnetic wave propagation. We take the principle to the next level by numerically simulating seismoelectric interferometry by cross-correlation. de Ridder et al. [46] have already shown, with three numerical examples, that it is indeed possible (under certain conditions) to obtain accurate Green’s functions from boundary sources only. Here, we will increase the complexity of the numerical configuration by adding an extra layer to the system, to investigate the Green’s function retrieval for a 1D, three-layered system bounded by a free-surface.

Although the individual constituents of Pride’s model (i.e., Biot’s theory and Maxwell’s theory) have been experimentally validated, the dynamic *SP* coefficient that links these theories has been rarely studied (for a review see Jouniaux and Bordes, this issue). Also, despite the experimental verification of the coseismic and interface response fields, direct comparisons between electrokinetic wave propagation theory and measurements are scarce. In this paper we (1) validate electrokinetic theory by measurements and (2) investigate the applicability of correlation imaging with coupled seismic and electromagnetic wave propagation. First we present Pride’s electrokinetic governing equations. Second, the theoretical dynamic *SP* coefficient is compared against normalized measurements. Third, a seismoelectric wave model is formulated and model predictions are compared against seismoelectric wave propagation measurements.

It is shown that measurements of both the dynamic *SP* coefficient and the coseismic wave field are adequately described by the electrokinetic theory. This theory is subsequently adopted, when we numerically investigate the applicability of correlation imaging with seismoelectromagnetic waves.

2. Governing Equations

The governing equations for seismoelectric and electroseismic wave propagation in a fluid-saturated porous medium are derived from the compilation of Biot’s theory [60, 61]

together with Maxwell's theory. The Biot equations describe the acoustic side of electrokinetic phenomena. They are a combination of momentum equations and the stress strain relationships for an isotropic material, together with the continuity equations [62–64].

Expressing the expanded Biot equations, for the solid as well as the fluid and adopting an $e^{i\omega t}$ time dependence, yields the following linearized set of governing equations

$$G\nabla^2\hat{\mathbf{u}}_s + (A + G)\nabla(\nabla \cdot \hat{\mathbf{u}}_s) + Q\nabla(\nabla \cdot \hat{\mathbf{u}}_f) = -\omega^2[\rho_{11}(\omega)\hat{\mathbf{u}}_s + \rho_{12}(\omega)\hat{\mathbf{u}}_f] + \frac{\eta\phi L(\omega)}{k(\omega)}\hat{\mathbf{E}}, \quad (1)$$

$$Q\nabla(\nabla \cdot \hat{\mathbf{u}}_s) + R\nabla(\nabla \cdot \hat{\mathbf{u}}_f) = -\omega^2[\rho_{12}(\omega)\hat{\mathbf{u}}_s + \rho_{22}(\omega)\hat{\mathbf{u}}_f] - \frac{\eta\phi L(\omega)}{k(\omega)}\hat{\mathbf{E}}, \quad (2)$$

where A , Q , R are the Biot Gassmann constants [62], G the shear modulus, ρ_f is the fluid density, ρ_s is the solid density, α_∞ is the tortuosity, η is the fluid viscosity, k_0 is the (static) permeability, $\hat{\mathbf{E}}$ is the electric field, and $L(\omega)$ is the dynamic electrokinetic coupling [29]

$$\frac{L(\omega)}{L_0} = \left[1 + i\frac{\omega}{\omega_c} \frac{2}{m} \left(1 - 2\frac{d}{\Lambda} \right)^2 \left(1 + d\sqrt{\frac{i\omega\rho_f}{\eta}} \right)^2 \right]^{-1/2}, \quad (3)$$

where Λ is a characteristic pore size parameter and m is the shape factor. Please note that (3) is written in a slightly different form than in [29], because we used Johnson's definition of the shape factor [65]: $m = 8\alpha_\infty k_0 / (\phi\Lambda^2)$. The characteristic (or rollover) frequency ω_c is defined as $\omega_c = \eta\phi / (\alpha_\infty k_0 \rho_f)$ [59]. The Debye length is denoted by d (see, e.g., [29]) and L_0 represents the static electrokinetic coupling for a porous medium

$$L_0 = -\frac{\phi}{\alpha_\infty} \frac{\epsilon_0 \epsilon_{rf} \zeta}{\eta} \left(1 - 2\frac{d}{\Lambda} \right), \quad (4)$$

where ϵ_0 is the vacuum permittivity, ϵ_{rf} is the pore fluid relative permittivity, and ζ is the zeta-potential. We note that Pride [29] uses an additional relaxation mechanism when the complex viscous skin depth $\sqrt{\eta/(\omega\rho_f)}$ becomes smaller than the Debye length. However, due to the fact that the Debye length d for most salinity cases [22] is much smaller than Λ , Pride's relaxation mechanism can often be neglected. The dynamic permeability is closely related to the viscous correction factor

$$\frac{k(\omega)}{k_0} = \left(F(\omega) + \frac{i\omega}{\omega_c} \right)^{-1}, \quad (5)$$

the viscous correction factor is defined by Johnson et al. [59] as

$$F(\omega) = \sqrt{1 + m \frac{i\omega}{2\omega_c}}. \quad (6)$$

The coefficients $\rho_{11}(\omega)$, $\rho_{12}(\omega)$, and $\rho_{22}(\omega)$ are the so-called generalized effective density functions [65]

$$\begin{aligned} \rho_{11}(\omega) &= (1 - \phi)\rho_s - \rho_{12}(\omega), \\ \rho_{12}(\omega) &= \phi\rho_f \left[1 + i\frac{\eta\phi}{\omega\rho_f k(\omega)} \right], \\ \rho_{22}(\omega) &= \phi\rho_f - \rho_{12}(\omega). \end{aligned} \quad (7)$$

Considering the definitions for $\rho_{12}(\omega)$ and $\rho_{22}(\omega)$, (2) can be written as

$$i\omega\hat{\mathbf{w}} = \frac{k(\omega)}{\eta} (-\nabla\hat{p} + \omega^2\rho_f\hat{\mathbf{u}}_s) + L(\omega)\hat{\mathbf{E}}, \quad (8)$$

where $\hat{\mathbf{w}} = \phi(\hat{\mathbf{u}}_f - \hat{\mathbf{u}}_s)$ is the relative displacement. Pride [29] developed the following equation coupling the streaming and the conduction currents

$$\hat{\mathbf{J}} = L(\omega) (-\nabla\hat{p} + \omega^2\rho_f\hat{\mathbf{u}}_s) + \sigma(\omega)\hat{\mathbf{E}}, \quad (9)$$

where $\hat{\mathbf{J}}$ is the electric current density and $\sigma(\omega)$ the dynamic bulk conductivity. We recognize that the electrokinetic coupling is present in the mechanical and the electromagnetic equations (8) and (9) (see [29, 66]). The dynamic bulk conductivity $\sigma(\omega)$ for a porous medium of arbitrary pore structure is assumed to be independent of the frequency [22, 29] so that

$$\sigma(\omega) \approx \frac{\phi}{\alpha_\infty} \sigma_f, \quad (10)$$

or

$$\sigma_0 = \frac{\phi}{\alpha_\infty} \sigma_f, \quad (11)$$

where σ_0 represents the bulk electric conductivity and σ_f the pore-fluid conductivity. Closely related to the dynamic electrokinetic coupling (3) is the dynamic SP coefficient, defined as $L(\omega) = C(\omega)\sigma(\omega)$ [8]. Using this mutual relationship together with the hypothesis of frequency independence of the dynamic bulk conductivity (11), the measured dynamic SP coefficient and dynamic coupling are mutually related in their normalized form by

$$\frac{C(\omega)}{C_0} = \frac{L(\omega)}{L_0}. \quad (12)$$

Eliminating $(-\nabla\hat{p} + \omega^2\rho_f\hat{\mathbf{u}}_s)$ from (8) and (9), we obtain

$$i\omega\hat{\mathbf{w}} = L(\omega)\hat{\mathbf{E}} + \frac{k(\omega)}{\eta L(\omega)} (\hat{\mathbf{J}} - \sigma(\omega)\hat{\mathbf{E}}). \quad (13)$$

The Maxwell relation for the magnetic field is given by Ampère's Circuit Law

$$\hat{\mathbf{J}} = \nabla \times \hat{\mathbf{H}} - i\omega\epsilon\hat{\mathbf{E}}, \quad (14)$$

with $\hat{\mathbf{H}}$ the magnetic field and ϵ the electric permittivity for a fluid-saturated porous medium

$$\epsilon = \left[\frac{\phi}{\alpha_\infty} (\epsilon_{rf} - \epsilon_{rs}) + \epsilon_{rs} \right] \epsilon_0, \quad (15)$$

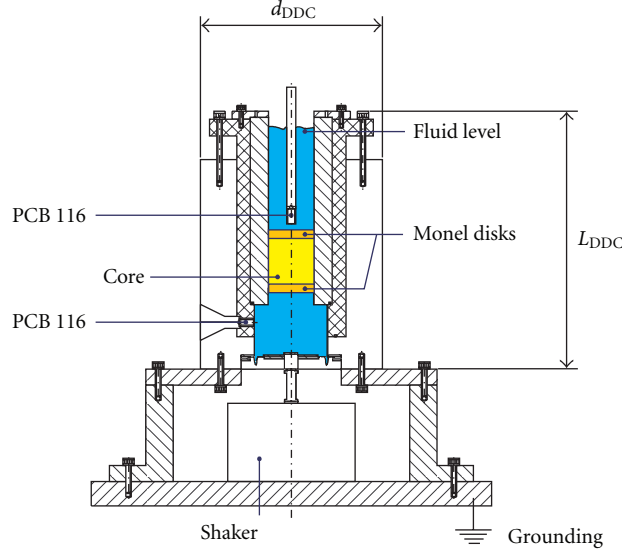


FIGURE 3: Schematic of the dynamic Darcy cell with borosilicate sample and Monel disks (modified from [27]).

where ϵ_{rs} is the solid relative permittivity. Faraday's induction law states that

$$i\omega\mu\hat{\mathbf{H}} = -\nabla \times \hat{\mathbf{E}}, \quad (16)$$

with μ the magnetic permeability. Substitution of (14) in (13) results in

$$i\omega\hat{\mathbf{w}} = L(\omega)\hat{\mathbf{E}} + \frac{k(\omega)}{\eta L(\omega)} (\nabla \times \mathbf{H} - [i\omega\epsilon + \sigma(\omega)]\hat{\mathbf{E}}). \quad (17)$$

Substituting the cross-product of Faraday's law (16) [29, 67] into (17) yields

$$\mu\bar{\epsilon}(\omega)\omega^2\hat{\mathbf{E}} + \omega^2\frac{\eta\mu}{k(\omega)}L(\omega)\hat{\mathbf{w}} = \nabla(\nabla \cdot \hat{\mathbf{E}}) - \nabla^2\hat{\mathbf{E}}, \quad (18)$$

where $\bar{\epsilon}(\omega)$ is the effective electric permittivity [67] of the porous continuum

$$\bar{\epsilon}(\omega) = \epsilon - i\frac{\sigma(\omega)}{\omega} + i\frac{\eta L^2(\omega)}{\omega k(\omega)}. \quad (19)$$

Here $-i\sigma(\omega)/\omega$ is a term accounting for the energy losses. The electrokinetic effect manifests itself in $\bar{\epsilon}(\omega)$ as an energy gain that is quadratic in $L(\omega)$ (third term in the right-hand side of (19)). Equations (1), (2), and (18) form a closed set of equations necessary to describe electrokinetic phenomena, for the displacements $\hat{\mathbf{u}}_s$, $\hat{\mathbf{u}}_f$ (mechanical part of the equations), and electric fields $\hat{\mathbf{E}}$ (the electromagnetic part).

3. Experimental Validation of the Dynamic Coupling Coefficients

We experimentally validate $k(\omega)/k_0$ and $C(\omega)/C_0$. The experiments are performed with the dynamic Darcy cell (DDC) as shown in Figure 3, within a steel cylinder (see [27]). At the bottom of the DDC an oscillating pressure is applied (generated by HP Agilent 33120A waveform Generator). A power

TABLE 1: Sample properties.

Property	Symbol	Value	Unit
Permeability ^a	k_0	$2.1 \cdot 10^{-10}$	[m ²]
Shape factor ^b	m	1.75	[—]
Porosity ^c	ϕ	0.093	[—]
Tortuosity ^d	α_∞	1.8	[—]
Debye length ^e	d	$2.9 \cdot 10^{-8}$	[m]
Weighted pore volume-to-surface ratio ^f	Λ	$1.3 \cdot 10^{-4}$	[m]

^aThe permeability is measured directly. ^{b,d}The shape factor and the tortuosity are derived from an independent dynamic head experiment [27, 69], by means of curve fitting. ^cThe porosity is computed from [70, 71]. ^{e,f}The Debye length and the characteristic pore size are computed from theory (see [29, 59], respectively).

amplified (Gearing and Watson) vibrating exciter (GW V20) drives a rubber membrane which induces an oscillating pressure. Vibrations are induced in a frequency band ranging from 5 Hz up to 150 Hz. Two identical piezoelectric transducers (PCB 116 Druck) are used to measure the pressure drop across the sample, one at the bottom inside the cylinder and the other mounted just above the sample in the center of the cylinder. On the top and bottom of the porous medium, electrodes are placed from which the streaming potential gradient is measured. These electrodes are sintered plates of Monel (an alloy primarily composed of Nickel and Copper). The signals from the two piezoelectric transducers are modified by means of amplifiers (Kistler 5011), and the signals of the electrodes amplified (Tektronix AM 502). The porous sample (parameters given in Table 1) consists of tubes of glass (borosilicate), which are glued together with an epoxy resin (Figure 4) and oriented in the flow direction. The combination of sintered plates together with a large surface area of the glass capillary tubes makes it possible to measure a relative strong signal. The sample is

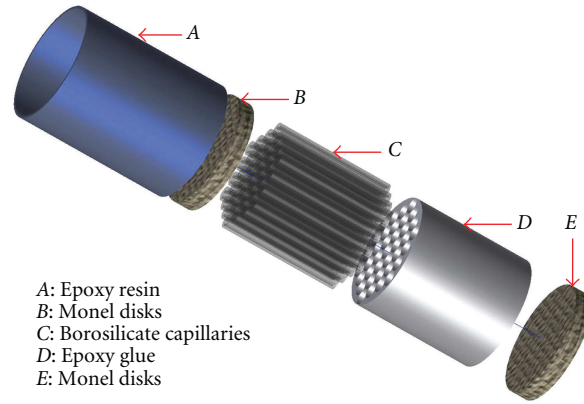


FIGURE 4: Exploded view of the capillary core.

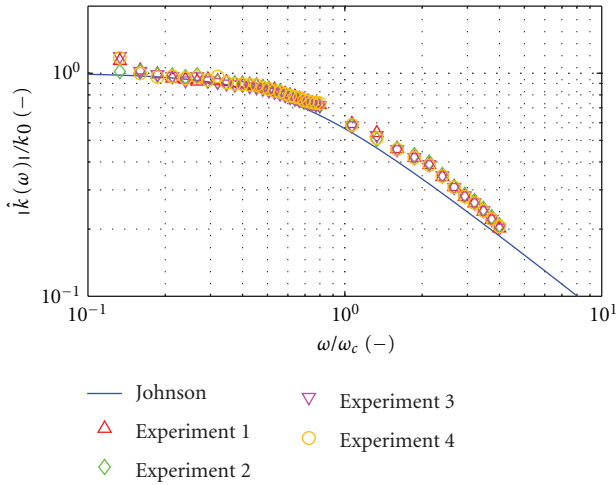


FIGURE 5: Amplitude of the normalized dynamic permeability. Theory of Johnson et al. [59] versus measurements, using the parameters as shown in Table 1. Experiments 1–4 denote repeated experiments at different times.

carefully saturated with degassed, demineralised water with a small amount of sodium chloride (with a density of $\rho_f = 1 \cdot 10^3 \text{ kg/m}^3$, a viscosity of $\eta = 0.9 \cdot 10^{-3} \text{ Pa s}$ obtained from [68], and a measured pore fluid conductivity of $\sigma_f = 1.3 \cdot 10^{-3} \text{ S/m}$), whereafter the setup is left until equilibrium of the salt solution is reached.

The 50 Hz electromagnetic frequency radiating from the equipment is suppressed by shielding the setup and its wires (therefore use has been made of shielded twisted cable pairs). To reduce uncorrelated noise the data are averaged multiple times.

In Figures 5 and 6, normalized amplitude and phase values of the dynamic permeability are plotted for the theoretical solution (5) together with the laboratory measurements. At low pulsation frequencies (viscosity dominated), the normalized dynamic permeability necessarily tends to its

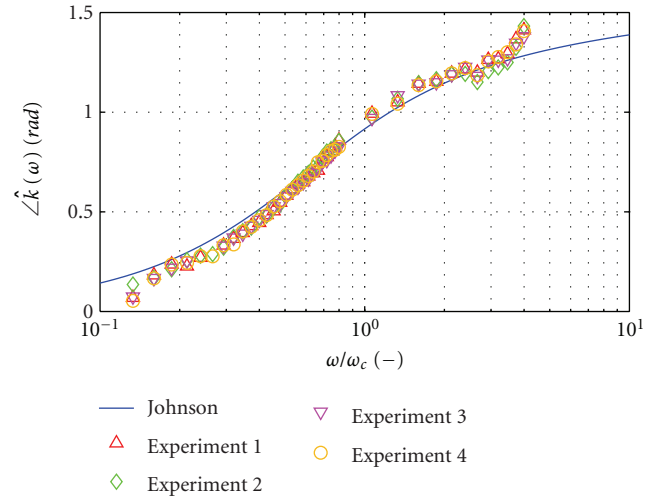


FIGURE 6: Phase value of the dynamic permeability. Theory of Johnson et al. [59] versus measurements, using the parameters as shown in Table 1. Experiments 1–4 denote repeated experiments at different times.

steady-state value, whereas above the characteristic pulsation frequency (the area where viscous dominated flow switches to inertia dominated flow [65]) a strong decline can be observed. The theory correlates well with the measurement. The offsets in the lower frequency range are caused by limitations of the equipment, while in the high frequency area this difference is mainly caused by resonance of the setup.

The measurements of the normalized dynamic SP coefficient (normalized to the measured value at 11 Hz, where $C_0 = 1.7 \cdot 10^{-5} \text{ V/Pa}$) shown in Figures 7 and 8 (using the parameters shown in Table 1), are performed by measuring the potential difference and the pressure difference across the sample between the Monel disks (see Figure 4). The rigid glass capillary tubes make it possible to assume no solid displacement $\mathbf{u}_s = \mathbf{0}$. Using (9) for a conservative (irrotational) electric field $\mathbf{E} = -\nabla U$ (with U the streaming

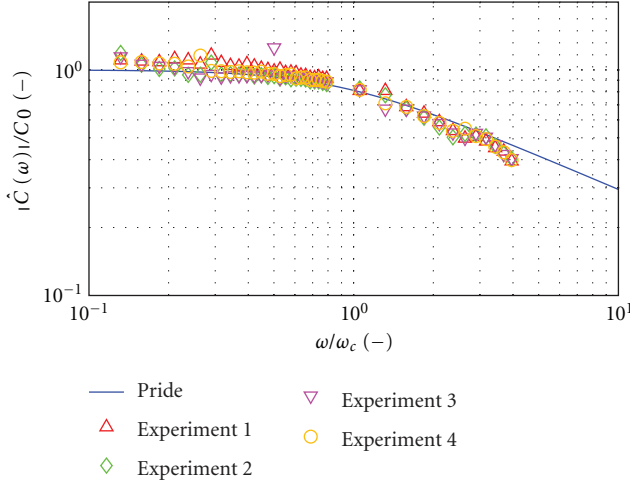


FIGURE 7: Amplitude of the normalized dynamic SP coefficient. Theory of Pride [29] versus measurements, using the parameters as shown in Table 1 and assuming $\sigma(\omega) = \sigma_0$. Experiments 1–4 denote repeated experiments at different times.

potential difference) in a setup where the electric current density is equal to $\mathbf{J} = 0$, we obtain

$$C(\omega) = -\frac{\nabla U(\omega)}{\nabla p(\omega)}, \quad (20)$$

with $C(\omega)$ being the dynamic SP coefficient. The dynamic SP coefficient theory agrees well with the measurement regarding the normalized amplitudes. The phase values show a large offset for the low as well as the high-frequency range. The offsets in the lower frequency range are caused by limitations of the equipment, while in the high frequency area this difference mainly is caused by resonance of the setup. This could be counteracted by applying notch filters at these higher frequencies. Due to the layering of the sample, the theory agrees well with the measurements. It is seen in measurements from [69, 72–74], that with a single capillary [8] it is possible to obtain remarkably consistent results between theory and measurement. However, the experimental setup (a set of capillaries combined with Monel disks) gives a more accurate representation of capillary networks in natural environments than a single capillary tube.

The difference between measurement and theory in the high-frequency range can be caused by the possibility of the system to function as a capacitor [8]. To prevent the capacitor effect, using insulating plates and electrodes perforated in them may be a solution. The impedance of the system can be determined using a two or four electrode method. The amplitude and phase of the impedance of the system can be determined and be used for data correction [8]. This can uplift particularly the phase values in the higher frequency range [8]. Also some offsets can be caused by the relative low permeability of the applied sample structure, especially the two Monel plates disturb the flow for high frequencies (which can also be observed in Figure 6). This limits the possibility of measuring samples with even lower permeability, in the current setup.

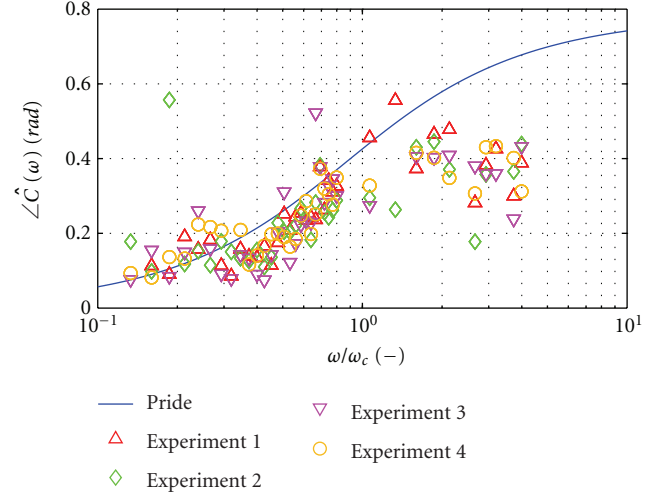


FIGURE 8: Phase values of the dynamic SP coefficient. Theory of Pride [29] versus measurements, using the parameters as shown in Table 1 and assuming $\sigma(\omega) = \sigma_0$. Experiments 1–4 denote repeated experiments at different times.

4. Seismoelectric Wave Propagation

4.1. Seismoelectric Wave Propagation Theory. Electrokinetic theory in isotropic, homogeneous, and fluid-saturated poroelastic media predicts the existence of a fast and a slow P-wave, a shear wave, and an electromagnetic wave. In this section, we derive wave speeds and attenuations (the dispersion relations) from the momentum equations (1), (2), and (18), for each of these waves. This derivation also yields the so-called fluid-to-solid and electric-to-solid field ratios. The fluid-to-solid ratio describes the fluid-to-solid displacement amplitude ratio, while the electric-to-solid field ratio describes the strength of the electric field with respect to the solid displacement field. These ratios and the dispersion relations are subsequently used to solve a boundary value problem and to formulate a full-waveform seismoelectric model.

Using (2) to eliminate the electric field $\hat{\mathbf{E}}$ from (1) and (18), we obtain two modified momentum equations for the fields $\hat{\mathbf{u}}_s$ and $\hat{\mathbf{u}}_f$

$$\begin{aligned} G\nabla^2 \hat{\mathbf{u}}_s + (A + G + Q)\nabla(\nabla \cdot \hat{\mathbf{u}}_s) + (Q + R)\nabla(\nabla \cdot \hat{\mathbf{u}}_f) \\ = -\omega^2 \left[(\rho_{11}(\omega) + \rho_{12}(\omega))\hat{\mathbf{u}}_s + (\rho_{12}(\omega) + \rho_{22}(\omega))\hat{\mathbf{u}}_f \right], \\ Q\nabla \nabla \cdot \hat{\mathbf{u}}_s + R\nabla \nabla \cdot \hat{\mathbf{u}}_f \\ = -\omega^2 \left(\bar{\rho}_{12}(\omega)\hat{\mathbf{u}}_s + \bar{\rho}_{22}(\omega)\hat{\mathbf{u}}_f \right) \\ + \frac{\rho_{12}(\omega)}{\mu\bar{\epsilon}(\omega)} (\nabla(\nabla \cdot \hat{\mathbf{u}}_s) - \nabla^2 \hat{\mathbf{u}}_s) \\ + \frac{\rho_{22}(\omega)}{\mu\bar{\epsilon}(\omega)} (\nabla(\nabla \cdot \hat{\mathbf{u}}_f) - \nabla^2 \hat{\mathbf{u}}_f), \end{aligned} \quad (21)$$

where complex effective densities $\bar{\rho}_{11}(\omega)$, $\bar{\rho}_{12}(\omega)$, and $\bar{\rho}_{22}(\omega)$, containing the electrokinetic coupling factor $E_K(\omega)$, are defined as follows

$$\begin{aligned}\bar{\rho}_{11}(\omega) &= \rho_{11}(\omega) - E_K(\omega), \\ \bar{\rho}_{12}(\omega) &= \rho_{12}(\omega) + E_K(\omega), \\ \bar{\rho}_{22}(\omega) &= \rho_{22}(\omega) - E_K(\omega), \\ E_K(\omega) &= \frac{\eta^2 \phi^2 L^2(\omega)}{\omega^2 k^2(\omega) \bar{\epsilon}(\omega)}.\end{aligned}\quad (22)$$

Employing Helmholtz decomposition for the fields $\hat{\mathbf{u}}_s$ and $\hat{\mathbf{u}}_f$ leads to

$$\begin{aligned}\hat{\mathbf{u}}_s &= \nabla \hat{\phi}^s + \nabla \times \hat{\Psi}^s, \\ \hat{\mathbf{u}}_f &= \nabla \hat{\phi}^f + \nabla \times \hat{\Psi}^f.\end{aligned}\quad (23)$$

Substituting expressions (23) into (21) yields

$$\begin{aligned}\nabla \left[((P+Q)\nabla^2 + \omega^2(1-\phi)\rho_s) \hat{\phi}^s + ((Q+R)\nabla^2 + \omega^2\phi\rho_f) \hat{\phi}^f \right] \\ + \nabla \times \left[(G\nabla^2 + \omega^2(1-\phi)\rho_s) \hat{\Psi}^s + \omega^2\phi\rho_f \hat{\Psi}^f \right] = \mathbf{0},\end{aligned}$$

$$\begin{aligned}\nabla \left[(Q\nabla^2 + \omega^2\bar{\rho}_{12}(\omega)) \hat{\phi}^s + (R\nabla^2 + \omega^2\bar{\rho}_{22}(\omega)) \hat{\phi}^f \right] \\ + \nabla \times \left[\left(\omega^2\bar{\rho}_{12}(\omega) + \frac{\rho_{12}(\omega)}{\mu\bar{\epsilon}(\omega)} \nabla^2 \right) \hat{\Psi}^s \right. \\ \left. + \left(\omega^2\bar{\rho}_{22}(\omega) + \frac{\rho_{22}(\omega)}{\mu\bar{\epsilon}(\omega)} \nabla^2 \right) \hat{\Psi}^f \right] = \mathbf{0},\end{aligned}\quad (24)$$

where $P = A + 2G$. For the longitudinal waves, associated with potentials $\hat{\phi}^s$ and $\hat{\phi}^f$, the first terms in square brackets of (24) are set equal to zero from which we obtain

$$\begin{pmatrix} P & Q \\ Q & R \end{pmatrix} \nabla^2 \begin{pmatrix} \hat{\phi}^s \\ \hat{\phi}^f \end{pmatrix} = -\omega^2 \begin{pmatrix} \bar{\rho}_{11}(\omega) & \bar{\rho}_{12}(\omega) \\ \bar{\rho}_{12}(\omega) & \bar{\rho}_{22}(\omega) \end{pmatrix} \begin{pmatrix} \hat{\phi}^s \\ \hat{\phi}^f \end{pmatrix}, \quad (25)$$

where we used that $(1-\phi)\rho_s - \bar{\rho}_{12}(\omega) = \bar{\rho}_{11}(\omega)$, and $\phi\rho_f - \bar{\rho}_{12}(\omega) = \bar{\rho}_{22}(\omega)$. Applying a spatial Fourier transformation and recasting (25) into an eigenvalue problem lead to

$$\frac{1}{PR - Q^2} \begin{pmatrix} \bar{\rho}_{11}(\omega)R - \bar{\rho}_{12}(\omega)Q & \bar{\rho}_{12}(\omega)R - \bar{\rho}_{22}(\omega)Q \\ \bar{\rho}_{12}(\omega)P - \bar{\rho}_{11}(\omega)Q & \bar{\rho}_{22}(\omega)P - \bar{\rho}_{12}(\omega)Q \end{pmatrix} \begin{pmatrix} \tilde{\phi}^s \\ \tilde{\phi}^f \end{pmatrix} = \frac{\mathbf{k} \cdot \mathbf{k}}{\omega^2} \begin{pmatrix} \tilde{\phi}^s \\ \tilde{\phi}^f \end{pmatrix}, \quad (26)$$

where \mathbf{k} is the wavenumber vector and tildes over a potential indicate frequency-wavenumber domain quantities. The complex eigenvalues correspond with the slownesses squared of the fast (Pf) and slow (Ps) longitudinal waves $s_k^2(\omega)$, $k = Pf, Ps$,

$$s_k^2(\omega) = \frac{-d_1(\omega)}{2d_2} \mp \frac{d_1(\omega)}{2d_2} \sqrt{1 - 4 \frac{d_0(\omega)d_2}{d_1^2(\omega)}}, \quad (27)$$

where

$$\begin{aligned}d_0(\omega) &= \bar{\rho}_{11}(\omega)\bar{\rho}_{22}(\omega) - [\bar{\rho}_{12}(\omega)]^2, \\ d_1(\omega) &= -[\bar{\rho}_{22}(\omega)P + \bar{\rho}_{11}(\omega)R - 2\bar{\rho}_{12}(\omega)Q], \\ d_2 &= PR - Q^2.\end{aligned}\quad (28)$$

The slowness yields the wave mode speed and intrinsic attenuation (see, e.g., [67]). For the transversal waves, associated with potentials $\tilde{\Psi}^s$ and $\tilde{\Psi}^f$, the second term in square brackets of (24) are set equal to the zero vector which gives

$$\begin{pmatrix} \left[-G \frac{\mathbf{k} \cdot \mathbf{k}}{\omega^2} + (1-\phi)\rho_s \right] \mathbf{I} & \phi\rho_f \mathbf{I} \\ \left[-\frac{\rho_{12}(\omega)}{\mu\bar{\epsilon}(\omega)} \frac{\mathbf{k} \cdot \mathbf{k}}{\omega^2} + \bar{\rho}_{12}(\omega) \right] \mathbf{I} & \left[-\frac{\rho_{22}(\omega)}{\mu\bar{\epsilon}(\omega)} \frac{\mathbf{k} \cdot \mathbf{k}}{\omega^2} + \bar{\rho}_{22}(\omega) \right] \mathbf{I} \end{pmatrix} \begin{pmatrix} \tilde{\Psi}^s \\ \tilde{\Psi}^f \end{pmatrix} = \begin{pmatrix} \mathbf{0} \\ \mathbf{0} \end{pmatrix}, \quad (29)$$

where a spatial Fourier transformation is applied. Nontrivial solutions for $\mathbf{k} \cdot \mathbf{k}/\omega^2$ are obtained by requiring the determinant of the matrix in (29) to be equal to zero. The solutions correspond with squared complex slownesses of the electromagnetic (EM) and seismic shear (S) waves. The dispersion relations are given in (27) for $k = \text{EM}, S$ where

$$\begin{aligned} d_0(\omega) &= \mu\bar{\epsilon}(\omega) \frac{\bar{\rho}_{11}(\omega)\bar{\rho}_{22}(\omega) - [\bar{\rho}_{12}(\omega)]^2}{G}, \\ d_1(\omega) &= -\mu\bar{\epsilon}(\omega)\bar{\rho}_{22}(\omega) - \frac{\rho_{11}(\omega)\rho_{22}(\omega) - [\rho_{12}(\omega)]^2}{G}, \\ d_2(\omega) &= \rho_{22}(\omega), \end{aligned} \quad (30)$$

and where we used that $(1 - \phi)\rho_s\rho_{22}(\omega) - \phi\rho_f\rho_{12}(\omega) = \rho_{11}(\omega)\rho_{22}(\omega) - [\rho_{12}(\omega)]^2$ and $(1 - \phi)\rho_s\bar{\rho}_{22}(\omega) - \phi\rho_f\bar{\rho}_{12}(\omega) = \bar{\rho}_{11}(\omega)\bar{\rho}_{22}(\omega) - [\bar{\rho}_{12}(\omega)]^2$. Note that d_2 in (27) is now frequency-dependent. Dispersion relations given by (27), (28), and (30) are equal to the expressions given by Pride and Haartsen [67].

The longitudinal fluid-solid ratio, which describes the fluid-to-solid displacement amplitude ratio, is derived from the first row in (25). By applying a spatial Fourier transformation we obtain for the longitudinal fluid-solid ratios

$$\beta_m(\omega) = \frac{\tilde{\varphi}_m^f}{\tilde{\varphi}_m^s} = \frac{\bar{\rho}_{11}(\omega) - Ps_m^2(\omega)}{Qs_m^2(\omega) - \bar{\rho}_{12}(\omega)}, \quad (31)$$

for $m = Pf, Ps$. By writing the vector potentials as $\tilde{\Psi}_n^s = (0, \tilde{\psi}_n^s, 0)^T$ and $\tilde{\Psi}_n^f = (0, \tilde{\psi}_n^f, 0)^T$, for $n = \text{EM}, S$, in (29) we obtain for the transversal fluid-solid ratios

$$\beta_n(\omega) = \frac{\tilde{\psi}_n^f}{\tilde{\psi}_n^s} = \frac{Gs_n^2(\omega) - (1 - \phi)\rho_s}{\phi\rho_f}. \quad (32)$$

The electric solid ratios, which describe the strength of the electric field with respect to the solid displacement field, are derived by applying Helmholtz decomposition (see (23)) to the fields in (18). This yields

$$\begin{aligned} \nabla \left[\omega^2 \mu\bar{\epsilon}(\omega) \hat{\varphi}^E + \omega^2 \frac{\eta\phi\mu L(\omega)}{k(\omega)} (\hat{\varphi}^f - \hat{\varphi}^s) \right] \\ + \nabla \times \left[(\omega^2 \mu\bar{\epsilon}(\omega) + \nabla^2) \hat{\Psi}^E \right] \\ + \omega^2 \frac{\eta\phi\mu L(\omega)}{k(\omega)} (\hat{\Psi}^f - \hat{\Psi}^s) = \mathbf{0}, \end{aligned} \quad (33)$$

where we note that the Helmholtz decomposition of the electric field is $\hat{\mathbf{E}} = \nabla \hat{\varphi}^E + \nabla \times \hat{\Psi}^E$, and $\hat{\Psi}_n^E = (0, \tilde{\psi}_n^E, 0)^T$. Again, the scalar potentials are associated with longitudinal wave behavior and the vector potentials with transversal wave behavior. By applying a spatial Fourier transformation to (33) we obtain

$$\alpha_m(\omega) = \frac{\tilde{\varphi}_m^E}{\tilde{\varphi}_m^s} = \frac{\eta\phi L(\omega)}{k(\omega)\bar{\epsilon}(\omega)} [1 - \beta_m(\omega)], \quad (34)$$

$$\alpha_n(\omega) = \frac{\tilde{\psi}_n^E}{\tilde{\psi}_n^s} = \frac{\eta\phi\mu L(\omega)}{k(\omega)[\mu\bar{\epsilon}(\omega) - s_n^2(\omega)]} [1 - \beta_n(\omega)]. \quad (35)$$

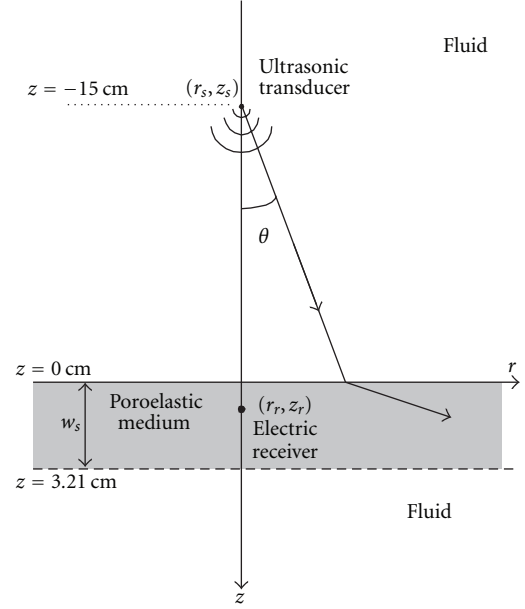


FIGURE 9: (Modified from [44].) Geometry of seismoelectric model and experiment. An acoustic wavefield emitted from (r_s, z_s) transmits into the poroelastic medium at $z = 0$, where it generates coseismic electric potentials. Fluid/poroelastic-medium interfaces are at $z = 0$ and $z = 3.21$ cm. The electric receiver is at 1 cm from the front interface, while the dominant wavelength of the fast P -wave is roughly 4 mm. The electric potential recordings of the electric receiver are with respect to ground level.

We now model coseismic electric potentials generated within a porous medium due to a fast P -wave, using its electric-solid ratio $\alpha_{Pf}(\omega)$, for the geometry of Figure 9. The interface field responses are not modelled, which simplifies the expressions. In the forthcoming, it will be shown that this simplified model describes the measured coseismic electric potentials adequately. An acoustic wavefield from a source in a compressible fluid impinges on an interface between the fluid and an isotropic, homogeneous, and fluid-saturated poroelastic medium. It transmits as a fast P -wave in the poroelastic medium, where it generates coseismic electric potentials. We model a transducer (piezoelectric) source, as it is used in the experiment described in the following section. The acoustic pressure due to the transducer is modeled as (see [44, 75])

$$\hat{p}^{fl}(\omega, R_s, \theta) = \frac{A(\omega)D(\theta)}{R_s} e^{-ik^{fl}R_s}, \quad (36)$$

where $R_s = \sqrt{(r - r_s)^2 + (z - z_s)^2}$ is the distance to the source, θ is the angle of incidence, $A(\omega)$ is the amplitude spectrum, and $k^{fl} = \omega s_P$ is the acoustic fluid wavenumber, where the fluid P -wave slowness is given by $s_P = \sqrt{\rho_f/K_f}$. The directivity function $D(\theta)$, which characterizes the radiation pattern of the source, is given by

$$D(\theta) = \frac{J_1(k^{fl}a \sin \theta)}{k^{fl}a \sin \theta}. \quad (37)$$

TABLE 2: (Modified from [44].) Parameters of the poroelastic medium and fluid layer. The temperature is 293.15 K.

Property	Symbol	Value	Unit
Bulk modulus skeleton grains ^a	K_{fr}	$50 \cdot 10^9$	[Pa]
Bulk modulus (pore) fluid ^b	K_f	$2.2 \cdot 10^9$	[Pa]
Bulk modulus framework of grains ^c	K_s	$0.93 \cdot 10^9$	[Pa]
Shear modulus framework of grains ^c	G	$0.88 \cdot 10^9$	[Pa]
Pore fluid viscosity ^b	η	$1 \cdot 10^{-3}$	[kg/(m s)]
Pore fluid density ^b	ρ_f	1000	[kg/m ³]
Solid density ^c	ρ_s	2570	[kg/m ³]
Weighted pore volume-to-surface ratio ^d	Λ	$9.4 \cdot 10^{-6}$	[m]
Porosity of the porous medium ^c	ϕ	0.52	[—]
Permeability ^c	k_0	$3.4 \cdot 10^{-12}$	[m ²]
Tortuosity ^c	α_∞	1.7	[—]
Sample width ^c	w_s	$3.21 \cdot 10^{-2}$	[m]
Relative permittivity of the (pore) fluid ^b	ϵ_{rf}	80.1	[—]
Relative permittivity of the solid ^b	ϵ_{rs}	4	[—]
Fluid magnetic permeability (=μ ₀)	μ_f	$4\pi \cdot 10^{-7}$	[H/m]
(Pore) fluid conductivity ^c	σ_f	$4.8 \cdot 10^{-2}$	[S/m]
Zeta-potential ^f	ζ	$-4.0 \cdot 10^{-2}$	[V]

^a[78], ^b[68]. We take the value of Pyrex 7070 glass for the solid permittivity. ^csee N5B in [79], ^d[29, 59, 80, 81], ^emeasured values, and ^fsee [22]. We assume that conductivity is due to a NaCl salt solution and pH = 6.

Here, J_1 is the Bessel function of the first kind and first order and a is the radius of the transducer. Schakel et al. [44] show that seismoelectric effects can be modelled by expanding the source pressure wavefield into conical waves, which leads to the so-called Sommerfeld integral, and by relating acoustic potentials to electric signals with reflection/transmission coefficients as well as electric-solid ratios. While Schakel et al. [44] model both coseismic and interface field responses, we only model the coseismic fields. We arrive at the following Sommerfeld integral for the coseismic electric potential $\hat{\varphi}(\omega, r_r, z_r)$ at receiver position (r_r, z_r) for $r_s = 0$, $z_s < 0$, $z_r > 0$,

$$\begin{aligned} \hat{\varphi}(\omega, r_r, z_r) &= -i \frac{A(\omega)}{\omega^2 \rho_f} \int_0^\infty \frac{k_r}{k_z^{fl}} D(k_r) J_0(k_r r_r) e^{ik_z^{fl} z_s} \alpha_{pf}(\omega) T_{pf}(k_r) \\ &\quad \left(e^{-ik_z^{pf} z_r} + R_{pf}(k_r) e^{-ik_z^{pf} (2w_s - z_r)} \right) dk_r, \end{aligned} \quad (38)$$

where $k_r = k^{fl} \sin \theta$ and $k_z^{fl} = k^{fl} \cos \theta$ are the radial and vertical components of k^{fl} , respectively, and k_z^{pf} is the vertical component of the fast P -wave wavenumber. The fast P -wave wavenumber is $k^{pf} = \omega s_{pf}(\omega)$, where the fast P -wave slowness is given by the dispersion relations (27)-(28). Note that the factor $\omega^2 \rho_f$ in the denominator of (38) is absent in Schakel et al. [44], because their reflection and transmission (conversion) coefficients are pressure normalized, whereas here they are displacement potential normalized. The transmission coefficient $T_{pf}(k_r)$ relates the incident acoustic wavefield to the transmitted fast P -wave signal. The transmitted signal generates a coseismic potential at $(r, z) = (r_r, z_r)$.

It also reflects $[R_{pf}(k_r)]$ at $z = w_s$, and travels back to the receiver position, where it generates a second coseismic potential. The transmission coefficient $T_{pf}(k_r)$ is derived from substituting plane wave expressions into the following (open-pore) boundary conditions [76]

$$\begin{aligned} \hat{u}_{s,z} + \hat{w}_z &= \hat{u}_z^{fl}, \\ \hat{p} &= \hat{p}^{fl}, \\ \hat{\sigma}_{13} &= \hat{\sigma}_{33} = 0, \end{aligned} \quad (39)$$

with subscript z denoting the z -component of the vectors and where \hat{u}^{fl} denotes the fluid displacement. By only solving the mechanical (Biot) boundary value problem (no electrokinetic coupling is present in (39)), the interface field responses are neglected. Pride and Garambois [77] discussed the influence of the Biot slow wave in the generation of interface response seismoelectric amplitudes and numerically showed that when the Biot slow wave is neglected, the amplitudes can easily be off by as much as an order of magnitude. In our approach, that aims to model coseismic fields rather than interface responses, the Biot slow wave is taken into account in the solution of the boundary value problem (39). Its coseismic field is not modeled. For the parameters of Table 2, the slow wave skin depth is approximately 5 mm at 500 kHz and is unlikely to cause any appreciable coseismic signal for larger distances. We substitute the following plane wave expressions into (39)

$$\begin{aligned} \hat{\varphi}_1^{fl} &= \tilde{\varphi}_1^{fl} e^{-i(k_r r_r \pm k_z^{fl} z)}, \\ \hat{\varphi}_m^s &= \tilde{\varphi}_m^s e^{-i(k_r r_r + k_z^m z)}, \\ \hat{\Psi}_{SV}^s &= \left(0, \tilde{\Psi}_{SV}^s e^{-i(k_r r_r + k_z^s z)}, 0 \right)^T, \end{aligned} \quad (40)$$

for $l = I, R$. Hence we consider an incident (I) acoustic wave that reflects (R) and transmits as Pf -, Ps -, and vertical shear (SV)-waves. Displacement fields are obtained from these expressions as follows

$$\begin{aligned}\hat{\mathbf{u}}_I^{fl} &= \nabla \hat{\varphi}_I^{fl}, \\ \hat{\mathbf{u}}_m &= \nabla \hat{\varphi}_m^s, \\ \hat{\mathbf{u}}_{SV} &= \nabla \times \hat{\Psi}_{SV}^s.\end{aligned}\quad (41)$$

Fluid pressure is related to fluid displacement by $\hat{p}^{fl} = -K_f \nabla \cdot \hat{\mathbf{u}}^{fl}$, with $\hat{\mathbf{u}}^{fl} = \hat{\mathbf{u}}_I^{fl} + \hat{\mathbf{u}}_R^{fl}$. For the poroelastic medium, solid displacement and pore-fluid displacement are obtained as follows

$$\begin{aligned}\hat{\mathbf{u}}_s &= \hat{\mathbf{u}}_{s,Pf} + \hat{\mathbf{u}}_{s,Ps} + \hat{\mathbf{u}}_{s,SV}, \\ \hat{\mathbf{u}}_f &= \beta_{Pf} \hat{\mathbf{u}}_{s,Pf} + \beta_{Ps} \hat{\mathbf{u}}_{s,Ps} + \beta_S \hat{\mathbf{u}}_{s,SV}.\end{aligned}\quad (42)$$

Following the basic equations described in [60–64], the pore-fluid pressure and intergranular stresses are obtained. We define the reflection and transmission coefficients as

$$\begin{aligned}R_P &= \frac{\tilde{\varphi}_R^{fl}}{\tilde{\varphi}_I^{fl}}, & T_{Pf} &= \frac{\tilde{\varphi}_{Pf}^s}{\tilde{\varphi}_I^{fl}}, & T_{Ps} &= \frac{\tilde{\varphi}_{Ps}^s}{\tilde{\varphi}_I^{fl}}, \\ T_{SV} &= \frac{\tilde{\Psi}_{SV}^s}{\tilde{\varphi}_I^{fl}},\end{aligned}\quad (43)$$

so that we arrive at the following linear system of equations

$$\mathbf{A} \cdot (R_P, T_{Pf}, T_{Ps}, T_{SV})^T = (k_z^{fl}, \phi \rho_f, 0, 0)^T, \quad (44)$$

where the elements of matrix \mathbf{A} are given in the appendix. By solving (44) and (A.3) we obtain T_{Pf} and R_{Pf} , respectively (see appendix).

For the geometry of Figure 9, where a source is located at $(r_s, z_s) = (0, -15)$ cm, and where the receiver is located at $(r_r, z_r) = (0, 1)$ cm, we numerically evaluate the integral of (38). An experimentally recorded 500 kHz single sine pressure waveform is used for the amplitude spectrum $A(\omega)$. The incident pressure is related to the mechanical displacement potential $\tilde{\varphi}_{Pf}^s$ in the denominator of $\alpha_{Pf}(\omega)$ (see (34)) by the factor $\omega^2 \rho_f$, which arises from the relation $\hat{p}^{fl} = -K_f \nabla \cdot \hat{\mathbf{u}}^{fl}$. The parameters of Table 2 are used and a 144–896 kHz numerical band-pass filter is applied. Figure 10(a) shows the resulting coseismic electric potentials caused by the fast P -wave. The first (CSP1) arrives at around 0.106 ms. This is the travel time of the acoustic wave from the source to the interface (approximately 0.101 ms) plus the travel time of the fast P -wave from the interface to the receiver location (approximately 0.005 ms). The predicted amplitude of the coseismic electric potential is approximately 0.5 mV, for an incident pressure amplitude of approximately 50 kPa. The second coseismic potential CSP2 arrives at around 0.130 ms and has an amplitude of approximately 0.15 mV. We conclude that coseismic electric potentials can be straightforwardly modelled in layered geometries by electric-solid ratios and solutions to mechanical boundary value problems.

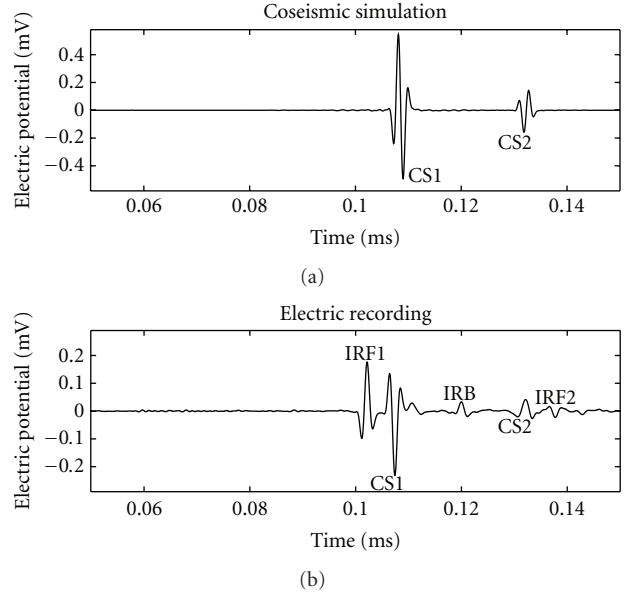


FIGURE 10: (Modified from [44].) Model of coseismic responses (a) and seismoelectric wave propagation measurements (b). Pulse abbreviations are: interface response (from the) front 1 (IRF1), coseismic response 1 (CS1), interface response (from the) back (IRB), coseismic response 2 (CS2), and interface response (from the) front 2 (IRF2).

4.2. Seismoelectric Wave Propagation Experiment. Schakel et al. [44] report on a seismoelectric wave propagation experiment in which coseismic electric and interface field responses are measured. The results are reproduced in Figure 10(b). The geometry of the experiment is that of Figure 9. A 500 kHz single sine pulse generated by a waveform generator (Agilent Technologies 33220A) was used as input to the source. The second interface corresponds with the back of a porous sample. The receiver located at $(r_r, z_r) = (0, 1)$ cm recorded several pulses. The first (IRF1) is the interface response generated at the front ($z = 0$) of the sample (see also Figure 2(c)). It arrives at around 0.100 ms, which corresponds with the acoustic wave travel time from the source to the interface. The travel time of the fast P -wave from the interface to the receiver location is approximately 0.005 ms. Therefore, the next pulse, labelled CS1, is the coseismic (electrical) response caused by the fast P -wave (see also Figure 2(a)). This wave also generates an interface response when it arrives at the back of the sample (IRB). It also reflects as a fast P -wave. When the reflected fast P -wave passes the receiver location for the second time, it generates another coseismic response (CS2). The last significant pulse, labelled (IRF2), is the interface response caused by the reflected fast P -wave when it arrives at the front of the sample. These experimental data were obtained using a 3.21 cm thick sample and a 500 kHz single sine pulse. It takes about 20 μ s for the fast wave to arrive at the second interface, while the (measured) pulse period does not exceed 5 μ s. Thus the pulses are clearly separated in time and do not cause amplitude and waveform changes.

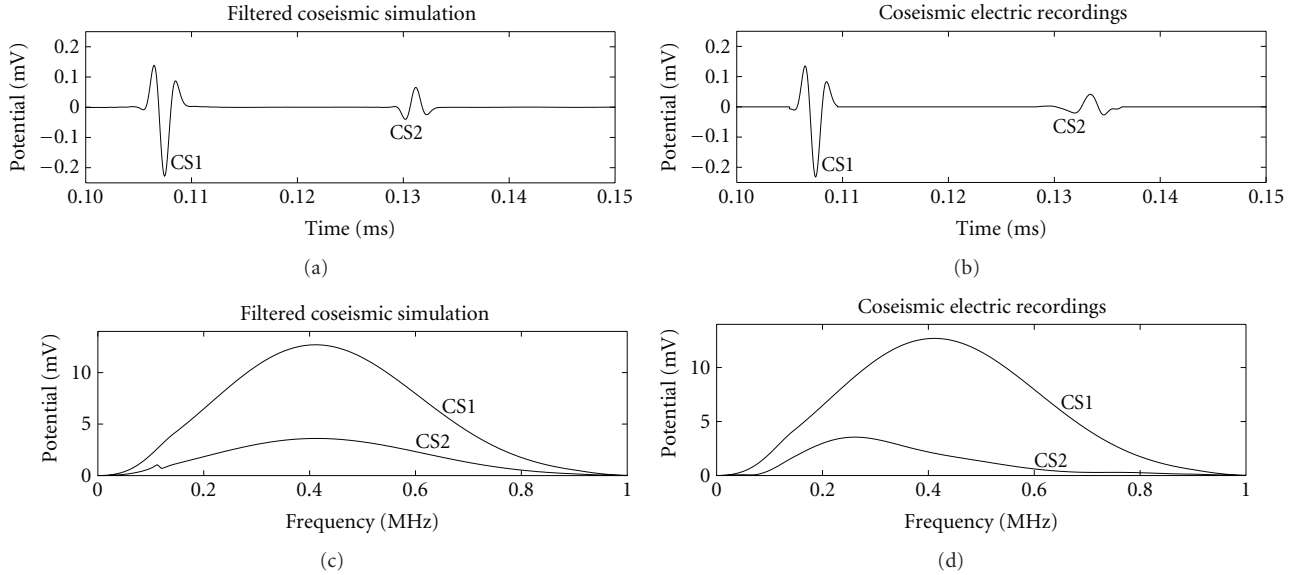


FIGURE 11: Model of filtered coseismic responses in time (a) and frequency domain (c) and coseismic measurements in time (b) and frequency domain (d). Pulse abbreviations are: coseismic response 1 (CS1) and coseismic response 2 (CS2).

By comparing the model for the first coseismic response (CS1 in Figure 10(a)) with the measurement (CS1 in Figure 10(b)) we observe agreement in travel time, waveform and amplitude. Small differences in waveform, such as the onset of the modelled waveform which is absent in the recording, are probably related to geometric misalignment and/or inaccuracies in the model/parameters (Table 2). The scale of Figure 10(a) is different from that of Figure 10(b). This amplitude difference is probably also related to geometric misalignment and/or inaccuracies in the model/parameters. For example, the model predictions are sensitive to the zeta-potential. This parameter was not directly measured but is obtained from an empirical relationship (see Table 2). For general field geometries the seismoelectric amplitudes of radiation generated at interfaces is significantly smaller than the coseismic amplitudes. For field geometries, electric receivers are typically positioned at several seismic wavelengths from the interfaces that generate seismoelectric conversion. In our experiment, the electric receiver is at 1 cm from the front interface, while the fast P -wave wavelength is roughly 4 mm. For this configuration, the measurements are as shown in Figure 10(b).

The model for the second coseismic response (CS2 in Figure 10(a)) shows less agreement with its corresponding measurement (CS2 in Figure 10(b)). We investigate the reason for this observation by matching the theory to the measurement for CS1. A frequency filter is constructed from the selected theoretical and measured CS1 pulses. This filter is subsequently applied to the selected theoretical CS2. The results are shown in Figure 11. The filtered theoretical CS1 fits the measurements exactly because it is forced to coincide with the measured CS1. The filtered theoretical CS2 now shows better agreement in terms of waveform and amplitude (Figures 11(a) and 11(b)). However there also remains to be

mismatch, particularly the measured CS2 has its energy distributed over smaller frequencies than the filtered theoretical CS2. The latter fact is illustrated in Figures 11(c) and 11(d). The filtered theoretical CS2 differs from the filtered theoretical CS1 by the term $R_{Pf}(k_r)e^{-2ik_z^P(w_s-z_r)}$ (see (38)). Thus this observation indicates that the theory underpredicts the amount of seismic attenuation. It is well known that Biot's theory can underestimate seismic attenuation [82]. However, the observation of Figure 11 could also be related to geometric misalignment in the experimental setup. We note that the possibility of underestimation by the electrokinetic coupling ratio $\alpha(\omega)$ is excluded as it is effectively removed by the filter. In this paper we focus only on comparing theoretical and measured coseismic amplitudes rather than the seismoelectric responses at interfaces. The receiver is located at a constant distance from the interface, so that we do not compare the amplitudes to those generated by a (vertical) dipole located at the interface. A thorough comparison of seismoelectric amplitudes radiated from interfaces as a function of distance towards the interface with the pattern due to a dipole is given by [45].

It is possible to model all interface responses and coseismic effects of Figure 10(b) by adopting full electrokinetic theory for the poroelastic medium in the boundary value problem [44]. This results in complicated expressions for the so-called seismoelectric reflection and conversion coefficients, which describe the interface responses, and also for the transmission coefficient T_{Pf} and R_{Pf} . Therefore, in the above, we only adopted Biot's poroelastic theory to solve for T_{Pf} and used the electric-solid ratio $\alpha_{Pf}(\omega)$ to describe the coseismic electric potential of Figure 10(a). The disadvantage of the approach is that interface response effects cannot be modelled. On the other hand, it results in simpler expressions for the coseismic fields.

5. Seismoelectric Interferometry

Considering the combined character of seismo-electromagnetic waves it can be very beneficial to use them for a wide range of applications. (The application for oil-field exploration has already been shown by Thompson et al. [83].) From an imaging point of view, the principle of interferometry has already been proven useful for a wide class of phenomena, for example in seismic systems or electromagnetic systems (e.g., [47, 48]). Hence, we are taking this principle to the next level: correlation imaging with seismo-electromagnetic waves. Before showing some examples, the principle of interferometry will be explained first.

5.1. Theory. Interferometry makes use of the cross-correlation of responses at different receivers in order to obtain the Green's function of the field response between these stations. In other words, it is the deterministic response from one station to the other.

Figure 12 shows a possible seismoelectric interferometry setting. The cross-correlation of electric (E_x) and acoustic signals (v_z) from sources located at the surface (Figure 12(a)) or in the bulk (Figure 12(c)) results in the direct electric response of an acoustic source (f_z) generating a seismoelectric wave (Figure 12(b)). The known challenging problems in using seismo-electromagnetics as a geophysical exploration tool can potentially be addressed by applying interferometric Green's function retrieval techniques to seismo-electromagnetic phenomena [46]. First of all, sources in "classical" seismoelectric surveys need to be strong. This is not always possible and therefore it is beneficial to be able to replace those strong sources by receivers.

A second well-known problem in these conventional seismoelectric surveys is the very low signal-to-noise ratio. By doing interferometry, stacking inherently takes place with a possible improvement of the signal-to-noise ratio as a result.

After deriving the system of equations for coupled seismic and electromagnetic waves in saturated porous media [29], the convolution-type reciprocity theorem and a power balance for seismoelectric waves was derived by Pride and Haartsen [67]. In 2003, this result was extended to a reciprocity theorem of the correlation-type for seismoelectric waves [84].

Following Wapenaar and Fokkema [85], de Ridder et al. [46] showed that the 1D seismoelectric system for the SH-TE propagation mode can be captured in the following matrix-vector equation

$$i\omega\hat{\mathbf{A}}\hat{\mathbf{u}} + \mathbf{D}_x\hat{\mathbf{u}} = \hat{\mathbf{s}}, \quad (45)$$

where matrix $\hat{\mathbf{A}}$ contains the space-dependent material parameters, $\hat{\mathbf{u}}$ represents the field vector (in the space-frequency domain), matrix \mathbf{D}_x contains the spatial differential operator $\partial/\partial x$, $\hat{\mathbf{s}}$ denotes the source vector, and where $i\omega$ arises due to Fourier transformation of the temporal derivative of a field. It is important to capture the 1D seismoelectric system in such a general diffusion, flow and wave equation, in order to employ the derived expressions for unified Green's function retrieval by cross-correlation [47] and to finally end up with interferometric seismoelectric Green's function representations.

Next, considering the Fourier transform of an impulsive source acting at time $t = 0$ s and at location $x = x_s$, $\hat{\mathbf{s}}$ in (45) is replaced by $\mathbf{I}\delta(x - x_s)$. As a consequence, the field vector $\hat{\mathbf{u}}$ can be replaced by a Green's matrix $\hat{\mathbf{G}}(x, x_s, \omega)$. In this way, (45) is changed to

$$i\omega\hat{\mathbf{A}}\hat{\mathbf{G}}(x, x_s, \omega) + \mathbf{D}_x\hat{\mathbf{G}}(x, x_s, \omega) = \mathbf{I}\delta(x - x_s), \quad (46)$$

where the Green's matrix $\hat{\mathbf{G}}(x, x_s, \omega)$ is given by

$$\hat{\mathbf{G}}(x, x_s, \omega) = \begin{pmatrix} \hat{G}^{E,J^e}(x, x_s, \omega) & \hat{G}^{E,J^m}(x, x_s, \omega) & \hat{G}^{E,f}(x, x_s, \omega) & \hat{G}^{E,h^b}(x, x_s, \omega) \\ \hat{G}^{H,J^e}(x, x_s, \omega) & \hat{G}^{H,J^m}(x, x_s, \omega) & \hat{G}^{H,f}(x, x_s, \omega) & \hat{G}^{H,h^b}(x, x_s, \omega) \\ \hat{G}^{v^s,J^e}(x, x_s, \omega) & \hat{G}^{v^s,J^m}(x, x_s, \omega) & \hat{G}^{v^s,f}(x, x_s, \omega) & \hat{G}^{v^s,h^b}(x, x_s, \omega) \\ \hat{G}^{r^b,J^e}(x, x_s, \omega) & \hat{G}^{r^b,J^m}(x, x_s, \omega) & \hat{G}^{r^b,f}(x, x_s, \omega) & \hat{G}^{r^b,h^b}(x, x_s, \omega) \end{pmatrix}. \quad (47)$$

The first superscript (v^s) in $\hat{G}^{v^s,J^e}(x, x_s, \omega)$ denotes the type of response measured at location x , resulting from the type of impulsive source located at x_s , which is denoted by the second superscript (J^e).

Starting from the general interferometric Green's function representation (48) as derived by Wapenaar et al. [47]

$$\begin{aligned} & \hat{\mathbf{G}}(x_B, x_A, \omega) + \hat{\mathbf{G}}^\dagger(x_A, x_B, \omega) \\ &= -\left\{ \hat{\mathbf{G}}(x_B, x, \omega) \mathbf{N}_x \hat{\mathbf{G}}^\dagger(x_A, x, \omega) \right\}_{x_1}^{x_2} \\ & \quad + \int_{\mathcal{D}} \left\{ \hat{\mathbf{G}}(x_B, x, \omega) \left[i\omega(\hat{\mathbf{A}} - \hat{\mathbf{A}}^\dagger) \right] \hat{\mathbf{G}}^\dagger(x_A, x, \omega) \right\} dx, \end{aligned} \quad (48)$$

where it is assumed that the two reciprocity states have the same medium parameters and where \mathbf{N}_x represents the normal vector matrix containing the components of a normal vector \mathbf{n} , arranged in the same way as the partial spatial derivative $\partial/\partial x$ in the matrix \mathbf{D}_x

$$\mathbf{N}_x = \begin{pmatrix} 0 & -1 & 0 & 0 \\ -1 & 0 & 0 & 0 \\ 0 & 0 & 0 & 1 \\ 0 & 0 & 1 & 0 \end{pmatrix}, \quad (49)$$

de Ridder et al. [46] derived the following interferometric integral representation for one element of the seismoelectric

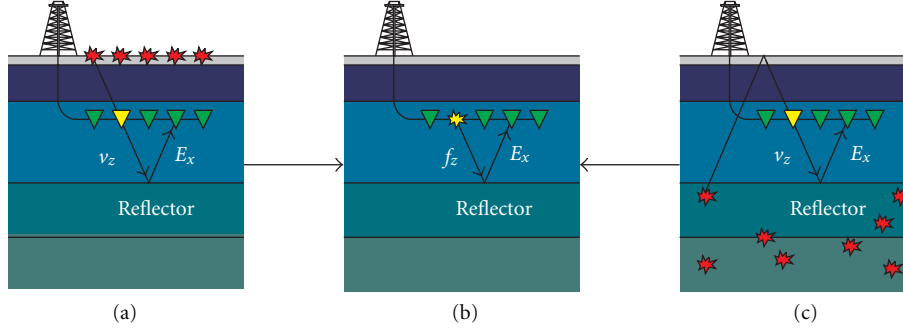


FIGURE 12: Schematic seismoelectric interferometry setting. Cross-correlation of electric (E_x) and acoustic signals (v_z) from sources located at the surface (a) or in the bulk (c) results in the direct electric response of an acoustic source (f_z) generating a seismoelectric wave (b).

SH-TE Green's matrix in 1D (50), using seismoelectric reciprocity theorems

$$\begin{aligned}
 & \left\{ \hat{G}^{E,f}(x_B, x_A, \omega) + \hat{G}^{v^s, J^e}(x_A, x_B, \omega) \right\} \hat{S} \\
 &= \left\{ \hat{G}^{E, J^e}(x_B, x, \omega) \hat{G}^{v^s, J^m*}(x_A, x, \omega) \right. \\
 & \quad + \hat{G}^{E, J^m}(x_B, x, \omega) \hat{G}^{v^s, J^e*}(x_A, x, \omega) \\
 & \quad - \hat{G}^{E, f}(x_B, x, \omega) \hat{G}^{v^s, h*}(x_A, x, \omega) \\
 & \quad \left. - \hat{G}^{E, h}(x_B, x, \omega) \hat{G}^{v^s, f*}(x_A, x, \omega) \right\} \Big|_{x_1}^{x_2} \hat{S} \\
 &+ 2i\omega \int_{\mathcal{D}} \left\{ \hat{G}^{E, J^e}(x_B, x, \omega) i\mathfrak{I} \{ \hat{\epsilon} \} \hat{G}^{v^s, J^e*}(x_A, x, \omega) \right. \\
 & \quad + \hat{G}^{E, f}(x_B, x, \omega) \mathfrak{R} \{ \rho_f \hat{\mathcal{L}}_0 \} \hat{G}^{v^s, J^e*}(x_A, x, \omega) \\
 & \quad - \hat{G}^{E, J^e}(x_B, x, \omega) \mathfrak{R} \{ \rho_f \hat{\mathcal{L}}_0 \} \hat{G}^{v^s, f*}(x_A, x, \omega) \\
 & \quad \left. + \hat{G}^{E, f}(x_B, x, \omega) i\mathfrak{I} \{ \hat{\rho}^c \} \hat{G}^{v^s, f*}(x_A, x, \omega) \right\} dx \hat{S}. \quad (50)
 \end{aligned}$$

To arrive at this form, they have chosen the $\{1, 3\}$ element of the 1D SH-TE seismoelectric Green's matrix (47) and expanded (48) using this element. Here, \hat{S} denotes the power spectrum of the emitted source signal and $\hat{\rho}^c = \rho_b - i\omega k_0(\rho_f)^2/\eta$.

We can distinguish two terms in this integral representation. The first term on the right-hand side represents correlations of recorded responses of sources on the boundary of the domain of reciprocity, whereas the second term on the righthand-side represents correlations of recorded responses of sources throughout the reciprocity domain.

As shown by de Ridder et al. [46], the following source-receiver reciprocity holds

$$\hat{G}^{v^s, J^e}(x_A, x_B, \omega) = -\hat{G}^{E, f}(x_B, x_A, \omega). \quad (51)$$

Hence, the left-hand side of (50) can be rewritten as $2i\mathfrak{I} \{ \hat{G}^{E, f}(x_B, x_A, \omega) \} \hat{S}$. This signal will be antisymmetric around $t = 0$ s in the time-domain.

Looking at expression (50) in more detail it can be seen that the left-hand side, the electric field response registered at x_B generated by an elastic force source located at x_A , is obtained by cross-correlating the registered electric fields at x_B with the registered particle velocities at x_A , which are the

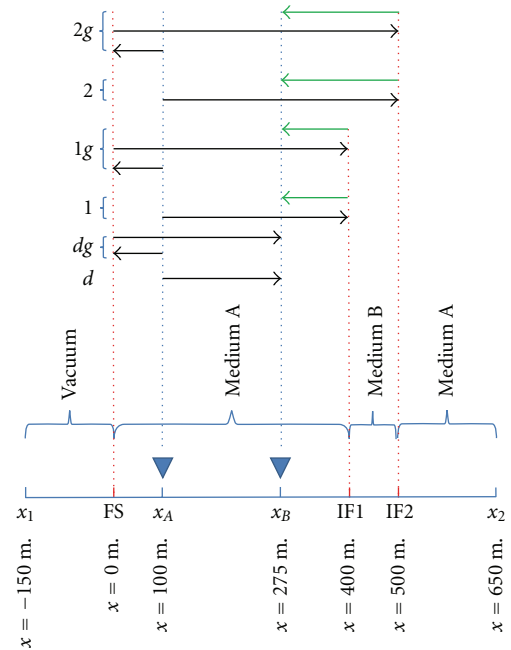


FIGURE 13: The geometry of the 1D numerical experiment. Positions x_A and x_B represent the receiver positions, denoted by the top-down triangles. The upper boundary is called x_1 and the lower boundary x_2 , located at $x = -150$ m and $x = 650$ m, respectively. The positions of the interfaces are visualized by the red bars. FS denotes the free-surface, whereas IF1 and IF2 correspond to the first and second subsurface interfaces, respectively. Furthermore, schematic ray paths of events in the seismoelectric Green's function $G^{E,f}(x_B, x_A, t)$ are shown. The black arrows represent shear wave ray paths, whereas the green arrows depict electromagnetic ray paths. The labels correspond to the labelled events in Figures 14 and 15, where d denotes the direct event and dg its source-side ghost, which are both coseismic field responses, 1 represents the interface response of the most shallow interface and $1g$ its source-side ghost, 2 corresponds to the interface response of the second, deeper interface and event $2g$ represents again its source-side ghost.

result of four different types of boundary sources and two types of domain sources. The two types of domain sources, an electric current source and an elastic force source, are both weighted with two different medium parameters.

TABLE 3: Overview of the relevant medium parameters for the 1D seismoelectric interferometry model.

Property	Unit	Value medium A	Value medium B	Dimension
Porosity	ϕ	0.4	0.2	[—]
Pore fluid density	ρ_f	$1.0 \cdot 10^3$	$1.0 \cdot 10^3$	[kg/m ³]
Solid density	ρ_s	$2.7 \cdot 10^3$	$2.7 \cdot 10^3$	[kg/m ³]
Shear modulus framework of grains	G	$9.0 \cdot 10^9$	$9.0 \cdot 10^9$	[Pa]
Pore fluid viscosity	η	$1.0 \cdot 10^{-3}$	$1.0 \cdot 10^{-3}$	[kg/(m s)]
Static permeability	k_0	$1.3 \cdot 10^{-12}$	$1.6 \cdot 10^{-12}$	[m ²]
Static electrokinetic coupling	\mathcal{L}_0	$1.0 \cdot 10^{-8}$	$1.0 \cdot 10^{-9}$	[m ² /(s V)]
Tortuosity	α_∞	3.0	3.0	[—]
Relative perm. of the (pore) fluid	ϵ_{rf}	80	80	[—]
Relative perm. of the solid	ϵ_{rs}	4	4	[—]
Bulk electric conductivity	σ_0	$1.0 \cdot 10^{-1}$	$1.0 \cdot 10^{-1}$	[S/m]

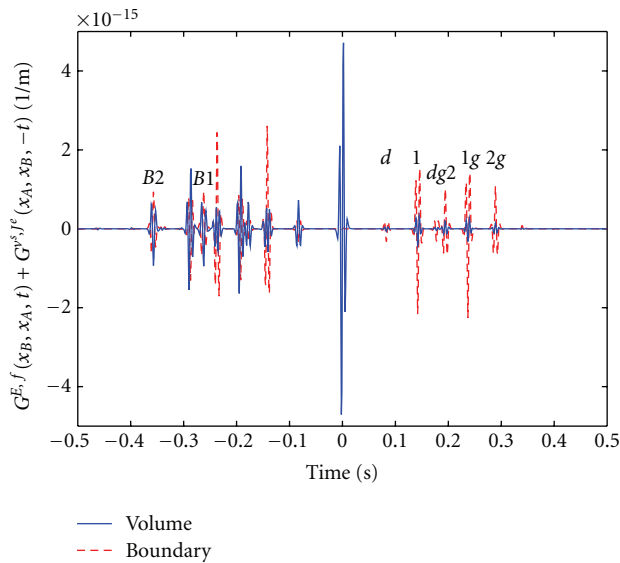


FIGURE 14: Separated contributions of the domain integral and the boundary points to the retrieved Green's functions. In other words, it shows the relative contributions of the two right-hand side terms in (50) to the retrieved Green's functions, for a three-layered medium bounded by a vacuum.

Due to the fact that wave energy is dissipated during wave propagation, the domain sources are necessary to account for these losses. However, these sources are not likely to exist in reality or cannot be rewritten for practical applications and therefore we would like to be able to ignore their contributions.

As is already shown in three examples by de Ridder et al. [46], it is indeed possible (under certain conditions) to obtain accurate Green's functions from boundary sources only. The most complex situation considered by de Ridder et al. [46] was a medium consisting of two layers bounded by a vacuum. For this situation it was shown that the domain integral contribution could be neglected as long as the domain of reciprocity was chosen in such a way, that it included the heterogeneities (i.e., the interface between the

two layers). Then, spurious events would only occur on one side of the symmetrized, retrieved Green's function.

In the following section, we will increase the complexity of the numerical configuration by adding an extra layer to the system, to investigate the Green's function retrieval for a 1D, three-layered system bounded by a free-surface. In other words, we will look at the applicability of the interferometric seismoelectric Green's function representation (50) when there are two interfaces located in the subsurface. We will consider a configuration where a medium B is sandwiched between two identical layers (medium A) with different medium parameters, as given in Table 3. We have chosen the medium parameters in such a way, that there is a very small seismic contrast between the layers; the porosity is the only contrasting seismic parameter between the layers. In this way, we are minimizing the dominant coseismic field response from the two subsurface interfaces and are able to focus mainly on the retrieval of the interface response field. The free-surface on the other hand, acts as a reflector for the seismic waves and therefore the coseismic fields related to this interface are still preserved. In this way, we are able to investigate separately the retrieval of both the coseismic field responses and the interface response fields. For field geometries, the amplitudes of the coseismic field responses related to the subsurface interfaces are often much higher than the interface response field amplitudes.

5.2. Results. We consider a three-layered 1D medium bounded by a vacuum half-space. The top and bottom layer consist of medium parameters belonging to medium A and the sandwiched layer has the properties of medium B (see Table 3). The bottom layer is in fact a half-space. The whole three-layered system is bounded by a vacuum half-space in which only electromagnetic waves can propagate. The interface separating the subsurface from the vacuum is called the free-surface. According to Wapenaar and Fokkema [86], the free-surface acts as a mirror to both shear waves and electromagnetic waves (the latter due to the fact that a 1D geometry is considered here). Therefore, the sources on the domain boundary at the free surface can be neglected and also the contributions of the vacuum above the free-surface can be

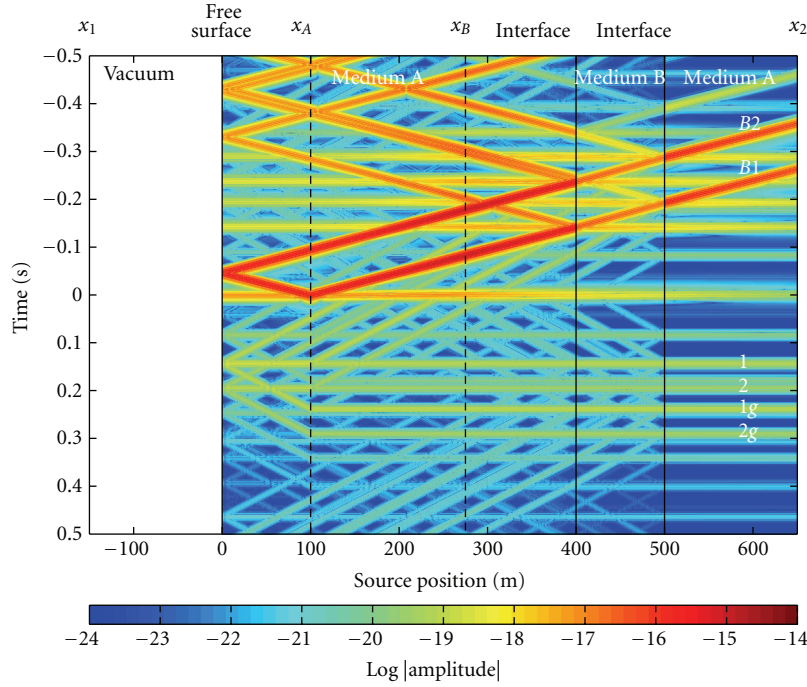


FIGURE 15: The obtained correlation gather of the domain integral for a three-layered medium bounded by a vacuum. The scale is taken as the logarithm of the absolute value of the amplitude. Summing this correlation gather panel yields the total contribution of the domain integral as shown in Figure 14 by the blue volume line. Several events can be recognized.

disregarded. The range of the domain integral contribution is from 0 to 650 m (see Figure 13 for an overview of the geometry). The receivers at x_A and x_B are located at $x = 100$ m and $x = 275$ m, respectively. The upper boundary is called x_1 and the lower boundary x_2 , located at $x = -150$ m and $x = 650$ m, respectively.

Figure 14 shows the time-domain equivalent of the separated contributions of the domain integral and the boundary points to the retrieved Green's functions. In other words, it shows the relative contributions of the two right-hand side terms in (50) to the retrieved Green's functions. The positive time corresponds to the Green's function $G^{E,f}(x_B, x_A, t)$, the electric field response registered at x_B due to an impulsive seismic source located at x_A . As is visible, the dominant contribution in the positive time window comes from just the boundary term. Therefore, it is shown that this Green's function can be mainly reconstructed by using the boundary contribution only. In contrast, the negative time window contains strong domain integral contributions as well. The negative times correspond to the Green's function $G^{v^s, J^e}(x_A, x_B, -t)$, the particle velocity response measured at x_A due to an impulsive electrical current source at x_B . These strong volume source contributions correct the polarity of the single boundary term contribution.

Several events can be recognized in Figure 14. The purely diffusive electromagnetic field is the first event to arrive, with its maximum at approximately $t = 0.58$ ms ($t = -0.58$ ms for the time-reversed causal signal). The second arrival, at approximately $t = 83$ ms corresponds to a direct coseismic

shear wave event (labelled d). Its time-reversed causal equivalent arrives around $t = -83$ ms. The source-side ghost of this direct coseismic shear wave event (labelled dg) arrives at approximately $t = 0.18$ s. The overlapping causal and time-reversed causal electromagnetic events at $t = 0$ s are constructed completely by the sources in the domain integral. In contrast, the shear wave event is retrieved by mainly boundary source contributions. This makes sense, considering the sources of wave energy loss. As mentioned already, the electromagnetic event is, in the considered seismic frequency range, primarily a diffusive field. Therefore, volume sources are required to compensate for the wave energy loss. For the shear wave event, the amount of wave energy loss is relatively small. Hence, the need for volume source energy compensation is negligible. Considering this in terms of the interferometric seismoelectric integral representation (50),

$$\begin{aligned}
 & \left\{ \hat{G}^{E,f}(x_B, x_A, \omega) + \hat{G}^{v^s, J^e*}(x_A, x_B, \omega) \right\} \hat{\mathcal{S}} \\
 &= \left\{ \hat{G}^{E, J^e}(x_B, x, \omega) \hat{G}^{v^s, J^m*}(x_A, x, \omega) \right. \\
 & \quad + \hat{G}^{E, J^m}(x_B, x, \omega) \hat{G}^{v^s, J^e*}(x_A, x, \omega) \\
 & \quad - \hat{G}^{E, f}(x_B, x, \omega) \hat{G}^{v^s, h*}(x_A, x, \omega) \\
 & \quad \left. - \hat{G}^{E, h}(x_B, x, \omega) \hat{G}^{v^s, f*}(x_A, x, \omega) \right\} \Big|_{x_1}^{x_2} \hat{\mathcal{S}} \\
 & + 2i\omega \int_{\mathcal{D}} \left\{ \hat{G}^{E, J^e}(x_B, x, \omega) i\mathfrak{I} \{ \hat{\epsilon} \} \hat{G}^{v^s, J^e*}(x_A, x, \omega) \right.
 \end{aligned}$$

$$\begin{aligned}
& + \widehat{G}^{E,f}(x_B, x, \omega) \Re \left\{ \rho_f \widehat{\mathcal{L}}_0 \right\} \widehat{G}^{v^s, J^e*}(x_A, x, \omega) \\
& - \widehat{G}^{E, J^e}(x_B, x, \omega) \Re \left\{ \rho_f \widehat{\mathcal{L}}_0 \right\} \widehat{G}^{v^s, f*}(x_A, x, \omega) \\
& + \widehat{G}^{E,f}(x_B, x, \omega) i \Im \left\{ \widehat{\rho}^c \right\} \widehat{G}^{v^s, f*}(x_A, x, \omega) \} dx \widehat{\mathcal{S}},
\end{aligned} \tag{52}$$

we can omit the volume source contributions

$$\begin{aligned}
2i\omega \int_{\mathcal{D}} & \left\{ \widehat{G}^{E, J^e}(x_B, x, \omega) i \Im \left\{ \widehat{\epsilon} \right\} \widehat{G}^{v^s, J^e*}(x_A, x, \omega) \right. \\
& + \widehat{G}^{E,f}(x_B, x, \omega) \Re \left\{ \rho_f \widehat{\mathcal{L}}_0 \right\} \widehat{G}^{v^s, J^e*}(x_A, x, \omega) \\
& - \widehat{G}^{E, J^e}(x_B, x, \omega) \Re \left\{ \rho_f \widehat{\mathcal{L}}_0 \right\} \widehat{G}^{v^s, f*}(x_A, x, \omega) \\
& \left. + \widehat{G}^{E,f}(x_B, x, \omega) i \Im \left\{ \widehat{\rho}^c \right\} \widehat{G}^{v^s, f*}(x_A, x, \omega) \right\} dx \widehat{\mathcal{S}} \approx 0.
\end{aligned} \tag{53}$$

The free-surface acts as a mirror to both shear waves and electromagnetic waves and therefore the sources on the domain boundary at the free-surface can be neglected and also the contributions of the vacuum medium above the free-surface can be disregarded. For (52), this effectively means that the contributions of the boundary sources at x_1 can be omitted. The first two terms on the right-hand side of (52) represent the correlation products of the two fields generated by either electrical or magnetic current sources. The contribution of these two correlation products to the positive time window is very small, due to the fact that the causal fields registered at x_B are electric fields which, without any wavetype conversion, only contribute significantly at $t = 0$ (they arrive instantaneously). The contributions of the electric signals with positive seismic traveltimes are negligible, because these signals have encountered at least two wavetype conversions; this implies significant energy losses. Therefore, we can additionally neglect the contributions of the electromagnetic boundary sources (J^e and J^m), ending up with the following reduced interferometric seismoelectric integral representation

$$\begin{aligned}
& \left\{ \widehat{G}^{E,f}(x_B, x_A, \omega) + \widehat{G}^{v^s, J^e*}(x_A, x_B, \omega) \right\} \widehat{\mathcal{S}} \\
& = \left\{ -\widehat{G}^{E,f}(x_B, x_2, \omega) \widehat{G}^{v^s, h*}(x_A, x_2, \omega) \right. \\
& \quad \left. - \widehat{G}^{E,h}(x_B, x_2, \omega) \widehat{G}^{v^s, f*}(x_A, x_2, \omega) \right\} \widehat{\mathcal{S}}.
\end{aligned} \tag{54}$$

Figure 16 shows the result of using this reduced interferometric seismoelectric integral representation. The figure displays a comparison between the exact Green's function in the positive time window $G^{E,f}(x_B, x_A, t)$ and the Green's function retrieved by using (54), that is, by considering only seismic boundary source contributions (f and h) at x_2 . As is visible, the amplitude errors between the exact and retrieved Green's functions are still very small in this situation (about 10% or less), showing that neglecting these types of sources is allowed. When comparing these losses with Figure 14, it is visible that these amplitude losses are probably related to the fact that the volume source contributions (blue solid line in Figure 14) are neglected in Figure 16. In addition, Figure 17 shows the differences between the exact Green's function and

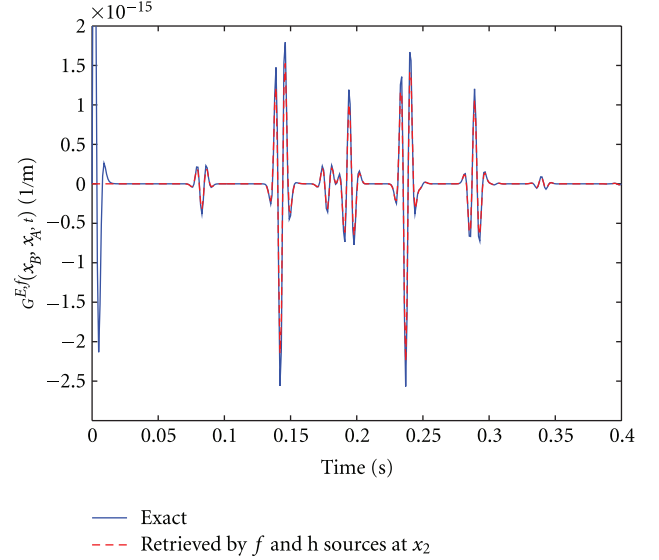


FIGURE 16: Comparison between the exact Green's function $G^{E,f}(x_B, x_A, t)$ and the Green's function retrieved by considering only seismic boundary source contributions in the right-hand side of (52). In other words, the contributions of the domain sources and electromagnetic boundary sources are neglected. As can be seen, the amplitude errors between the exact and retrieved Green's functions are acceptable (about 10% or less). Because only the Green's function corresponding to the positive time window is considered here, no spurious events (which reside in the negative time window) are visible.

the Green's function retrieved by considering only electromagnetic boundary source contributions (J^e and J^m). As is visible, the electromagnetic boundary sources have a negligible contribution to the retrieved Green's function in the positive time window $G^{E,f}(x_B, x_A, t)$. Hence, the amplitude losses visible in Figure 16 are indeed caused by ignoring the volume source contributions. However, the electromagnetic boundary sources do contribute to the Green's function retrieval in the negative time window, that is, $G^{v^s, J^e}(x_A, x_B, -t)$. The two red-dashed peaks at roughly $t = -0.28$ s and $t = -0.38$ s correspond to the spurious events B1 and B2, respectively. These spurious events result from the boundary and volume sources that are related to the edges of the modeling domain. They will remain present when considering only boundary sources or domain sources and will vanish when considering both. It is visible that the spurious events are not present in the exact case. Figure 17 clearly illustrates the contribution of the electromagnetic boundary sources in cancelling out the spurious events in the negative time window. As visible in Figure 15, the spurious events B1 and B2 are never stationary. Due to the bounded modeling domain, a contribution exists of sources at the edge of the modeling domain and that contribution needs to be compensated for by a source at that boundary surface.

Looking at Figure 14, several other events are present as well. For seismoelectric exploration purposes, the events arriving at roughly $t = 0.14$ s and $t = 0.23$ s are of major

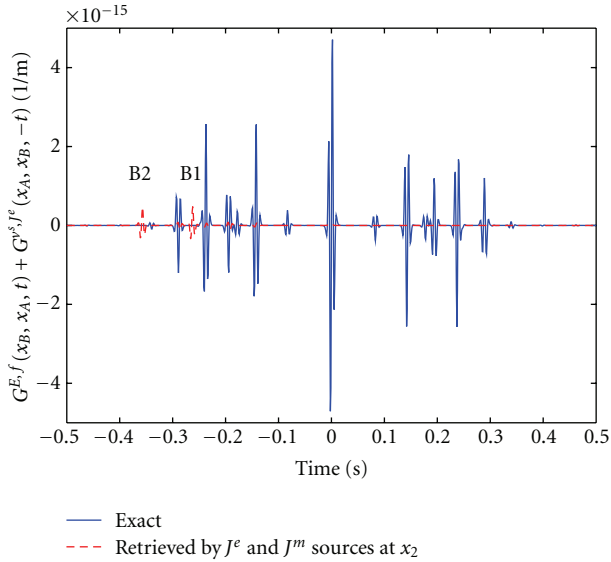


FIGURE 17: Comparison between the exact Green's function $G^{E,f}(x_B, x_A, t) + G^{v^s, J^e}(x_A, x_B, -t)$ and the Green's function retrieved by considering only electromagnetic boundary source contributions (J^e and J^m) in the right-hand side of (52). In other words, the contributions of the domain sources and seismic boundary sources are neglected. As is visible, the electromagnetic boundary sources have a negligible contribution to the retrieved Green's function in the positive time window $G^{E,f}(x_B, x_A, t)$. However, the electromagnetic boundary sources do contribute to the Green's function retrieval in the negative time window, that is, $G^{v^s, J^e}(x_A, x_B, -t)$. The two red-dashed peaks at roughly $t = -0.28$ s and $t = -0.38$ s correspond to the spurious events B_1 and B_2 , respectively. It is visible that the spurious events are not present in the exact case. The contribution of the electromagnetic boundary sources in cancelling out the spurious events in the negative time window is clearly illustrated.

interest. These represent the interface response (labelled 1) of the most shallow interface and its source-side ghost (labelled 1g). Similarly, the other two strong arrivals in the positive time window correspond to the interface response of the second, deeper interface (labelled 2) and its source-side ghost (labelled 2g). The schematic ray paths of these events are displayed in Figure 13. Especially worth noticing are two additional nonphysical events that reside in the negative time-window, labelled B_1 and B_2 . As can be seen in Figure 14, the spurious event B_1 generated by the boundary sources is equal but opposite in sign to the spurious event B_1 from the volume sources. The same holds for spurious event B_2 . So, when retrieving the Green's functions by using the complete right hand side of (52) these spurious events will vanish. However, when considering either boundary sources or domain sources, B_1 and B_2 will remain. The spurious events exist due to a correlation between a seismic and an electromagnetic wave event. Because the correlation implicitly subtracts the traveltime of the seismic event, which is relatively long compared with the traveltime of the electromagnetic wave (which arrives almost immediately), from the

traveltime of the electromagnetic wave, the resulting spurious event resides in the negative time window.

This is visible in Figure 15. This figure represents the obtained correlation gather of the domain integral for a three-layered medium bounded by a vacuum. In other words, it represents the cross-correlation results for different source positions in the domain integral. The scale is taken as the logarithm of the amplitude. This, in order to be able to present the different events despite their large amplitude differences. Summing this correlation gather panel yields the total contribution of the domain integral as shown in Figure 14 by the blue volume line.

As is visible, the correlation gather of this relatively simple 1D example already shows a great complexity of events. It contains lots of multiple arrivals and free-surface ghosts. Therefore, distinguishing all the different events is quite a task. Looking at the different events, some contributions are so-called non-stationary. That means that this contribution of a certain source position to a certain event shifts in time as a function of the source position [46]. For example, looking at the area in between the receiver positions x_A and x_B , all the non-horizontal events are non-stationary. However, outside the range enclosed by the two receivers, the contributions of the sources in the domain integral of the interferometric Green's function representation are stationary. This combined with the slight amplitude losses visible in Figure 16 (about 10% or less), partly confirms both the analyses of Snieder [87] and Slob et al. [48]. They show that, for respectively the seismic interferometry and the electromagnetic interferometry, no spurious events will be created by neglecting the contribution of the domain integral in weakly dissipative media. Only the amplitudes of the retrieved events will be affected. Furthermore, the spurious events that are created in our modeling indeed only reside in the negative time window, as should be the case. Because Figure 16 only considers the Green's function corresponding to the positive time window, no spurious events are visible.

The numerical 1D SH-TE example presented here has shown that the presence of seismic sources only is sufficient to retrieve an accurate seismoelectric response. This means effectively that both seismic and electromagnetic signals are registered at different receivers (without the need of explicit electromagnetic sources) and that by cross-correlating these registered signals, the accurate seismoelectric Green's function (less than 10% amplitude difference) is retrieved. In addition, it has been shown that the electromagnetic boundary source contribution to the Green's function retrieval in the positive time window is negligible. However, the numerical example presented here is of course far from resembling a real Earth setting. Nevertheless, recent seismic interferometry studies performed on real data have shown that, for example, by using seismic noise sources (e.g. from microseisms), P -wave reflection responses can be correctly retrieved [88]. Here it is shown that for the seismoelectric case, the use of seismic sources only is sufficient to correctly retrieve the seismoelectric Green's function response (for the coseismic field responses as well as the interface response fields). This seems promising for real applications of seismoelectric interferometry. We are currently investigating

seismoelectric interferometry for both propagation modes (SH-TE and P-SV-TM) for 3D configurations.

6. Conclusion and Prospects

It was shown that the computed amplitude and phase for the dynamic permeability correlate well with the normalized measurements, whereas for the dynamic SP coefficient, only the normalized amplitude correlates well with the predictions of the theory. This difference could be due to a capacitor effect of the set-up. To prevent the capacitor effect, using insulating plates and electrodes perforated in them may be a solution. In addition, this difference could be related to a slight frequency-dependence of the bulk conductivity. Using independent impedance measurements of the sample could also improve the results. A full-waveform seismoelectric model in a layered geometry was obtained from the solution of a mechanical boundary value problem and the electric-solid ratio of the fast P -wave. The model was simplified by neglecting the interface response. The predictions of fast P -wave coseismic fields were compared against coseismic field measurements. Agreement was found in terms of travel time and waveform, while predicted amplitudes fell within the range of the measured amplitudes. Further modeling indicated that the (Biot) theory underestimates the measured seismic attenuation. The experimental results confirm the existing electrokinetic theory for the seismoelectric wave effect. Moreover, it was shown that coseismic fields can be modeled in a relatively simple way. The electrokinetic theory was subsequently adopted to study the applicability of seismoelectric interferometry. It was shown that the 1D interferometric seismoelectric SH-TE Green's function representation retrieves accurate results for a three-layered 1D medium bounded by a vacuum. From the numerical results it can be concluded that seismic sources at a single boundary location are sufficient to extract the 1D electric field response generated by an impulsive seismic source in a layered model, both for the coseismic field responses and the interface response fields. In addition, it has been shown that the electromagnetic boundary source contribution to the Green's function retrieval in the positive time window is negligible. However, the numerical example presented here is of course far from resembling a real Earth setting. Nevertheless, recent seismic interferometry studies performed on real data have shown that by using seismic noise sources, for example P -wave reflection responses can be correctly retrieved. Here it is shown that for the seismoelectric case, the use of seismic sources only is sufficient to correctly retrieve the

seismoelectric Green's function response (for the coseismic field responses as well as the interface response fields). This seems promising for real applications of seismoelectric interferometry.

Appendix

Substituting plane wave expressions into the poroelastic boundary conditions (39) for an incident acoustic wave from the fluid which impinges on a fluid/poroelastic-medium boundary leads to the following linear system of equations

$$\mathbf{A} \cdot (R_p, T_{Pf}, T_{Ps}, T_{SV})^T = (k_z^{fl}, \phi \rho_f, 0, 0)^T, \quad (\text{A.1})$$

where the elements of matrix \mathbf{A} are

$$\begin{aligned} a_{11} &= k_z^{fl}, \\ a_{21} &= -\phi \rho_f, \\ a_{12} &= [1 - \phi + \phi \beta_{Pf}(\omega)] k_z^{Pf}, \\ a_{22} &= [Q + R \beta_{Pf}(\omega)] s_{Pf}^2(\omega), \\ a_{32} &= k_r k_z^{Pf}, \\ a_{42} &= k_r^2 - \frac{\omega^2 s_{Pf}^2(\omega) N_{Pf}(\omega)}{(2G)}, \\ a_{13} &= [1 - \phi + \phi \beta_{Ps}(\omega)] k_z^{Ps}, \\ a_{23} &= [Q + R \beta_{Ps}(\omega)] s_{Ps}^2(\omega), \\ a_{33} &= k_r k_z^{Ps}, \\ a_{43} &= k_r^2 - \frac{\omega^2 s_{Ps}^2(\omega) N_{Ps}(\omega)}{(2G)}, \\ a_{14} &= [1 - \phi + \phi \beta_S(\omega)] k_r, \\ a_{34} &= k_r^2 - \frac{\omega^2 s_S^2(\omega)}{2}, \\ a_{44} &= -k_r k_z^{SV}, \end{aligned} \quad (\text{A.2})$$

and $a_{31} = a_{41} = a_{24} = 0$, and where $N_m(\omega) = P - (1 - \phi)Q/\phi + [Q - (1 - \phi)R/\phi]\beta_m(\omega)$, for $m = P_f, P_s$.

Substituting plane wave expressions into the poroelastic boundary conditions (39) for an incident fast P -wave from a poroelastic-medium which impinges on a fluid/poroelastic-medium boundary leads to the following linear system of equations

$$\begin{aligned} \mathbf{B} \cdot (T_p, R_{Pf}, R_{Ps}, R_{SV})^T \\ = \left([1 - \phi + \phi \beta_{Pf}(\omega)] k_z^{Pf}, [Q + R \beta_{Pf}(\omega)] s_{Pf}^2(\omega), k_r k_z^{Pf}, - \left[k_r^2 - \frac{\omega^2 s_{Pf}^2(\omega) N_{Pf}(\omega)}{2G} \right] \right)^T \end{aligned} \quad (\text{A.3})$$

where the elements of matrix \mathbf{B} are

$$\begin{aligned}
b_{11} &= k_z^{fl}, \\
b_{21} &= \phi \rho_f, \\
b_{12} &= [1 - \phi + \phi \beta_{Pf}(\omega)] k_z^{Pf}, \\
b_{22} &= -[Q + R \beta_{Pf}(\omega)] s_{Pf}^2(\omega), \\
b_{32} &= k_r k_z^{Pf}, \\
b_{42} &= k_r^2 - \frac{\omega^2 s_{Pf}^2(\omega) N_{Pf}(\omega)}{2G}, \\
b_{13} &= [1 - \phi + \phi \beta_{Ps}(\omega)] k_z^{Ps}, \\
b_{23} &= -[Q + R \beta_{Ps}(\omega)] s_{Ps}^2(\omega), \\
b_{33} &= k_r k_z^{Ps}, \\
b_{43} &= k_r^2 - \frac{\omega^2 s_{Ps}^2(\omega) N_{Ps}(\omega)}{2G}, \\
b_{14} &= -[1 - \phi + \phi \beta_S(\omega)] k_r, \\
b_{34} &= -\left[k_r^2 - \frac{\omega^2 s_S^2(\omega)}{2} \right], \\
b_{44} &= k_r k_z^{SV},
\end{aligned} \tag{A.4}$$

and $b_{31} = b_{41} = b_{24} = 0$. The reflection and transmission coefficients are defined as

$$\begin{aligned}
T_p &= \frac{\tilde{\varphi}^{fl}}{\tilde{\varphi}_{Pf,I}^s}, & R_{Pf} &= \frac{\tilde{\varphi}_{Pf,R}^s}{\tilde{\varphi}_{Pf,I}^s}, & R_{Ps} &= \frac{\tilde{\varphi}_{Ps}^s}{\tilde{\varphi}_{Pf,I}^s}, \\
R_{SV} &= \frac{\tilde{\psi}_{SV}^s}{\tilde{\varphi}_{Pf,I}^s}.
\end{aligned} \tag{A.5}$$

The potentials occur in the following plane wave expressions

$$\begin{aligned}
\hat{\varphi}^{fl} &= \tilde{\varphi}^{fl} e^{-i(k_r r_r + k_z^{fl} z)}, \\
\hat{\varphi}_q^s &= \tilde{\varphi}_q^s e^{-i(k_r r_r \pm k_z^{Pf} z)}, \\
\hat{\varphi}_{Ps}^s &= \tilde{\varphi}_{Ps}^s e^{-i(k_r r_r - k_z^{Ps} z)}, \\
\hat{\Psi}_{SV}^s &= \left(0, \tilde{\psi}_{SV}^s e^{-i(k_r r_r - k_z^{SV} z)}, 0 \right)^T,
\end{aligned} \tag{A.6}$$

for q is Pf , I or Pf , R . The subscript I and R refer to the incident and reflected wave, respectively. These potentials are related to the displacement fields as follows

$$\begin{aligned}
\hat{\mathbf{u}}^{fl} &= \nabla \hat{\varphi}^{fl}, \\
\hat{\mathbf{u}}_{s,q} &= \nabla \hat{\varphi}_q^s, \\
\hat{\mathbf{u}}_{s,Ps} &= \nabla \hat{\varphi}_{Ps}^s, \\
\hat{\mathbf{u}}_{s,SV} &= \nabla \times \hat{\Psi}_{SV}^s, \\
\hat{\mathbf{u}}_s &= \hat{\mathbf{u}}_{s,Pf,I} + \hat{\mathbf{u}}_{s,Pf,R} + \hat{\mathbf{u}}_{s,Ps} + \hat{\mathbf{u}}_{s,SV}, \\
\hat{\mathbf{u}}_f &= \beta_{Pf} \hat{\mathbf{u}}_{s,Pf,I} + \beta_{Pf} \hat{\mathbf{u}}_{s,Pf,R} + \beta_{Ps} \hat{\mathbf{u}}_{s,Ps} + \beta_S \hat{\mathbf{u}}_{s,SV}.
\end{aligned} \tag{A.7}$$

Fluid pressure is related to fluid displacement by $\hat{p}^{fl} = -K_f \nabla \cdot \hat{\mathbf{u}}^{fl}$. Pore-fluid pressure and intergranular stresses are obtained following the basic equations described in [60–64].

Acknowledgments

The research was performed at Delft University of Technology. The research was partly funded as Shell-FOM (Fundamental Research on Matter) projects within the research programs “The physics of fluids and sound propagation” and “Innovative physics for oil and gas.” The authors would like to thank Kees Wapenaar for useful comments, as well as the editor and two anonymous reviewers for constructive remarks and suggestions to improve this journal paper.

References

- [1] F. Reuss, “Sur un nouvel effet de l’électricité galvanique,” *Mémoires de la Société Imperiale de Naturalistes de Moscou*, vol. 2, pp. 327–336, 1809.
- [2] J. G. Sunderland, “Electrokinetic dewatering and thickening—I. Introduction and historical review of electrokinetic applications,” *Journal of Applied Electrochemistry*, vol. 17, no. 5, pp. 889–898, 1987.
- [3] J. H. Masliyah and S. Bhattacharjee, *Electrokinetic and Colloid Transport Phenomena*, John Wiley & Sons, 2006.
- [4] E. J. W. Verwey and J. T. H. G. Overbeek, *Theory of the Stability of Lyophobic Colloids*, Elsevier, 1948.
- [5] S. S. Haines, *Seismoelectric imaging of shallow targets*, Ph.D. thesis, Stanford University, 2004.
- [6] B. Kroeger, *Modellierung und sensitivitätsanalysen für seismoelektrik mit finiten elementen*, Ph.D. thesis, Technischen Universität Berlin, 2007.
- [7] G. I. Block and J. G. Harris, “Conductivity dependence of seismoelectric wave phenomena in fluid-saturated sediments,” *Journal of Geophysical Research B*, vol. 111, no. 1, Article ID B01304, 2006.
- [8] P. M. Reppert, F. D. Morgan, D. P. Lesmes, and L. Jouniaux, “Frequency-dependent streaming potentials,” *Journal of Colloid and Interface Science*, vol. 234, no. 1, pp. 194–203, 2001.
- [9] W. Lowrie, *Fundamentals of Geophysics*, Cambridge University Press, 2007.
- [10] G. Quincke, “Über eine neue art elektrischer ströme,” *Annalen der Physik und Chemie*, vol. 107, no. 5, pp. 1–48, 1859.
- [11] H. Helmholtz, “Studien über elektrische grenzschichten,” *Annalen der Physik und Chemie*, vol. 7, pp. 337–387, 1879.
- [12] M. von Smoluchowski, “Contribution à la théorie de l’endosmose électrique et de quelques phénomènes corrélatifs,” *Bulletin International de l’Academie des Sciences de Cracovie*, vol. 8, pp. 182–199, 1903.
- [13] L. Onsager, “Reciprocal relations in irreversible processes—I,” *Physical Review*, vol. 37, no. 4, pp. 405–426, 1931.
- [14] L. Onsager, “Reciprocal relations in irreversible processes—II,” *Physical Review*, vol. 38, no. 12, pp. 2265–2279, 1931.
- [15] Leibniz-Institut fuer Angewandte Geophysik (LIAG) Hannover, 2008, <http://www.liag-hannover.de/>.
- [16] G. Gouy, “Sur la constitution de la électrique a la surface d’un électrolyte,” *Journal de Physique*, vol. 9, pp. 457–468, 1910.
- [17] D. L. Chapman, “A contribution to the theory of electrocapilarity,” *Philosophical Magazine*, vol. 25, pp. 475–481, 1913.
- [18] O. Stern, “The theory of the electrolytic double-layer,” *Electrochemistry*, vol. 30, p. 508, 1924.
- [19] B. Derjaguin and L. Landau, “Theory of the stability of strongly charged lyophobic soils and of the adhesion of strongly charged particles in solution of electrolytes,” *Progress in Surface Science*, vol. 50, pp. 633–662, 1941.

- [20] R. R. Thompson, "The seismic electric effect," *Geophysics*, vol. 1, no. 2, pp. 327–335, 1936.
- [21] J. Frenkel, "On the theory of seismic and seismoelectric phenomena in moist soil," *Journal of Physics, USSR*, vol. 8, pp. 230–241, 1944.
- [22] S. R. Pride and S. Garambois, "Electroseismic wave theory of Frenkel and more recent developments," *Journal of Engineering Mechanics*, vol. 131, no. 9, pp. 898–907, 2005.
- [23] S. T. Martner and N. R. Sparks, "The electroseismic effect," *Geophysics*, vol. 14, no. 2, pp. 297–308, 1959.
- [24] R. A. Broding, S. D. Buchanan, and D. P. Hearn, "Field experiments on the electroseismic effect," *Geophysics*, vol. 58, pp. 898–903, 1963.
- [25] L. T. Long and W. K. Rivers, "Field measurement of the electroseismic response," *Geophysics*, vol. 40, no. 2, pp. 233–245, 1975.
- [26] A. H. Thompson, S. Hornbostel, J. Burns et al., "Field tests of electroseismic hydrocarbon detection," *Geophysics*, vol. 72, no. 1, pp. N1–N9, 2007.
- [27] O. Kelder, *Frequency-dependent wave propagation in water saturated porous media*, Ph.D. thesis, Delft University of Technology, 1998.
- [28] J. Neev and F. R. Yeatts, "Electrokinetic effects in fluid-saturated poroelastic media," *Physical Review B*, vol. 40, no. 13, pp. 9135–9141, 1989.
- [29] S. Pride, "Governing equations for the coupled electromagnetics and acoustics of porous media," *Physical Review B*, vol. 50, no. 21, pp. 15678–15696, 1994.
- [30] S. S. Haines and S. R. Pride, "Seismoelectric numerical modeling on a grid," *Geophysics*, vol. 71, no. 6, pp. N57–N65, 2006.
- [31] Z. Zhu, M. W. Haartsen, and M. N. Toksöz, "Experimental studies of electrokinetic conversions in fluid-saturated borehole models," *Geophysics*, vol. 64, no. 5, pp. 1349–1356, 1999.
- [32] Z. Zhu, M. W. Haartsen, and M. N. Toksöz, "Experimental studies of seismoelectric conversions in fluid-saturated porous media," *Journal of Geophysical Research B*, vol. 105, no. 12, pp. 28055–28064, 2000.
- [33] Z. Zhu and M. N. Toksoöz, "Crosshole seismoelectric measurements in borehole models with fractures," *Geophysics*, vol. 68, no. 5, pp. 1519–1524, 2003.
- [34] C. Bordes, L. Jouniaux, M. Dietrich, J.-P. Pozzi, and S. Garambois, "First laboratory measurements of seismo-magnetic conversions in fluid-filled Fontainebleau sand," *Geophysical Research Letters*, vol. 33, no. 1, Article ID L01302, pp. 1–5, 2006.
- [35] K. E. Butler, R. D. Russell, A. W. Kepic, and M. Maxwell, "Measurement of the seismoelectric response from a shallow boundary," *Geophysics*, vol. 61, no. 6, pp. 1769–1778, 1996.
- [36] O. V. Mikhailov, M. W. Haartsen, and M. N. Toksöz, "Electroseismic investigation of the shallow subsurface: field measurements and numerical modeling," *Geophysics*, vol. 62, no. 1, pp. 97–105, 1997.
- [37] D. Beamish, "Characteristics of near-surface electrokinetic coupling," *Geophysical Journal International*, vol. 137, no. 1, pp. 231–242, 1999.
- [38] S. Garambois and M. Dietrich, "Seismoelectric wave conversions in porous media: field measurements and transfer function analysis," *Geophysics*, vol. 66, no. 5, pp. 1417–1430, 2001.
- [39] S. S. Haines, S. R. Pride, S. L. Klemperer, and B. Biondi, "Seismoelectric imaging of shallow targets," *Geophysics*, vol. 72, no. 2, pp. G9–G20, 2007.
- [40] J. C. Dupuis, K. E. Butler, and A. W. Kepic, "Seismoelectric imaging of the vadose zone of a sand aquifer," *Geophysics*, vol. 72, no. 6, pp. A81–A85, 2007.
- [41] Z. Zhu and M. N. Toksöz, "Seismoelectric and seismomagnetic measurements in fractured borehole models," *Geophysics*, vol. 70, no. 4, pp. F45–F51, 2005.
- [42] C. Bordes, L. Jouniaux, S. Garambois, M. Dietrich, J. P. Pozzi, and S. Gaffet, "Evidence of the theoretically predicted seismomagnetic conversion," *Geophysical Journal International*, vol. 174, no. 2, pp. 489–504, 2008.
- [43] M. Charara, I. Zaretsky, and M. Zamora, "Seismoelectric modeling of laboratory experiments," in *Proceedings of the 71st Annual International Conference & Technical Exhibition (EAGE '09)*, Rock Physics, Experimental Studies, 2009.
- [44] M. D. Schakel, D. M. J. Smeulders, E. C. Slob, and H. K. J. Heller, "Laboratory measurements and theoretical modeling of seismoelectric interface response and coseismic wave fields," *Journal of Applied Physics*, vol. 109, no. 7, Article ID 074903, pp. 1–5, 2011.
- [45] M. D. Schakel, D. M. J. Smeulders, E. C. Slob, and H. K. J. Heller, "Seismoelectric interface response: experimental results and forward model," *Geophysics*, vol. 76, no. 4, pp. N29–N36, 2011.
- [46] S. A. L. de Ridder, E. Slob, and K. Wapenaar, "Interferometric seismoelectric Green's function representations," *Geophysical Journal International*, vol. 178, no. 3, pp. 1289–1304, 2009.
- [47] K. Wapenaar, E. Slob, and R. Snieder, "Unified green's function retrieval by cross correlation," *Physical Review Letters*, vol. 97, no. 23, Article ID 234301, pp. 1–4, 2006.
- [48] E. Slob, D. Draganov, and K. Wapenaar, "Interferometric electromagnetic Green's functions representations using propagation invariants," *Geophysical Journal International*, vol. 169, no. 1, pp. 60–80, 2007.
- [49] K. Wapenaar, D. Draganov, R. Snieder, X. Campman, and A. Verdel, "Tutorial on seismic interferometry—part 1—basic principles and applications," *Geophysics*, vol. 75, no. 5, pp. A195–A209, 2010.
- [50] J. F. Claerbout, "Synthesis of a layered medium from its acoustic transmission response," *Geophysics*, vol. 33, no. 2, pp. 264–269, 1968.
- [51] K. Wapenaar, D. Draganov, J. van der Neut, and J. Thorbecke, "Seismic interferometry: a comparison of approaches," in *Proceedings of the 74th SEG Annual Meeting SEG*, Session SP 2.7, Denver, Colo, USA, 2004.
- [52] K. Wapenaar, "Retrieving the elastodynamic Green's function of an arbitrary inhomogeneous medium by cross correlation," *Physical Review Letters*, vol. 93, no. 25, Article ID 254301, pp. 1–4, 2004.
- [53] K. Wapenaar, D. Draganov, and J. Robertsson, "Introduction to the supplement on seismic interferometry," *Geophysics*, vol. 71, no. 4, pp. SI1–SI4, 2006.
- [54] K. Wapenaar, D. Draganov, and J. O. A. Robertsson, *Seismic Interferometry: History and Present Status*, Geophysics Reprint Series No. 26, Society of Exploration Geophysicists, 2008.
- [55] K. Wapenaar, E. Slob, R. Snieder, and A. Curtis, "Tutorial on seismic interferometry—part 2—underlying theory and new advances," *Geophysics*, vol. 75, no. 5, pp. A211–A227, 2010.
- [56] G. T. Schuster, *Seismic Interferometry*, Cambridge University Press, 2009.
- [57] K. Wapenaar, D. Draganov, J. Thorbecke, and J. Fokkema, "Theory of acoustic daylight imaging revisited," in *Proceedings of the 72nd Annual International Meeting of the Society of Exploration Geophysicists*, Expanded Abstracts, pp. 2269–2272, 2002.

- [58] D. Draganov, K. Wapenaar, and J. Thorbecke, "Synthesis of the reflection response from the transmission response in the presence of white noise sources," in *Proceedings of the 65th Annual International Conference and Exhibition (EAGE '03)*, Extended Abstracts, P218, 2003.
- [59] D. L. Johnson, J. Koplik, and R. Dashen, "Theory of dynamic permeability and tortuosity in fluid saturated porous media," *Journal of Fluid Mechanics*, vol. 176, pp. 379–402, 1987.
- [60] M. A. Biot, "Theory of propagation of elastic waves in a fluid-saturated porous solid—I—low frequency range," *Journal of the Acoustical Society of America*, vol. 28, no. 2, pp. 168–178, 1956.
- [61] M. A. Biot, "Theory of propagation of elastic waves in a fluid-saturated porous solid—II—higher frequency range," *Journal of the Acoustical Society of America*, vol. 28, no. 2, pp. 179–191, 1956.
- [62] A. Verruijt, "The theory of consolidation," in *Proceedings of the NATO Advanced Study Institute on Mechanics of Fluids in Porous Media*, pp. 349–368, Nijhoff, 1982.
- [63] M. A. Biot and D. G. Willis, "The elastic coefficients of the theory of consolidation," *Journal of Applied Physics*, vol. 24, pp. 594–601, 1957.
- [64] F. Gassmann, "Über die Elastizität poröser Medien," *Vierteljahrsschrift der Naturforschenden Gesellschaft Zürich*, vol. 96, pp. 1–23, 1951.
- [65] D. M. J. Smeulders, "Experimental evidence for slow compressional waves," *Journal of Engineering Mechanics*, vol. 131, no. 9, pp. 908–917, 2005.
- [66] S. X. Li, D. B. Pengra, and P. Z. Wong, "Onsager's reciprocal relation and the hydraulic permeability of porous media," *Physical Review E*, vol. 51, no. 6, pp. 5748–5751, 1995.
- [67] S. R. Pride and M. W. Haartsen, "Electroseismic wave properties," *Journal of the Acoustical Society of America*, vol. 100, no. 3, pp. 1301–1315, 1996.
- [68] D. R. Lide, *Physical Chemistry*, CRC Press/Taylor and Francis, 2002, <http://www.hbcnpnetbase.com/>.
- [69] D. M. J. Smeulders, R. L. G. M. Eggels, and M. E. H. van Dongen, "Dynamic permeability: reformulation of theory and new experimental and numerical data," *Journal of Fluid Mechanics*, vol. 245, pp. 211–227, 1992.
- [70] GKN Sinter Metals, "Reference document of material properties Monel disks," in *Filter-Elements High Porosity Sintered Parts SIKA-RAX*, 2002.
- [71] VitroCOM precision Glass products, (9/99). Reference document of borosilicate capillaries Precision Glass products, Vol. 5.
- [72] E. Charlaix, A. P. Kushnick, and J. P. Stokes, "Experimental study of dynamic permeability in porous media," *Physical Review Letters*, vol. 61, no. 14, pp. 1595–1598, 1988.
- [73] R. G. Packard, "Streaming potentials across glass capillaries for sinusoidal pressure," *The Journal of Chemical Physics*, vol. 21, no. 2, pp. 303–307, 1953.
- [74] A. R. Sears and J. N. Groves, "The use of oscillating laminar flow streaming potential measurements to determine the zeta potential of a capillary surface," *Journal of Colloid And Interface Science*, vol. 65, no. 3, pp. 479–482, 1978.
- [75] D. E. Hall, *Basic Acoustics*, John Wiley & Sons, 1987.
- [76] H. Deresiewicz and R. Skalak, "On uniqueness in dynamic poroelasticity," *Bulletin of the Seismological Society of America*, vol. 53, no. 4, pp. 783–788, 1963.
- [77] S. R. Pride and S. Garambois, "The role of Biot slow waves in electroseismic wave phenomena," *Journal of the Acoustical Society of America*, vol. 111, no. 2, pp. 697–706, 2002.
- [78] D. L. Johnson and T. J. Plona, "Acoustic slow waves and the consolidation transition," *Journal of the Acoustical Society of America*, vol. 72, no. 2, pp. 556–565, 1982.
- [79] C. J. Wisse, *On frequency dependence of acoustic waves in porous cylinders*, Ph.D. thesis, Delft University of Technology, 1999.
- [80] D. L. Johnson, D. L. Hemmick, and H. Kojima, "Probing porous media with first and second sound. I. Dynamic permeability," *Journal of Applied Physics*, vol. 76, no. 1, pp. 104–114, 1994.
- [81] J. Jocker and D. Smeulders, "Ultrasonic measurements on poroelastic slabs: determination of reflection and transmission coefficients and processing for Biot input parameters," *Ultrasonics*, vol. 49, no. 3, pp. 319–330, 2009.
- [82] S. R. Pride, J. G. Berryman, and J. M. Harris, "Seismic attenuation due to wave-induced flow," *Journal of Geophysical Research B*, vol. 109, no. 1, Article ID B01201, 2004.
- [83] A. H. Thompson, J. R. Sumner, and S. C. Hornbostel, "Electromagnetic-to-seismic conversion: a new direct hydrocarbon indicator," *Leading Edge*, vol. 26, no. 4, pp. 428–435, 2007.
- [84] C. P. A. Wapenaar, "Reciprocity theorems for seismoelectric waves," *Journal of Seismic Exploration*, vol. 12, no. 2, pp. 103–112, 2003.
- [85] K. Wapenaar and J. Fokkema, "Reciprocity theorems for diffusion, flow, and waves," *Journal of Applied Mechanics, Transactions ASME*, vol. 71, no. 1, pp. 145–150, 2004.
- [86] K. Wapenaar and J. Fokkema, "Green's function representations for seismic interferometry," *Geophysics*, vol. 71, no. 4, pp. SI33–SI46, 2006.
- [87] R. Snieder, "Extracting the Green's function of attenuating heterogeneous acoustic media from uncorrelated waves," *Journal of the Acoustical Society of America*, vol. 121, no. 5, pp. 2637–2643, 2007.
- [88] E. N. Ruigrok, X. Campman, and K. Wapenaar, "Extraction of P-wave reflections from microseisms," *Comptes Rendus*, vol. 343, no. 8-9, pp. 512–525, 2011.

Research Article

On the Validity of the “Thin” and “Thick” Double-Layer Assumptions When Calculating Streaming Currents in Porous Media

Matthew D. Jackson and Eli Leinov

Department of Earth Science and Engineering, Imperial College London, London SW7 2AZ, UK

Correspondence should be addressed to Matthew D. Jackson, m.d.jackson@imperial.ac.uk

Received 10 August 2011; Revised 1 December 2011; Accepted 19 January 2012

Academic Editor: Laurence Jouniaux

Copyright © 2012 M. D. Jackson and E. Leinov. This is an open access article distributed under the Creative Commons Attribution License, which permits unrestricted use, distribution, and reproduction in any medium, provided the original work is properly cited.

We find that the thin double layer assumption, in which the thickness of the electrical diffuse layer is assumed small compared to the radius of curvature of a pore or throat, is valid in a capillary tubes model so long as the capillary radius is >200 times the double layer thickness, while the thick double layer assumption, in which the diffuse layer is assumed to extend across the entire pore or throat, is valid so long as the capillary radius is >6 times smaller than the double layer thickness. At low surface charge density ($<10 \text{ mC} \cdot \text{m}^{-2}$) or high electrolyte concentration ($>0.5 \text{ M}$) the validity criteria are less stringent. Our results suggest that the thin double layer assumption is valid in sandstones at low specific surface charge ($<10 \text{ mC} \cdot \text{m}^{-2}$), but may not be valid in sandstones of moderate- to small pore-throat size at higher surface charge if the brine concentration is low ($<0.001 \text{ M}$). The thick double layer assumption is likely to be valid in mudstones at low brine concentration ($<0.1 \text{ M}$) and surface charge ($<10 \text{ mC} \cdot \text{m}^{-2}$), but at higher surface charge, it is likely to be valid only at low brine concentration ($<0.003 \text{ M}$). Consequently, neither assumption may be valid in mudstones saturated with natural brines.

1. Introduction

Streaming potentials in porous materials arise from the electrical double layer which forms at solid-fluid interfaces (e.g., [1]). The solid surfaces typically become electrically charged, in which case an excess of countercharge accumulates in the adjacent fluid, in an arrangement called the electrical double layer. The double layer comprises an inner compact (Stern) layer and an outer diffuse (Gouy-Chapman) layer. Most of the countercharge typically resides within the Stern layer; however, if the fluid is induced to flow by an external pressure gradient, then some of the excess charge within the diffuse layer is transported with the flow, giving rise to a streaming current. Divergence of the streaming current density establishes an electrical potential, termed the streaming potential (e.g., [2–4]).

Within the diffuse layer, the Poisson-Boltzmann equation is typically used to describe the variation in electrical potential with distance from the solid surface; in cylindrical coordinates and assuming a symmetric, monovalent

electrolyte, the Poisson-Boltzmann equation is given in dimensionless form by [5]

$$\frac{1}{R} \frac{\partial}{\partial R} \left(R \frac{\partial \psi}{\partial R} \right) = \left(\frac{r}{\lambda} \right)^2 \sinh(\psi), \quad (1)$$

where the dimensionless electrical potential is $\psi \equiv V/(kT/e)$, and dimensionless radial position is $R \equiv y/r$ (Figure 1) (see Table 1 for the nomenclature). The electrical potential is denoted V , T is temperature, k is Boltzmann's constant, e is the electron charge, λ is a characteristic lengthscale termed the Debye length, and r is the radius of a cylindrical pore (capillary). The Debye length is a measure of the diffuse layer thickness; its value depends upon the concentration of the salt species and, assuming (1) is valid, is given by

$$\lambda = \left(\frac{2000 N_A C_f e^2}{\epsilon k T} \right)^{-1/2}, \quad (2)$$

where N_A is Avogadro's number, C_f is molar concentration, and T is temperature (e.g., [2]). The derivation of (1)

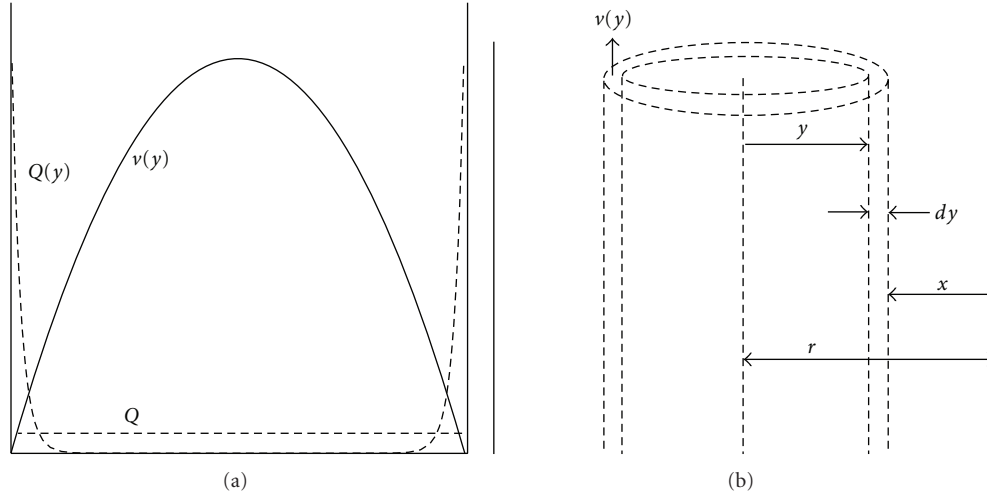


FIGURE 1: (a) Flow velocity (solid line) and excess countecharge within a capillary, invoking the “thin” (short dashes) and “thick” (long dashes) double-layer assumption and assuming a constant excess surface charge density. The width of the “thin” double-layer has been greatly exaggerated. The excess charge on the capillary surface, and hence the total excess countercharge within the capillary, are the same for both the “thin” and “thick” double layer assumptions; the only difference between the models is the distribution of the countercharge within the capillary. (b) Calculation of the streaming current. Assuming Poiseuille flow, each cylinder of fluid of thickness dy travels at velocity $v(y)$ and transports an excess charge density $Q(y)$. The distribution of excess charge within the capillary impacts on the streaming current because excess charge at the centre of the capillary is transported more rapidly by the flow than excess charge at the margin of the capillary. Modified from Jackson [6].

assumes that the ions are point charges, the fluid is continuous and characterized by a constant permittivity which is not affected by the overall electrical field strength, and that the only work done in bringing an ion to a location in the electrical field is related to the field and not to displacement of the fluid or interactions with other ions (e.g., [2]). The Debye length ranges from c. 1 nm in a monovalent electrolyte at 0.1 M concentration, to c. 10 nm at a concentration of 0.001 M, and is independent of the radius of the pore or capillary; if the Debye length exceeds the pore radius, there is double-layer overlap (e.g., [2, pages 363–369]).

In many porous materials of interest to earth and material scientists, it is reasonable to assume that the thickness of the diffuse layer (λ) is small compared to the pore radius (r). This is the so-called “thin double layer assumption” which is valid when $r \gg \lambda$. Under this limiting condition, curvature of the pore surface can be neglected, and the equations describing fluid flow can be linearized in the region of the pore surface. The thin double-layer assumption has been invoked by numerous authors to model streaming potentials in porous media (e.g., [3, 4, 11–14]) and is also invoked in the derivation of the widely applied Helmholtz-Smoluchowski equation (see [2], and references therein):

$$C = \frac{\epsilon \zeta}{\mu \sigma_f}, \quad (3)$$

where C is the streaming potential coupling coefficient, ζ is the zeta potential, which is the electrical potential defined at the inner boundary of the mobile part of the diffuse layer, ϵ is the fluid permittivity, μ is the fluid viscosity, and σ_f is the fluid electrical conductivity.

The Helmholtz-Smoluchowski equation has been used to determine the zeta potential from streaming potential

measurements in numerous studies (see [15], for a review) with appropriate corrections to account for surface electrical conductivity (e.g., [13, 16, 17]). However, a number of recent papers have proposed a different approach to model streaming potential, in which the thickness of the double layer is assumed to be large compared to the radius of the pores (i.e., the Debye length is much greater than the pore radius) [18, 19]. This is the so-called “thick double layer assumption” in which the excess charge density within the pore (Q) is assumed to be constant and independent of distance from the pore surface. The streaming potential coupling coefficient is then given by

$$C = \frac{Q\kappa}{\mu\sigma_f}, \quad (4)$$

where κ is the permeability of the porous material (e.g., [18]).

The advantage of both the “thin” and “thick” double layer assumptions is that calculation of the streaming current is greatly simplified because there is no need to explicitly solve the Poisson-Boltzmann equation (1). Obtaining such solutions is challenging, especially when the pore space has a complex topology; analytical solutions are available only for some restricted cases (e.g., [2], and references therein, [20, 21]). In the thin double-layer assumption, the Poisson-Boltzmann equation is linearized in the region close to the pore surface; in the thick double-layer assumption, the excess charge is assumed to be uniformly distributed across each pore or throat.

It is well known that the thin double-layer assumption is valid if the thickness of the double-layer is “much less” than the radius of the pore or throat ($r \gg \lambda$), while the thick double layer assumption is valid if the thickness of

TABLE 1: Nomenclature.

Symbol	Description	Units
C_f	Fluid concentration	M
e	Charge on an electron	C
ϵ	Fluid permittivity	F m^{-1}
I	Electrical (streaming) current	A
I_d	Dimensionless streaming current	—
k	Boltzmann's constant	$\text{m}^2 \text{kg s}^{-2} \text{K}^{-1}$
κ	Permeability	m^2
L	Capillary length	m
λ	Debye length	m
μ	Fluid viscosity	Pa s
N_A	Avogadro's number	Mol^{-1}
P	Fluid pressure	Pa
q	Volumetric flow rate	$\text{m}^3 \text{s}^{-1}$
Q	Excess charge density	C m^{-3}
Q_s	Surface charge density	C m^{-2}
Q_d	Dimensionless surface charge density	—
r	Capillary radius	m
r_d	Dimensionless capillary radius	—
R	Dimensionless radial position	—
σ_f	Fluid conductivity	S m^{-1}
T	Temperature	K
V	Electrical potential	V
ψ	Dimensionless electrical potential	—
y	Radial position	m
ζ	Zeta potential	V

the double layer is “much greater” than the radius of the pore or throat ($r \ll \lambda$). However, perhaps surprisingly, the conditions for which these assumptions are valid have not yet been determined quantitatively. Yet the two models predict different streaming potential behaviour for a given specific surface charge (Q_s) because excess charge at the centre of a pore or throat is transported more rapidly by the flow than excess charge at the margin of a pore or throat [6, see Figure 1]. Moreover, porous materials encountered in both earth and materials science cover a broad range of pore size (r) and are saturated with fluids of varying salt concentration (salinity) which, assuming the electrical potential in the diffuse layer is described by (1), controls the thickness of the diffuse layer (λ) through (2). Consequently, the assumption of a thin or thick double layer may often be invalid.

Westermann-Clark and Christoforou [5] compared the exclusion-diffusion potential predicted across a single capillary, using a space-charge model that includes a numerical solution of the Poisson-Boltzmann equation, with that obtained using the Meyers-Sievers model, in which the excess charge density is assumed to be independent of distance from the pore surface. They found that the Meyers-Sievers model was a good approximation of the space-charge model when (i) the pore surface charge is small, (ii) when $r/\lambda \rightarrow 0$,

and (iii) when $r/\lambda \rightarrow \infty$. The Meyers-Sievers model is equivalent to the thick double-layer assumption when $r/\lambda \rightarrow 0$. However, it is not equivalent to the thin double-layer assumption when $r/\lambda \rightarrow \infty$. In the Meyers-Sievers model, the diffuse layer thickness is zero in this limit, in which case there is no streaming current and no streaming potential. Consequently, the results of Westermann-Clark and Christoforou [5] cannot be used to determine the validity of the thin and thick double-layer assumptions when calculating streaming current. The thin double-layer assumption invokes a small but nonzero diffuse layer thickness, which gives rise to non-zero streaming potentials. Experimental evidence for a non-zero diffuse layer thickness, even at high ionic strength when (2) predicts that λ becomes infinitesimally small, has been provided by Dukhin et al. [22] and Vinogradov et al. [23].

The aim of this paper is to determine the conditions for which it is valid to invoke the thin and thick double-layer assumptions when calculating the streaming current in a simple bundle of capillary tubes model. Although it is a poor representation of the pore space of most geologic porous media, the advantage of a capillary tubes model is that the capillary scale distribution and transport of excess charge associated with the electrical double-layer is easy to describe; capillary models have been used to calculate the streaming potential in numerous previous studies (see [2], and references therein; [6, 24–26]). Our approach combines those of Jackson [6] and Westermann-Clarke and Christoforou [5]. We investigate the validity of streaming current calculations, rather than streaming potential calculations, because the former is an essential step in calculating the latter, but the latter also requires a model for the electrical conductivity, which is consistent with the pore level distribution of excess charge. The development of such a model is left for future study.

2. Model Formulation

The capillary tubes model is simplified from that described in detail by Jackson [6, 25], so only a brief overview is provided here. Each capillary has the same length L , radius r , and orientation; there are no intersections between capillaries, so the macroscopic mass and charge transport are in one direction only. The charge per unit surface area (the specific surface charge) Q_s is the same in all capillaries, which is reasonable so long as the chemical composition of the fluid and the capillary surfaces do not vary between capillaries. The specific surface charge (Q_s) is evenly distributed along the capillary surfaces and incorporates the contribution of adsorbed charge within the Stern layer; this is equivalent to defining the capillary surface to be the plane separating the Stern and diffuse layers. To maintain a consistent model, we assume that the radius of each capillary (r) is defined between its centre and this plane, which is equivalent to defining the capillary surface to be the shear plane. Since the capillaries are identical, the model is analyzed as if it were a single capillary. A similar approach was followed by Westermann-Clark and Christoforou [5].

The streaming current is calculated assuming laminar flow, in which each concentric cylinder of fluid moving with velocity $v(y)$ along the capillary, transports an excess charge density $Q(y)$ (Figure 1). The fluid velocity is given by Poiseuille's Law:

$$v(y) = \frac{1}{4\mu}(r^2 - y^2)\frac{\Delta P}{L}, \quad (5)$$

where ΔP is the pressure drop along the capillary, and L is the length of the capillary. The streaming current is given by [2, page 65]:

$$I = \int_0^r 2\pi y Q(y) v(y) dy, \quad (6)$$

where we neglect the impact on the streaming current of the electrical potential difference along the capillary [27]. The description of the excess charge density $Q(y)$ depends upon whether we invoke the thin or thick double-layer assumptions, or explicitly model $Q(y)$ using the Poisson-Boltzmann equation.

We begin by invoking the thin double-layer assumption and, for simplicity, the Debye-Hückel approximation in which the electrical potential within the double layer is assumed to be small (<25.7 mV at 25°C ; Hunter [2]). The excess charge density within the diffuse layer can then be described as a function of distance from the capillary surface using

$$Q(x) = Q(x=0) \exp\left(-\frac{x}{\lambda}\right), \quad (7)$$

where $Q(x=0)$ is the excess charge density in the fluid at the capillary surface (which is not equal in magnitude to the surface charge density) and $x = (r - y)$ [2]. The thickness of the diffuse layer is much less than the capillary radius ($\lambda \ll r$), so the velocity profile in the diffuse layer close to the capillary surface can be assumed linear by taking

$$\begin{aligned} (r^2 - y^2) &\approx 2r(r - y), \\ r^2 \left(\frac{x - x^2}{r}\right) &\approx r^2 x, \end{aligned} \quad (8)$$

(see Hunter [2, page 66]). The streaming current can then be written as ([2, equation 3.2.2])

$$I = \frac{Q(x=0)\pi r^2 \Delta P}{\mu L} \int_0^r x \exp\left(-\frac{x}{\lambda}\right) dx. \quad (9)$$

Integrating by parts and recognizing that $Q(x)$ is zero at $x = r$ (indeed, long before $x = r$) the streaming current through a single capillary becomes

$$I = -\frac{Q(x=0)\pi \lambda^2 r^2 \Delta P}{\mu L}. \quad (10)$$

We can express (10) in terms of the surface charge density by recognizing that the total surface charge on the capillary must be balanced by the excess countercharge within the fluid occupying the capillary:

$$2\pi r Q_s L = -L \int_0^r 2\pi y Q(y) dy. \quad (11)$$

Given that $\lambda \ll r$, this yields

$$I|_{\lambda \ll r} = -\frac{Q_s \pi \lambda r^2 \Delta P}{\mu L}. \quad (12)$$

Equation (12) describes the streaming current through a capillary tube of radius r , assuming a thin electrical double layer for which the Debye-Hückel approximation is valid, associated with specific surface charge Q_s . It is easy to show that (12) can also be expressed in terms of the zeta potential at the shear plane (see, e.g., (3.2.3) in Hunter [2]), rather than the specific surface charge.

We now invoke the thick double-layer assumption. The excess charge density in a given phase is constant across the capillary, in which case the streaming current can be written as

$$I = -\frac{Q \pi r^4 \Delta P}{8 \mu L}. \quad (13)$$

As before, we can express (13) in terms of the surface charge density using (11) to give

$$I|_{\lambda \gg r} = -\frac{Q_s \pi r^3 \Delta P}{4 \mu L}. \quad (14)$$

Equation (14) describes the streaming current through a capillary tube of radius r , assuming a thick electrical double layer associated with specific surface charge Q_s .

Finally, we consider explicit solutions to the Poisson-Boltzmann equation to determine $Q(y)$. In cylindrical coordinates, suitable for a capillary tube model, the Poisson-Boltzmann equation is given by (1). There is no variation in electrical potential along the axis of the capillary because there is no concentration difference. The excess charge at a dimensionless radial position $R \equiv y/r$ is related to the dimensionless potential ψ by

$$Q(R) = 2000eC_f N_A \sinh(\psi(R)). \quad (15)$$

Substituting (15) into (6) and simplifying yields the following expression for the streaming current:

$$I = \frac{1000eC_f N_A \pi r^4 \Delta P}{\mu L} \int_0^1 R \cdot \sinh(\psi(R)) \cdot (1 - R^2) dR, \quad (16)$$

with the dimensionless electrical potential (ψ) given by (1). There are no exact analytical solutions to (1), so we use a modified implicit Runge-Kutta scheme with residual control (see [28]) to obtain numerical solutions subject to the following boundary conditions at the shear plane ($R = 1$) and at the centre of the capillary ($R = 0$) [5]:

$$\left. \frac{\partial \psi}{\partial R} \right|_{R=0} = 0, \quad (17a)$$

$$\left. \frac{\partial \psi}{\partial R} \right|_{R=1} = Q_d, \quad (17b)$$

where Q_d is the dimensionless surface charge density, defined as

$$Q_d = -\frac{erQ_s}{\varepsilon kT}. \quad (18)$$

Having determined $\psi(R)$, we integrate (16) numerically over R to determine I_s . Note that the boundary condition (17a) allows us to account for double-layer overlap in our solutions of the Poisson-Boltzmann equation (1).

The behaviour of the dimensionless electrical potential and hence the excess charge, as a function of the radial position, is governed by the dimensionless pore wall surface charge density (Q_d) and the dimensionless capillary radius (r_d). The latter is defined as the ratio of the capillary radius to the Debye length:

$$r_d = \frac{r}{\lambda}. \quad (19)$$

As $r_d \rightarrow 0$, the double-layer thickness becomes very large compared to the capillary radius ($r \ll \lambda$; the limit of a thick double layer), while as $r_d \rightarrow \infty$, the double layer thickness becomes very small compared to the capillary radius ($r \gg \lambda$; the limit of a thin double layer). We quantify the validity of the thin and thick double layer assumptions by plotting dimensionless streaming current (I_d) as a function of dimensionless capillary radius (r_d). The dimensionless streaming current is given by

$$I_d = \frac{I(r_d) - I|_{\lambda \gg r}}{I|_{\lambda \ll r} - I|_{\lambda \gg r}}, \quad (20)$$

where $I(r_d)$ is given by the numerical solution of (16), $I|_{\lambda \ll r}$ is the streaming current in the limit of a thin double layer (12), and $I|_{\lambda \gg r}$ is the streaming current in the limit of a thick double layer (14). If $I_d = 0$, the streaming current calculated by solving the Poisson-Boltzmann equation to determine $Q(R)$ is identical to that obtained assuming a thick double layer, while if $I_d = 1$, the streaming current calculated by solving the Poisson-Boltzmann equation is identical to that obtained assuming a thin double layer.

We select values of surface charge (Q_s) and concentration (C_f) and hold these constant whilst varying the value of r to investigate how the dimensionless streaming current (I_d) varies as a function of r_d . We assume the double-layer thickness (λ) is related to concentration via (2). We investigate concentration (C_f) over the range 10^{-3} –2 M ($\text{mol} \cdot \text{L}^{-1}$) and specific surface electrical charge (Q_s) over the range 1–100 $\text{mC} \cdot \text{m}^{-2}$ to capture the range typically observed in natural systems and laboratory membranes. We discuss the validity of the Poisson-Boltzmann equation (1) over the concentration range investigated, and its impact on our results, later in the paper. Surface charge and electrolyte concentration are varied independently, although the former may depend upon the latter (e.g., [3, 21, 29]). The pH is assumed to remain fixed at 7. Our definition of surface charge includes the contribution of adsorbed charge within the Stern layer, and the range we investigate is based on (i) published values for quartz and clay minerals in contact with NaCl brine (e.g., [18, 21, 29]) and (ii) published zeta

potential data (see Vinogradov et al. [23] for a compilation of values on quartz and glass in NaCl electrolyte, and Kosmulski and Dahlsten [30] for values of clay minerals in NaCl electrolyte), with surface charge related to zeta potential using the Gouy-Chapman model [2]:

$$Q_s = 2\sqrt{2000kTC_fN_A\varepsilon} \sinh\left(\frac{e\zeta}{2kT}\right). \quad (21)$$

Measured values of zeta potential on quartz and clay minerals vary in magnitude from c. 100 mV (at low concentration) to c. 2 mV (at high concentration) over the concentration range investigated here; corresponding values of surface charge density, calculated using (21), lie well within the range we have chosen to investigate and are consistent with published values. Note that the results of our analysis depend only upon the magnitude of the surface charge, not its polarity. The dimensionless surface charge density (Q_d) depends on the fluid permittivity, which varies with concentration (18). We capture this using

$$\varepsilon = 8.85 \times 10^{-12} (80 - 13C_f + 1.065C_f^2 - 0.03006C_f^3), \quad (22)$$

where concentration is in M, and permittivity is in $\text{F} \cdot \text{m}^{-1}$ [31].

Note that our approach, in which we hold Q_s and C_f (and therefore λ) constant and vary r_d , differs from that of Westermann-Clark and Christoforou [5]. They held Q_d constant and varied r_d without acknowledging that this requires Q_s to vary as r_d varies, regardless of whether r_d is varied by changing the capillary radius (r) or diffuse layer thickness (λ). Variations in λ are associated with changes in concentration that impact on permittivity (ε) and hence Q_d (18); variations in r require variations in Q_s to maintain constant Q_d (18). Assuming constant Q_s whilst varying r is more physically plausible than assuming constant Q_d .

3. Results

The variation in excess charge with distance from the capillary wall is shown in Figure 2, for a capillary radius of $r = 4$ nm, two values of Q_s reasonable for geologic porous media (Table 2), and two values of C_f chosen to yield $\lambda \ll r$ at high concentration and $\lambda \gg r$ at low concentration. Also shown is the variation in excess charge with distance, calculated assuming a thin and thick double layers. The latter is constant and given by

$$Q(x) = \frac{Q_s}{r}. \quad (23)$$

The former is obtained using two models: the Debye-Hückel model which assumes that Q_s is small ($< 13.9 \text{ mC} \cdot \text{m}^{-2}$ at

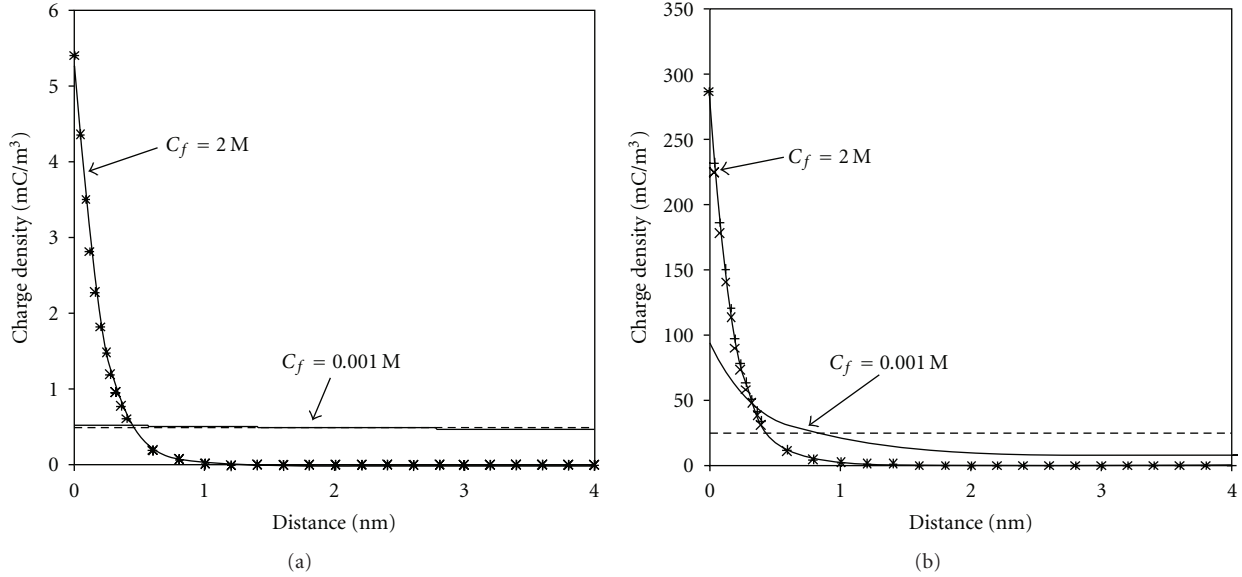


FIGURE 2: Excess charge density (Q) as a function of distance from the capillary centre (x) in a circular capillary of radius 4 nm, for a surface charge of (a) $1 \text{ mC}\cdot\text{m}^{-2}$ and (b) $50 \text{ mC}\cdot\text{m}^{-2}$. Each plot shows results for electrolyte salinities of 0.001 M and 2 M, corresponding to dimensionless capillary radii of 0.41 (i.e., towards the limit for which the thick double layer assumption is valid) and 21.6 (i.e., towards the limit for which the thin double-layer assumption is valid). Solid lines show Q obtained from a numerical solution of the Poisson-Boltzmann equation (1) in conjunction with (16); crosses show Q obtained from an analytic solution to the Poisson-Boltzmann equation assuming a thin double-layer (diagonal crosses show the Gouy-Chapman model given by (24); vertical crosses show the Debye-Hückel model given by (7)); dashed lines show constant Q assuming a thick double layer.

25°C , corresponding to a zeta potential of 25.7 mV) and is given by (7), and the Gouy-Chapman model [2]:

$$Q(x) = 2000eC_fN_A \sinh \left[-2 \ln \left(\frac{1 + \exp(-x/\lambda) \tanh \left((1/2) \sin^{-1} \left(Q_s/2\sqrt{2000kTC_fN_A\epsilon} \right) \right)}{1 - \exp(-x/\lambda) \tanh \left((1/2) \sin^{-1} \left(Q_s/2\sqrt{2000kTC_fN_A\epsilon} \right) \right)} \right) \right]. \quad (24)$$

The results shown in Figure 2 confirm that the excess charge density calculated numerically tends towards the constant value given by (23) when $\lambda \gg r$, while the excess charge calculated numerically agrees with the values given by (7) and (24) when $\lambda \ll r$. This suggests that our numerical solutions to the Poisson-Boltzmann equation yield accurate results. Also note that the Debye-Hückel model provides a reasonably close match to the Gouy-Chapman model up to the largest value of surface charge investigated ($100 \text{ mC}\cdot\text{m}^{-2}$), even though it is strictly valid only for $Q_s < 13.9 \text{ mC}\cdot\text{m}^{-2}$. In this study, the Debye-Hückel model provides an appropriate limiting case for the thin double-layer approximation when calculating the dimensionless streaming current.

Figure 3 shows the variation of dimensionless streaming current (I_d) with dimensionless capillary radius (r_d) for the range of values of surface charge and concentration given in Table 2. Each plot corresponds to a different value of concentration; each curve corresponds to a different value of surface charge. In all cases, I_d reaches zero at small r_d and 1

at large r_d (within a tolerance of 0.1%), which confirms that the thick double-layer assumption is valid at small r_d ($r \ll \lambda$) and the thin double-layer assumption is valid at large r_d ($r \gg \lambda$). However, at intermediate r_d , the curves diverge from zero or 1, demonstrating that there is a range of values of r and λ for which neither assumption is valid. At these intermediate values of r_d , the dimensionless streaming current increases to large values. This reflects the dependence of $I|_{\lambda \ll r}$ on r^2 (12) and $I|_{\lambda \gg r}$ on r^3 (14), which yields a value of r_d at which the values of $I|_{\lambda \ll r}$ and $I|_{\lambda \gg r}$ are identical, and the denominator of (20) falls to zero. An example of this is shown in Figure 4, where the streaming current obtained assuming a thin ($I|_{\lambda \ll r}$) or thick ($I|_{\lambda \gg r}$) double layers (using (12) and (24) resp.) is plotted against dimensionless capillary radius (r_d), and compared to that obtained from a full solution of the Poisson-Boltzmann equation. At intermediate values of r_d , the $I|_{\lambda \ll r}$ and $I|_{\lambda \gg r}$ deviate from the full solution which shows that the thin and thick double-layer assumptions are not valid. When $I|_{\lambda \ll r}$ and $I|_{\lambda \gg r}$ intersect, the dimensionless streaming current is undefined because the denominator of

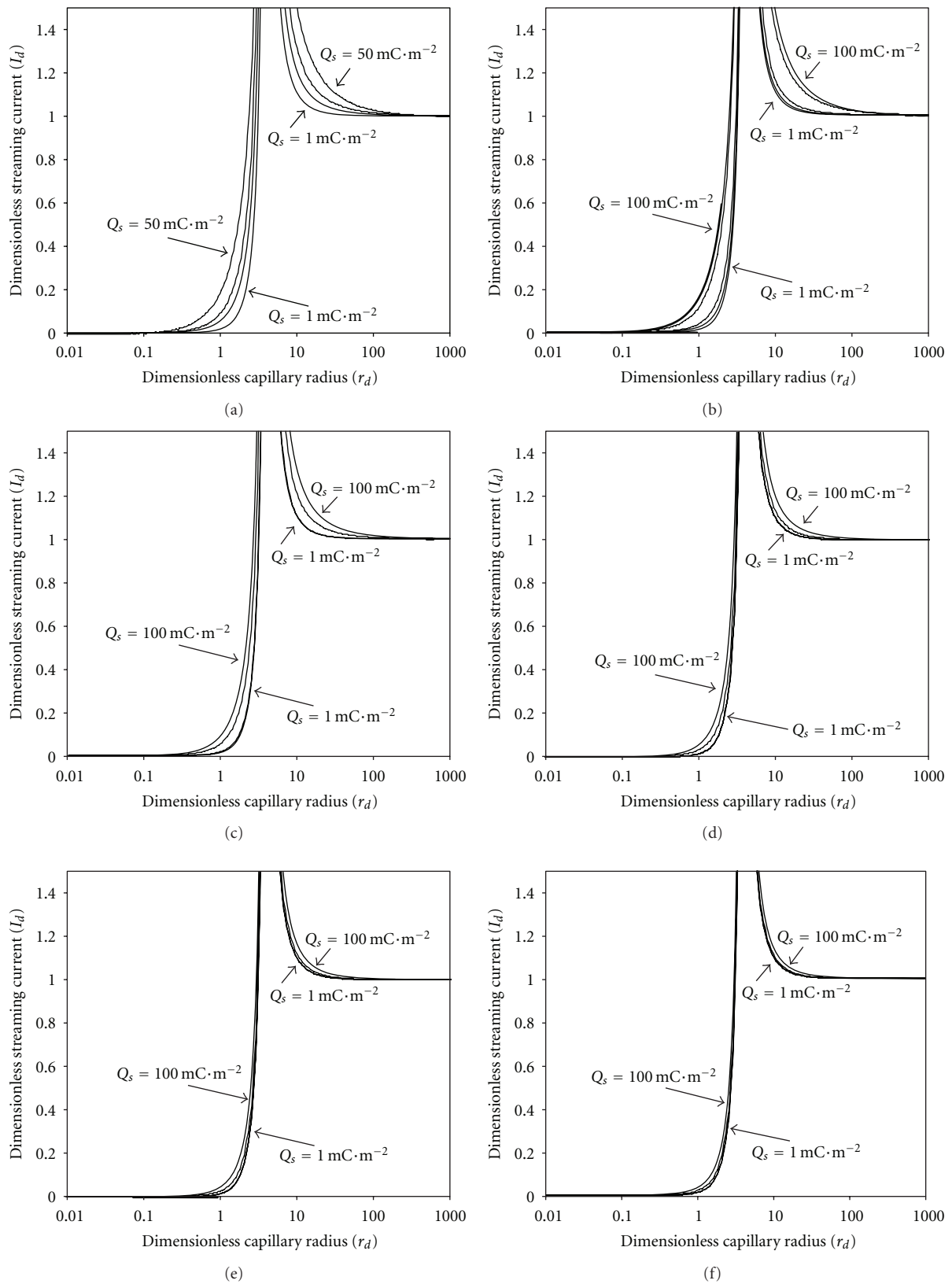


FIGURE 3: Dimensionless streaming current (I_d) as a function of dimensionless pore radius (r_d) for concentration values of (a) 0.001 M; (b) 0.01 M; (c) 0.1 M; (d) 0.5 M; (e) 1 M; (f) 2 M. Curves denote surface charge values of 1, 5, 10, 50, and 100 $\text{mC}\cdot\text{m}^{-2}$, with curves ordered between the maximum and minimum values indicated on the plots. The 100 $\text{mC}\cdot\text{m}^{-2}$ case is not shown in Figure 3(a).

TABLE 2: Values of the properties used in the model.

Property	Value	Units
C_f	$1 \times 10^{-3}-2$	M
e	$1.60217646 \times 10^{-19}$	C
ϵ	0.708–0.514	nF m ⁻¹
k	1.38065×10^{-23}	m ² kg s ⁻² K ⁻¹
λ	9.72–0.185	nm
N_A	6.0221415×10^{23}	Mol ⁻¹
Q_s	1–100	mC m ⁻²
T	298.15	K

(20) is zero. However, the dimensionless streaming current at intermediate r_d has no physical significance, as the calculated values of $I|_{\lambda \ll r}$ and $I|_{\lambda \gg r}$ are not valid. We are interested here only in determining the range of values of r_d for which I_d is zero or 1, to identify the range of validity of the thick and thin double-layer approximations, respectively.

At low concentration (e.g., Figure 3(a)), the range of values of r_d for which the thick and thin double-layer assumptions are valid depends on the specific surface charge, with high values of surface charge yielding a smaller range of validity. For example, at the lowest concentration investigated, the thick double-layer assumption is valid (defined as a divergence of I_d from 0 of <1%) at low surface charge for $r_d < 0.81$, while the thin double-layer assumption is valid (defined as a divergence of I_d from 1 of <1%) for $r_d > 24$ (Figure 3(a)). However, at high surface charge, the thick double layer assumption is valid only for $r_d < 0.17$, while the thin double layer assumption is valid only for $r_d > 200$. As the concentration increases, the effect of varying the specific surface charge decreases. The curves cluster towards the low surface charge case, for which the curves are similar regardless of concentration (Figure 5).

Figure 6 shows the critical value of dimensionless capillary radius for which each assumption is valid (using the definitions given above) over the range of concentration and surface charge investigated. As the electrolyte concentration increases, and the specific surface charge decreases, the critical value of r_d below which the thick double layer is validly increases with increasing concentration and decreasing surface charge, from a minimum of 0.17 to a maximum of 0.96. Conversely, the critical value of r_d above which the thin double-layer assumption is validly decreases with increasing concentration and decreasing surface charge, from a maximum of 200 to a minimum of 22.

These results demonstrate that there is not a single value of dimensionless capillary radius below which the thick double layer assumption is valid, or a single value above which the thin double layer assumption is valid; rather the critical dimensionless radius depends upon both concentration and specific surface charge. A conservative estimate of the dimensionless capillary radius below which the thick double-layer assumption is valid, applicable over the range of concentration and surface charge investigated, is $r_d < 0.17$, while a conservative estimate for the validity of the thin double-layer assumption is $r_d > 200$. This is equivalent

to requiring the capillary radius to be c. 5 times smaller than the diffuse layer thickness for the thick double-layer assumption to be valid, and the capillary radius to be c. 200 larger than the diffuse layer thickness for the thin double layer assumption to be valid. However, at concentrations of 0.1 M and higher, and specific surface charge of 10 mC·m⁻² and lower, the thick double layer assumption is typically valid when the pore radius is slightly smaller than the Debye length ($r_d < 0.95$), while the thin double-layer limit is typically valid when the pore radius is c. 25 times larger than the Debye length ($r_d > 25$). We discuss the implications of these results for modelling streaming potentials in natural systems in the next section.

The results presented here can be compared with those of Westermann-Clark and Christoforou [5], who found that the Meyers-Sievers model, in which the excess charge density is assumed to be independent of distance from the pore surface, was a good approximation of the exclusion-diffusion potential across a single capillary regardless of the value of r_d (which they termed a/λ) at low surface charge, and when $r_d < 1$ or $r_d > 20$ at high surface charge (estimated from Figure 4 of Westermann-Clark and Christoforou [5]). The Meyers-Sievers model is equivalent to the thick double-layer assumption when $r_d \rightarrow 0$ but is equivalent to the thin double layer assumption when $r_d \rightarrow \infty$ only in the trivial case of a zero streaming current. Our results are similar to those of Westermann-Clark and Christoforou [5] in that we do find critical values of r_d for which the thin and thick double-layer assumptions are valid, and these critical values depend on the specific surface charge. However, our results differ from those of Westermann-Clark and Christoforou [5] in a number of ways. Firstly, Westermann-Clark and Christoforou [5] did not investigate or identify any concentration dependence of the critical value of r_d . Secondly, we always find values of r_d for which the thick and thin double-layer assumptions are not valid, regardless of the value of the surface charge investigated (Figure 3). The thin and thick double-layer assumptions only become independent of r_d as the surface charge tends to zero, in which case the streaming current tends to zero and the solution is trivial. Finally, we find rather more restrictive limits on the validity of the thin and thick double-layer assumptions at high surface charge (Figure 6). The values of r_d , for which charge exclusion from the pore-space at high surface charge is adequately described by the Meyers-Sievers model, are different from the values of r_d for which the streaming current (and, hence, the streaming potential) at high surface charge is adequately described by the thin or thick double-layer assumptions.

We have compared the values of dimensionless streaming current (I_d) that we obtained at large values of r_d and Q_s using (12), which was derived using the Debye-Hückel model to calculate $Q(x)$, with those obtained using the Gouy-Chapman model (24) to calculate $Q(x)$, and confirmed that the curves are identical within the line widths used in Figure 3. The results are similar because, as r_d becomes large, the thickness of the double layer becomes small in comparison to the radius of the capillary, so small differences in $Q(x)$ between the Debye-Hückel and Gouy-Chapman models (e.g., Figure 2(b)) have negligible impact on the calculated

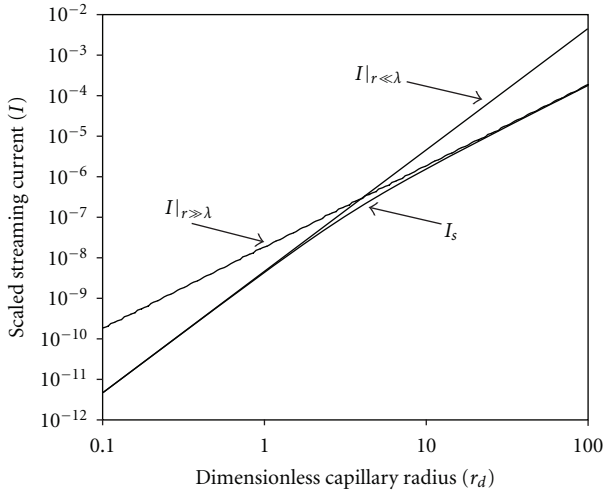


FIGURE 4: Typical results showing streaming current calculated using (i) the Poisson-Boltzmann equation (I_s), (ii) assuming a thin double layer ($I|_{\lambda \ll r}$), and (iii) assuming a thick double layer ($I|_{\lambda \gg r}$), as a function of dimensionless capillary radius (r_d). The reported streaming currents have been scaled to the value of $I|_{\lambda \gg r}$ at $r_d = 1000$. Note that there is a value of r_d for which $I|_{\lambda \gg r} = I|_{\lambda \ll r}$. At this value of r_d , the dimensionless streaming current I_d is undefined (20).

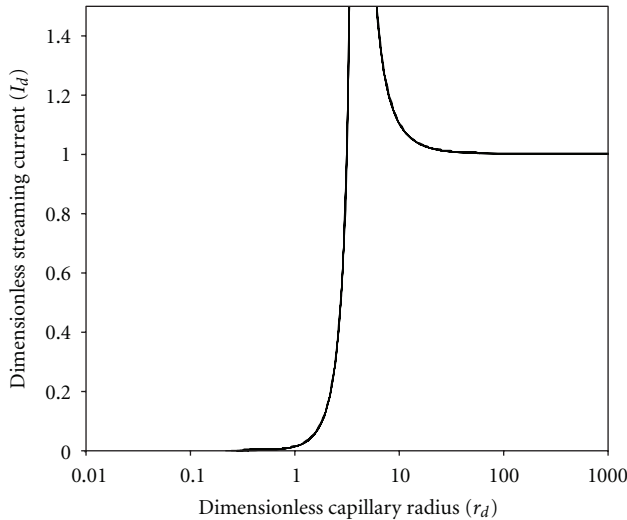


FIGURE 5: Dimensionless streaming current (I_d) as a function of dimensionless capillary radius (r_d) for a surface charge of $Q_s = 1 \text{ mC} \cdot \text{m}^{-2}$. Curves corresponding to concentration values of 0.001 M, 0.01 M, 0.1 M, 0.5 M, 1 M, and 2 M are shown but cannot be distinguished.

streaming current. Even at large Q_s , (12) provides an appropriate limiting case for the thin double-layer approximation when calculating the dimensionless streaming current.

4. Discussion

Our results suggest that in a capillary tubes model, with values of surface charge up to $100 \text{ mC} \cdot \text{m}^{-2}$, the thin double-layer assumption is valid so long as the capillary radius is

more than 200 times greater than the thickness of the double layer, while the thick double layer assumption is valid so long as the capillary radius is more than 6 times smaller than the thickness of the double layer. At lower surface charge density ($<10 \text{ mC} \cdot \text{m}^{-2}$) or higher concentration ($>0.1 \text{ M}$), the validity criteria are less stringent: the thin double-layer assumption is valid so long as the capillary radius is more than 25 times the thickness of the double-layer, while the thick double layer assumption is valid so long as the capillary radius is slightly less than the thickness of the double layer. It is interesting to test these criteria for the range of pore size and concentration typical of natural porous media.

Figure 7 shows the (dimensional) critical capillary radius above and below which the thin and thick double-layer assumptions are valid, respectively. The curves were calculated using the data reported in Figure 6 and (2) and (19). Also shown are typical ranges of pore and pore throat sizes in sandstones and mudstones. The pore space topology of capillary tubes model is very different from that of natural sandstones and mudstones (see Jackson [6] for a discussion); however, the results presented here provide first-order estimates of the validity of the thin and thick double-layer assumptions in natural porous media. The transport properties of sandstones and mudstones are generally controlled by the connectivity of the larger pores and the size of the connecting throats [7–10], and we assume the same is true of the streaming current, with the capillaries modeled here representing the connecting pore-throats (see also [18]).

The results shown in Figure 7 suggest that at low surface charge ($<10 \text{ mC} \cdot \text{m}^{-2}$), sandstones lie comfortably in the region for which the thin double-layer assumption is valid, except those with the smallest pore-throat sizes saturated with electrolyte of low concentration. This result supports the assumptions of numerous previous studies of the electrokinetic properties of sandstones (e.g., [13, 14, 23, 32]). However, at higher surface charge, the thin double layer assumption may not be valid in sandstones of moderate- to small-pore-throat size (c. $1\text{--}5 \mu\text{m}$), if the electrolyte concentration is less than c. 10^{-3} M . It has long been recognized that the classical Helmholtz-Smoluchowski equation (3) fails in sandstones and other porous materials of similar pore-size, saturated with electrolytes at low concentration; this is usually attributed to the contribution of surface electrical conductivity, which is neglected in (3) (e.g., [2, 13, 14, 17, 33]). Here we suggest that the thin double-layer assumption, upon which (3) is based, may not be valid in fine-grained or cemented sandstones saturated with low-salinity brine.

The results shown in Figure 7 also suggest that mudstones can lie within the validity range of either the thin or thick double-layer assumption, depending upon their pore-throat size and surface charge, and the electrolyte concentration. However, they may often be poorly described by either assumption. The thin double-layer assumption is likely to be valid at high electrolyte concentration ($>0.2 \text{ M}$), regardless of the value of surface charge, if there is well-connected macroporosity that dominates the transport properties (yielding a majority of pore-throat sizes $>10 \text{ nm}$). Moreover, the thick double-layer assumption is likely to be valid in mudstones with pore-throat size greater than a few

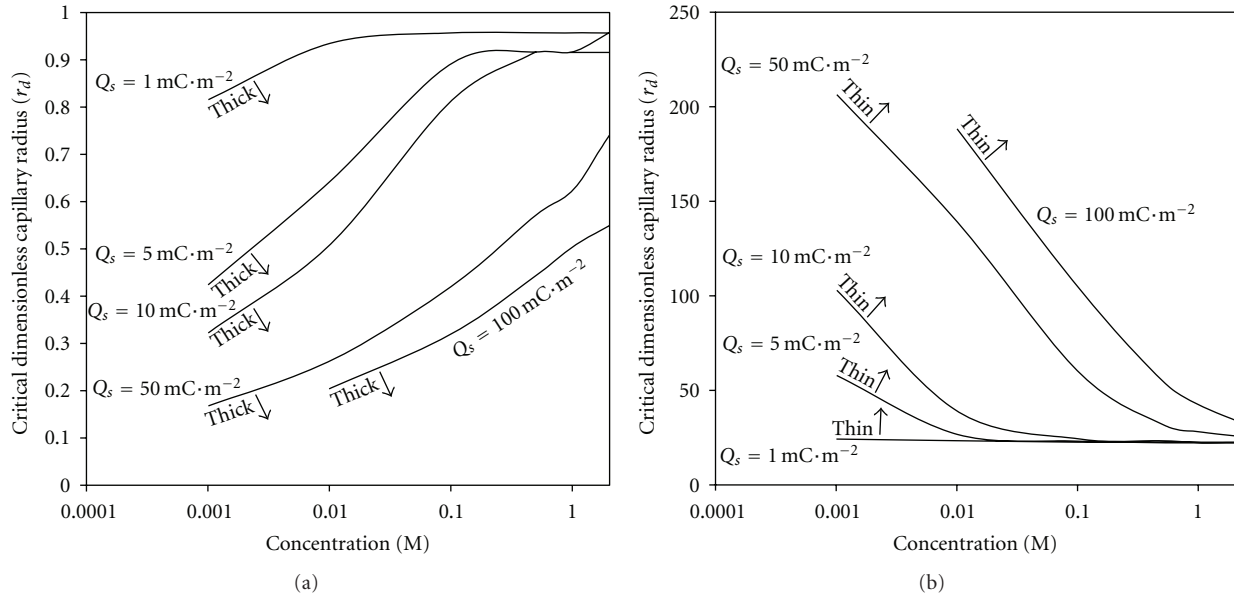


FIGURE 6: Critical dimensionless capillary radius (determined from Figure 3) (a) below which the thick double-layer assumption is valid and (b) above which the thin double layer assumption is valid, as a function of electrolyte concentration. Curves correspond to surface charge values of 1, 5, 10, 50, and 100 $\text{mC}\cdot\text{m}^{-2}$. The thick double-layer assumption is taken to be valid when the dimensionless streaming current I_d deviates from 0 by less than 1%; the thin double-layer assumption is taken to be valid when I_d deviates from 1 by less than 1%.

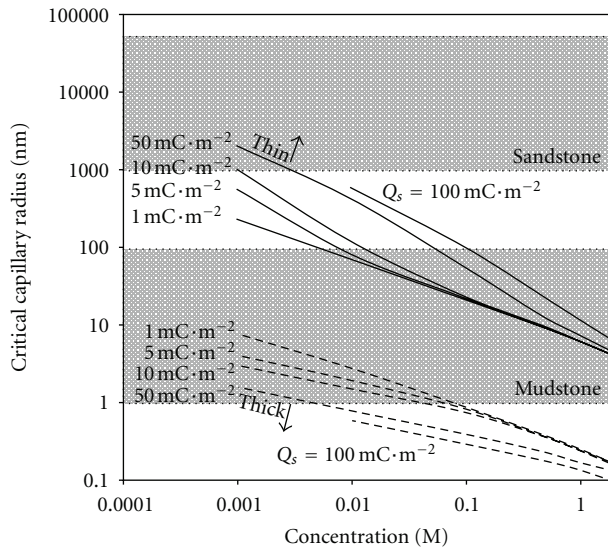


FIGURE 7: Critical capillary radius (determined from Figure 6) above which the thin double-layer approximation is valid (solid lines) and below which the thick double-layer assumption is valid (dashed lines), as a function of electrolyte concentration. Curves correspond to surface charge values of 1, 5, 10, 50, and 100 $\text{mC}\cdot\text{m}^{-2}$. Also shown are typical ranges of pore and pore-throat radii in sandstones and mudstones [7–10].

nanometres, at electrolyte concentrations below c. 0.1 M and surface charge below 10 $\text{mC}\cdot\text{m}^{-2}$. This finding supports the approach of Revil and coworkers, who invoke the thick double-layer assumption in their streaming potential model for mudstones and claystones [18, 19, 26]. However,

at higher surface charge ($>50 \text{mC}\cdot\text{m}^{-2}$), the thick double-layer assumption is likely to be valid in mudstones only at electrolyte concentrations below c. 0.003 M, even if the pore-throat size is as small as 1 nm. This is a rather restrictive limit in natural systems. Models based on the thick double-layer assumption are never likely to be applicable to sandstones, or other rock types with larger pore and pore-throat sizes than mudstones.

We have derived the validity criteria presented in Figure 7 for a circular capillary tube of uniform radius. As discussed previously, a capillary tube model is a poor approximation for the pore-space topology of real rocks. Here, we assume that charge transport and, hence, the streaming current, is dominated by charge exclusion in the smaller pore-throats, rather than the larger pore-bodies, and equate the radius of the capillary tube with the pore-throat radius in real rocks. Extending the analysis to more realistic pore geometries and pore size distributions is outside the scope of this paper. However, we note that Westermann-Clark and Christoforou [5] investigated both circular and slit-like capillary geometries (the slit-like capillary was modeled as two parallel, infinite plates) and found that their criteria for the validity of the Meyers-Sievers model for exclusion-diffusion potentials, in which the excess charge density is assumed to be independent of distance from the pore surface, were the same regardless of the capillary geometry. We suggest that the same is likely to be the case for streaming current calculations. Clearly, there is a need to model more realistic pore-space topologies, but the results we present here provide at least first-order estimates of the validity of the thin and thick double-layer assumptions in natural porous media.

It should also be noted that we have applied the Poisson-Boltzmann equation (1) to describe the charge distribution in the diffuse layer at electrolyte concentrations up to 2 M. It is well known that the assumptions upon which (1) is based begin to break down at high electrolyte concentration (e.g., [2]). Consequently, the criteria we deduce for the thin double-layer limit may be in error. Application of more sophisticated models for the excess charge density, which account for high concentration effects, suggest that corrections to the Poisson-Boltzmann equation are of order 2% at 0.1 M, but may be as large as 25% at concentrations above 1 M [2]. However, we argue that high concentration effects impact only on our assessment of the thin double-layer assumption in fine-grained rocks such as mudstones, because the limit of the thin double-layer assumption in sandstones is only approached at low concentration.

5. Conclusions

We find that, for values of surface charge up to $100 \text{ mC} \cdot \text{m}^{-2}$, the thin double-layer assumption is valid in a capillary tubes model saturated with a symmetric, monovalent electrolyte, so long as the pore radius is more than 200 times the thickness of the double-layer. The thick double-layer assumption is valid so long as the pore radius is more than 6 times smaller than the thickness of the double layer. At lower surface charge density ($<10 \text{ mC} \cdot \text{m}^{-2}$) or higher electrolyte concentration ($>0.5 \text{ M}$), the validity criteria are less stringent: the thin double-layer assumption is valid so long as the pore radius is more than 25 times the thickness of the double-layer, while the thick double-layer assumption is valid so long as the pore radius is slightly less than the thickness of the double layer.

Applying these criteria to sandstones suggests that if the specific surface charge is less than $10 \text{ mC} \cdot \text{m}^{-2}$, the thin double-layer assumption is valid over the range of electrolyte concentrations likely to be encountered in nature and in laboratory experiments. However, at higher surface charge, the thin double-layer assumption may not be valid in sandstones of moderate to small pore-throat size if the electrolyte concentration is less than c. 0.001 M. Previous studies have assumed that the Helmholtz-Smoluchowski equation, which follows from the thin double-layer assumption, fails at low electrolyte concentration because of the contribution of surface electrical conductivity. Here, we suggest that the assumption of a thin double layer may be at fault. The thick double-layer assumption is unlikely to be valid in sandstones.

Applying the criteria to mudstones suggests that the thin double layer assumption is likely to be valid if the pore-throat size is greater than c. 10 nm for electrolyte concentration $>0.1 \text{ M}$. The thick double layer assumption is likely to be valid in mudstones at concentrations below c. 0.1 M and surface charge below $10 \text{ mC} \cdot \text{m}^{-2}$ but, at higher surface charge, it is likely to be valid only at electrolyte concentrations below c. 0.003 M. Mudstones often lie in the range where neither the thin nor thick double layer assumption is valid.

Acknowledgments

The comments of two anonymous reviewers and the associate editor greatly improved the paper.

References

- [1] L. Jouniaux and T. Ishido, "Electrokinetics in Earth sciences: a tutorial," *International Journal of Geophysics*, vol. 2012, Article ID 286107, 16 pages, 2012.
- [2] R. J. Hunter, *Zeta Potential in Colloid Science*, Academic Press, New York, NY, USA, 1981.
- [3] A. Revil, P. A. Pezard, and P. W. J. Glover, "Streaming potential in porous media 1. Theory of the zeta potential," *Journal of Geophysical Research B*, vol. 104, no. 9, pp. 20021–20031, 1999.
- [4] A. Revil, H. Schwaeger, L. M. Cathless III, and P. D. Manhardt, "Streaming potential in porous media 2. Theory and application to geothermal systems," *Journal of Geophysical Research B*, vol. 104, no. 9, pp. 20033–20048, 1999.
- [5] G. B. Westermann-Clark and C. C. Christoforou, "The exclusion-diffusion potential in charged porous membranes," *Journal of Electroanalytical Chemistry*, vol. 198, no. 2, pp. 213–231, 1986.
- [6] M. D. Jackson, "Multiphase electrokinetic coupling: insights into the impact of fluid and charge distribution at the pore-scale from a bundle of capillary tubes model," *Journal of Geophysical Research*, vol. 115, Article ID B07206, 2010.
- [7] T. Bourbie and B. Zinszner, "Hydraulic and acoustic properties as a function of porosity in Fontainebleau sandstone," *Journal of Geophysical Research*, vol. 90, no. B13, pp. 11524–11532, 1985.
- [8] P. M. Doyen, "Permeability, conductivity, and pore geometry of sandstone," *Journal of Geophysical Research*, vol. 93, no. 7, pp. 7729–7740, 1988.
- [9] F. A. L. Dullien, *Porous media: fluid transport and pore structure*, Academic Press, San Diego, Calif, USA, 2nd edition, 1992.
- [10] A. Hildenbrand, S. Schlomer, and B. M. Krooss, "Gas breakthrough experiments on fine-grained sedimentary rocks," *Geofluids*, vol. 2, no. 1, pp. 3–23, 2002.
- [11] T. Ishido and H. Mizutani, "Experimental and theoretical basis of electrokinetic phenomena in rock-water systems and its applications to geophysics," *Journal of Geophysical Research*, vol. 86, no. 3, pp. 1763–1775, 1981.
- [12] F. D. Morgan, E. R. Williams, and T. R. Madden, "Streaming potential properties of westerly granite with applications," *Journal of Geophysical Research*, vol. 94, no. 9, pp. 12,449–12,461, 1989.
- [13] L. Jouniaux and J. P. Pozzi, "Streaming potential and permeability of saturated sandstones under triaxial stress: consequences for electrotelluric anomalies prior to earthquakes," *Journal of Geophysical Research*, vol. 100, no. 6, pp. 10,197–10,209, 1995.
- [14] B. Lorne, F. Perrier, and J. P. Avouac, "Streaming potential measurements: 2. Relationship between electrical and hydraulic flow patterns from rock samples during deformation," *Journal of Geophysical Research B*, vol. 104, no. 8, pp. 17879–17896, 1999.
- [15] A. V. Delgado, F. Gonzalez-Caballero, R. J. Hunter, L. K. Koopal, and J. Lyklema, "Measurement and interpretation of electrokinetic phenomena," *Journal of Colloid and Interface Science*, vol. 309, no. 2, pp. 194–224, 2007.

- [16] L. Jouniaux, M. L. Bernard, M. Zamora, and J. P. Pozzi, "Streaming potential in volcanic rocks from Mount Pelee," *Journal of Geophysical Research B*, vol. 105, no. 4, pp. 8391–8401, 2000.
- [17] P. W. J. Glover and N. Déry, "Streaming potential coupling coefficient of quartz glass bead packs: dependence on grain diameter, pore size, and pore throat radius," *Geophysics*, vol. 75, no. 6, pp. F225–F241, 2010.
- [18] A. Revil and P. Leroy, "Constitutive equations for ionic transport in porous shales," *Journal of Geophysical Research B*, vol. 109, Article ID B03208, 19 pages, 2004.
- [19] A. Revil and N. Linde, "Chemico-electromechanical coupling in microporous media," *Journal of Colloid and Interface Science*, vol. 302, no. 2, pp. 682–694, 2006.
- [20] R. E. Rice, "Exact solution to the linearized Poisson-Boltzmann equation in cylindrical coordinates," *The Journal of Chemical Physics*, vol. 82, no. 9, pp. 4337–4340, 1985.
- [21] J. F. Dufrêche, V. Marry, O. Bernard, and P. Turq, "Models for electrokinetic phenomena in montmorillonite," *Colloids and Surfaces A*, vol. 195, no. 1-3, pp. 171–180, 2001.
- [22] A. Dukhin, S. Dukhin, and P. Goetz, "Electrokinetics at high ionic strength and hypothesis of the double layer with zero surface charge," *Langmuir*, vol. 21, no. 22, pp. 9990–9997, 2005.
- [23] J. Vinogradov, M. Z. Jaafar, and M. D. Jackson, "Measurement of streaming potential coupling coefficient in sandstones saturated with natural and artificial brines at high salinity," *Journal of Geophysical Research B*, vol. 115, no. 12, Article ID B12204, 2010.
- [24] H. Vink, "Electrokinetics of polyelectrolyte solutions in capillary tubes," *Journal of the Chemical Society, Faraday Transactions 1*, vol. 84, no. 1, pp. 133–149, 1988.
- [25] M. D. Jackson, "Characterization of multiphase electrokinetic coupling using a bundle of capillary tubes model," *Journal of Geophysical Research B*, vol. 113, no. 4, Article ID B04201, 2008.
- [26] A. Revil, W. F. Woodruff, and N. Lu, "Constitutive equations for coupled flows in clay materials," *Water Resources Research*, vol. 47, Article ID W05548, 21 pages, 2011.
- [27] Y. Bernabé, "Streaming potential in heterogeneous networks," *Journal of Geophysical Research B*, vol. 103, no. 9, pp. 20827–20841, 1998.
- [28] J. Kierzenka and L. F. Shampine, "A BVP solver based on residual control and the Matlab PSE," *ACM Transactions on Mathematical Software*, vol. 27, no. 3, pp. 299–316, 2001.
- [29] P. M. Dove and C. M. Craven, "Surface charge density on silica in alkali and alkaline earth chloride electrolyte solutions," *Geochimica et Cosmochimica Acta*, vol. 69, no. 21, pp. 4963–4970, 2005.
- [30] M. Kosmulski and P. Dahlsten, "High ionic strength electrokinetics of clay minerals," *Colloids and Surfaces A*, vol. 291, no. 1-3, pp. 212–218, 2006.
- [31] C. G. Malmberg and A. A. Maryott, "Dielectric constant of water from 0 to 100°C," *Journal of Research of the National Bureau of Standards*, vol. 56, no. 1, pp. 1–8, 1956.
- [32] M. Z. Jaafar, J. Vinogradov, and M. D. Jackson, "Measurement of streaming potential coupling coefficient in sandstones saturated with high salinity NaCl brine," *Geophysical Research Letters*, vol. 36, no. 21, Article ID L21306, 2009.
- [33] A. Bolève, A. Crespy, A. Revil, F. Janod, and J. L. Mattiuzzo, "Streaming potentials of granular media: influence of the dukhin and reynolds numbers," *Journal of Geophysical Research B*, vol. 112, no. 8, Article ID B08204, 2007.

Research Article

Frequency-Dependent Streaming Potential of Porous Media—Part 1: Experimental Approaches and Apparatus Design

P. W. J. Glover,¹ J. Ruel,² E. Tardif,² and E. Walker¹

¹Department of Geology and Engineering Geology, Université Laval, Québec, QC, Canada G1V 0A6

²Department of Mechanical Engineering, Université Laval, Québec, QC, Canada G1V 0A6

Correspondence should be addressed to P. W. J. Glover, paglover@ggl.ulaval.ca

Received 3 June 2011; Revised 21 October 2011; Accepted 12 December 2011

Academic Editor: Tsuneo Ishido

Copyright © 2012 P. W. J. Glover et al. This is an open access article distributed under the Creative Commons Attribution License, which permits unrestricted use, distribution, and reproduction in any medium, provided the original work is properly cited.

Electrokinetic phenomena link fluid flow and electrical flow in porous and fractured media such that a hydraulic flow will generate an electrical current and *vice versa*. Such a link is likely to be extremely useful, especially in the development of the electroseismic method. However, surprisingly few experimental measurements have been carried out, particularly as a function of frequency because of their difficulty. Here we have considered six different approaches to make laboratory determinations of the frequency-dependent streaming potential coefficient. In each case, we have analyzed the mechanical, electrical, and other technical difficulties involved in each method. We conclude that the electromagnetic drive is currently the only approach that is practicable, while the piezoelectric drive may be useful for low permeability samples and at specified high frequencies. We have used the electro-magnetic drive approach to design, build, and test an apparatus for measuring the streaming potential coefficient of unconsolidated and disaggregated samples such as sands, gravels, and soils with a diameter of 25.4 mm and lengths between 50 mm and 300 mm.

1. Introduction

While there are a growing number of streaming potential measurements on rocks and other porous media that are made with constant fluid flow, there are surprisingly few available for flow that varies in time. This is probably because such measurements have been considered very difficult to carry out. However, such measurements are likely to be of great importance in a number of fields, not least in the understanding and development of the seismoelectric exploration method.

The few previous measurements can be classified into two groups: (i) transient measurements with a percussive source and (ii) harmonic measurements with a vibrating source. The first of these approaches mimics many of the possible applications more closely, while the latter is capable of providing higher-quality frequency-specific data.

The percussive source studies measure transient electrokinetic processes in sand columns that arise when a controlled impact is made on a column of saturated sand [1–3]. These are difficult studies that require the impact to be repeatable and the seismoelectric and/or seismomagnetic

conversion to be measured. Such transient measurements have confirmed the presence of seismo-electrokinetic and seismo-electromagnetic phenomena at high frequencies. However, the percussive seismic source does not produce a single frequency, so it cannot be used to measure the coupling coefficients as a function of frequency. Although it should be possible to examine the Fourier components of the seismic impact and the measured electric and magnetic signals in order to extract more specific information about the frequency dependence of the coupling coefficients [4], a pilot study in our laboratory indicated that such a process would be extremely difficult to carry out.

One would expect that a better approach would be to arrange a harmonically varying fluid flow at a specific frequency and then to measure the streaming potential and the fluid pressure difference from which a streaming potential coefficient at that frequency could be calculated. Repeating the experiment at different, well-defined frequencies should then allow the variation of the streaming potential coefficient as a function of frequency to be obtained. There have been only a few experiments using this approach. These experiments have made measurements on only 5 glass

capillaries, one fritted glass filter, and 2 ceramic filters [5–9]. Only one rock has ever been measured at frequencies greater than 100 Hz—a Boise sandstone with 35% porosity [8].

The first measurements were made by Packard [5] using a cell with two rubber membranes and two platinum electrodes that was mounted on a reservoir. A “geophone-type push-pull driver” provided a harmonic signal to the reservoir while a single hydrophone measured the driving fluid pressure. In this cell the pressure measurement and streaming potential measurements are not colocated which may lead to systematic errors in the calculated streaming potential coefficient. Packard measured 4 glass capillary tubes in the frequency range 20 Hz to 200 Hz and developed a theoretical model to describe his results. Cooke [6] seems to have used a similar apparatus to that of Packard [5]. He obtained measurements on three fritted glass filters and two capillaries. Unfortunately, data from only one of the fritted glass filters is of sufficient quality to compare with other measurements; the other measurements are either not reported or cover an insufficiently large frequency range to calculate a transition frequency. However, Cooke [6] did show that measurements could be made up to 400 Hz.

Sears and Groves [7] used chemical glassware as input and output reservoirs. Platinum electrodes were placed in each of the reservoirs and a steady-state pressure transducer was used to measure the fluid pressure. While a steady-state pressure transducer is not suitable for such an application, the low frequencies attained by Sears and Groves (0.385 Hz to 21.28 Hz) probably ensure that the pressure measurements are close to the real values. Sears and Groves used a piston that was driven by a scotch yoke. We examine this method and conclude that it can only be used up to 33 Hz with current technology. Unfortunately, while Sears and Groves measured capillary tubes of three different diameters, they only show frequency-dependent data for one.

More recently [8, 9], a higher-quality experimental approach has used an electromechanical shaker as the source of the vibration and a rubber diaphragm, while nonpolarisable Ag/AgCl electrodes were used to measure the streaming potential and miniature hydrophones were used to measure the fluid pressures. While these studies seem to be of high quality, unfortunately this apparatus was only used to measure a few samples, specifically 2 diameters of capillary tube [9], 2 porous filters [9], and a single sample of Boise sandstone [8] over the range 1 Hz to 500 Hz.

For completeness it should be noted that measurements have also been made by Pengra et al. [10] up to about 100 Hz, while Sheffer et al. [11] have published a design for measuring the streaming potential of soils but only for frequencies less than 0.5 Hz.

The lack of data is associated with the experimental difficulties that such a measurement presents. This paper is the first of two linked papers. It seeks to explore the conceptual design of apparatuses that may be used to make frequency-dependent streaming potential coefficient measurements and to describe one such apparatus that has been constructed to measure unconsolidated and disaggregated porous media. The second paper [12] presents some of the initial data that the apparatus has provided and explores how that data

compares with a number of theoretical models that have been proposed to describe AC streaming potential coefficients.

2. Frequency-Fluid Pressure Difference-Pore Size Relationships

Since high-quality streaming potential measurements can be made in the millivolt range and most porous media have streaming potential coefficients that vary between 1 mV/MPa and several hundred mV/MPa, we need to be able to generate a pressure difference across the sample in the order of megapascals. This section examines how the pressure difference $\Delta P(\omega)$ depends upon the length of the sample (L), the dynamic viscosity of the fluid (η_f), the density of the fluid (ρ_f), the piston displacement driving the fluid (d), the frequency of the driving force (ω), and the effective pore size of the sample material that we take to be equal to the radius of a capillary tube (r) in the first instance.

The mean flow velocity $v(\omega)$ (in m/s) in a capillary tube of radius r in the AC regime (with an angular frequency ω) is given by Johnson et al. [13] and Reppert et al. [9] and can be calculated easily from the work of Bernabé [14] as

$$v(\omega) = \frac{\Delta P(\omega)}{\eta_f L k^2} \left(\frac{2}{kr} \frac{J_1(kr)}{J_0(kr)} - 1 \right), \quad \text{where } k = \sqrt{\frac{-i\omega\rho_f}{\eta_f}} \quad (1)$$

The AC permeability κ_{AC} can then be calculated to be

$$\kappa_{AC}(\omega) = \frac{\eta_f L}{\Delta P(\omega)} v(\omega) = \frac{1}{k^2} \left[\frac{2}{kr} \frac{J_1(kr)}{J_0(kr)} - 1 \right], \quad (2)$$

which is consistent with Bernabé [14–16] and Charlaix et al. [17].

The limit of (2) as $\omega \rightarrow 0$ is simply $r^2/8$, which is consistent with the steady-state permeability of a tube with radius r given by Poiseuille’s law $\kappa_{DC} = \pi r^4/8A_{\text{tube}}$ for a single tube, where $A_{\text{tube}} = \pi r^2$. We can use (1) to derive an expression for the fluid pressure difference

$$\Delta P(\omega) = v(\omega)\eta_f L k^2 \left(\frac{2}{kr} \frac{J_1(kr)}{J_0(kr)} - 1 \right)^{-1}. \quad (3)$$

The frequency-dependent fluid velocity and pressure difference are not linear functions of frequency and are not simple to calculate. However, we do not need to calculate the pressure difference as a function of frequency in order to constrain the design of the pressure cell and to choose the fluid pressure transducers. What we need is the maximum pressure difference as a function of frequency, porosity, sample length, piston displacement, and fluid properties (density and viscosity).

If we assume that the sample is completely saturated with the process fluid and is incompressible, we can define a maximum mean velocity within the sample as

$$v_{\max} = \frac{df}{\phi} \frac{A_p}{A}, \quad (4)$$

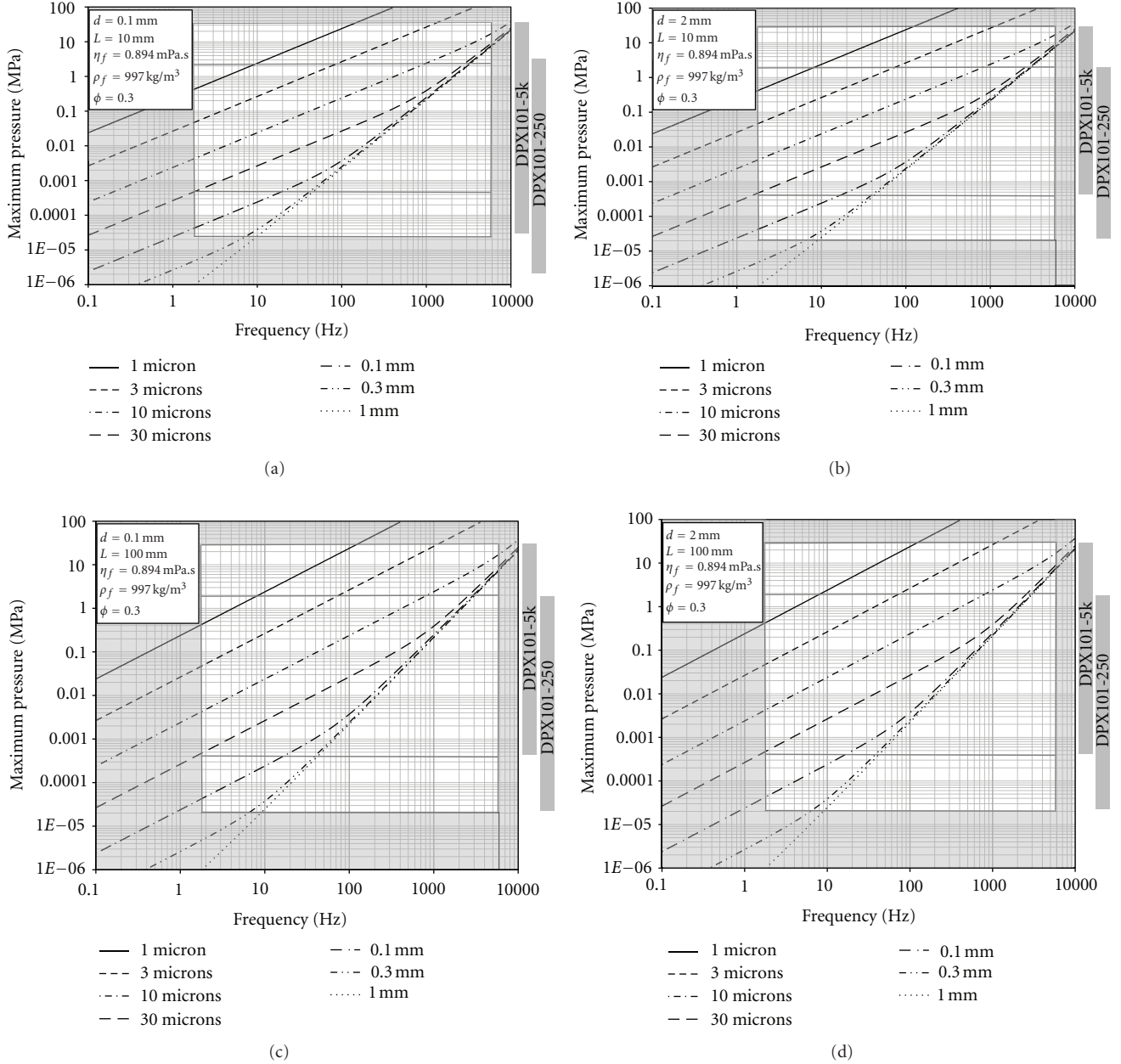


FIGURE 1: The maximum pressure difference generated by flowing an aqueous fluid through a porous medium using a harmonic piston. Imposed piston frequency (from 0.1 to 10^4 Hz), $\phi = 0.3$, sample length L (10 and 100 mm) and piston displacement d (0.1 mm and 2 mm), with the fluid parameters $\eta_f = 8.96 \times 10^{-4}$ Pa.s and $\rho_f = 997$ kg/m³, which correspond to a 10^{-3} mol/L solution of NaCl at 25°C.

where ϕ is the sample porosity, d is the piston displacement, A_p is the area of the piston, A is the area of the sample, and $\omega = 2\pi f$. Substituting (4) into (3) allows us to calculate the maximum pressure difference across the sample

$$\Delta P_{\max} = \frac{df}{\phi} \frac{A_p}{A} \eta_f L k^2 \left(\frac{2}{kr} \frac{J_1(kr)}{J_0(kr)} - 1 \right)^{-1}. \quad (5)$$

We have implemented (5) in Figure 1 for a sample with a porosity of 0.3, a range of pore sizes, two values of piston displacement, and two values of sample length. In this figure the grey areas represent conditions that fall outside the

specifications of the instruments that we are planning to construct. The minimum frequency (2 Hz) and maximum frequency (6.5 kHz) are those defined by the electromagnetic shaker that we have subsequently used in our experimental apparatus. There are a limited number of pressure transducers on the market that can measure signals varying at high frequencies. The ranges of two of these transducers are shown on the right-hand side of each of the parts of the figure as grey bars. The specifications of the transducers are discussed in greater detail in Section 5.

Figure 1(a) shows that it is possible to make measurements in the frequency range $2 \text{ Hz} < f < 1000 \text{ Hz}$ on samples

TABLE 1: Specifications of an apparatus for making frequency-dependent streaming potential coefficient measurements.

Characteristic	Unit	Min.	Max.	Comment
Frequency	Hz	2	1000 (6500)	VTS-100 EM shaker (max. shaker spec. in parentheses)
Piston displacement	mm	0.1	22	VTS-100 EM shaker
Piston position precision	mm		± 0.05	LVDT LD610-15 (Omega)
Dynamic pressure measurement	MPa (psi)		1.72 (250)	DPX101-250 dynamic pressure transducer (Omega)
			34.47 (5000)	DPX101-5K dynamic pressure transducer (Omega)
Pressure transducer proof pressure	MPa		34.5	DPX101-250 dynamic pressure transducer (Omega)
			103.4	DPX101-5K dynamic pressure transducer (Omega)
Pressure transducer noise floor	MPa		27.6×10^{-6}	DPX101-250 dynamic pressure transducer (Omega)
			482.6×10^{-6}	DPX101-5K dynamic pressure transducer (Omega)
Pressure transducer frequency range	Hz	0.08	1.7×10^5	DPX101-250 dynamic pressure transducer (Omega)
		0.003	1.7×10^5	DPX101-5K dynamic pressure transducer (Omega)
Pressure rise time	μs		1	DPX101-250 dynamic pressure transducer (Omega)
			1	DPX101-5K dynamic pressure transducer (Omega)
Pressure transducer resonant frequency	MHz		0.5	DPX101-250 dynamic pressure transducer (Omega)
			0.5	DPX101-5K dynamic pressure transducer (Omega)
Pressure transducer maximum frequency	MHz		0.17	DPX101-250 dynamic pressure transducer (Omega)
			0.17	DPX101-5K dynamic pressure transducer (Omega)
Pressure transducer preamp input impedance	Ω		10^{12}	TL074IN J-FET input operational amplifiers
Electrode preamp input impedance	Ω		10^{12}	TL074IN J-FET input operational amplifiers
Preamplification slew rate	V/ μs		13	TL074IN J-FET input operational amplifiers
Maximum preamplification frequency	MHz	—	4.83	TL074IN J-FET, assuming maximum amplified signal is 10 V
Streaming potential measurement	mV	5×10^{-2}	10^4	Min. set by the noise floor. Max. limited by the preamp. circuits
Streaming potential constant	mV/MPa		0.029	DPX101-250 dynamic pressure transducer (Omega)
			0.00145	DPX101-5K dynamic pressure transducer (Omega)
Sample length	cm		0.5	For rocks and clayey soils
			5	For sands and gravels and clay-free soils
Sample diameter	cm		1	For rocks and clayey soils
			2.54	For sands and gravels and clay-free soils
Temperature range	$^{\circ}C$	-70	120	Defined by the pressure transducers

with a length of 10 mm, a porosity of 0.3, and characteristic pore sizes in the range $1 \times 10^{-6} \text{ m} < r_{\text{pore}} < 3 \times 10^{-5} \text{ m}$ using either type of transducer and a piston displacement of 0.1 mm. This range seems rather restrictive. However, the displacement of the piston can be controlled and increased up to 22 mm, allowing the measureable range of pore sizes to be extended to $1 \times 10^{-6} \text{ m} < r_{\text{pore}} < 1 \times 10^{-3} \text{ m}$. Figure 1(b) shows the maximum pressure for a piston displacement of 2 mm for comparison. This range covers the normal range of pore sizes found in reservoir rocks.

If the porous material is disaggregated, such as sand the sample permeability is often lower and longer samples may be used. Figure 1(c) shows the results for a sample with a length of 100 mm and a porosity of 0.3. The range of pore sizes which can be measured is now restricted to $3 \times 10^{-5} \text{ m} < r_{\text{pore}} < 1 \times 10^{-3} \text{ m}$ by using piston displacements in the range 0.1 mm–2 mm (Figure 1(d)), which poses no real problems for sands and gravels which generally do not

contain micropores. It would, however, be a restriction on the measurement of soils which may contain smaller pores than 10 microns that are associated with clays.

3. General Specifications

We aim to design an apparatus for measuring the streaming potential of porous media as a function of frequency for the greatest range of frequency, porosity, permeability, and sample size possible. We have shown in the previous section that these parameters are mutually dependent, which leads to compromises in the specifications. Table 1 shows the specifications at which we have arrived for the apparatus described in this work, the details of which are discussed in the following section.

A minimum frequency of 2 Hz has been specified, which is the lower limit of the electromagnetic shaker that was available to us during testing (VTS-100). The maximum

limit of this shaker is 6.5 kHz. However, a maximum frequency of 1 kHz was specified for the following reason. Figure 1 shows that if we use a DPX101-250 dynamic pressure transducer, for which the maximum fluid pressure is 250 psi (1.724 MPa), it is possible to make measurements on samples up to 10 mm long with a piston displacement of 0.1 mm, a porosity of 0.3, and pore radii larger than 3 microns, or with pore radii greater than 30 microns if a 2 mm piston displacement is used. If a longer sample is used (say 100 mm), measurements may be made on porous media with pore radii greater than 10 microns for a 0.1 mm piston displacement and greater than 100 microns for a piston displacement of 2 mm. It is clear therefore that apparatuses for rock samples should be designed to take small samples so that the piston displacement may be sufficiently large to be controlled accurately, whereas apparatuses for unconsolidated samples of sands and gravels, which tend to have larger porosities and pore radii can be designed to use larger samples.

We should also consider the theoretical relationship between transition frequency and characteristic sample pore radius [18]

$$\omega_t = \frac{\phi}{\tau_e \kappa_{DC}} \frac{\eta_f}{\rho_f} = \frac{8}{r_{eff}^2} \frac{\eta_f}{\rho_f}, \quad (6)$$

where η_f (Pa.s) is the dynamic viscosity of the fluid, ρ_f (kg/m³) is the density of the bulk fluid, τ_e (unitless) is the electrical tortuosity of the pore network, ϕ (unitless) is the porosity of the sample, κ_{DC} (m²) is the steady-state fluid permeability, and r_{eff} (m) is the effective pore radius of the rock. The parameter ω_t (rad/s) is the transition frequency, at which the quadrature component of the dispersive system is greatest [18, 19].

If we specify a maximum frequency of 1 kHz, (6) implies that we are able to measure samples with hydraulically conductive pores greater than 33.8 μ m (using a typical aqueous pore fluid with $\rho_f = 997$ kg/m³ and $\eta_f = 8.94 \times 10^4$ Pa.s). Reference to Figure 1(b) shows that this criterion is met for a piston displacement of 2 mm. Samples with larger pores may use larger piston displacements up to about 22 mm, which is the limit of the VTS-100 electro-mechanical shaker, while samples with smaller pores (or larger lengths) can use smaller piston displacements or use a higher-range pressure transducer (the DPX101-5 K has a maximum pressure of 5000 psi, i.e., 34.474 MPa). The higher range transducer would be preferable from the point of view of data quality. These initial specifications also allow us the possibility of extending the frequency range to 6.5 kHz for samples with large pores if we install pressure transducer with the higher range.

The maximum and minimum physical limits to the piston displacement are defined by the electromagnetic shaker as discussed in the appendix. However, the practical lower limit is controlled by (i) our ability to distinguish a measureable streaming potential from the background noise and (ii) the resolution of the LVDT that measures the position of the piston (± 50 μ m).

Since a streaming potential will be generated and measured, we have specified that the sample cell is made of

insulating material such that the only counter current is that generated within the sample. It is equally important that no part of the cell, driver, fluid, or fluid tanks acts as an antenna in order to reduce electrical noise. Since the apparatus is to be used with a range of fluid salinities ($10^{-6} - 2$ mol/L) and pH (4–11), it is important that its wetted parts are sufficiently resistant to corrosion.

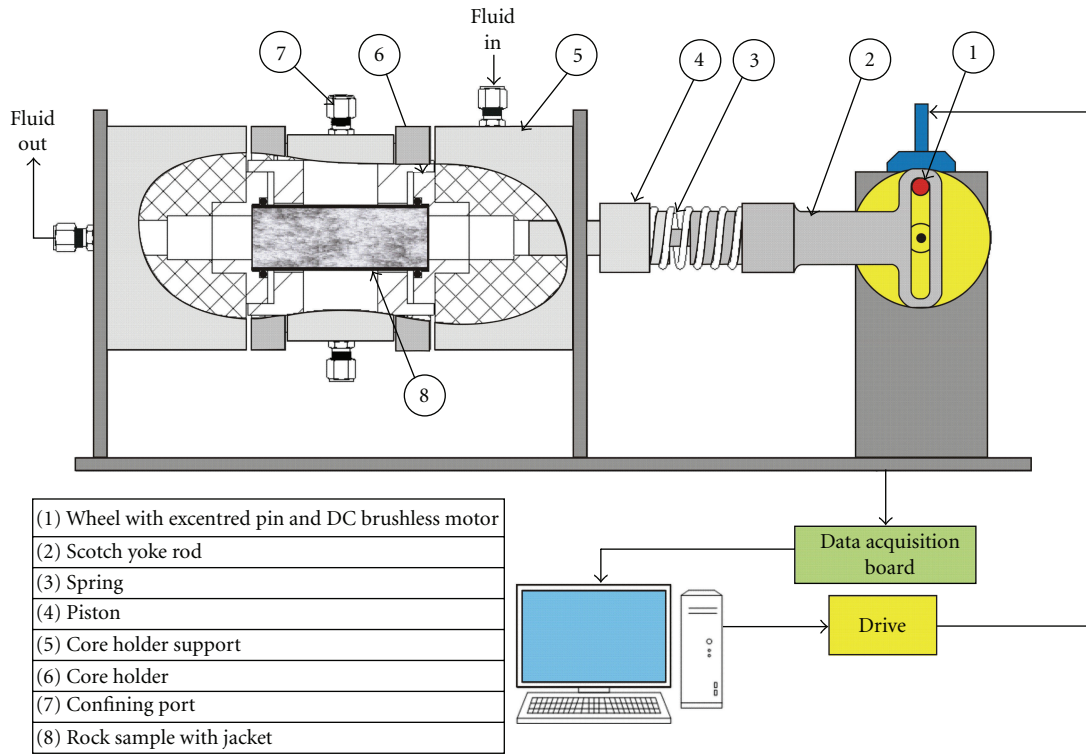
4. Experimental Design

There are three main aspects of the design. These are as follows.

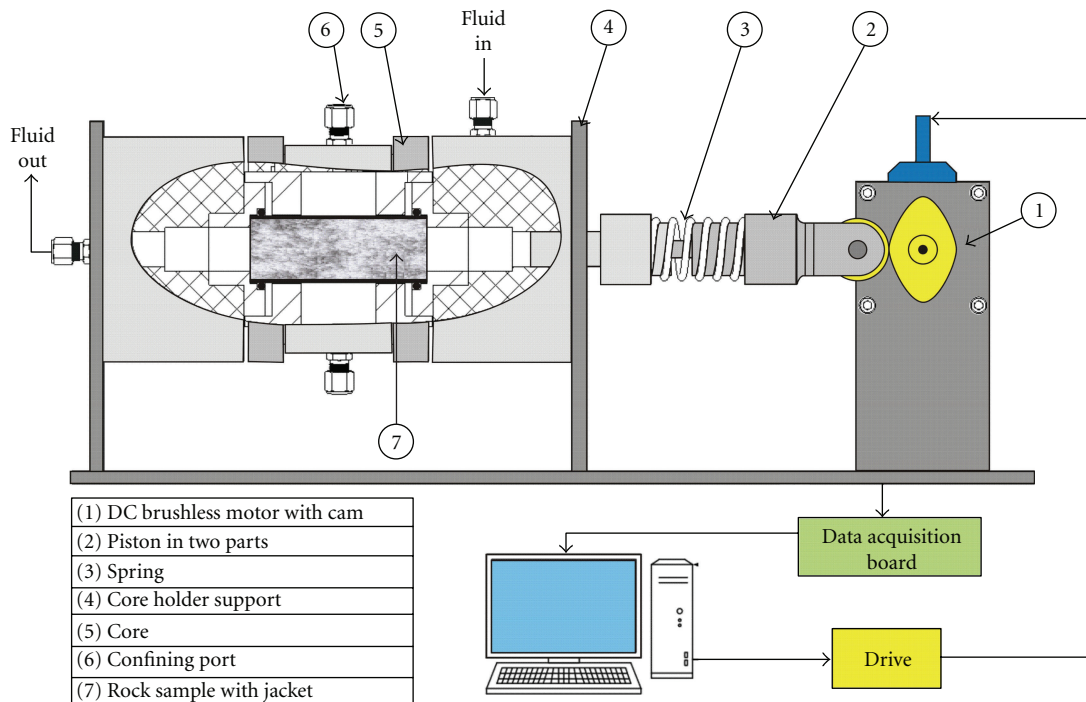
- (1) The design of a pressure vessel that accommodates a moveable piston, and in which the sample is held within a tube or a sleeve such that the fluid may be pushed through it. A number of standard pressure vessel designs can be used. We prefer a simple Perspex tube for unconsolidated samples and a modified Haskell Cell-type vessel for solid samples.
- (2) The design of transducer and electrode assemblages to measure and log the data at the required frequencies. These are described in Section 5.
- (3) The design of a mechanism to drive fluids through the sample at the required frequencies. There are many ways of driving the cell, all of which are discussed in detail below and in the appendix.

We considered several methods of creating an alternating flow of fluid through a porous sample, which can be categorised as follows: (i) mechanical drive using a connecting pin (Figure 2(a)) or a cam (Figure 2(b)), (ii) pneumatic drive (Figure 3(a)), (iii) hydraulic drive, (iv) electromagnetic drive (Figure 3(b)), and (v) piezoelectric coupling. We have examined all six methods in this paper giving a detailed analysis in the appendix and summarising the main findings below and listing the main advantages and disadvantages of each method in Table 2 for easy comparison.

In summary, the hydraulic drive was discounted at an early stage because it is very difficult to drive hydraulic fluid at high frequencies. Four of the remaining five approaches were discounted because they are not capable of providing a well-controlled dynamic fluid flow up to 1 kHz. For the connecting-pin (sometimes called “scotch yoke”) and the cam designs, neither a motor with a combination of sufficient torque and speed, nor a spring with sufficient stiffness per mass is currently available in order for frequencies up to 1 kHz to be reached. Such systems would be possible, but could attain frequencies only up to about 33 Hz with current technology. A pneumatic actuator approach can only be used to 100 Hz, which represents the maximum speed of the fastest servovalves that are presently available. A piezoelectric drive was rejected as it is very difficult to vary the frequency, and equally difficult to provide sufficient piston displacement. The electromagnetic shaker design was clearly the best choice as a dynamic drive.



(a)



(b)

FIGURE 2: Conceptual AC electrokinetic cells with (a) connecting-pin drive and (b) cam drive.

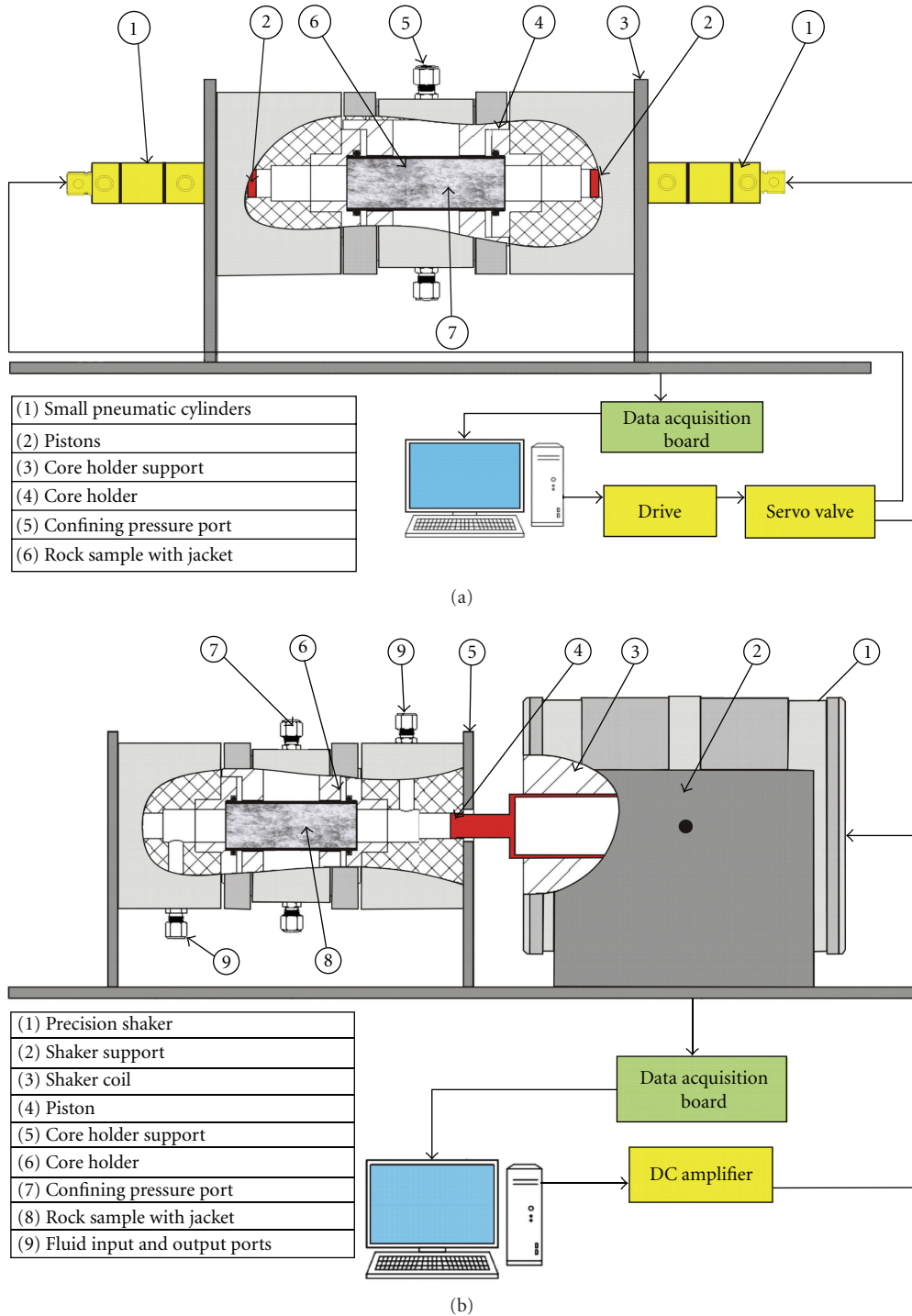


FIGURE 3: Conceptual AC electrokinetic cells with (a) pneumatic and (b) electromagnetic drive.

5. Experimental Apparatus

We have designed, constructed, and tested an experimental apparatus for measuring the AC streaming potential coefficient of granular materials such as sands using an electromagnetic drive. Figure 4 shows the conceptual model and image of the resulting apparatus, while Figure 5 shows more detailed drawings of its construction and an expanded view

of the piston entry. We restricted ourselves to using granular materials for these tests in order to avoid constructing a sample holder where the sample is sleeved. Potentially the most complex part of the apparatus is the piston. We opted initially to use pistons from a standard 60 mL laboratory syringe (Figures 4 and 5). These are robust as well as being cheap and easy to replace. They have an external working diameter of 2.54 cm and an extremely well-designed seal.

TABLE 2: Summary of the main characteristics and limitations of each of the drive methods. Please see the appendix for details.

Drive method	Maximum practical frequency range (Hz)	Comments
Hydraulic	0–5	<i>Design limited by</i> (i) Maximum frequency of hydraulic valves.
Connecting pin (scotch yoke)	0–33	<i>Design limited by</i> (i) Lack of a motor with a combination of sufficient torque and speed. (ii) Lack of a spring with sufficient stiffness per mass.
Cam	0–33	<i>Design limited by</i> (i) Lack of a motor with a combination of sufficient torque and speed. (ii) Lack of a spring with sufficient stiffness per mass. <i>Advantages:</i> (i) Has a lower friction than the connecting pin approach, which reduces the torque that the motor must provide. (ii) The profile of the imposed fluid pulse can be varied by changing the shape of the cam.
Pneumatic	0–100	<i>Design limited by</i> (i) Speed of servovalves. <i>Advantage:</i> (i) Does not require a spring for smooth operation because of the compressibility of the gas.
Electromagnetic	2–6500	<i>Design limited by</i> (i) The specification of the electromagnetic shaker used (here a VTS-100). (ii) Electromagnetic noise is a problem to be overcome with shielding and signal preamplification. <i>Advantages:</i> (i) Does not require a spring for stable operation due to EM damping. (ii) Covers the range of frequencies most useful in the characterisation of sands, rocks, soils and gravels. (iii) Control of piston displacement allows the fluid pressure to be well controlled.
Piezoelectric	200–10000	<i>Design limited by</i> (i) Lack of availability of transducers for frequencies less than about 200 Hz. (ii) It is not possible to drive a piezoelectric system at a wide range of frequencies. (iii) The generated displacements are very small, and it is not certain that the electrokinetic effect is fully developed with such small displacements. (iv) It is unclear whether check valves can be made to operate effectively at such small swept volumes and high frequencies. <i>Advantages:</i> (i) Frequencies above 10 kHz may be attained. (ii) Covers the range of frequencies most useful in the study of seismoelectric exploration. (iii) Forces far greater than that possible with an electromagnetic shaker are possible with a stack of piezoelectric transducers, allowing the study of low porosity, low permeability rocks at specific frequencies.

However, subsequently we have used a piston with a jointed design that is made from brass with an 'O'-ring seal. The jointed design improves the alignment and reduces seal wear.

The sample is held in a thick horizontal Perspex tube by perforated Perspex discs and a spring. There are four ports at each end of the tube. These are arranged radially with an offset of 90° and can accommodate up to two nonpolarizing electrodes, a pressure transducer, and a check

valve (Figure 5). The piston end of the tube is either left open to accept a piston with a rubber seal or can be covered with a rubber membrane. The output end is connected directly to the output fluid reservoir. While it is possible to raise the output fluid pressure with the aid of a backpressure regulator, the output fluid pressure was kept at atmospheric pressure for most of the initial tests. The sample tube is held extremely rigidly in a frame to which the shaker is also attached. The

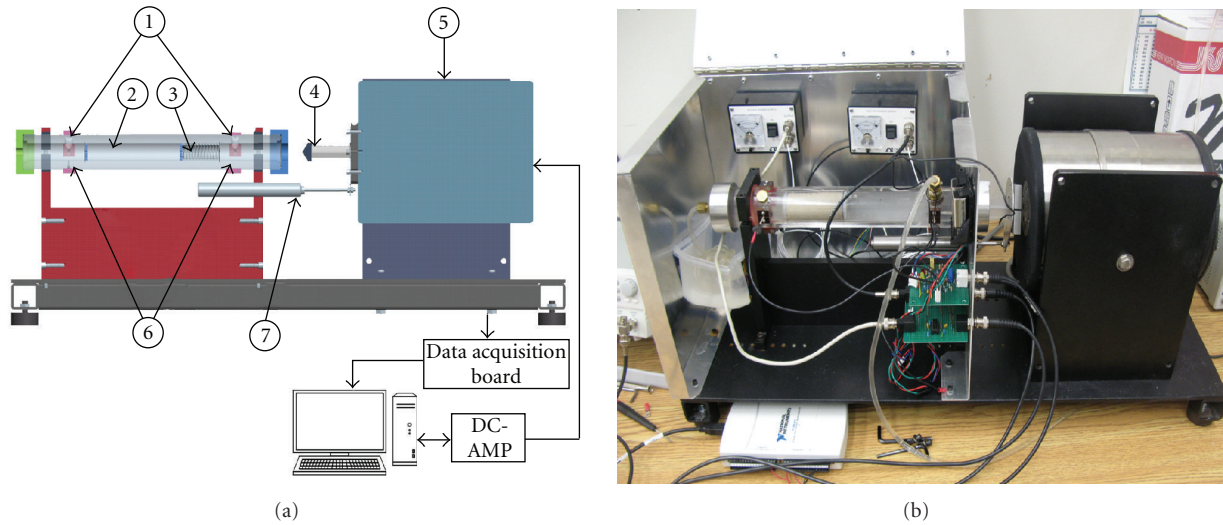


FIGURE 4: The electromagnetic drive apparatus for measuring the time-dependent streaming potential coefficient of granular media; (a) diagram, (b) photograph. (1) Port for fluid circulation or pressure transducer (2 at each end), (2) space for sample, (3) support spring and perforated end-piece, (4) piston, (5) precision electromagnetic shaker, (6) position of electrodes, and (7) linear motion sensor (LVDT).

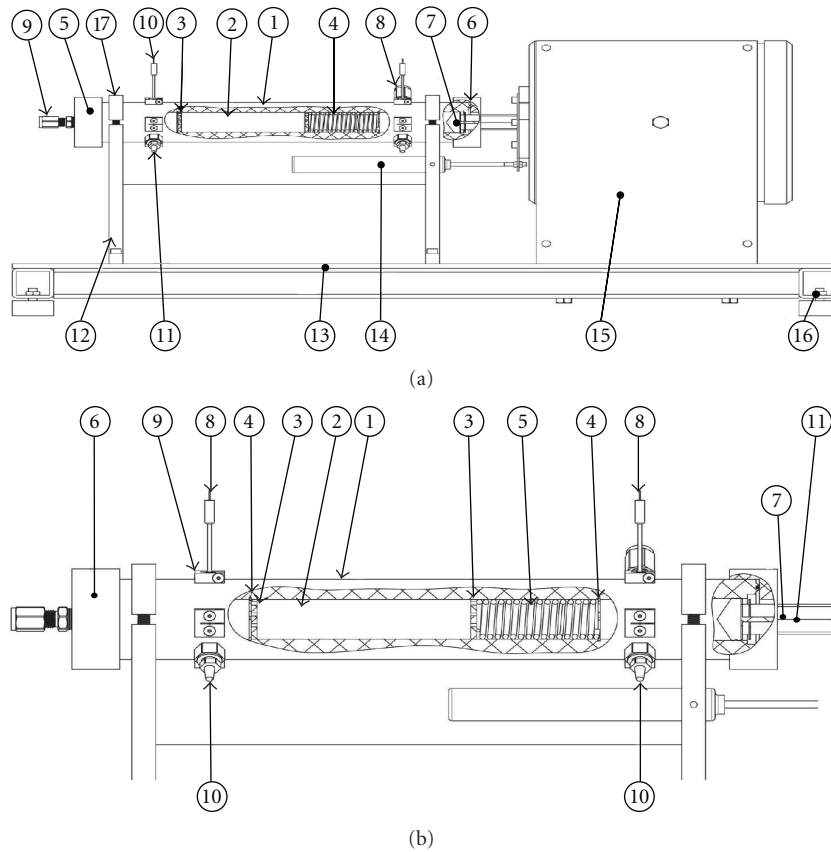


FIGURE 5: Detailed design of the electromagnetic drive apparatus: (a) complete, (1) perspex tube, (2) sample, (3) drilled polycarbonate disk, (4) spring, (5) screwed output end enclosure, (6) screwed input end enclosure, (7) piston, (8) fluid input check valve (Swagelok), (9) fluid output connector (Swagelok), (10) downstream streaming potential electrode, (11) downstream dynamic pressure transducer, (12) steel frame, (13) steel base, (14) LVDT, (15) EM shaker, (16) adjustable vibration damping feet, and (17) clamp to hold tube. (b) Details of the piston assembly, (1) perspex tube, (2) sample, (3) drilled polycarbonate disk, (4) circlip, (5) spring, (6) screwed output end enclosure, (7) screwed input end enclosure, (8) streaming potential electrodes ($\times 2$), (9) sealing mechanism for inserting streaming potential electrodes, (10) dynamic pressure transducers ($\times 2$) downstream, and (11) piston.

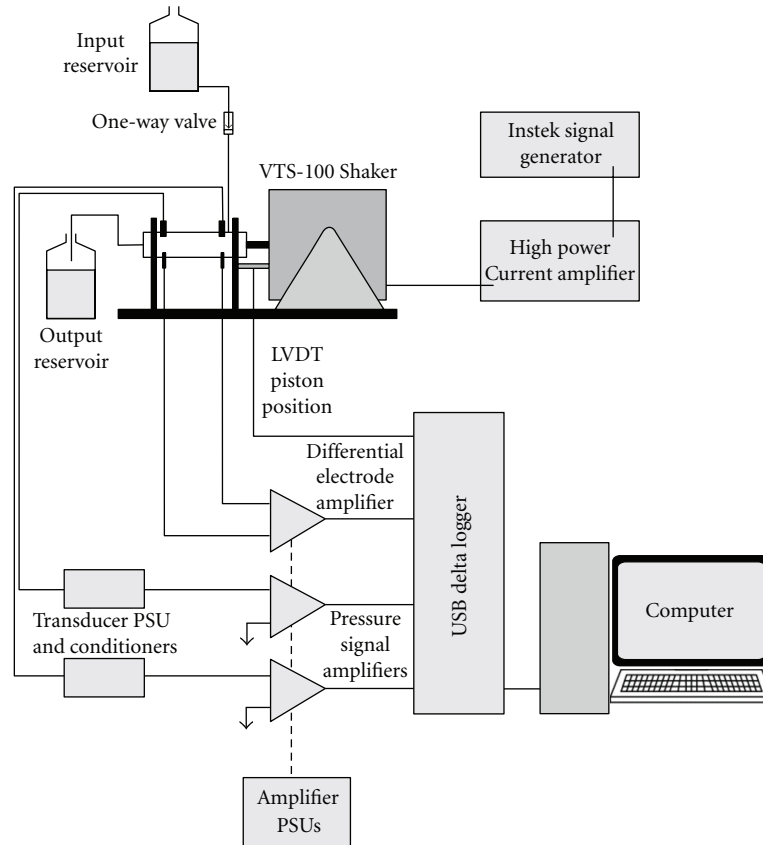


FIGURE 6: Experimental setup.

electromagnetic shaker drives the piston directly along the axis of the sample cell. Hence the system is conceptually and in reality extremely simple.

There are a number of different ways in which the system can be used. The drive may be imposed by the piston directly or by the piston working on the rubber membrane. There are 4 modes of fluid transport:

- with a closed fluid system (i.e., no fluid input or output) (push-pull AC mode);
- with fluid being drawn into the cell through a check valve on the backstroke of the piston and then driven through the sample on the compression stroke (pumping AC mode);
- while a constant fluid flow is imposed by an external pump (DC mode);
- a combination of (b) and (c). In this mode we have an AC signal imposed upon a DC signal, but the DC flow elevates the upstream fluid pressure sufficiently to counter any tendency to cavitation on the return stroke of the piston.

The apparatus imposes a time-varying fluid flow while measuring and logging (i) the displacement of the piston, (ii) the instantaneous pressure at each end of the sample, and (iii) the instantaneous electrical potential difference between the ends of the sample. The instantaneous streaming potential coefficient is the ratio of the electrical potential difference

and the fluid pressure difference. Hence we required high-quality fluid pressure and electrical potential measurements to enable accurate streaming potential coefficient measurements to be made, while an independent measurement of piston displacement was also desirable. Figure 6 shows the overall data acquisition setup, the elements of which are described below.

Fluid pressure measurements are made using DPX101-250 and DPX101-5K dynamic pressure transducers from Omega. These transducers have a maximum pressure of 1.72 MPa (250 psi) and 34.4 MPa (5000 psi), respectively. The DPX-250 transducer allows samples up to 150 mm long with a diameter of 25.4 mm, porosities up to 0.3, and with hydraulically conductive pores greater than $33.8\ \mu\text{m}$ to be measured up to 1 kHz. The larger range transducer can be used if the samples are longer, have a smaller diameter, have a smaller porosity, or contain smaller pores. Shorter, more porous samples with larger pores can be measured with the DPX-250 transducer and by increasing the piston displacement. Both of these transducers are designed for measuring pressures that change at a high frequency. They have a rise time of $1\ \mu\text{s}$, a resonant frequency of 0.5 MHz, and can be used at frequencies up to 170 kHz. Each of the transducers is operated by a separate driver and signal conditioning unit (ACC-PS1), which can be seen in Figure 4(b) as the boxes with small panel meters. The two pressure signals are passed to two matched preamplifiers and hence to a National Instruments USB-6229 data acquisition

system that is controlled by LabView. The preamplifiers, which were designed and constructed in our laboratory, are based on a quad low noise TL074IN J-FET input operational amplifier chip from Texas Instruments.

We have used a number of different electrodes with various degrees of success. The measurements shown in the associated paper [12] were made using nonpolarising Ag/AgCl electrodes from Cypress Systems. However, we have also used platinum black electrodes with success. The electrical potential difference measurements are amplified using a differential preamplifier that we have designed and constructed specifically for the task. Since the resistance of rocks ranges from very low values for high porosity, highly connected rocks that are saturated with saline pore fluids to extremely high values for low porosity rocks that are saturated with low salinity fluids, we required the input impedance of the measurement circuitry to be at least $10^9 \Omega$. The differential preamplifier we built has an input impedance of $10^{12} \Omega$ and is based on TL074IN J-FET input operational amplifier chips from Texas Instruments. These amplifiers have a slew rate of $13 \text{ V}/\mu\text{s}$, which is sufficient for the amplifiers to follow a signal up to 4.83 MHz. The output of the preamplifier is logged by a National Instruments USB-6229 data acquisition system and controlled by LabView.

An LVDT from Omega (LD610-15) has also been incorporated in the experimental apparatus in order that the precise position of the piston can be logged together with the potential and pressure signals. This allows us to confirm that the movement of the piston is correct and may also allow us to add a control loop at some future date.

Power-line electrical noise was a problem initially, swamping the signal (29 dB with respect to the signal). The cell was enclosed in a Faraday cage as shown in Figure 4(b). In addition, the measured signals were amplified by custom designed preamplifiers that were placed close to the transducers and inside the Faraday cage. While low noise active power supplies were used to drive the preamplifiers in initial tests, they were soon replaced by batteries in order to reduce power line noise further. The combined effect of the Faraday cage and the preamplification reduced the noise by 46 dB so that the noise was reduced to -17 dB with respect to the signal. Signal averaging is then used to reduce the final noise level to -51 dB with respect to the signal.

The electromagnetic shaker is driven by its own power amplifier and controlled by a GW Instek (SFG-2110) function generator. The function generator allows the type of wave and its frequency to be defined, while the power amplifier controls the displacement of the piston and the force it can impart. The temperatures of the fluid and of the cell are also routinely measured using calibrated K-type thermocouples.

Although it is possible to calculate the instantaneous streaming potential coefficient, such data is noisy. In our data analysis we prefer to use the RMS fluid pressure difference and the RMS electrical potential difference calculated over at least 100 cycles to calculate the streaming potential coefficient. This method provides a robust and accurate value for the streaming potential coefficient. We are currently examining ways of using active digital filtering

to improve the quality of the data by removing harmonic noise from the data, but since this is a paper concerned with mechanical and experimental design, we will report our data processing advances elsewhere. However, there does exist an excellent article on the collection and processing of streaming potential data by Reppert and Morgan [4].

6. Conclusions

Six different approaches to the design of an experimental apparatus for measuring the time-dependent streaming potential coefficient of porous and granular media have been examined. There are fundamental or practical limitations to five of them.

A hydraulic drive was eliminated at an early stage due to the difficulty of driving liquids at high frequencies. The connecting pin and spring (scotch yoke) approach is first constrained to $f < 125 \text{ Hz}$ by the spring design, and then to $f < 33 \text{ Hz}$ by the lack of an electric motor with sufficient torque and speed. This design has been used once in the past but only in the range $f < 21.28 \text{ Hz}$ [7]. The cam and spring design is similar being first constrained to $f < 125 \text{ Hz}$ by the spring design, and then to $f < 33 \text{ Hz}$ by the electric motor specification. The pneumatic drive approach is constrained to $f < 100 \text{ Hz}$ by the maximum frequency of commercially available servovalves, while the use of a piezoelectric drive has a number of disadvantages, the most serious of which are that they can only be used for $f > 200 \text{ Hz}$ and for a very small range of frequencies.

The most promising approach was that of using an electromagnetic drive, which can, in principle, provide a measurement in the range $1 \text{ Hz} < f < 6.5 \text{ kHz}$ (using a VTS-100 shaker) with accurate frequency and amplitude control. This approach was implemented as a full experimental rig for samples of disaggregated and unconsolidated porous media such as sands. The apparatus can take samples with a diameter of 2.54 cm that are packed into a Perspex tube. Sample lengths between 5 and 30 cm are possible. We have tested the apparatus successfully and give some initial data in an associated paper [12]. Since the differential fluid pressure depends strongly on the porosity and permeability of the sample and solid samples require a pressure vessel with a sample sleeve, we have developed a separate apparatus for solid samples of porous media including rocks, which is in development. Early results from this apparatus suggest that cavitation is a problem that needs to be overcome using some method other than check valves.

Appendix

A. Analysis of Drive Mechanisms

In the following analyses we assume that the sample and piston diameters are equal and in the range 5 to 40 mm. This implies that the force that the piston must impart to the fluid is in the range 39.27 N to 2513 N in order to obtain a maximum fluid differential pressure of 2 MPa.

A.1. Connecting-Pin Drive. A conceptual design for an AC electrokinetic apparatus using a connecting-pin drive is shown in Figure 2(a). The driving force is provided by an electric motor and a system of connecting pins and springs. The motor drives a wheel upon which an eccentred pin has been attached. The rotation of the motor is transformed into a linear motion by the action of the eccentred pin (Figure 2(a) (1)) within a slot in the scotch yoke rod (Figure 2(a) (2)). The linear movement compresses a spring Figure 2(a) (3), which is calibrated to require 160 N for each 1 cm of compression. The spring acts upon the compression piston Figure 2(a) (4) in such a manner that a maximum pressure can be applied to the pore fluid. The spring is necessary to allow the motor to turn while using low porosity samples with an incompressible pore fluid, which would otherwise lock up the mechanism.

Assuming that the sample and piston diameter falls in the range $5 < d_p < 40$ mm, the spring constant k_{sp} required to generate a maximum pore fluid pressure $P_{max} = 2$ MPa with a piston displacement of 1 cm falls in the range $3.93 \times 10^3 \text{ N/m} < k_{sp} < 2.51 \times 10^5 \text{ N/m}$. This type of spring is commercially available. The mean flow rate varies between 0.39 cm^3 per cycle and 25.13 cm^3 per cycle. It is also necessary to calculate the maximum frequency that such a system could reach while remaining stable. We have used the equations in Juvinal and Marshek [20] to obtain the natural frequency $f_n = 198$ Hz for spring with dimensions conforming to our experimental design (5.55 cm diameter spring). Such a spring is stable only if the 13th harmonic of the mechanical system is smaller than f_n , which implies that the maximum drive frequency we could use is 15.23 Hz using this drive method. If we use the smallest spring and sample combination possible (5 mm diameter) the highest stable frequency is 125 Hz.

In order to reach frequencies of 1 kHz we need a motor that will be capable of a speed of 60,000 revolutions per minute (rpm). Knowing the forces that must be overcome in order to turn the drive wheel allows us to calculate the specifications of the motor. If the distance between the centre of the connecting pin and the motor axis is B , the force experienced by the connecting pin is given by $F = mB\omega^2 \sin(\omega t) + k_{sp}B \sin(\omega t)$, where m is the mass of the piston, spring, and connecting pin (i.e., those parts that are moved by the connecting wheel) and ω is the angular frequency. This equation assumes that damping in this system is negligible, which is reasonable if the sample is fully saturated with a noncompressible fluid. However, if the sample is not fully saturated, there is a damping term of the form $B\omega \cos(\omega t)$. The force F creates a torque due to its tangent component and the tangent component of the resulting friction force which operates between the surface of the connecting pin and the inner surface of the slot in the connecting pin. The motor must develop a torque that is sufficient to compress the spring and accelerate the masses. It must therefore develop a torque given by $M = FB \cos(\omega t) + F\mu B \sin(\omega t)$, where μ is the coefficient of friction, which leads to $M = (B^2/2)(m\omega^2 + k_{sp})(\mu + \sin(2\omega t) - \mu \cos(2\omega t))$, and where the frequency of the torque M is twice that of the force. The torque is zero at $2n\pi/4$, where n is an integer (including

zero), but does not reach its maxima at $(2n + 1)\pi/4$ because the torque is not symmetrical but reaches its maximum value at about 0.84 rad (about 48 degrees). One should note that the position of the maximum value is not a function of m , k_{sp} , ω , or B , but does depend upon the coefficient of friction μ .

Figure 7(a) shows the maximum torque that needs to be overcome to drive a connecting pin design as a function of frequency for different values of coefficient of friction and for ($m = 0.5$ kg, $k_{sp} = 1.6 \times 10^4$ N/m, $\omega = 6283$ rad/s (1000 Hz), $B = 1$ cm). It is clear that a well-lubricated system is needed to reduce the coefficient of friction to as low a value as possible. The value of the coefficient of friction also governs when in the cycle of the motor the maximum torque is attained (Figure 7(b)). For the scenario shown in Figure 7, the value of the maximum torque is about 1090 Nm. We have found that commercially available electric motors that can operate at the required speed are not able to provide a torque this high, not even close. Furthermore, reducing the piston diameter to 5 mm only provides a marginal reduction in the maximum torque that needs to be overcome. Indeed, if we relax the frequency specification to that which would be possible with the spring system, we obtain a torque of 17.04 Nm. It is possible to find brushless motors that can provide such a torque, but only for speeds up to about 2000 rpm (i.e., about 33 Hz).

In conclusion, neither an electric motor with a combination of sufficient torque and speed, nor a spring with sufficient stiffness per mass is currently available for the connecting-pin design to be feasible up to 1 kHz. Such a system would be possible, but could attain frequencies only up to about 33 Hz with current technology. Indeed, Sears and Groves [7] who used such a system were only able to attain a maximum frequency of 21.28 Hz.

A.2. Cam Drive. A conceptual design for an AC electrokinetic apparatus using a cam drive is shown in Figure 2(b). This mechanical system works in a similar manner to the connecting-pin design. The motor turns a cam with a variable diameter. The cam acts on a wheel which is attached to a pin that compresses a spring in the same manner as for the connecting-pin design. The spring has the same purpose as in the connecting pin design, but also acts to maintain good contact between the wheel and the spring. The main advantage of the cam mechanism is that it has a lower friction, which reduces the torque that the motor must provide. A secondary advantage is that the profile of the imposed fluid pulse can be varied by changing the shape of the cam.

Many of the same design considerations that were made for the connecting pin design are also valid for this design. The lack of a spring with a sufficiently high natural frequency makes the design unworkable above about 125 Hz. The lower internal friction of the design (approaching 0.01) reduces the torque required by the motor to about 997 Nm. However, this is, once more, much higher than electric motors of a modern design can provide. At 125 Hz, the torque is 15.57 Nm, which again can be reached by brushless motors but only for frequencies up to about 33 Hz.

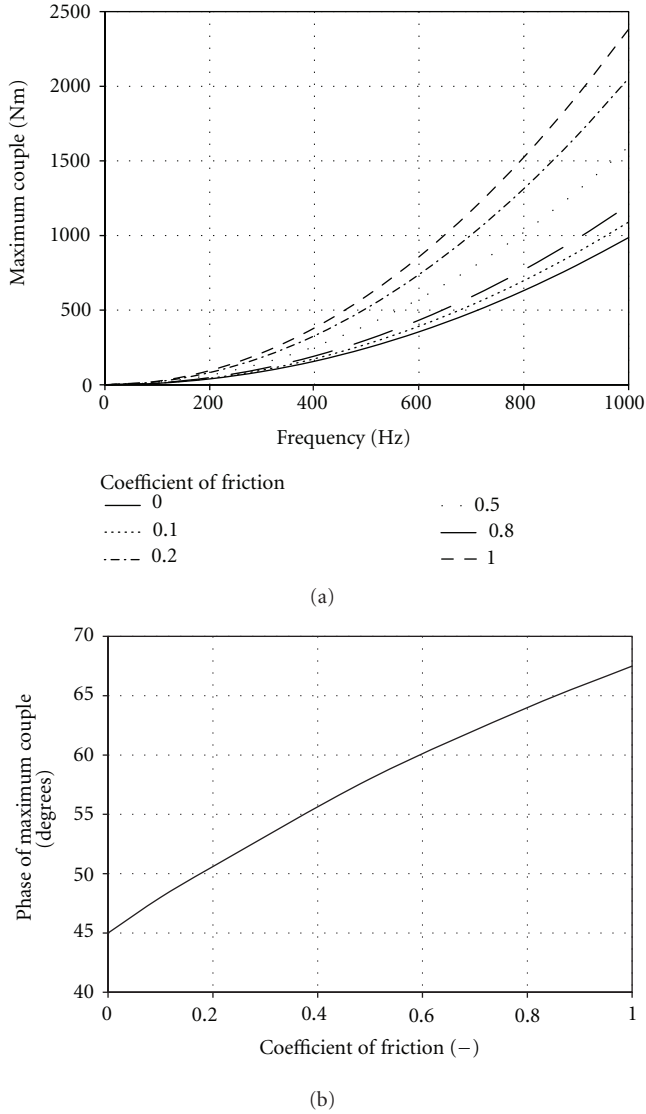


FIGURE 7: (a) The maximum torque that needs to be overcome to drive a connecting pin design as a function of frequency for different values of coefficient of friction. (b) The phase at which the maximum torque occurs as a function of the coefficient of friction.

A.3. Pneumatic Drive. A conceptual design for an AC electrokinetic apparatus using a pneumatic drive is shown in Figure 3(a). The pneumatic system consists of two small actuators that are situated on each side of the sample vessel. We consider a mode of operation where the actuators are controlled in extension and allowed to retract under the influence of the fluid pressure in the cell (i.e., neutral mode). This mode of operation decreases both the response time and fluid friction in the pipes, but requires there to be an actuator at each side of the sample in order to complete the full cycle. The two-actuator approach also allows an external reservoir to be eliminated, while using the space that is occupied by the piston in the other designs to act as an internal fluid reservoir. In order to impose a sinusoidal fluid pressure in the process fluid, a rectified half-wave is first sent to the servo-valve controlling the first actuator, while the other actuator is subject

to atmospheric pressure. When the first rectified half-wave returns to zero (i.e., atmospheric pressure), a rectified half-wave is sent to the servo-valve controlling the second actuator, while the first actuator is subject to atmospheric pressure.

The advantage of the pneumatic system is that the air is compressible. The compressible air allows the imposition of the force without the need for a spring, which eliminates the frequency limit that was caused by the springs in the mechanical designs. A variation on this design might replace both actuators with membranes that are activated by pneumatic pressure. Such a design has the potential to reach higher frequencies still. We have calculated that if a standard 100 psi (689 kPa) pneumatic system is used, the diameter of the actuator needs to be between 0.85 cm and 6.81 cm in order to generate a maximum fluid pressure of 2 MPa. Although actuators with this diameter are available, the servo-valve would have to operate at very high speeds in order to attain a frequency of 1 kHz. Presently the fastest available servovalves only allows speeds up to 100 Hz to be reached. Hence, a pneumatic system is currently not possible above about 100 Hz.

A.4. Electromagnetic Drive. A conceptual design for an AC electrokinetic apparatus using an electromagnetic drive is shown in Figure 3(b). The electromagnetic drive system relies on the use of an electromagnetic shaker. Such shakers provide high-quality sinusoidal displacements at low or high frequencies. Their main use is in the testing of mechanical structures and aircraft. A sine wave generator is used to drive a DC amplifier which provides an amplified current sufficient to drive the electromagnetic shaker. This current passes through the coils of the shaker producing an electromagnetic field which in turn displaces a magnetic rod. The force on the rod is proportional to the current. The rod (Figure 3(b) (4)) is attached to a piston that drives the fluid through the sample with a sinusoidally varying force. Two one-way valves are arranged at each end of the sample to allow new fluid to be drawn into cell on the return stroke which is then pushed through the sample on the compression stroke. The result is a sinusoidally varying fluid pressure during the compression stroke, and a quasisinusoidally varying fluid pressure during the return stroke. There are a range of different shakers available, some of which have maximum frequencies of the order of 4500 Hz, rod displacements up to 50 mm, and maximum forces ranging from 100 N to 178 000 N.

It is possible to control the piston displacement of a shaker by varying the control current. However there exists a maximum displacement which decreases with frequency. We need to ensure that the maximum piston displacement at 1 kHz is sufficient to make high-quality measurements. The force provided by a shaker is given classically by $F = F_o \sin(\omega t) = ma$, where F_o is the maximum force that the shaker can provide, m is the mass of fluid accelerated at an acceleration a , ω is the angular frequency, and t is time. The acceleration a , velocity v , and displacement x of the shaker rod (and any piston that is attached to it) can be obtained by rearrangement and integration of the force equation to give $a = F_o \sin(\omega t)/m$; $v = F_o \cos(\omega t)/m\omega$; $x = -F_o \sin(\omega t)/m\omega^2$. For a typical shaker such as the one we

have subsequently used (Dynamic solutions, VTS-100) $F_o = 100$ lbf (444.82 N), which easily supplies the force required to generate a fluid pressure difference of 2 MPa for samples with diameters in the range 5 to 40 mm (i.e., 39.27 N to 2513 N, resp.). For an accelerated mass $m = 0.5$ kg and a frequency of 1 kHz, these applied forces imply a maximum peak-to-peak displacement that varies between $4 \mu\text{m}$ and 0.254 mm for sample and piston diameters of 0.5 and 4 cm, respectively, and the volume of fluid moved by the shaker varies between $0.628 \text{ cm}^3/\text{s}$ and $39.9 \text{ cm}^3/\text{s}$ for sample and piston diameters of 0.5 and 4 cm, respectively.

If we use (5) with the range of peak-to-peak displacement values ($4 \times 10^{-6} \text{ m} < x < 2.54 \times 10^{-4} \text{ m}$) for typical clastic rocks with porosities in the range $0.05 < \phi < 0.3$, with characteristic pore sizes in the range $3 \times 10^{-6} \text{ m} < r_{\text{eff}} < 1 \times 10^{-3} \text{ m}$ we generate maximum fluid pressures in the range measurable by a DPX101-5K transducer for frequencies in the range $2 < f < 1000$ Hz if the samples are between 0.5 and 2 cm long. Repeating this analysis for typical sands and gravels with porosities in the range $0.25 < \phi < 0.5$ and characteristic pore sizes in the range $1 \times 10^{-5} \text{ m} < r_{\text{eff}} < 1 \times 10^{-3} \text{ m}$ generates fluid pressures in the range measurable by a DPX101-250 transducer for frequencies in the range $2 < f < 1000$ Hz if the samples are between 30 mm and 100 mm long.

Figure 8 shows the maximum piston displacement and maximum piston velocity. The maximum piston acceleration is not a function of frequency and takes values of 1472, 640, 320, 213 and 160 m/s^2 for masses of 0.1, 0.25, 0.5, 0.75, and 1 kg, respectively. The thresholds shown in the diagram represent the maximum values possible using a VTS-100 Shaker from Dynamic Solutions Inc. For a mass of 100 g the acceleration of 1472 m/s^2 also represents the maximum value possible with this instrument. The displacement can be controlled by varying the current in the coils of the shaker, either manually, or using a feedback mechanism. Hence, it is possible to limit the displacement and the velocity of the piston to values that are less than the threshold values for the shaker, but still sufficient to drive the fluid through the sample.

We conclude that the electromagnetic drive has the power to drive the AC electrokinetic system up to 1 kHz. However, at low frequencies the piston displacement must be limited to ensure that it, and the piston velocity, do not reach the maximum values specified for the shaker.

A.5. Piezoelectric Drive. The last conceptual possibility is to use a piezoelectric drive to attain the required frequencies. It is certain that piezoelectric transducers can be used at the specified maximum frequency. However, they suffer from a number of practical disadvantages.

- (1) It is difficult to drive a piezoelectric system at a wide range of frequencies.
- (2) It is impossible to carry out tests at low frequencies (less than about 200 Hz).
- (3) The displacements are very small, and it is not certain that the electrokinetic effect is fully developed with such small displacements.

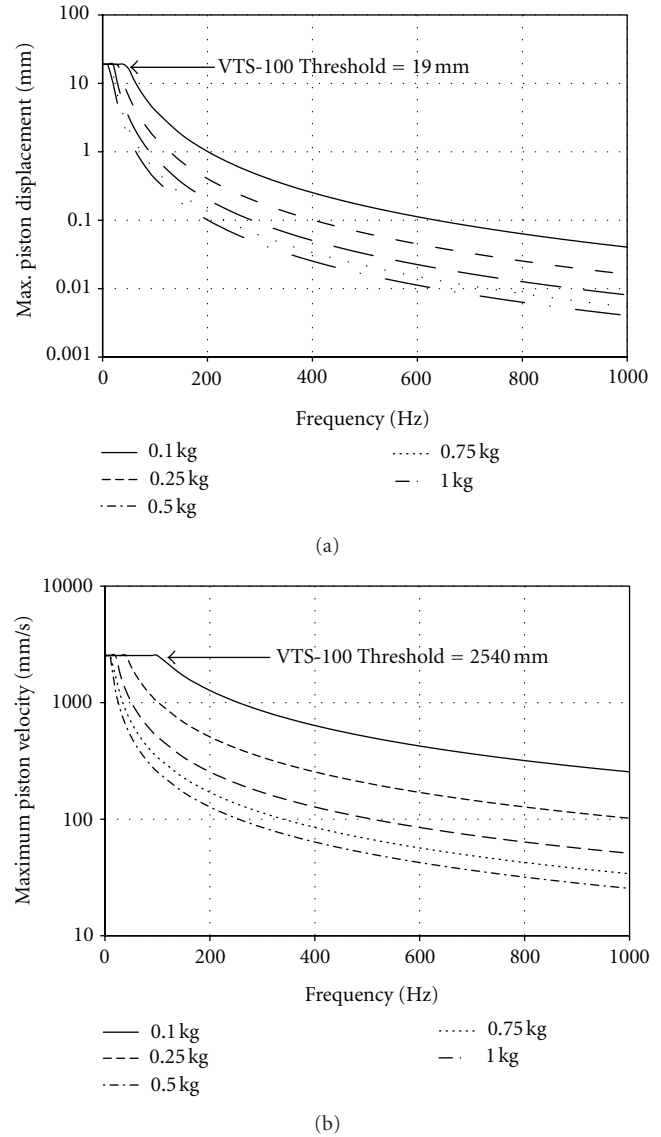


FIGURE 8: Dynamic properties of a system powered by an electromagnetic shaker, with a sample and piston diameter of 1 cm and a maximum fluid pressure of 2 MPa. (a) Maximum piston displacement as a function of frequency and driven mass. (b) Maximum piston velocity as a function of frequency and driven mass.

Consequently, we have not pursued the piezoelectric drive. However, we do recognize that the force that a stack of piezoelectric transducers can impose is far greater than that possible with a shaker, and consequently useful for low porosity and permeability rocks. Moreover, there is no reason why measurements might not be made up to far higher frequencies (above 10 kHz).

Acknowledgments

This work has been made possible thanks to funding by the Natural Sciences and Engineering Research Council of Canada (NSERC) Discovery Grant Programme. The

authors would also like to thank Guillaume Lalande and the members of the mechanical engineering workshop for their help.

References

- [1] C. Bordes, L. Jouniaux, S. Garambois, M. Dietrich, J. P. Pozzi, and S. Gaffet, "Evidence of the theoretically predicted seismo-magnetic conversion," *Geophysical Journal International*, vol. 174, no. 2, pp. 489–504, 2008.
- [2] C. Bordes, L. Jouniaux, M. Dietrich, J. P. Pozzi, and S. Garambois, "First laboratory measurements of seismo-magnetic conversions in fluid-filled Fontainebleau sand," *Geophysical Research Letters*, vol. 33, no. 1, Article ID L01302, 2006.
- [3] R. Chandler, "Transient streaming potential measurements on fluid-saturated porous structures: an experimental verification of Biot's slow wave in the quasi-static limit," *Journal of the Acoustical Society of America*, vol. 70, no. 1, pp. 116–121, 1981.
- [4] P. M. Reppert and F. D. Morgan, "Streaming potential collection and data processing techniques," *Journal of Colloid and Interface Science*, vol. 233, no. 2, pp. 348–355, 2001.
- [5] R. G. Packard, "Streaming potentials across glass capillaries for sinusoidal pressure," *The Journal of Chemical Physics*, vol. 21, no. 2, pp. 303–307, 1953.
- [6] C. E. Cooke, "Study of electrokinetic effects using sinusoidal pressure and voltage," *The Journal of Chemical Physics*, vol. 23, no. 12, pp. 2299–2303, 1955.
- [7] A. R. Sears and J. N. Groves, "The use of oscillating laminar flow streaming potential measurements to determine the zeta potential of a capillary surface," *Journal of Colloid And Interface Science*, vol. 65, no. 3, pp. 479–482, 1978.
- [8] P. M. Reppert, *Electrokinetics in the earth*, Ph.D. thesis, Massachusetts Institute of Technology, 2000.
- [9] P. M. Reppert, F. D. Morgan, D. P. Lesmes, and L. Jouniaux, "Frequency-dependent streaming potentials," *Journal of Colloid and Interface Science*, vol. 234, no. 1, pp. 194–203, 2001.
- [10] D. B. Pengra, S. X. Li, and P. Z. Wong, "Determination of rock properties by low-frequency AC electrokinetics," *Journal of Geophysical Research B*, vol. 104, no. 12, pp. 29485–29508, 1999.
- [11] M. R. Sheffer, P. M. Reppert, and J. A. Howie, "A laboratory apparatus for streaming potential and resistivity measurements on soil samples," *Review of Scientific Instruments*, vol. 78, no. 9, Article ID 094502, 2007.
- [12] P. W. J. Glover, J. Ruel, and E. Tardif, "Frequency-dependent streaming potential of porous media: 2. Experimental measurement of unconsolidated materials," *International Journal of Geophysics*. In press.
- [13] D. L. Johnson, J. Koplik, and R. Dashen, "Theory of dynamic permeability and tortuosity in fluid-saturated porous media," *Journal of Fluid Mechanics*, vol. 176, pp. 379–402, 1987.
- [14] Y. Bernabé, "The frequency dependence of harmonic fluid flow through networks of cracks and pores," *Pure and Applied Geophysics*, vol. 149, no. 3, pp. 489–506, 1997.
- [15] Y. Bernabé, "Oscillating flow of a compressible fluid through deformable pipes and pipe networks: wave propagation phenomena," *Pure and Applied Geophysics*, vol. 166, no. 5–7, pp. 969–994, 2009.
- [16] Y. Bernabé, "Propagation of Biot slow waves in heterogeneous pipe networks: effect of the pipe radius distribution on the effective wave velocity and attenuation," *Journal of Geophysical Research B*, vol. 114, no. 11, Article ID B11202, 2009.
- [17] E. Charlaix, A. P. Kushnick, and J. P. Stokes, "Experimental study of dynamic permeability in porous media," *Physical Review Letters*, vol. 61, no. 14, pp. 1595–1598, 1988.
- [18] E. Walker and P. W. J. Glover, "Characteristic pore size, permeability and the electrokinetic coupling coefficient transition frequency in porous media," *Geophysics*, vol. 75, no. 6, pp. E235–E246, 2010.
- [19] E. Tardif, P. W. J. Glover, and J. Ruel, "Frequency-dependent streaming potential of Ottawa sand," *Journal of Geophysical Research B*, vol. 116, no. 4, Article ID B04206, 2011.
- [20] K. M. Juvinal and R. C. Marshek, *Fundamentals of Machine Component Design*, John Wiley & Sons, New York, NY, USA, 2005.

Review Article

Frequency-Dependent Streaming Potentials: A Review

L. Jouniaux¹ and C. Bordes²

¹*Institut de Physique du Globe de Strasbourg, UdS-CNRS UMR 7516, Université de Strasbourg, 5 rue René Descartes, 67084 Strasbourg, France*

²*Laboratoire des Fluides Complexes et leurs Réservoirs, UPPA-CNRS UMR5150, Université de Pau et des Pays de l'Adour, 64013 Pau, France*

Correspondence should be addressed to L. Jouniaux, laurence.jouniaux@unistra.fr

Received 1 July 2011; Accepted 14 November 2011

Academic Editor: Tsuneo Ishido

Copyright © 2012 L. Jouniaux and C. Bordes. This is an open access article distributed under the Creative Commons Attribution License, which permits unrestricted use, distribution, and reproduction in any medium, provided the original work is properly cited.

The interpretation of seismoelectric observations involves the dynamic electrokinetic coupling, which is related to the streaming potential coefficient. We describe the different models of the frequency-dependent streaming potential, mainly Packard's and Pride's model. We compare the transition frequency separating low-frequency viscous flow and high-frequency inertial flow, for dynamic permeability and dynamic streaming potential. We show that the transition frequency, on a various collection of samples for which both formation factor and permeability are measured, is predicted to depend on the permeability as inversely proportional to the permeability. We review the experimental setups built to be able to perform dynamic measurements. And we present some measurements and calculations of the dynamic streaming potential.

1. Introduction

Electrokinetics arise from the interaction between the rock matrix and the pore water. Therefore electrokinetic phenomena are often observed in aquifers, volcanoes, and hydrocarbon or hydrothermal reservoirs. Observations show that seismoelectromagnetic signals associated to earthquakes can be induced by electromagnetic induction [1, 2] or by electrokinetic effect [3, 4]. The electrokinetic phenomena are due to pore pressure gradients leading to fluid flow in the porous media or fractures and inducing electrical fields. These electrokinetic effects are associated to the electrical double layer which was originally described by Stern. The electrokinetic signals can be induced by global displacements of the reservoir fluids (streaming potential) or by the propagation of seismic waves (seismoelectromagnetic effect). As soon as these pressure gradients have a transient signature, the dynamic part of the electrokinetic coupling has to be taken into account by introducing the dependence on fluid transport properties.

It is generally admitted that two kinds of seismoelectromagnetic effects can be observed. The dominant contribution, commonly called “coseismic”, is generated close to the

receivers during the passage of seismic waves. The second kind, so-called “interfacial conversion” [5], is very similar to dipole radiation and is generated at physicochemical interfaces due to strong electrokinetic coupling discontinuities. This interface conversion is often perceived to have the potential to detect fine fluids transitions with higher resolution than seismic investigations, but in practice, signals are often masked by electromagnetic disturbances, especially when generated at great depth.

Nevertheless recent field studies have focused on the seismoelectric conversions linked to electrokinetics in order to investigate oil and gas reservoirs [6] or hydraulic reservoirs [5, 7–13]. It has been shown using these investigations that not only the depth of the reservoir can be deduced, but also the geometry of the reservoir can be imaged using the amplitudes of the electroseismic signals [14]. Moreover fractured zones can be detected and permeability can be measured using seismoelectrics in borehole [15–18]. This method is especially appealing to hydrogeophysics for the detection of subsurface interfaces induced by contrasts in permeability, in porosity, or in electrical properties (salinity and water content) [19–21].

The analytical interpretation of the seismoelectromagnetic phenomenon has been described by Pride [22], by connecting the theory of Biot [23] for the seismic wave propagation in a two-phase medium with Maxwell's equations, using dynamic electrokinetic couplings. The seismoelectromagnetic conversions have been modeled in homogeneous or layered saturated media [12, 21, 24–26] with applications to reservoir geophysics [27].

Theoretical developments showed that the electrical field induced by the P -waves propagation is related to the acceleration [12]. The electrokinetic coupling is created at the interface between grains and water, when there is a relative motion of electrolyte ions with respect to the mineral surface. Thus, seismic wave propagation in fluid-filled porous media generates conversions from seismic to electromagnetic energy which can be observed at the macroscopic scale, due to this electrokinetic coupling at the pore scale. The seismoelectric coupling is directly dependent on the fluid conductivity, the fluid density, and the electric double layer (the electrical interface between the grains and the water) (see [28], in this special issue “Electrokinetics in Earth Sciences” for more details). For more details on the surface complexation reactions see Davis et al. [29] or Guichet et al. [30]. It can be accurately quantified in the broad band by a dynamic coupling [22] which can be linked in the low-frequency limit to the steady-state streaming potential coefficient largely studied in porous media [30–44].

Laboratory experiments have also been investigated for a better understanding of the seismoelectric conversions [45–56]. These papers describe the laboratory studies performed to investigate this dynamic coupling. An oscillating pore pressure must be applied to a rock sample, and because of the relative motion between the rock and the fluid, an induced streaming potential can be measured. Depending on the oscillating frequency of the fluid, the fluid makes a transition from viscous dominated flow to inertial dominated flow. As the frequency increases, the motion of the fluid within the rock is delayed and larger pressure is needed. In order to know the dynamic coupling, both real and imaginary parts of the streaming potential must be measured.

2. From Dynamic Streaming Potential to Seismoelectromagnetic Coupling

The steady-state streaming potential coefficient is defined as the ratio of the streaming potential to the driving pore pressure:

$$C_{s0} = \frac{\Delta V}{\Delta P} = \frac{\varepsilon \zeta}{\eta \sigma_f}, \quad (1)$$

which is called the Helmholtz-Smoluchowski equation, where σ_f , ε , and η are the fluid conductivity, the dielectric constant of the fluid, and the fluid dynamic viscosity respectively (see [28]). In this formula the surface electrical conductivity is neglected compared to the fluid electrical conductivity. The potential ζ is the electrical potential within the double layer on the slipping plane. Although the zeta potential can hardly be modeled for a rock and although it

cannot be directly measured within a rock, the steady-state streaming potential coefficient can be measured in laboratory, by applying a fluid pressure difference (ΔP) and by measuring the induced streaming electric potential (ΔV) [30, 38, 39, 44, 57]. The electrical potential ζ itself depends on fluid composition and pH and the water conductivity [29–31, 38, 40, 42, 44, 58].

2.1. Packard's Model. Packard [59] proposed a model for the frequency-dependent streaming potential coefficient for capillary tubes, assuming that the Debye length is negligible compared to the capillary radius, based on the Navier-Stokes equation:

$$C_{s0}(\omega) = \frac{\Delta V(\omega)}{\Delta P(\omega)} = \left(\frac{\varepsilon \zeta}{\eta \sigma_f} \right) \left(\frac{2}{a \sqrt{i\omega \rho_f / \eta}} \frac{J_1(a \sqrt{i\omega \rho_f / \eta})}{J_0(a \sqrt{i\omega \rho_f / \eta})} e^{-i\omega t} \right), \quad (2)$$

where ω is the angular frequency, a is the capillary radius, J_1 and J_0 are the Bessel functions of the first order and the zeroth order, respectively, and ρ_f is the fluid density.

The transition angular frequency for a capillary is

$$\omega_c = \frac{\eta}{\rho_f a^2}. \quad (3)$$

More recently Reppert et al. [60] used the low- and high-frequency approximations of the Bessel functions to propose the following formula, which corresponds to their equation 26 corrected with the right exponents -2 and $-1/2$:

$$C_{s0}(\omega) = \left(\frac{\varepsilon \zeta}{\eta \sigma_f} \right) \left[1 + \left(\frac{-2}{a} \sqrt{\frac{\eta}{\omega \rho_f}} \left(\frac{1}{\sqrt{2}} - \frac{1}{\sqrt{2}} i \right) \right)^{-2} \right]^{-1/2} \quad (4)$$

with the transition angular frequency

$$\omega_c = \frac{8\eta}{\rho_f a^2} \quad (5)$$

and showed that this model was not very different from the model proposed by Packard [59].

The complete development relating Biot's theory and Maxwell's equations has been published by Pride in 1994 [22].

2.2. Pride's Model. Pride [22] derived the equations governing the coupling between seismic and electromagnetic wave propagation in a fluid-saturated porous medium from first principles for porous media. The following transport equations express the coupling between the mechanical and electromagnetic wavefields ([22] (174), (176), and (177)):

$$\begin{aligned} \mathbf{J} &= \sigma(\omega) \mathbf{E} + L(\omega) \left(-\nabla p + i\omega^2 \rho_f \mathbf{u}_s \right), \\ -i\omega \mathbf{w} &= L(\omega) \mathbf{E} + \frac{k(\omega)}{\eta} \left(-\nabla p + i\omega^2 \rho_f \mathbf{u}_s \right). \end{aligned} \quad (6)$$

In the first equation, the macroscopic electrical current density \mathbf{J} is the sum of the average conduction and streaming current densities. The filtration velocity \mathbf{w} of the second equation is separated into electrically and mechanically induced contributions. The electrical fields and mechanical forces that create the current density \mathbf{J} and filtration velocity \mathbf{w} are, respectively, \mathbf{E} and $(-\nabla p + i\omega^2\rho_f\mathbf{u}_s)$, where p is the pore-fluid pressure, \mathbf{u}_s is the solid displacement, and \mathbf{E} is the electric field. The complex and frequency-dependent electrokinetic coupling $L(\omega)$, which describes the coupling between the seismic and electromagnetic fields [22, 60], is the most important parameter in these equations. The other two coefficients, $\sigma(\omega)$ and $k(\omega)$, are the electric conductivity and dynamic permeability of the porous material, respectively.

The seismoelectric coupling that describes the coupling between the seismic and electromagnetic fields is complex and frequency-dependent Pride [22]:

$$L(\omega) = L_0 \left[1 - i \frac{\omega}{\omega_c} \frac{m}{4} \left(1 - 2 \frac{d}{\Lambda} \right)^2 \left(1 - i^{3/2} d \sqrt{\frac{\omega \rho_f}{\eta}} \right)^2 \right]^{-1/2}, \quad (7)$$

where L_0 is the low-frequency electrokinetic coupling, d is related to the Debye-length, Λ is a porous-material geometry term [65], and m is a dimensionless number (detailed in Pride [22]).

The transition angular frequency ω_c separating low-frequency viscous flow and high-frequency inertial flow is defined as

$$\omega_c = \frac{\phi \eta}{\alpha_\infty k_0 \rho_f}, \quad (8)$$

where ϕ is the porosity, k_0 is the intrinsic permeability, and α_∞ is the tortuosity.

2.3. Further Considerations. The low-frequency electrokinetic coupling L_0 is related to the steady-state streaming potential coefficient \mathbf{C}_{s0} by

$$L_0 = -\mathbf{C}_{s0} \sigma_r, \quad (9)$$

where σ_r is the rock conductivity. The electrokinetic coupling $L(\omega)$ can be estimated by considering that steady-state models of \mathbf{C}_{s0} can be applied to the calculation of L_0 . When writing $\sigma_r = \sigma_f/F$ with surface conductivity neglected, the steady-state electrokinetic coupling can be written as

$$L_0 = -\frac{\epsilon \zeta}{\eta F}. \quad (10)$$

We can see that the steady-state electrokinetic coupling is inversely proportional to the formation factor.

The transition angular frequency separating viscous and inertial flows in porous medium can be rewritten by inserting $\alpha_\infty = \phi F$ with F , as follows:

$$\omega_c = \frac{1}{F} \frac{\eta}{k_0 \rho_f}, \quad (11)$$

where F is the formation factor that can be deduced from resistivity measurements using Archie's law.

Since the permeability and the formation factor are not independent but can be related by $k_0 = CR^2/F$ [66] with C being a geometrical constant usually in the range 0.3–0.5 and R being the hydraulic radius, the transition angular frequency can be written as

$$\omega_c = \frac{\eta}{\rho_f CR^2}. \quad (12)$$

Equation (12) shows that the transition angular frequency in porous medium is inversely proportional to the square of the hydraulic radius.

Recently Walker and Glover [74] proposed a simplified equation of Pride's development assuming that the Debye length is negligible compared to the characteristic pore size, and assuming the following parameter:

$$m = 8 \left(\frac{\Lambda}{r_{\text{eff}}} \right)^2 \quad (13)$$

leading to

$$L(\omega) = L_0 \left[1 - 2i \frac{\omega}{\omega_c} \left(\frac{\Lambda}{r_{\text{eff}}} \right)^2 \right]^{-1/2} \quad (14)$$

with r_{eff} being the effective pore radius, and a transition angular frequency being

$$\omega_c = \frac{8\eta}{\rho_f r_{\text{eff}}^2}. \quad (15)$$

Garambois and Dietrich [12] studied the low-frequency assumption valid at seismic frequencies, meaning at frequencies lower than Biot's frequency separating viscous and inertial flows and gave the coseismic transfer function for low-frequency longitudinal plane waves. In this case, and assuming Biot's moduli $C \ll H$, they showed that the seismoelectric field \mathbf{E} is proportional to the grain acceleration:

$$\mathbf{E} \simeq -\frac{L_0}{\sigma_r} \rho_f \ddot{\mathbf{u}} = \frac{\epsilon \zeta}{\eta \sigma_f} \rho_f \ddot{\mathbf{u}}. \quad (16)$$

Equations (16), (9), and (1) show that transient seismoelectric magnitudes will be affected by the bulk density of the fluid, and the streaming potential coefficient which is inversely proportional to the water conductivity and proportional to the zeta potential (which depends on the water pH).

2.4. The Electrokinetic Transition Frequency Compared to Hydraulic's One. The theory of dynamic permeability in porous media has been studied by many authors [61, 65, 75–77].

The frequency behavior of the permeability is given by Pride (1994) [22]

$$\frac{k(\omega)}{k_0} = \left[\left(1 - i \frac{\omega}{\omega_c} \frac{4}{m} \right)^{1/2} - i \frac{\omega}{\omega_c} \right]^{-1}. \quad (17)$$

TABLE 1: Measured or predicted transition frequency for dynamic streaming potential and permeability, for samples of porosity ϕ , formation factor F , permeability k_0 , and half of the mean particle size r , from (SED) Smeulders et al. [61], (CKS) Charlaix et al. [62], (SG) Sears and Groves [63], (P) Packard [59], (TGR) Tardif et al. [64], and (RMLJ) Reppert et al. [60]. *Indicates predicted transition frequency from (3) and **indicates the transition frequency computed by the authors.

Sample	Particle size μm	ϕ [%]	F	k_0 [m^2]	f_c [Hz]	Source
Capillary	254 (radius)			10^{-8}	10–2.5* Hz	CKS
Capillary	508 (radius)				1.3–0.62* Hz	SG
Capillary G4	720 (radius)				0.31*–0.28** Hz	P
Capillary G2	826 (radius)				0.23*–0.21** Hz	P
Capillary 1	800–1100 (radius)				7.1 Hz	RMLJ
Glass beads	1.25–1.75	32	7.8	4.2×10^{-9}	4.8 Hz	SED
Glass beads	850 (r)	50	2.8	10^{-8}	6.2 Hz	CKS
Glass beads	580–700	31	8.7	9×10^{-10}	20 Hz	SED
Glass beads	450 (r)	50	3.2	2×10^{-9}	25 Hz	CKS
Glass beads	250 (r)	50	3	5×10^{-10}	108 Hz	CKS
Glass beads	200–270	31	9	1.4×10^{-10}	126 Hz	SED
Crushed glass	440 (r)	50	3	10^{-9}	44 Hz	CKS
Crushed glass	265 (r)	50	3.2	2×10^{-10}	45–103 Hz	CKS
Porous filter A	72.5–87				269 Hz	RMLJ
Porous filter B	35–50				710 Hz	RMLJ
Sand grains	1000–2000	31	9	26×10^{-10}	6.7 Hz	SED
Sand grains	150–300	29	10.7	10^{-10}	149 Hz	SED
Ottawa sand	200–250 (r)	31	4.7	1.2×10^{-10}	230–273 Hz	TGR

The transition angular frequency for a porous medium is the same as (8). Charlaix et al. [62] measured the behavior of permeability with frequency on capillary tube, glass beads, and crushed glass. The dynamic permeability is constant up to the transition frequency above which it decreases, and the more permeable the sample is, the lower the transition frequency is. Other measurements have been performed on glass beads and sand grains [61]. The transition frequency ($f_c = \omega_c/2\pi$) varies from 4.8 Hz to 149 Hz for samples having permeability in the range 10^{-8} to 10^{-10} m^2 (see Table 1), which are extremely high permeabilities.

The transition frequency indicates the beginning of the transition for both the permeability and the electrokinetic coupling. However the transition behavior and the cutoff frequency are different between permeability and electrokinetic coupling ((7) and (17)), both depending on the pore-space geometry term m but in different manner.

We calculated the predicted transition frequency $f_c = \omega_c/2\pi$ with ω_c from (11) with $\eta = 10^{-3}$ Pa.s and $\rho_f = 10^3$ kg/ m^3 . The other parameters F and k_0 are measured from different authors cited in Bernabé [78] (see Table 2). We also calculated the parameters for four Fontainebleau sandstone samples. It has been shown for these samples that $F = \phi^{-2.01}$ (from Ruffet et al. [79]) and that $k_0 = a\phi^n$ with different values for n according to the porosity. The following laws were chosen: $k_0 = 1.66 \times 10^{-4}\phi^8$ for $\phi < 6\%$ and $k_0 = 2.5 \times 10^{-10}\phi^3$ for ϕ ranging between 8 and 25% [80]. We can see that the transition frequencies are of the order of kHz and MHz and no more from 0.2 to 150 Hz as measured or calculated on glass beads, sand grains, crushed glass, or capillaries. We plotted the results of the transition frequency

as a function of the permeability on these various samples in Figure 1. Although the formation factor is not constant with the permeability, it is clear that the transition frequency is inversely proportional to the permeability as

$$\log_{10}(f_c) = -0.78\log_{10}(k) - 5.5, \quad (18)$$

and varies from about 100 MHz for 10^{-17} m^2 to about 10 Hz for 10^{-8} m^2 , so by seven orders of magnitude for nine orders of magnitude in permeability.

3. Experimental Apparatus and Procedure

Several experimental setups were proposed to provide the sinusoidal pressure variations.

The first experimental apparatus proposed a sinusoidal motion delivered by a slyphon bellows which was driven by a geophone-type push-pull driver (Figure 2 from Packard [59]). The low-frequency oscillator (0.01 Hz to 1 kHz) was used for operation of the push-pull geophone driver. Similar setups were proposed by Thurston [81] (Figure 3) and Cooke [82], so that frequency of this kind of source was 1–400 Hz [82], 20–200 Hz [59], and 10–700 Hz [81]. The induced pressure was up to 2 kPa. More recently Schoemaker et al. [83] used a so-called Dynamic Darcy Cell (DCC) with a mechanical shaker connected to a rubber membrane leading to a frequency range for the oscillating pressure 5 to 200 Hz. The sinusoidal fluid flow was also applied by a displacement piston pump directly connected to the electrodes chambers (Figure 4 from [63, 88]). The piston was mounted on a Scotch Yoke drive attached to a controllable speed AC motor [84]. The frequency range of this source was then 0.4 Hz to

TABLE 2: Predicted transition frequency (from (11)), for dynamic streaming potential, for samples of porosity ϕ , formation factor F , and permeability k_0 , from (1) calculated in the present study, and measured by (2) Taherian et al. [67], (3) Morgan et al. [68], (4) Fatt [69], (5) Wyble [70], (6) Dobrynin [71], (7) Chierici et al. [72], and (8) Yale [73].

Sample	ϕ [%]	F	k_0 [m^2]	f_c [Hz]
Fontainebleau sandstone ¹	20	25	2×10^{-12}	3.2 kHz
Fontainebleau sandstone ¹	15	45	8×10^{-13}	4.4 kHz
Fontainebleau sandstone ¹	10	102	2.5×10^{-13}	6.2 kHz
Sandstone-S22 ²	31.2	6	2.7×10^{-12}	9.7 kHz
Sandstone-S47 ²	20	14.4	8.5×10^{-13}	13 kHz
Boise ⁸	26	12	9×10^{-13}	14.7 kHz
Berea sandstone500 ⁸	20	20	4.9×10^{-13}	16.2 kHz
Sandstone-S42 ²	19.7	14.7	6.7×10^{-13}	16.2 kHz
Sandstone-S45 ²	21	11.7	7.2×10^{-13}	18.8 kHz
Fahler 162 ⁸	3	294	2.7×10^{-14}	20 kHz
Sandstone-S43 ²	21.2	13	5.1×10^{-13}	23.5 kHz
Pliocene 41 ⁷	21	144.9	4.2×10^{-14}	26.1 kHz
Pliocene 35 ⁷	20	156.2	3.7×10^{-14}	27.5 kHz
Berea sandstoneC2H ³	19.8	15.1	3.8×10^{-13}	27.7 kHz
Sandstone-S50 ²	18.3	17.2	3.1×10^{-13}	30 kHz
Triassic38 ⁷	21	12.6	4×10^{-12}	31.4 kHz
Triassic34 ⁷	20	13.9	3.5×10^{-13}	32.7 kHz
Berea sandstoneB2 ³	20.3	15.2	2.64×10^{-13}	39.7 kHz
Sandstone-S5 ²	26.4	8.7	4.1×10^{-13}	45 kHz
Sandstone-S35 ²	18.75	17.4	2×10^{-13}	46.5 kHz
Massillon DH ⁸	16	23.8	1.3×10^{-13}	51.4 kHz
Cambrian 16 ⁷	14	312.5	9.5×10^{-15}	53.6 kHz
Fontainebleau sandstone ¹	5	412	6.5×10^{-15}	59.4 kHz
Berea sandstoneD1 ³	18.5	18.4	1.3×10^{-13}	66.5 kHz
Tensleep1 ⁴	15	18.9	1.2×10^{-13}	70.3 kHz
Tertiary 807 ⁸	22	14.9	1.5×10^{-13}	71.1 kHz
Cambrian 6 ⁷	8.1	90.9	2.3×10^{-14}	76.1 kHz
Torpedo ⁶	20	41.7	4.5×10^{-14}	84.9 kHz
Miocene 7 ⁷	8.3	384.6	4.4×10^{-15}	94 kHz
Cambrian 14 ⁷	11	52.6	3.2×10^{-14}	94.5 kHz
Sandstone Triassic27 ⁷	18	20	7.2×10^{-14}	110.5 kHz
Sandstone-S9 ²	20.9	12	1×10^{-13}	126.2 kHz
Triassic26 ⁷	18	17.2	6.8×10^{-14}	135.7 kHz
Sandstone-S6 ²	22.8	10.6	8.3×10^{-14}	180.7 kHz
Berea 100H ⁸	17	17.2	4.9×10^{-14}	188.4 kHz
Sandstone S15 ²	21.8	13.9	4.5×10^{-14}	256.7 kHz
Kirkwood ⁵	15	40	1.2×10^{-14}	331.6 kHz
Indiana DV ⁸	27	12	3×10^{-14}	440.3 kHz
Island Rust A1 ³	14.6	52.5	5.2×10^{-15}	579 kHz
Bradford ⁵	11	90	2.5×10^{-15}	700.3 kHz
Austin chalk ³	23.6	22.7	9.7×10^{-15}	763 kHz
Massillon DV ⁸	19	27.8	6.9×10^{-15}	830.4 kHz
Sandstone-S34 ²	21.35	13.7	1.1×10^{-14}	1.06 MHz
Sandstone S44 ²	15.7	24.5	4.2×10^{-15}	1.5 MHz
Indiana L. SA1 ³	18	29.2	1.9×10^{-15}	2.9 MHz
Tennessee A1 ³	5.5	180.3	2.3×10^{-16}	3.8 MHz
AZPink (Coconino) ³	10.3	62.4	6.3×10^{-16}	4.04 MHz
Leuders L.SA1 ³	15.2	41.5	7.1×10^{-16}	5.3 MHz

TABLE 2: Continued.

Sample	ϕ [%]	F	k_0 [m ²]	f_c [Hz]
Sandstone-S40 ²	10.9	130	1.9×10^{-16}	6.4 MHz
Sandstone-S23 ²	18.8	40.7	4.8×10^{-16}	8.1 MHz
Fahler 189 ⁸	1.9	714.3	2×10^{-17}	11.1 MHz
Penn blue A1 ³	3.9	219	6.2×10^{-17}	11.7 MHz
AZChocolate ²³	9.5	159.3	5.8×10^{-17}	17.2 MHz
Fahler 161 ⁸	2.3	416.7	1×10^{-17}	38.2 MHz
Fahler 142 ⁸	7.6	164	2×10^{-17}	48.5 MHz
Sandstone S21 ²	12.1	65	3×10^{-17}	81.7 MHz
Fahler 154 ⁸	4.6	263.1	7×10^{-18}	86.4 MHz
Fahler 192 ⁸	4.4	128.2	9×10^{-18}	137.9 MHz

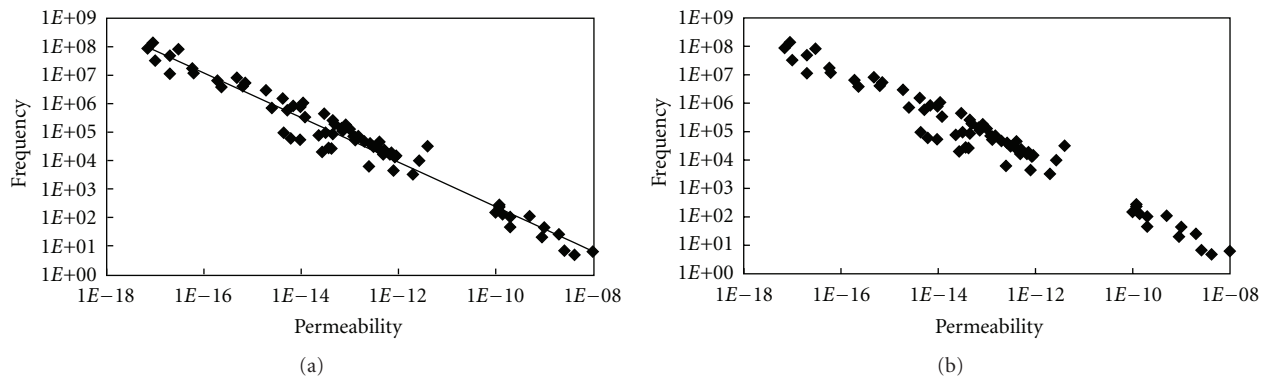


FIGURE 1: The transition frequency $f_c = \omega_c/2\pi$ (in Hz) predicted in the present study with ω_c from (11) with $\eta = 10^{-3}$ Pa.s and $\rho_f = 10^3$ kg/m³ as a function of the permeability (in m²). The transition frequency varies as $\log_{10}(f_c) = -0.78\log_{10}(k) - 5.5$. The parameters of the samples, F and k_0 , are measured from different authors on various samples cited in Tables 1 and 2.

21 Hz and the pressure up to 15 kPa. Pengra et al. [85] used a piston rod attached to a loudspeaker driven by an audio power amplifier (Figure 5). They performed measurements up to 100 Hz, with an applied pressure of 5 kPa RMS. More recently it was proposed by Reppert et al. [60] to use an electromechanical transducer (Figure 6), and these authors covered a frequency range 1–500 Hz. The vibrating exciter proposed by Schoemaker et al. [86] was used from 5 Hz to 200 Hz. Recently Tardif et al. [64] used an electromagnetic shaker operating in the range 1 Hz to 1 kHz and provided measurements up to 200 Hz. Higher frequencies have been investigated [49, 50, 52, 54, 55] for the detection of the interfacial conversions.

The electromagnetic noise radiating from such equipment must be suppressed by shielding the setup and wires (shielded twisted cable pairs) [64, 86]. Moreover it is essential to have a rigid framework. A mechanical resonance can occur in the cell/transducer system (at 70 Hz in [85]), and the noise associated with mechanical vibration can be suppressed putting an additional mass to the frame [64].

Once the oscillatory pressure is applied, the pressure must be measured. Most of the setups include piezoelectric transducers to measure the pressure difference over the capillary or the porous sample. Reppert et al. [60] proposed to use hydrophones that have a flat response from 1 to 20 kHz.

Tardif et al. [64] proposed to use dynamic transducers with a low-frequency limit 0.08 Hz and a maximum frequency of 170 kHz.

The electrodes are usually Ag/AgCl or platinum electrodes. The electrodes used by Schoemaker et al. [86] were sintered plates of Monel (composed of nickel and copper). The electrical signal must be measured using preamplifiers or a high-input impedance acquisition system. Since the impedance of the sample depends on the frequency, one must correct the measurements from this varying-impedance to be able to have a correct streaming potential coefficient [60]. Moreover the electrodes at top and bottom of the sample can behave as a capacitor, requiring a correction using impedance measurements too [86].

The sample is usually saturated and it is emphasized that the sample should be left until equilibrium with water. This equilibrium can be obtained by leaving the sample in contact with water for some time, and by flowing the water within the sample several times by checking the pH and the water conductivity until an equilibrium is reached [39]. The procedure including water flow is better because the properties of the water can be measured. When the properties of the water are measured only before saturating the sample, the resulting water once in contact with the sample is not known. Usually the water is more conductive

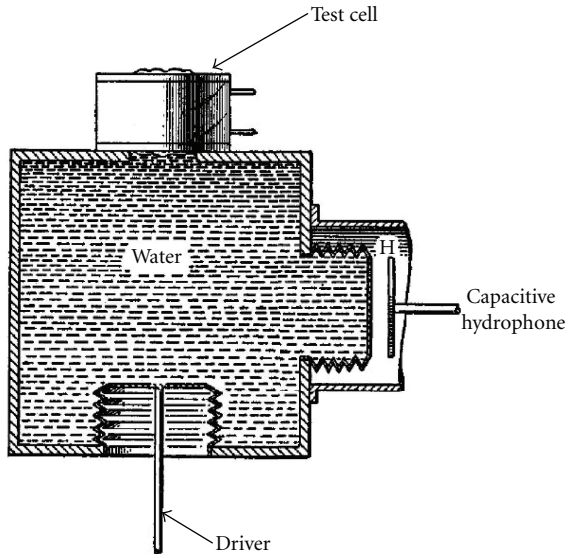


FIGURE 2: The syphon bellows is driven by a geophone-type push-pull driver to apply a sinusoidal motion to the sample (modified from [59]).

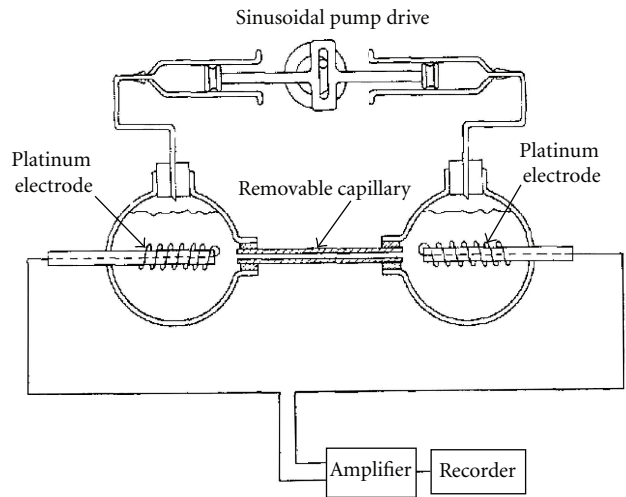


FIGURE 4: Experimental setup used by Groves and Sears (modified from [88]).

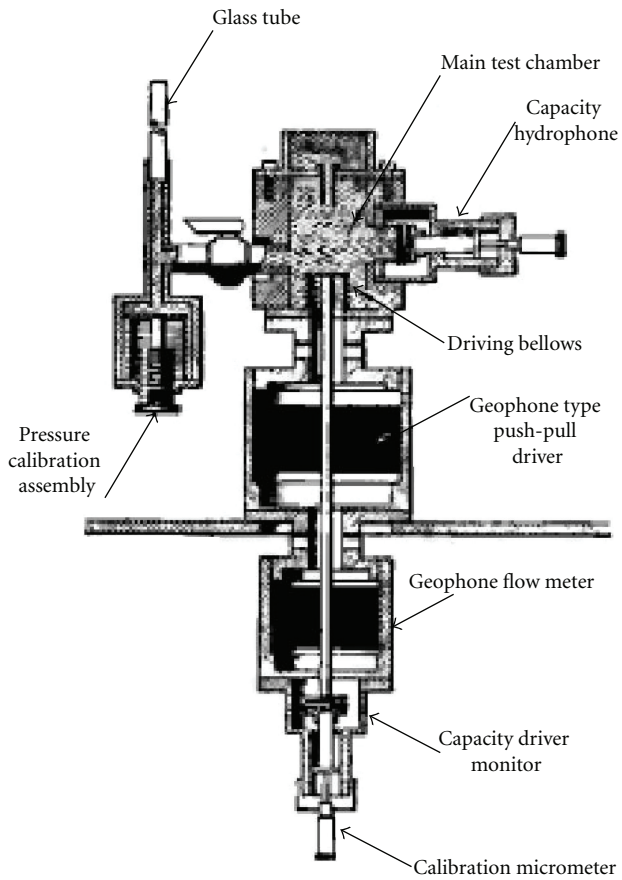


FIGURE 3: Experimental setup used by Thurston [87] (modified from [87]).

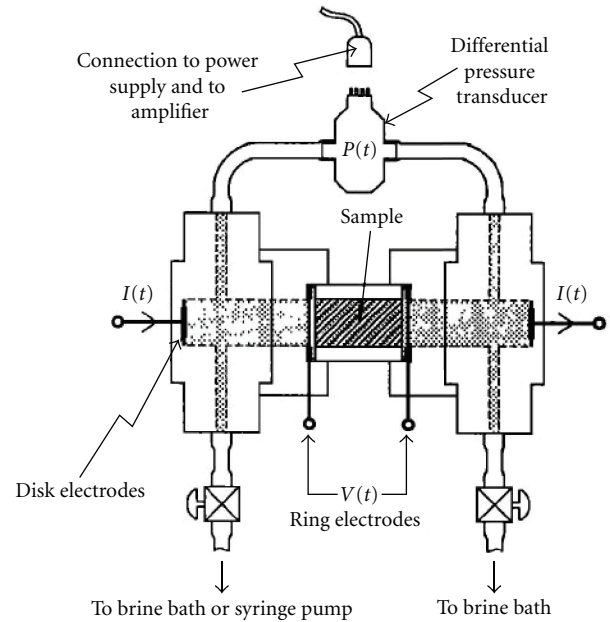


FIGURE 5: Experimental setup used by Pengra et al. [85] for streaming potential and electro-osmosis measurements (modified from [85]).

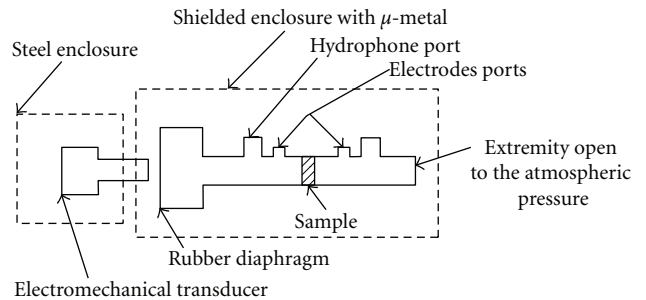


FIGURE 6: Experimental setup used by Reppert et al. [60] (modified from [60]).

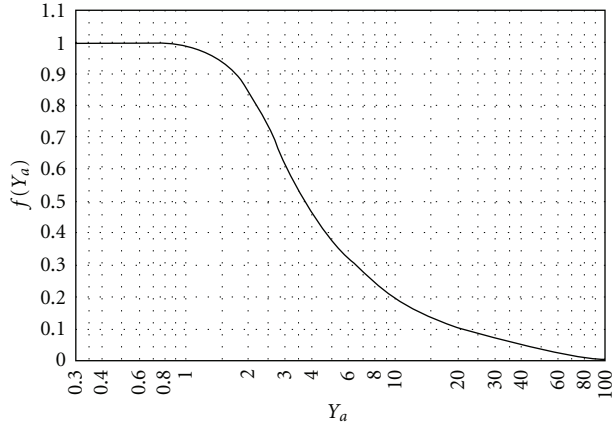


FIGURE 7: The absolute magnitude of the normalized streaming potential coefficient calculated by Packard [59] using (19) where $Y_a = a\sqrt{\omega\rho_f/\eta}$, equivalent to (2) (modified from [59]).

when in contact with the sample, and the pH can change. Recalling that the streaming potential is proportional to the zeta potential (which depends on pH) and inversely proportional to the water conductivity (1), it is essential to know properly the pH and the water conductivity.

4. Measurements and Calculations of the Dynamic Electrokinetic Coefficient

The absolute magnitude of the streaming potential coefficient normalized by the steady-state value was calculated by Packard [59] as

$$f(Y_a) = \left(\frac{-2 i\sqrt{i}J_1(\sqrt{i}Y_a)}{Y_a J_0(\sqrt{i}Y_a)} e^{-i\omega t} \right), \quad (19)$$

which is equal to (2), but expressed as a function of the parameter $Y_a = a\sqrt{(\omega\rho_f)/\eta}$, the transition frequency being obtained for $Y_a = 1$ (Figure 7). The streaming potential coefficient is constant up to the transition angular frequency and then decreases with increasing frequency.

Sears and Groves [63] measured the streaming potential coefficient on a capillary of radius $508 \mu\text{m}$ which was coated with clay-Adams Siliclad and then incubated with 1% bovine serum albumin and filled with 0.02 M Tris-HCl at pH 7.32. They reported the streaming potential and the pressure difference as a function of frequency in the range 0–20 Hz. We calculated the resulting streaming potential coefficient (see Figure 8) which decreases from about 1.3×10^{-7} to 4×10^{-8} V/Pa. These authors computed the zeta potential and concluded that the zeta potential is independent of the frequency with an average value of 28.8 mV. Moreover they concluded that the zeta potential is also independent of the capillary radius and capillary length.

The value of the streaming potential coefficient on Ottawa sand measured at 5 Hz by Tardif et al. [64] was -5.2×10^{-7} V/Pa using a 0.001 mol/L NaCl solution to saturate the sample. Values between 1 and 2×10^{-8} V/Pa were

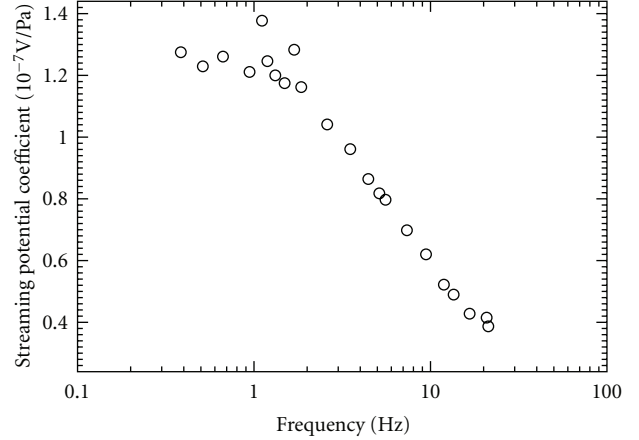


FIGURE 8: The streaming potential coefficient measured as a function of frequency by Sears and Groves [63] on a capillary coated with clay, incubated with BSA in 0.02 M Tris-HCl.

measured on samples saturated by 0.1 M/L NaCl brine [85]. A compilation of numerous streaming potential coefficients measured on sands and sandstones at various salinities in DC domain [44] showed that $C_{s0} = -1.2 \times 10^{-8} \sigma_f^{-1}$, where C_{s0} is in V/Pa and σ_f in S/m. A zeta potential of -17 mV can be inferred from these collected data, assuming the other parameters (see (1)) independent of water conductivity. These assumptions are not exact, but the value of zeta is needed for numerous modellings which usually assume the other parameters independent of the fluid conductivity. Therefore an average value of -17 mV for such modellings can be rather exact, at least for medium with no clay nor calcite.

Reppert et al. [60] calculated the real part and the imaginary part of the theoretical Packard's streaming potential coefficient (2) for different capillary radii (see Figure 9). It can be seen that the larger the radius is, the lower the transition frequency is, as shown previously by the different theories. Recent developments by the group of Glover have been performed to build a new setup and to make further measurements on porous samples: two papers detail these studies in this special issue on Electrokinetics in Earth Sciences.

5. Conclusion

Since the theory of Pride in 1994 [22], the dynamic behavior of the streaming potential is known for porous media. However few experimental results are available, because of the difficulty to perform correct measurements at high frequency. Up to now, measurements of the frequency-dependence of the streaming potential have been performed up to 200 Hz on high-permeable samples. The main difficulty arises from electrical noise induced by mechanical vibration. Moreover it has been emphasized that the measurements must be corrected by impedance measurements as a function of frequency too because the impedance of the sample depends on frequency. Further theoretical

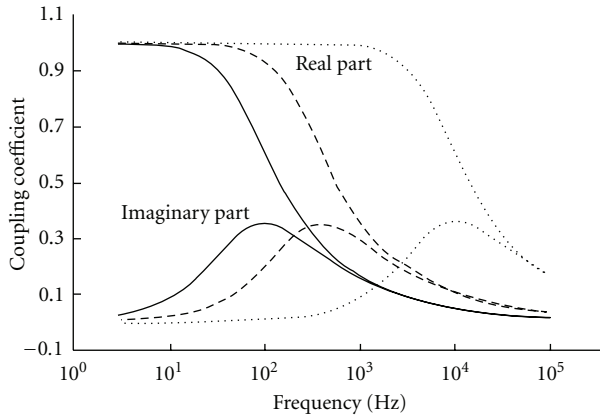


FIGURE 9: The real and imaginary part of Packard's model (2) calculated by Reppert et al. [60] for three capillary radii: $100\ \mu\text{m}$ (continuous line), $50\ \mu\text{m}$ (dashed line), and $10\ \mu\text{m}$ (point line) (modified from [60]).

developments performed by Garambois and Dietrich [12] studied the low-frequency assumption valid at frequencies lower than the transition frequency. We show that this transition frequency, on a various collection of samples for which both formation factor and permeability are measured, is predicted to depend on the permeability as inversely proportional to the permeability.

Acknowledgments

This work was supported by the French National Scientific Center (CNRS), by the National Agency for Research (ANR) through TRANSEK, and by REALISE the "Alsace Region Research Network in Environmental Sciences in Engineering" and the Alsace Region. The authors thank two anonymous reviewers and the associate editor T. Ishido for very constructive remarks that improved this paper.

References

- [1] Y. Honkura, Y. Ogawa, M. Matsushima, S. Nagaoka, N. Ujihara, and T. Yamawaki, "A model for observed circular polarized electric fields coincident with the passage of large seismic waves," *Journal of Geophysical Research B*, vol. 114, no. 10, Article ID B10103, 2009.
- [2] M. Matsushima, Y. Honkura, N. Oshiman et al., "Seismoelectromagnetic effect associated with the İzmit earthquake and its aftershocks," *Bulletin of the Seismological Society of America*, vol. 92, no. 1, pp. 350–360, 2002.
- [3] N. Takeuchi, N. Chubachi, S. Hotta, and K. Narita, "Analysis of earth potential difference signals by using seismic wave signals," *Electrical Engineering in Japan*, vol. 125, no. 4, pp. 52–58, 1998.
- [4] M. A. Fenoglio, M. J. S. Johnston, and J. D. Byerlee, "Magnetic and electric fields associated with changes in high pore pressure in fault zones: application to the Loma Prieta ULF emissions," *Journal of Geophysical Research*, vol. 100, no. 7, pp. 12951–12958, 1995.
- [5] J. C. Dupuis, K. E. Butler, A. W. Kepic, and B. D. Harris, "Anatomy of a seismoelectric conversion: Measurements and conceptual modeling in boreholes penetrating a sandy aquifer," *Journal of Geophysical Research B*, vol. 114, no. 10, Article ID B10306, 2009.
- [6] A. Thompson, S. Hornbostel, J. Burns et al., "Field tests of electroseismic hydrocarbon detection," SEG Technical Program Expanded Abstracts, 2005.
- [7] J. C. Dupuis and K. E. Butler, "Vertical seismoelectric profiling in a borehole penetrating glaciofluvial sediments," *Geophysical Research Letters*, vol. 33, no. 16, Article ID L16301, 2006.
- [8] J. C. Dupuis, K. E. Butler, and A. W. Kepic, "Seismoelectric imaging of the vadose zone of a sand aquifer," *Geophysics*, vol. 72, no. 6, pp. A81–A85, 2007.
- [9] M. H. P. Strahser, W. Rabbal, and F. Schildknecht, "Polarisation and slowness of seismoelectric signals: a case study," *Near Surface Geophysics*, vol. 5, no. 2, pp. 97–114, 2007.
- [10] S. S. Haines, A. Guittou, and B. Biondi, "Seismoelectric data processing for surface surveys of shallow targets," *Geophysics*, vol. 72, no. 2, pp. G1–G8, 2007.
- [11] M. Strahser, L. Jouniaux, P. Sailhac, P.-D. Matthey, and M. Zillmer, "Dependence of seismoelectric amplitudes on water content," *Geophysical Journal International*, vol. 187, no. 3, pp. 1378–1392, 2011.
- [12] S. Garambois and M. Dietrich, "Seismoelectric wave conversions in porous media: field measurements and transfer function analysis," *Geophysics*, vol. 66, no. 5, pp. 1417–1430, 2001.
- [13] S. S. Haines, S. R. Pride, S. L. Klemperer, and B. Biondi, "Seismoelectric imaging of shallow targets," *Geophysics*, vol. 72, no. 2, pp. G9–G20, 2007.
- [14] A. H. Thompson, J. R. Sumner, and S. C. Hornbostel, "Electromagnetic-to-seismic conversion: a new direct hydrocarbon indicator," *The leading Edge*, vol. 26, no. 4, pp. 428–435, 2007.
- [15] J. Singer, J. Saunders, L. Holloway et al., "Electrokinetic logging has the potential to measure the permeability," in *the 46th Annual Logging Symposium of the Society of Petrophysicists and Well Log Analysts*, 2005.
- [16] C. C. Pain, J. H. Saunders, M. H. Worthington et al., "A mixed finite-element method for solving the poroelastic Biot equations with electrokinetic coupling," *Geophysical Journal International*, vol. 160, no. 2, pp. 592–608, 2005.
- [17] O. V. Mikhailov, J. Queen, and M. N. Toksöz, "Using borehole electroseismic measurements to detect and characterize fractured (permeable) zones," *Geophysics*, vol. 65, no. 4, pp. 1098–1112, 2000.
- [18] L. Jouniaux, "Electrokinetic techniques for the determination of hydraulic conductivity," in *Hydraulic Conductivity—Issues, Determination and Applications*, L. Elango, Ed., InTech, 2011.
- [19] M. D. Schakel, D. M. J. Smeulders, E. C. Slob, and H. K. J. Heller, "Seismoelectric interface response: experimental results and forward model," *Geophysics*, vol. 76, no. 4, pp. N29–N36, 2011.
- [20] M. Schakel and D. Smeulders, "Seismoelectric reflection and transmission at a fluid/porous-medium interface," *Journal of the Acoustical Society of America*, vol. 127, no. 1, pp. 13–21, 2010.
- [21] S. Garambois and M. Dietrich, "Full waveform numerical simulations of seismoelectromagnetic wave conversions in fluid-saturated stratified porous media," *Journal of Geophysical Research B*, vol. 107, no. 7, article 2148, 2002.
- [22] S. Pride, "Governing equations for the coupled electromagnetics and acoustics of porous media," *Physical Review B*, vol. 50, no. 21, pp. 15678–15696, 1994.

- [23] M. A. Biot, "Theory of propagation of elastic waves in a fluid-saturated porous solid: I. Low frequency range," *Journal of the Acoustical Society of America*, vol. 28, no. 2, pp. 168–178, 1956.
- [24] M. W. Haartsen and S. R. Pride, "Electroseismic waves from point sources in layered media," *Journal of Geophysical Research B*, vol. 102, no. 11, pp. 24745–24769, 1997.
- [25] M. W. Haartsen, W. Dong, and M. N. Toksöz, "Dynamic streaming currents from seismic point sources in homogeneous poroelastic media," *Geophysical Journal International*, vol. 132, no. 2, pp. 256–274, 1998.
- [26] Y. Gao and H. Hu, "Seismoelectromagnetic waves radiated by a double couple source in a saturated porous medium," *Geophysical Journal International*, vol. 181, no. 2, pp. 873–896, 2010.
- [27] J. H. Saunders, M. D. Jackson, and C. C. Pain, "A new numerical model of electrokinetic potential response during hydrocarbon recovery," *Geophysical Research Letters*, vol. 33, no. 15, Article ID L15316, 2006.
- [28] L. Jouniaux and T. Ishido, "Electrokinetics in Earth Sciences: a tutorial," *International Journal of Geophysics*, vol. 2012, Article ID 286107, 16 pages, 2012.
- [29] J. A. Davis, R. O. James, and J. O. Leckie, "Surface ionization and complexation at the oxide/water interface. I. Computation of electrical double layer properties in simple electrolytes," *Journal of Colloid And Interface Science*, vol. 63, no. 3, pp. 480–499, 1978.
- [30] X. Guichet, L. Jouniaux, and N. Catel, "Modification of streaming potential by precipitation of calcite in a sand-water system: laboratory measurements in the pH range from 4 to 12," *Geophysical Journal International*, vol. 166, no. 1, pp. 445–460, 2006.
- [31] T. Ishido and J. Muzutani, "Experimental and theoretical basis of electrokinetic phenomena in rock-water systems and its applications to geophysics," *Journal of Geophysical Research*, vol. 86, no. 3, pp. 1763–1775, 1981.
- [32] J. P. Pozzi and L. Jouniaux, "Electrical effects of fluid circulation in sediments and seismic prediction," *Comptes Rendus—Academie des Sciences, Serie II*, vol. 318, no. 1, pp. 73–77, 1994.
- [33] L. Jouniaux and J. P. Pozzi, "Permeability dependence of streaming potential in rocks for various fluid conductivities," *Geophysical Research Letters*, vol. 22, no. 4, pp. 485–488, 1995.
- [34] L. Jouniaux and J. P. Pozzi, "Streaming potential and permeability of saturated sandstones under triaxial stress: consequences for electrotelluric anomalies prior to earthquakes," *Journal of Geophysical Research*, vol. 100, no. 6, pp. 10197–10209, 1995.
- [35] L. Jouniaux and J. P. Pozzi, "Laboratory measurements anomalous 0.1–0.5 Hz streaming potential under geochemical changes: implications for electrotelluric precursors to earthquakes," *Journal of Geophysical Research B*, vol. 102, no. 7, pp. 15335–15343, 1997.
- [36] L. Jouniaux, S. Lallemand, and J. P. Pozzi, "Changes in the permeability, streaming potential and resistivity of a claystone from the Nankai prism under stress," *Geophysical Research Letters*, vol. 21, no. 2, pp. 149–152, 1994.
- [37] L. Jouniaux, J. P. Pozzi, J. Berthier, and P. Massé, "Detection of fluid flow variations at the Nankai Trough by electric and magnetic measurements in boreholes or at the seafloor," *Journal of Geophysical Research B*, vol. 104, no. 12, pp. 29293–29309, 1999.
- [38] L. Jouniaux, M. L. Bernard, M. Zamora, and J. P. Pozzi, "Streaming potential in volcanic rocks from Mount Pelée," *Journal of Geophysical Research B*, vol. 105, no. 4, pp. 8391–8401, 2000.
- [39] X. Guichet, L. Jouniaux, and J. P. Pozzi, "Streaming potential of a sand column in partial saturation conditions," *Journal of Geophysical Research B*, vol. 108, no. 3, article 2141, 2003.
- [40] M. Z. Jaafar, J. Vinogradov, and M. D. Jackson, "Measurement of streaming potential coupling coefficient in sandstones saturated with high salinity NaCl brine," *Geophysical Research Letters*, vol. 36, no. 21, Article ID L21306, 2009.
- [41] L. Jouniaux, A. Maineult, V. Naudet, M. Pessel, and P. Sailhac, "Review of self-potential methods in hydrogeophysics," *Comptes Rendus—Geoscience*, vol. 341, no. 10–11, pp. 928–936, 2009.
- [42] J. Vinogradov, M. Z. Jaafar, and M. D. Jackson, "Measurement of streaming potential coupling coefficient in sandstones saturated with natural and artificial brines at high salinity," *Journal of Geophysical Research B*, vol. 115, no. 12, Article ID B12204, 2010.
- [43] M. D. Jackson, "Multiphase electrokinetic coupling: insights into the impact of fluid and charge distribution at the pore scale from a bundle of capillary tubes model," *Journal of Geophysical Research*, vol. 115, Article ID B07206, 2010.
- [44] V. Allègre, L. Jouniaux, F. Lehmann, and P. Sailhac, "Streaming potential dependence on water-content in Fontainebleau sand," *Geophysical Journal International*, vol. 182, no. 3, pp. 1248–1266, 2010.
- [45] N. Migunov and A. Kokorev, "Dynamic properties of the seismoelectric effect of water-saturated rocks," *Izvestiya, Earth Physics*, vol. 13, no. 6, pp. 443–445, 1977.
- [46] R. Chandler, "Transient streaming potential measurements on fluid-saturated porous structures: an experimental verification of Biot's slow wave in the quasi-static limit," *Journal of the Acoustical Society of America*, vol. 70, no. 1, pp. 116–121, 1981.
- [47] S. A. Mironov, E. I. Parkhomenko, and G. Y. Chernyak, "Seismoelectric effect in rocks containing gas or fluid hydrocarbon (english translation)," *Izvestiya, Physics of the Solid Earth*, vol. 29, no. 11, pp. 1000–1006, 1994.
- [48] Y. G. Jiang, F. K. Shan, H. M. Jin, and L. W. Zhou, "A method for measuring electrokinetic coefficients of porous media and its potential application in hydrocarbon exploration," *Geophysical Research Letters*, vol. 25, no. 10, pp. 1581–1584, 1998.
- [49] Z. Zhu, M. W. Haartsen, and M. N. Toksöz, "Experimental studies of electrokinetic conversions in fluid-saturated borehole models," *Geophysics*, vol. 64, no. 5, pp. 1349–1356, 1999.
- [50] Z. Zhu, M. W. Haartsen, and M. N. Toksöz, "Experimental studies of seismoelectric conversions in fluid-saturated porous media," *Journal of Geophysical Research B*, vol. 105, no. 12, pp. 28055–28064, 2000.
- [51] Z. Zhu and M. N. Toksoöz, "Crosshole seismoelectric measurements in borehole models with fractures," *Geophysics*, vol. 68, no. 5, pp. 1519–1524, 2003.
- [52] B. Chen and Y. Mu, "Experimental studies of seismoelectric effects in fluid-saturated porous media," *Journal of Geophysics and Engineering*, vol. 2, no. 3, pp. 222–230, 2005.
- [53] C. Bordes, L. Jouniaux, M. Dietrich, J. P. Pozzi, and S. Garambois, "First laboratory measurements of seismo-magnetic conversions in fluid-filled Fontainebleau sand," *Geophysical Research Letters*, vol. 33, no. 1, Article ID L01302, 2006.
- [54] G. I. Block and J. G. Harris, "Conductivity dependence of seismoelectric wave phenomena in fluid-saturated sediments," *Journal of Geophysical Research B*, vol. 111, no. 1, Article ID B01304, 2006.
- [55] Z. Zhu, M. N. Toksöz, and D. R. Burns, "Electroseismic and seismoelectric measurements of rock samples in a water tank," *Geophysics*, vol. 73, no. 5, pp. E153–E164, 2008.

- [56] C. Bordes, L. Jouniaux, S. Garambois, M. Dietrich, J. P. Pozzi, and S. Gaffet, "Evidence of the theoretically predicted seismomagnetic conversion," *Geophysical Journal International*, vol. 174, no. 2, pp. 489–504, 2008.
- [57] V. Allègre, L. Jouniaux, F. Lehmann, and P. Sailhac, "Reply to comment by A. Revil and N. Linde on 'Streaming potential dependence on water-content in Fontainebleau sand'" *Geophysical Journal International*, vol. 186, no. 1, pp. 115–117, 2011.
- [58] B. Lorne, F. Perrier, and J. P. Avouac, "Streaming potential measurements: 1. Properties of the electrical double layer from crushed rock samples," *Journal of Geophysical Research B*, vol. 104, no. 8, pp. 17857–17877, 1999.
- [59] R. G. Packard, "Streaming potentials across glass capillaries for sinusoidal pressure," *The Journal of Chemical Physics*, vol. 21, no. 2, pp. 303–307, 1953.
- [60] P. M. Reppert, F. D. Morgan, D. P. Lesmes, and L. Jouniaux, "Frequency-dependent streaming potentials," *Journal of Colloid and Interface Science*, vol. 234, no. 1, pp. 194–203, 2001.
- [61] D. M. J. Smeulders, R. L. G. M. Eggels, and M. E. H. Van Dongen, "Dynamic permeability: reformulation of theory and new experimental and numerical data," *Journal of Fluid Mechanics*, vol. 245, pp. 211–227, 1992.
- [62] E. Charlaix, A. P. Kushnick, and J. P. Stokes, "Experimental study of dynamic permeability in porous media," *Physical Review Letters*, vol. 61, no. 14, pp. 1595–1598, 1988.
- [63] A. R. Sears and J. N. Groves, "The use of oscillating laminar flow streaming potential measurements to determine the zeta potential of a capillary surface," *Journal of Colloid And Interface Science*, vol. 65, no. 3, pp. 479–482, 1978.
- [64] E. Tardif, P. W. J. Glover, and J. Ruel, "Frequency-dependent streaming potential of Ottawa sand," *Journal of Geophysical Research B*, vol. 116, no. 4, Article ID B04206, 2011.
- [65] D. L. Johnson, J. Koplik, and R. Dashen, "Theory of dynamic permeability in fluid saturated porous media," *Journal of Fluid Mechanics*, vol. 176, pp. 379–402, 1987.
- [66] M. S. Paterson, "The equivalent channel model for permeability and resistivity in fluid-saturated rock-A re-appraisal," *Mechanics of Materials*, vol. 2, no. 4, pp. 345–352, 1983.
- [67] M. R. Taherian, W. E. Kenyon, and K. A. Safinya, "Measurement of dielectric response of water-saturated rocks," *Geophysics*, vol. 55, no. 12, pp. 1530–1541, 1990.
- [68] D. Morgan, D. Lesmes, F. Samstag et al., *Laboratory reports for geophysics 612: Rock physics*, Texas A&M University, 1990.
- [69] I. Fatt, "Effect of overburden and reservoir pressure on electric logging formation factor," *Bulletin of American Association of Petroleum Geologists*, vol. 41, pp. 2456–2466, 1957.
- [70] D. Wyble, "Effect of applied pressure on the conductivity, porosity and permeability of sandstones," *Transactions of the AIME*, vol. 213, pp. 430–432, 1958.
- [71] V. Dobrynin, "Effect of overburden pressure on some properties of sandstones," *Society of Petroleum Engineers Journal*, no. 2, pp. 360–366, 1962.
- [72] G. Chierici, G. Ciucci, F. Eva, and G. Long, "Effect of the overburden pressure on some petrophysical parameters of reservoir rocks," in *Proceeding of the 7th World Petroleum Congress*, vol. 2, pp. 309–338, 1967.
- [73] D. Yale, *Network modelling of flow, storage and deformation in porous rocks*, Ph.D. thesis, Stanford University, 1984.
- [74] E. Walker and P. W. J. Glover, "Permeability models of porous media: Characteristic length scales, scaling constants and time-dependent electrokinetic coupling," *Geophysics*, vol. 75, no. 6, pp. E235–E246, 2010.
- [75] J. L. Auriault, L. Borne, and R. Chambon, "Dynamics of porous saturated media, checking of the generalized law of Darcy," *Journal of the Acoustical Society of America*, vol. 77, no. 5, pp. 1641–1650, 1985.
- [76] P. Sheng and M. Y. Zhou, "Dynamic permeability in porous media," *Physical Review Letters*, vol. 61, no. 14, pp. 1591–1594, 1988.
- [77] P. Sheng, M. Zhou, E. Charlaix, A. Kushnick, and J. Stokes, "Scaling function for dynamic permeability in porous media, reply," *Physical Review Letters*, vol. 63, p. 581, 1988.
- [78] Y. Bernabé, "Pore geometry and pressure dependence of the transport properties in sandstones," *Geophysics*, vol. 56, no. 4, pp. 436–446, 1991.
- [79] C. Ruffet, Y. Guéguen, and M. Darot, "Complex conductivity measurements and fractal nature of porosity," *Geophysics*, vol. 56, no. 6, pp. 758–768, 1991.
- [80] T. Bourbié, O. Coussy, and B. Zinszner, *Acoustic of Porous Media*, Institut Francais du petrole Publications, Editions Technip, 1987.
- [81] G. Thurston, "Periodic fluid flow through circular tubes," *Journal of the Acoustical Society of America*, vol. 24, no. 6, pp. 653–656, 1952.
- [82] C. E. Cooke, "Study of electrokinetic effects using sinusoidal pressure and voltage," *The Journal of Chemical Physics*, vol. 23, no. 12, pp. 2299–2303, 1955.
- [83] F. C. Schoemaker, D. M. J. Smeulders, and E. C. Slob, "Simultaneous determination of dynamic permeability and streaming potential," *SEG Technical Program Expanded Abstracts*, vol. 26, no. 1, pp. 1555–1559, 2007.
- [84] C. M. Cerda and K. Non-Chhom, "The use of sinusoidal streaming flow measurements to determine the electrokinetic properties of porous media," *Colloids and Surfaces*, vol. 35, no. 1, pp. 7–15, 1989.
- [85] D. B. Pengra, S. X. Li, and P. Z. Wong, "Determination of rock properties by low-frequency AC electrokinetics," *Journal of Geophysical Research B*, vol. 104, no. 12, pp. 29485–29508, 1999.
- [86] F. C. Schoemaker, D. M. J. Smeulders, and E. C. Slob, "Electrokinetic effect: theory and measurement," *SEG Technical Program Expanded Abstracts*, vol. 27, no. 1, pp. 1645–1649, 2008.
- [87] G. Thurston, "Apparatus for absolute measurement of analogous impedance of acoustic elements," *Journal of the Acoustical Society of America*, vol. 24, no. 6, pp. 649–656, 1952.
- [88] J. N. Groves and A. R. Sears, "Alternating streaming current measurements," *Journal of Colloid And Interface Science*, vol. 53, no. 1, pp. 83–89, 1975.

Research Article

Implications of Self-Potential Distribution for Groundwater Flow System in a Nonvolcanic Mountain Slope

Tada-nori Goto,¹ Kazuya Kondo,² Rina Ito,² Keisuke Esaki,² Yasuo Oouchi,² Yutaka Abe,³ and Maki Tsujimura³

¹Graduate School of Engineering, Kyoto University, C1-1-113, Kyodai-Katsura, Nishikyo, Kyoto 615-8540, Japan

²Department of Environmental Earth Sciences, Aichi University of Education, 1 Hirosawa, Igaya-cho, Kariya, Aichi 448-8542, Japan

³Graduate School of Life and Environmental Sciences, University of Tsukuba, 1-1-1 Tennodai, Tsukuba 305-8572, Japan

Correspondence should be addressed to Tada-nori Goto, goto.tadanori.8a@kyoto-u.ac.jp

Received 10 August 2011; Revised 25 December 2011; Accepted 18 January 2012

Academic Editor: Tsuneo Ishido

Copyright © 2012 Tada-nori Goto et al. This is an open access article distributed under the Creative Commons Attribution License, which permits unrestricted use, distribution, and reproduction in any medium, provided the original work is properly cited.

Self-potential (SP) measurements were conducted at Mt. Tsukuba, Japan, which is a nonvolcanic mountain, to infer groundwater flow system in the mountain. Survey routes were set around the northern slope, and the reliability of observed SP anomaly was checked by using SP values along parallel survey routes; the error was almost within 10 mV. The FFT analysis of the spatial SP distribution allows us a separation of raw data into two components with shorter and longer wavelength. In the shorter (altitudinal) wavelength than ~200 meters, several positive SP peaks of more than 100 mV in magnitude are present, which indicate shallow perched water discharges along the slope. In the regional SP pattern of longer wavelength, there are two major perturbations from the general trend reflecting the topographic effect. By comparing the SP and hydrological data, the perturbation around the foothill is interpreted to be caused by heterogeneous infiltration at the ground surface. The perturbation around the summit is also interpreted to be caused by heterogeneous infiltration process, based on a simplified numerical modeling of SP. As a result, the SP pattern is well explained by groundwater flow and infiltration processes. Thus, SP data is thought to be very useful for understanding of groundwater flow system on a mountain scale.

1. Introduction

Spatial distribution of self-potential or spontaneous potential (SP), which is time-invariant natural electrical potential, has been observed at the ground surface along a topographic slope. In general, a negative correlation between altitude and SP value along a slope is reported (e.g., [1–3]), which is called as terrain effect or topographic effect on SP. For example, Sasai et al. [3] have found relatively high SP values at the foothills of the Miyake-jima volcano, decreasing toward the middle altitude of the mountain. The SP profile is well correlated with the topographic profile, and the mean coefficient of topographic effect was -1.07 mV/m in the case of the Miyake-jima volcano.

Topographic effect on SP is thought to be caused by subsurface fluid flow along the slope through electrokinetic

coupling (e.g., [4]). In rock-water systems, the flow of groundwater can drag excess electrical charges located in the close vicinity of the pore water/mineral interface in the electrical double layer with it, resulting in macroscopic electric current called as streaming current or drag current and the development of electric potential called as streaming potential in the direction of fluid flow (e.g., [5, 6]). Because the zeta potential, characteristic potential difference across the electrical double layer, is commonly negative for typical crustal rocks in water of pH higher than ~2 [6], the pore fluid flow carries positive charges with it; so a negative correlation between the hydraulic head and the streaming potential is expected. Yasukawa and Mogi [7] conducted numerical calculations of groundwater flow and associated streaming potential and confirmed a negative correlation between the altitude and SP value, which has observable amplitude on

the slope surface. Although SP can be generated by other effects such as thermoelectric coupling [8], electrochemical effects (diffusion potential, redox potential, etc.; e.g., [8, 9]), SP along a mountain slopes is thought to be mainly caused by the electrokinetic effects.

On the basis of the topographic effect, a number of attempts to estimate hydrological features along mountain slopes have been made. For example, Fournier [10] assumed that main SP sources were aligned on water table and tried to estimate the water table elevation using SP data taken at the ground surface. Revil et al. [11] developed a sophisticated method for water table estimation; they inferred the water table elevations below a slope using an inverse technique with the observed SP data. Linde et al. [12] modeled both SP sources in the vadose zone and along the water table and tried to estimate the water table below a slope more precisely. The SP measurement is nonintrusive, quick, and inexpensive; therefore, these benefits tend to accelerate the applications of the SP method to groundwater studies, engineering, and environmental investigations.

There is still some debate, however, about the origin of topographic effect on SP along mountain slopes. Previous studies adopt very simple assumptions of hydrological process. Fournier [10] and Revil et al. [11] excluded the contribution of streaming current associated with downward flow of vadose-zone water, which was taken as the primary source for SP generation by Aubert and Atangana [13]. Although Linde et al. [12] considered both SP sources in the vadose and underlying water-saturated zones, they assumed a homogeneous vadose zone and uniform infiltration at the ground surface. However, numerical studies (e.g., [14]) suggest that complicated downward liquid flow in the vadose zone will make complicated SP pattern on the ground surface.

For small-scale slopes, less than 100 m in length, Ernstson and Scherer [15] suggest various causes of SP anomalies along the slopes: biological root activity, lateral water movements in alternating permeable and impermeable layers, discharge of perched-water aquifers, and infiltration and evapotranspiration together with groundwater recharge. However, the origins of SP along a larger-scale slope (e.g., a few km in length) have not been discussed enough. Detailed interpretation of topographic effect on mountain-scale SP pattern is useful to apply the SP method to estimate subsurface fluid motions, especially in volcanoes. As many former studies said [3, 16–19], SP anomalies of positive polarity are frequently found around volcano summits and near fumaroles. In order to discuss such SP anomalies, knowledge of SP distribution caused by topographic effect is necessary as a basis.

In order to discuss possible causes of SP along a mountain slope, comparison between the SP pattern and hydrological data along the slope is required, but few field studies were reported. In this study, we investigate self-potential distribution around the northern slope of Mt. Tsukuba, located in Japan, where extensive hydrological studies have been carried out. Mt. Tsukuba mainly consists of granitic basement, so that the SP distribution along Mt. Tsukuba will be a typical example of topographic

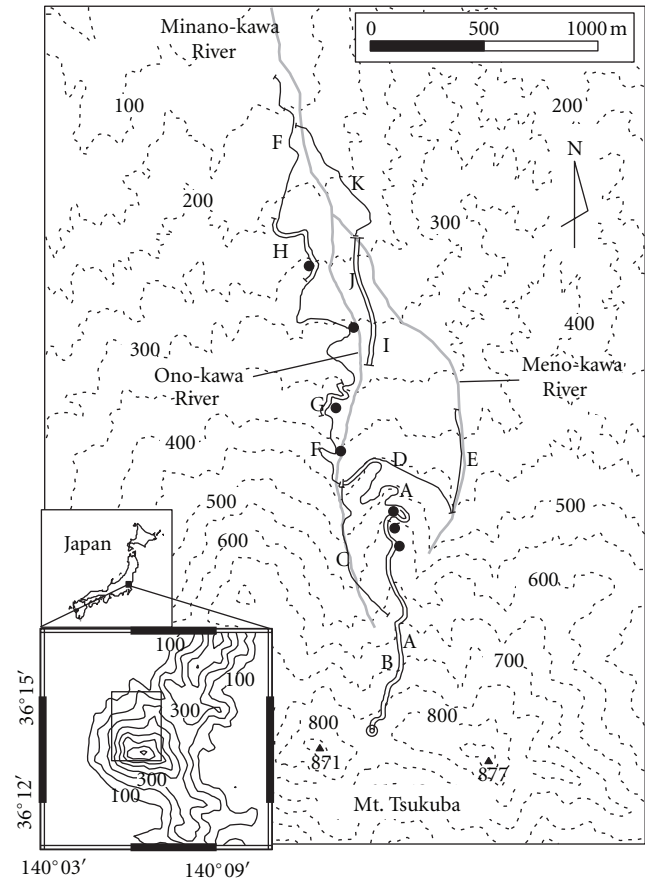


FIGURE 1: Location of Mt. Tsukuba and SP survey routes. Thick solid lines: the SP survey routes. A double circle: reference point for SP measurement. Solid circles: locations of DC resistivity survey. Thin solid lines: equi-topographic contour. Gray lines: rivers.

effect on a plutonic mountain. We compare the SP data with hydrological results to discuss main causes of the SP anomalies.

2. Self-Potential Measurement

Mt. Tsukuba is located near Tsukuba, central Japan (Figure 1). The maximum altitude is 877 m. The slope gradient is about 20 and 10 degrees at altitude around 500 and 300 meters, respectively. The basement of Mt. Tsukuba mainly consists of granitic rocks, and partly gabbroic rocks and debris [20]. There are many hydrological studies: for example, isotope analysis of river water [21], discharge analysis of river water [22], isotope analysis of spring water, and estimation of water table elevation [23].

SP survey was carried out along eleven routes (A to K) from August 20 to 22 in 2000 (Figure 1). The survey area covers the northern slope of Mt. Tsukuba with altitude range between 130 m and 780 m. The “leapfrog” method was used for SP observation with electrode spacing of 12–120 m (mainly 50 m). We used two types of paired electrodes and voltmeters as shown in Figure 2. Cu-CuSO₄ electrodes named AUE-type are suitable for the flat soil

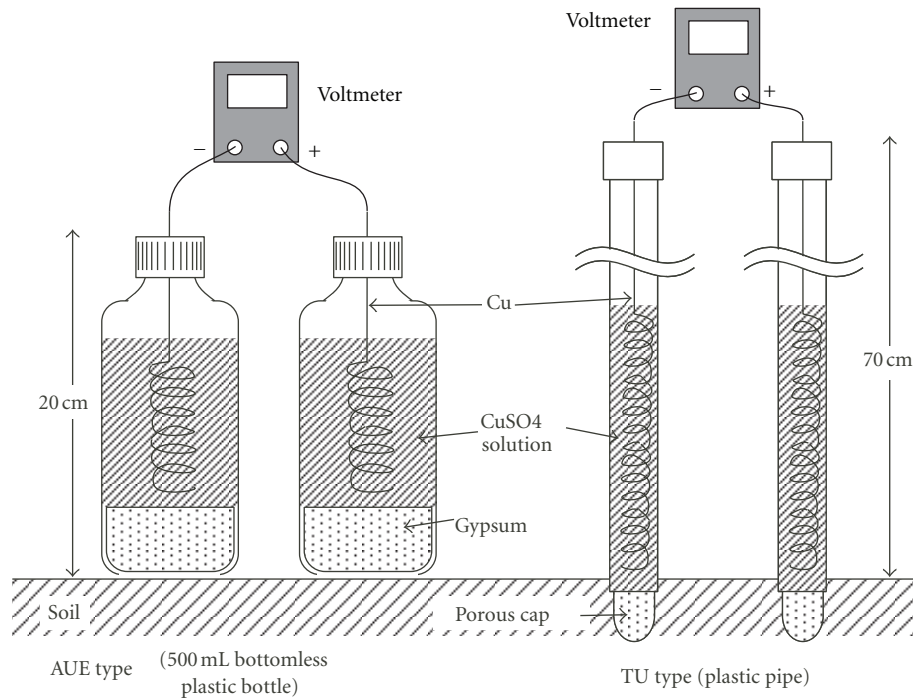


FIGURE 2: Schematic diagram of Cu-CuSO₄ electrodes used in this study.

surface, and those named TU-type are used for thick soil cases with stabbing. Electrode position at start or end of each survey route is common among several routes (Figure 1). All observed SP values are represented as relative ones to the reference station near the summit (shown by a double circle in Figure 1).

Stability of the electrode pair was checked by voltage measurement between the two electrodes set on the ground with 10 cm separation. Such offset check was done at start, end, and several points along each survey route. The offset voltages were within 5 mV in this study. We also confirmed accuracy of the observed SP values by making SP measurements along parallel additional routes (e.g., B, G, H, C, and J-K in Figure 1), whose electrode positions at start and end of profiles were common with main survey routes (A-F in Figure 1).

In addition to SP surveys, DC resistivity surveys were conducted at six sites in this area (Figure 1). A one-dimensional forward modeling algorithm [24] and a one-dimensional inversion algorithm [25] were applied to obtain near-surface resistivity values. The approximate sounding depth was 10–20 m.

3. Results

The observed SP anomalies are shown in Figure 3. Along the main SP profile (A–F), several sharp and local SP anomalies are recognized, in particularly at 770, 640, 520, and 360 m in altitude. Some of the amplitudes exceed 100 mV, and the typical altitudinal extent is about 50 m (corresponding to the horizontal spatial extent of about 150 m) or less. As shown

in Figure 3(a), similar local SP anomalies are also observed along the neighboring survey routes, B, G, and H. Note that voltage difference between routes A and B was less than 10–20 mV, which is thought to be due to small difference (typically less than ~10 m) in the electrode position between these two survey routes except the start and end points.

The spectrum analysis gives us more quantitative features of the local and sharp SP anomalies. We applied the fast Fourier transform (FFT) to the obtained SP data along the main profile, A–F. Since the data spacing is not equal through the entire SP profile, we calculated SP values at equispaced points using the natural cubic splines. A linear increasing trend of SP toward the foothill (about -0.12 mV/m estimated by the least square regression) is subtracted before the FFT. Finally, the FFT was applied to SP values at 512 points equally spaced with altitude interval of about 1.286 m. The spectrum obtained by the FFT is shown in Figure 4. Three peaks of spectrum were clearly identified at altitudinal wavelength of 131.6 m, 65.8 m, and 43.9 m. To delineate characters of the spectrum peaks in Figure 4 more clearly, we first created a “regional” SP pattern with longer wavelength by applying the inverse FFT to a spectrum portion with longer wavelength (219–658 m) denoted by “A” in Figure 4 and adding the linear trend of SP described above to it. The resultant “regional” SP pattern is shown in Figure 5(a). Then, the “local” SP pattern with shorter wavelength is estimated by subtracting the regional SP pattern from the raw data. Figure 5(b) is the resultant local SP pattern with altitudinal wavelength shorter than 131.8 m. We found that the local SP anomalies have mainly positive peaks with altitudinal extent of 40–60 m. Note that large peaks are obvious at altitudes between 300 m and 700 m.

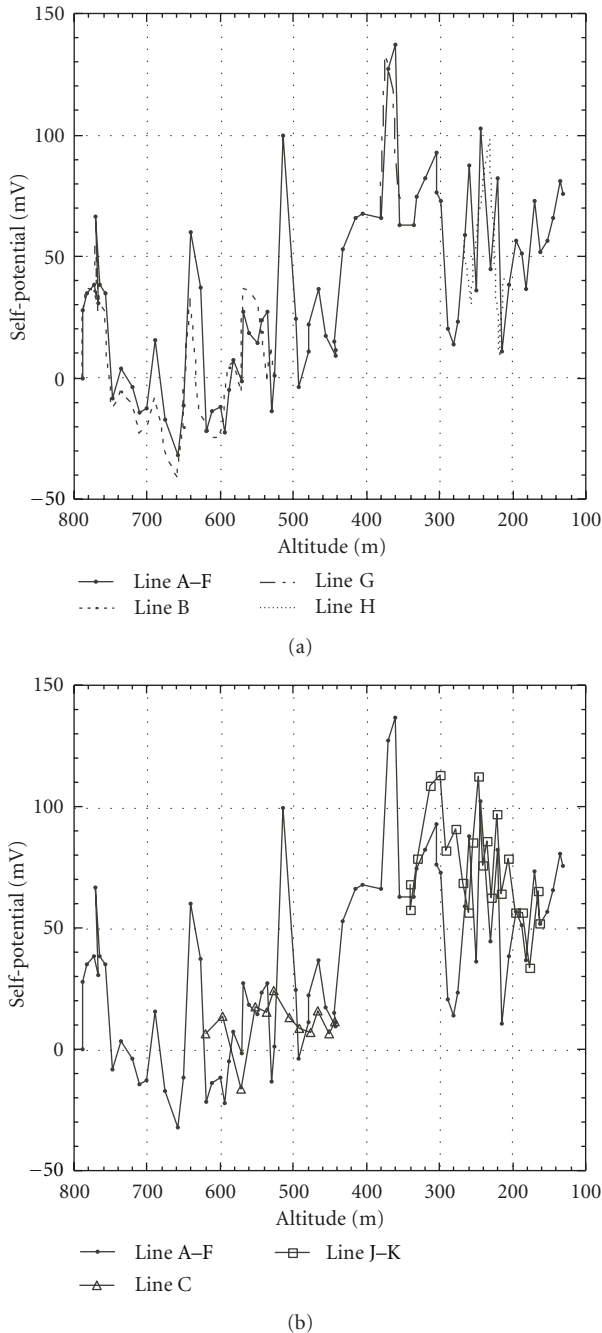


FIGURE 3: Observed SP profile along the northern slope of Mt. Tsukuba. (a) Those along the neighboring routes (A, F, B, G, and H) and (b) the parallel routes (C, J, and K) are plotted. The reference point is at the summit.

Concerning the longer wavelength (more than ~ 200 m in altitude), SP patterns along parallel survey routes show similar features (Figure 3(b)). For example, SP profiles along routes A and C are similar to each other except for local SP anomalies described above. The “regional” SP pattern (Figure 5(a)) indicates gradual increase toward the foothill of Mt. Tsukuba. However, the increasing trend is not monotonic and includes two major perturbations. One is

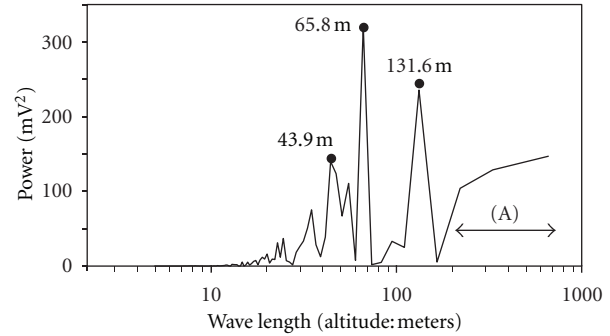


FIGURE 4: Power spectrum of spatial SP distribution against altitude. Three peaks are obvious. Spectrums with longer wavelength are denoted as “A.”

a decreasing trend toward lower altitude from 350 m to 250 m, and another is also a decreasing trend between 750 m and 650 m in altitude. The former decreasing trend is also recognized along parallel route J-K (Figure 3(b)), suggesting that this decreasing trend has substantial spatial extent in the same altitudes.

4. Discussion

4.1. Local SP Anomalies. “Local” SP anomalies of positive polarity (Figure 5(b)) have a limited spatial extent. The altitudinal extent of them is typically about 40–60 m, which corresponds to horizontal extent of 100–200 m (because of 10–20 degrees slope gradient). In order to estimate the approximate depth of electrical current source which generates such local SP anomalies, simple calculations were conducted. A point current source was assumed in a uniform resistivity (ρ) half-space. The depth of point source (d) was varied, and the surface potential field (V) was calculated using the following simple analytic solution:

$$V = \frac{\rho \cdot I}{2\pi\sqrt{r^2 + d^2}}, \quad (1)$$

where r is the horizontal distance between the source and the observation point, and I is the source current strength. The calculated potential profile with respective source depths is normalized by the SP value at $r = 0$ m (shown in Figure 6). For comparison between the calculated and observed SP, we plot two local SP anomalies (denoted by “A” and “B” in Figure 5(b)) in Figure 6. Zero level is fixed as an average SP values at the northern and southern edges of each anomaly, and SP values are normalized by the peak values. On the basis of Figure 6, the sources for local SP anomalies are thought to be located near the surface; we roughly estimate the depths to be shallower than ~ 10 meters, although the observed local SP values are substantially scattered.

A cause of local positive SP anomalies such as observed in the present study is generally inferred to be local springs, yielding a positive current source near the ground surface. The slope of Mt. Tsukuba is widely covered by debris or slope deposits, which consist of unconsolidated sediments and have high permeability. It is well known that perched

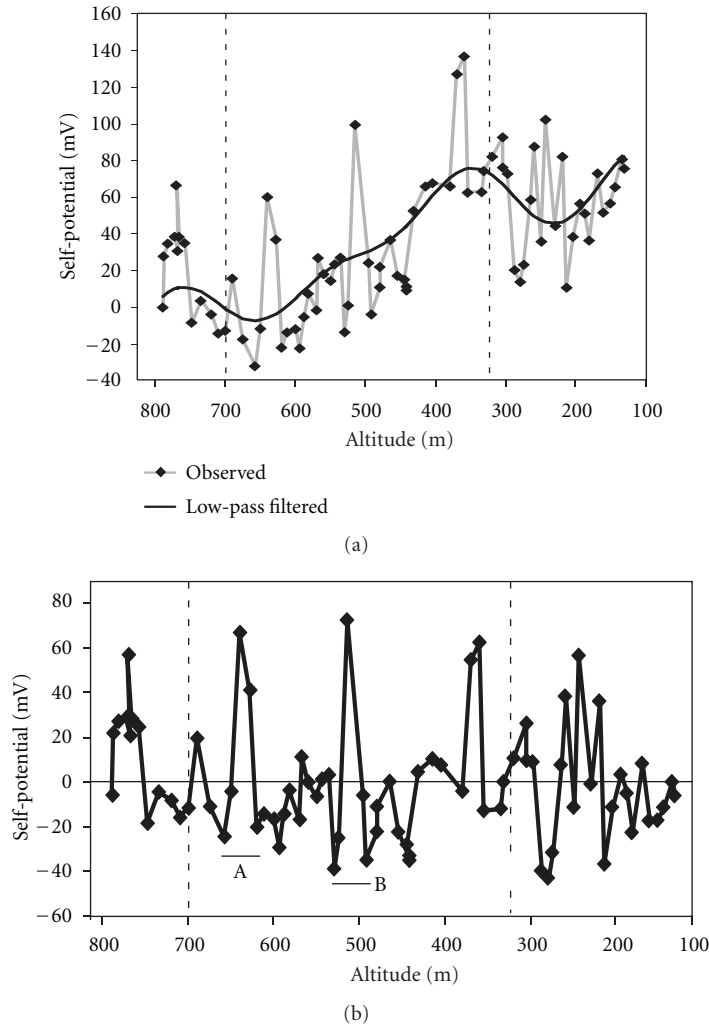


FIGURE 5: (a) The observed raw SP profile (gray line with diamonds) and low-pass filtered one called as “regional” pattern in this study (solid line). (b) Residual SP profile after subtracting regional SP from raw data, called as “local” anomalies.

water flow is present in a vadose zone developed in such slope deposits; therefore, we infer that the observed local SP anomalies reflect discharge of perched water. However, most of the anomalies are not located in the neighbor (within a few ten meters) of known springs. So instead of directly corresponding to surface springs, the current sources are thought to be located at underground transition zone of electrokinetic coupling coefficient where perched water flow loses its ability to carry electrical charges with it. In the area with altitude higher than about 450 m, the slope angle increases gently toward the summit (from 10 to 20 degrees), and larger gravels are conspicuous. Maybe, perched water flow becomes stream-like flow through underground channels (cavities), which does not transport sufficient electrical charges with it unlike the flow through porous media, at shallower depths than ~10 meters in the slope deposits. Such underground streams may start from the locations of local SP anomalies like “A” and “B” shown in Figure 5(b) and flow into nearby rivers. Anyway, such shallow phenomena seem to show seasonal variations. We

will need to make repeated measurements to observe a correlation with precipitation, and so forth in the future.

4.2. Regional SP Pattern. The general trend of “regional” SP pattern indicates gradual increase toward the foothill of Mt. Tsukuba (Figure 5(a)). This is a typical example of the topographic effect on SP, interpreted by the mountain-scale groundwater flow from summit to foothill. The mean coefficient of topographic effect was about -0.12 mV/m, and the maximum was about -0.45 mV/m at altitude of 400 m. It is noteworthy that the measured streaming potential coefficient for intact rock samples of Inada granite is about 0.03×10^{-6} V/Pa for 0.001 mol/L KCl solution below 50°C [26, 27]. If we apply this data to the granitic basement of Mt. Tsukuba, topographic effect of -0.3 mV/m is possible for the case that water table is located close to the upper surface of the granitic basement (Figure 7(a)). Substantial part of the general trend is thought to be caused by the water flow in the granitic basement.

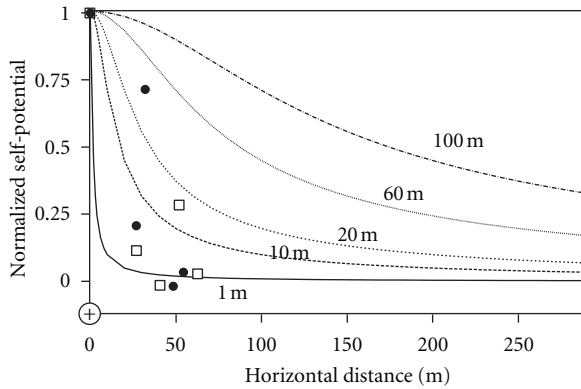


FIGURE 6: Calculated SP from various depths of a point source (1–100 m). The SP values are normalized by the respective value at 0 m in the horizontal distance where the source is located. The observed SP anomalies “A” and “B” in Figure 5(b) are shown by circles and rectangles, respectively.

There are two major perturbations from the general trend as mentioned in Section 3. Both of them seem to be present near geological contacts between different units along the mountain slope. The Holocene younger slope deposits (unconsolidated sediments) distribute below altitude of 320 m along the route F, while the Holocene older slope deposits distribute around altitude of 320–700 m (Figure 7(a)). Above 700 m in altitude, the gabbro basement rock is exposed with a cap-like distribution around the summit [20]. Two decreasing patterns toward the foothill (“RA” and “RB” in Figure 7(b)), which are inconsistent with the ordinal topographic effect, are located near these geological boundaries at the ground surface. In the following, we discuss causes of these two perturbations based upon the heterogeneity of subsurface structure and related groundwater flow.

4.2.1. Regional SP Perturbation at the Foot Hill. The decreasing pattern “RA” in Figure 7(b) is present near the boundary between older and younger slope deposits as mentioned above. One of the candidates for this perturbation is a difference in the coupling coefficient between the two deposits. Even though both slope deposits have the same material origin (gabbro and granite), the coupling coefficient may be different between them due to difference in the formation factor (porosity, tortuosity), and so forth (e.g., [6]). In addition to this, hydrological heterogeneities such as water table perturbation due to heterogeneous permeability distribution and heterogeneous infiltration of meteoric water can be candidates.

If the younger slope deposits (on the lower altitude side) are more permeable than the older slope deposits (on the higher altitude side), downward fluid flow crossing the boundary leaves positive charges there (with negative zeta potential) due to discontinuous pressure gradient normal to the boundary even if the coupling coefficient is homogeneous [28]. However, it depends on the hydrological boundary condition at the ground surface whether or not water flow through a heterogeneous permeability region

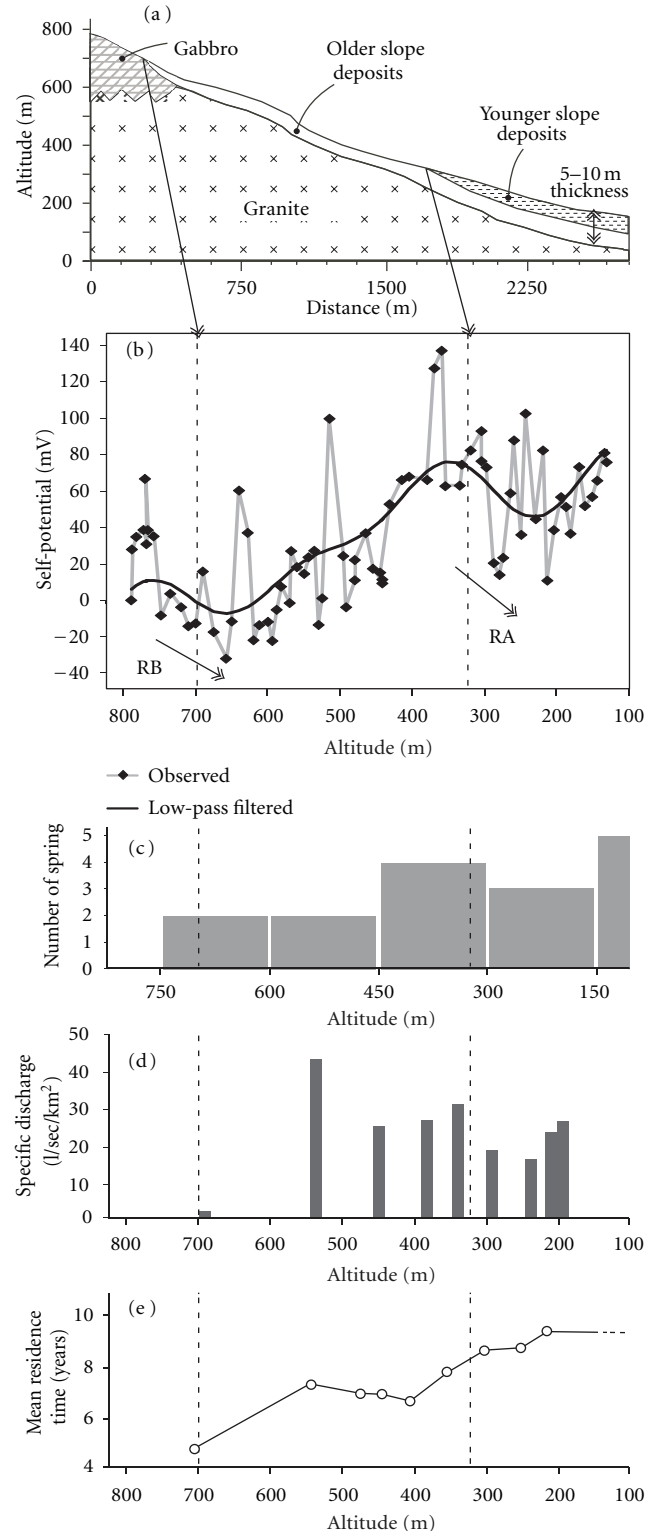


FIGURE 7: Comparison of the geological setting, SP distributions, and hydrological information along the northern slope of Mt. Tsukuba. (a) Geological structure [20]. Note that the surface layer is exaggerated vertically. (b) Raw and regional SP profiles are same as shown in Figure 5. (c) Histogram for number of springs around Mt. Tsukuba against altitude derived from [23]. (d) Specific discharge of the Ono-kawa river water [22]. (e) Mean residence time of stream water [21].

brings about surface SP anomalies. If it is pressure (hydraulic head) = constant, no SP anomaly will appear at the ground surface. Electrical charges appearing at the permeability boundary just work as sources to create potential distribution corresponding to the distorted pressure distribution at the boundary (see the tutorial by Jouniaux and Ishido [29], in this special issue “Electrokinetics in Earth Sciences” for more details). However, if the impermeable boundary condition (Neumann condition) is adopted, surface SP anomalies will appear corresponding to hydraulic head distribution along the surface boundary which is modified as a result of heterogeneous permeability distribution (T. Ishido, pers. comm., 2012). The effects of permeability heterogeneity on SP pattern are studied by Ozaki et al. [30]. In their numerical simulation using two-dimensional FDM (finite difference method), the Neumann boundary condition was adopted: no flow normal to all exterior boundaries of the model domain including the ground surface. In the present case (Figure 7(a)), water table (hydraulic head) will be lowered near the boundary between the younger and older slope deposits if the permeability is larger for the younger deposits. Since the lower water table corresponds to higher SP (e.g., [10, 11]), the observed decreasing trend “RA” toward the foothill cannot be explained by this mechanism.

Next, the possibility of heterogeneous infiltration is discussed hereinafter on the basis of a lot of hydrological information. Histogram of number of springs against altitude is made from a distribution of springs in the whole area of Mt. Tsukuba [23]. The histogram shown in Figure 7(c) indicates a clear correlation with the regional SP pattern. The higher SP value is, the more frequently springs are found. A distribution of specific discharge of river water also indicates a high correlation with the regional SP pattern around the foothill. Specific discharge is a flow rate of river water normalized by the catchment area and reflects the contribution of groundwater discharges into river water. Figure 7(d) is the observation result along the Ono-kawa River [22]. Lower specific discharges around 250 m altitude compared to those around 350 m altitude indicate that groundwater discharges into river water are relatively small in the catchment area around 250 m altitude. This means that the fraction of downward groundwater infiltration is relatively high around 250 m altitude compared to the area around 350 m altitude. This is consistent with the result of isotopic analysis [21]; the stream water shows relatively old and young ages at altitudes around 250 m and 350 m, respectively (Figure 7(e)). This means that the contribution of shallow groundwater originating from recent rainfalls to groundwater discharges is relatively small around 250 m altitude compared to that around 350 m altitude. These hydrological data imply that the vadose zone is relatively thick and thin at altitudes of 250 m and 350 m, respectively.

Our DC resistivity survey supports this implication; the average resistivity of the older slope deposits is 100–200 Ωm , while it is higher (200–500 Ωm) in the younger slope deposits, suggesting a highly unsaturated condition. Therefore, we may conclude that the SP decreasing pattern at the foothill (“RA” in Figure 7(b)) is mainly generated by vertical infiltration flow through the thicker vadose zone in

the younger slope deposits and underlying layers. If the thickness of the vadose zone is comparable to that of the younger slope deposits (less than 10 meters, Figure 7(a)), the vertical potential gradient in the vadose zone needs to be around -3 mV/m to explain the regional negative SP at altitude of 250 m. This gradient (-3 mV/m) is an order of magnitude greater than the observed general topographic effect, which suggests that the effective streaming potential coefficient of the vadose zone in the younger slope deposits is significantly larger in magnitude than that of the surrounding area.

4.2.2. Regional SP Perturbation Near the Summit. The decreasing pattern “RB” in Figure 7(b) is present at the lower perimeter of the gabbro rock body exposed around the summit. Water table around the summit is estimated to be quite deep and almost flat based on a hydrological study with isotope analysis and numerical modeling of groundwater flow [23]. The water table is located below the gabbroic body in the granitic basement at higher elevation areas than about 500 m, and the thickness of vadose zone is more than 200 m around the boundary between the gabbroic rocks and the slope deposits at $\sim 700\text{ m}$ altitude (Figure 7(a)). In order to discuss the main causes of the SP perturbation, we carried out a simple numerical modeling by assuming electrical current sources as shown in Figure 8.

The intensity of the current sources is given from the streaming current density J (in A/m^2) in the vadose zone (e.g., [11]):

$$J = -L\rho g \nabla h, \quad (2)$$

where L is the electrokinetic coupling coefficient for the vadose zone (in $\text{A/Pa}\cdot\text{m}$), ρ is the liquid water density ($\sim 10^3\text{ kg/m}^3$), g is the gravitational acceleration (9.8 m/sec^2), and h is the hydraulic head (in meter). As for vertical infiltration of water in the vadose zone, ∇h can be assumed to be ~ 1 . Although experimental data of L was reported for unsaturated sands (e.g., [31]), no data is available for liquid/gas two-phase flow in the granitic rocks. We simply assume $L = -2 \times 10^{-10}\text{ A/Pa}\cdot\text{m}$ for the vadose zone in the present calculation, which means $|J| = 2 \times 10^{-6}\text{ A/m}^2$ from (2). In all of the three models shown in Figure 8, the intensity of unit current source at the ground surface is given as $I = -0.002\text{ A}$ for a surface area of 20 m (along the slope) \times 50 m (perpendicular to the slope). Such current sources are assumed every 20 m between 0 m and 400 m along the slope, and current sources of the same intensity but with opposite sign ($I = +0.002\text{ A}$) are assumed every 20 m along the water table for charge conservation. As for the streaming current density in the underlying saturated region, we assume relatively large magnitude ($|J| = 4 \times 10^{-6}\text{ A/m}^2$, which may be too large considering a small ∇h value for the saturated region, T. Ishido, pers. comm., 2012). Thus, negative current sources (unit intensity of -0.004 A) are assumed every 20 m along the water table, and a positive current source of $+0.08\text{ A}$ ($=0.004\text{ A} \times 20$) is assumed for charge conservation on the slope surface (at 700 m foothill side from the origin of slope). A three-dimensional forward calculation code “3ddcxh” [32] is used to calculate the SP,

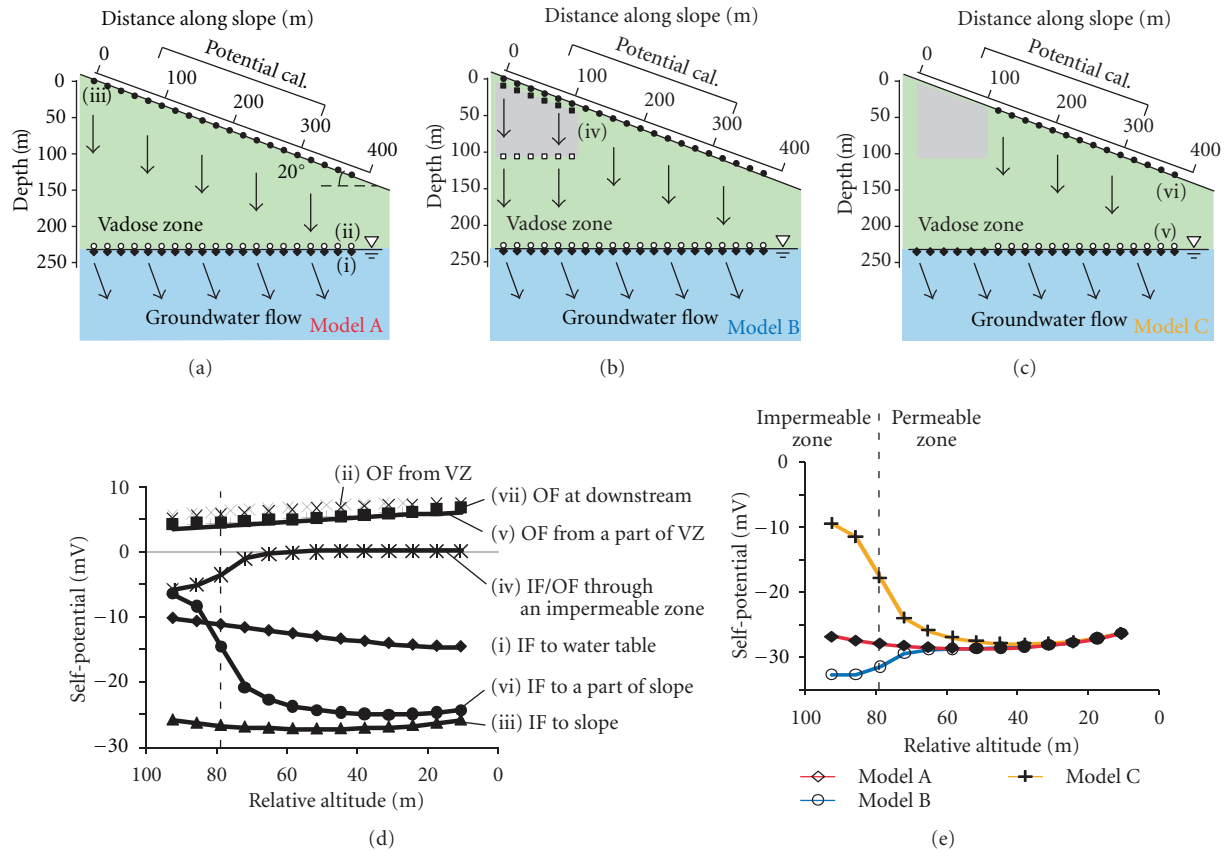


FIGURE 8: Numerical modeling of SP profiles along slopes. (a) Model A with homogeneous subsurface structure. (b) Model B with constant infiltration through both a less permeable zone (gray) and surroundings. (c) Model C with heterogeneous infiltration outside of an impermeable zone (gray). In all three models, diamonds, circles, and rectangular dots indicate electric current sources with intensity of 0.004, 0.002, and 0.001 A, respectively. Solid and open symbols mean negative and positive polarities, respectively. Arrows indicate assumed flow directions. SP profiles shown in (d) and (e) are calculated along the thick line portion on the slope for each case. (d) Calculated SP from respective current sources. The abbreviations are as follows: IF: inflow, OF: outflow, and VZ: vadose zone. (e) Resultant SP profiles from three models against altitude.

assuming a uniform subsurface resistivity of $200 \Omega\text{m}$ (which is estimated from the DC resistivity survey).

As shown in Figure 8, we consider three models: (A) with homogeneous permeability and infiltration, (B) with a less permeable zone (gabbro) and homogeneous infiltration, and (C) with an impermeable zone (gabbro) and heterogeneous infiltration. The SP from model A (Figure 8(a)) is regarded as a reference without heterogeneity, which shows almost flat profile (Figure 8(e)). The reason why a negative correlation between SP and altitude is not seen here is due to the effect of intense negative current sources assigned to mimic downward saturated water flow along the water table (see the curve (i) in Figure 8(d)). In model B (Figure 8(b)), the streaming current density is assumed to be $|J| = 3 \times 10^{-6} \text{ A/m}^2$ for the gabbroic body, that is, one and half times that for the surrounding vadose zone (this assumption may be plausible considering that the liquid-phase saturation can be higher in the less permeable zone). This assumption produces a negative SP near the summit (see the curve (iv) in Figure 8(d)), which results in an opposite feature to the observation (Figure 8(e)). In model C (Figure 8(c)),

no infiltration is assumed along the gabbroic rock surface, considering a situation that most of rainfall water is removed from the area due to rapid runoff along the almost impermeable rock surface and does not infiltrate downward. Due to this effect (see the curve (vi) in Figure 8(d)), the SP profile (shown in Figure 8(e)) shows a corresponding trend to the observed SP with decreasing pattern near the summit (“RB” in Figure 7(b)).

As a result of the above calculations, the heterogeneous infiltration at the surface is thought to be the most probable cause of the SP perturbation observed near the summit. A similar but more prominent feature observed near active volcano summits has been studied by numerical simulations (e.g., [14, 33]). Aizawa et al. [33] carried out a sophisticated modeling of both groundwater flow and SP and indicates that a heterogeneous infiltration due to a less permeable zone near the summit makes regional “sink” pattern of SP along the mountain slope. In their study, heterogeneous distributions of coupling coefficient and electrical conductivity are taken into account in addition to permeability heterogeneity. The presence of extensive alteration rocks around volcano

summits is very influential on the SP distribution due to its high electrical conductivity rather than its impervious nature [14]. In such situations, we need to take into account various factors other than heterogeneous permeability and infiltration distributions.

In field observations, similar SP patterns are also found at small-scale mountain slopes. For example, in the Nagano prefecture, Japan, Abe [22] found the relatively positive SP anomaly near a ridge and negative “sink” SP pattern off the ridge. We suppose that the ridge areas have a thin permeable layer at the surface, and infiltration mainly occurs off the ridge having a thicker surface permeable layer. We believe that this phenomenon is rather common at many mountain slopes, so it is very important to take into account heterogeneous infiltration effects to discuss groundwater flow systems beneath mountain slopes.

5. Summary

On the basis of the proposed causes for local and regional SP patterns in this study, we summarize the inferred groundwater flow system in Mt. Tsukuba. As discussed in Section 4.2.1, the water table comes close to the surface at altitude of about 400 m, inferred by the high regional SP values, the younger mean residence time of stream water, and distribution of springs (Figures 7(b), 7(e), and 7(c)). The water table goes down at the foothill (lower than 350 m in altitude) covered by thick younger slope deposits with high permeability, inferred by the regional SP sink pattern “RA” and the specific discharge of stream (Figures 7(b) and 7(d)). The thickness of the vadose zone will be over 10 m estimated by the DC resistivity survey. Around the summit, as discussed in Section 4.2.2, the thicker vadose zone expands above the water table located in the granitic basement. The infiltration is not homogeneous with simple vertical flow but is concentrated outside of the gabbro rocks at the summit, inferred from the regional SP pattern “RB” near the summit (Figure 7(b)). In addition to the regional flow systems, local flow of perched water is developed in the vadose zone in the slope deposits as discussed in Section 4.1. The local positive SP anomalies (Figure 5(b)) are thought to be associated with outflow of perched water near the ground surface.

The implication for groundwater flow system in Mt. Tsukuba is not solely derived from hydrological information. The combination of hydrological and SP surveys gives us a chance of sophisticated interpretation of groundwater flow system. The major contribution of SP surveys comes from wider spatial coverage with high measurement density than the conventional hydrological surveys along the mountain slope. On the other hand, SP data alone is not interpreted uniquely among various possible patterns of groundwater flow. Therefore, SP surveys are brought into a complementary relation with hydrological information. In the future, coupled numerical examinations of both groundwater flow and SP should be performed for many cases along mountain slopes, which is very helpful in evaluation of groundwater flow systems for environmental, engineering, agricultural, and scientific issues.

Acknowledgments

The authors thank Dr. Y. Tanaka, Dr. Y. Sasai, and Dr. H. Murakami for their valuable comments about field experiments. They thank Yumiko Tsutsui, Takuya Omura, Takayuki Kimura, Chisa Kobayashi, and Manabu Shibata for their help on preexperiments. This paper has been greatly improved by constructive remarks from the Academic Editor Dr. Tsuneo Ishido and two anonymous reviewers. This work was partially supported by a Grant for Scientific Research from the Ministry of Education, Japan (no. 23501241).

References

- [1] D. B. Jackson and J. Kauahikaua, “Regional self-potential anomalies at Kilauea Volcano (Hawaii),” *US Geological Survey Professional Paper*, vol. 1350, no. 2, pp. 947–959, 1987.
- [2] F. S. Birch, “Testing Fournier’s method for finding water table from self-potential,” *Ground Water*, vol. 31, pp. 50–56, 1993.
- [3] Y. Sasai, J. Zlotnicki, Y. Nishida et al., “Electromagnetic monitoring of Miyake-jima volcano, Izu-bonin arc, Japan: a preliminary report,” *Journal of Geomagnetism and Geoelectricity*, vol. 49, no. 11–12, pp. 1293–1316, 1997.
- [4] T. Ishido, “Self-potential generation by subsurface water flow through electrokinetic coupling, in Detection of subsurface flow phenomena,” *Lecture Notes in Earth Sciences*, vol. 27, pp. 121–131, 1989.
- [5] A. Revil and P. Leroy, “Hydroelectric coupling in a clayey material,” *Geophysical Research Letters*, vol. 28, no. 8, pp. 1643–1646, 2001.
- [6] T. Ishido and J. Muzutani, “Experimental and theoretical basis of electrokinetic phenomena in rock-water systems and its applications to geophysics,” *Journal of Geophysical Research*, vol. 86, no. 3, pp. 1763–1775, 1981.
- [7] K. Yasukawa and T. Mogi, “Topographic effects on Sp anomaly caused by subsurface fluid flow—numerical approach,” *Butsuri-Tansa*, vol. 51, pp. 17–26, 1998.
- [8] R. F. Corwin and D. B. Hoover, “Self-potential method in geothermal exploration,” *Geophysics*, vol. 44, no. 2, pp. 226–245, 1979.
- [9] F. Timm and P. Möller, “The relation between electric and redox potential: evidence from laboratory and field measurements,” *Journal of Geochemical Exploration*, vol. 72, no. 2, pp. 115–128, 2001.
- [10] C. Fournier, “Spontaneous potentials and resistivity surveys applied to hydrogeology in a volcanic area: case history of the Chaîne des Puys (Puy-de-Dôme, France),” *Geophysical Prospecting*, vol. 37, no. 6, pp. 647–668, 1989.
- [11] A. Revil, V. Naudet, and J. D. Meunier, “The hydroelectric problem of porous rocks: inversion of the position of the water table from self-potential data,” *Geophysical Journal International*, vol. 159, no. 2, pp. 435–444, 2004.
- [12] N. Linde, A. Revil, A. Bolève et al., “Estimation of the water table throughout a catchment using self-potential and piezometric data in a Bayesian framework,” *Journal of Hydrology*, vol. 334, no. 1–2, pp. 88–98, 2007.
- [13] M. Aubert and Q. Yéné Atangana, “Self-potential method in hydrogeological exploration of volcanic areas,” *Ground Water*, vol. 34, no. 6, pp. 1010–1016, 1996.
- [14] T. Ishido, “Electrokinetic mechanisms for the “W”-shaped self-potential profile on volcanoes,” *Geophysical Research Letters*, vol. 31, no. 15, pp. L15616–5, 2004.

- [15] K. Ernstson and H. U. Scherer, "Self-potential variations with time and their relation to hydrogeologic and meteorological parameters," *Geophysics*, vol. 51, no. 10, pp. 1967–1977, 1986.
- [16] C. J. Zablocki, "Some electrical and magnetic studies of Kilauea Iki lava lake," Open-File Report—U. S. Geological Survey, Report OF 76-0304, Hawaii, USA, 1976.
- [17] F. Massenet and P. Van Ngoc, "Mapping and surveillance of active fissure zones on a volcano by the self-potential method, Etna, Sicily," *Journal of Volcanology and Geothermal Research*, vol. 24, no. 3-4, pp. 315–338, 1985.
- [18] J. Zlotnicki, M. Feuillard, and G. Hammouya, "Water circulations on La Soufriere volcano inferred by self-potential surveys (Guadeloupe, Lesser Antilles). Renewal of volcanic activity?" *Journal of Geomagnetism & Geoelectricity*, vol. 46, no. 9, pp. 797–813, 1994.
- [19] T. Hashimoto and Y. Tanaka, "A large self-potential anomaly on Unzen volcano, Shimabara Peninsula, Kyushu Island, Japan," *Geophysical Research Letters*, vol. 22, no. 3, pp. 191–194, 1995.
- [20] S. Igi, *Geologic Atlas of Japan Kanto Region*, Asakura Shoten, Tokyo, Japan, 1990.
- [21] K. Sanjo, "Isotope hydrology of Mt. Tsukuba," *Science Reports—University of Tsukuba, Institute of Geoscience, Section A*, vol. 12, pp. 1–36, 1991.
- [22] Y. Abe, *Estimation of groundwater flow using self-potential measurement in hillslopes of College of Natural Sciences*, Graduation thesis, First Cluster of Colleges, University Tsukuba, 2001.
- [23] T. Matsumoto, *Age dating of spring and groundwater and its modeling in Mt. Tsukuba, central Japan*, M.S. thesis, University Tsukuba, 2011.
- [24] Y. Murakami, "Computer program for processing and interpreting Schlumberger and Wenner resistivity data," Open File Report number 42, Geological Survey of Japan, 1987.
- [25] K. Ushijima, H. Mizunaga, and A. Kato, "Interpretation of geoelectric sounding data by personal computer," *Butsuri-Tanasa*, vol. 40, pp. 423–435, 1987.
- [26] T. Tosha, N. Matsushima, and T. Ishido, "Zeta potential measured for an intact granite sample at temperatures to 200°C," *Geophysical Research Letters*, vol. 30, no. 6, pp. 28–1, 2003.
- [27] T. Ishido and N. Matsushima, "Streaming potential measured for an intact granite sample at temperatures to 200°C," in *Proceedings of the 32nd Workshop on Geothermal Reservoir Engineering, 2007*, SGP-TR-183, Stanford University.
- [28] W. R. Sill, "Self-potential modeling from primary flows," *Geophysics*, vol. 48, no. 1, pp. 76–86, 1983.
- [29] L. Jouniaux and T. Ishido, "Electrokinetics in earth sciences: a tutorial," *International Journal of Geophysics*, vol. 2012, Article ID 286107, 2012.
- [30] Y. Ozaki, H. Mikada, T. Goto, J. Takekawa, M. Tsujimura, and F. Hachani, "Effect of heterogeneity of hydraulic conductivity on streaming potential," in *Proceedings of the 14th International Symposium on Recent Advances in Exploration Geophysics (RAEG'10)*, pp. 115–117, 2010.
- [31] X. Guichet, L. Jouniaux, and J. P. Pozzi, "Streaming potential of a sand column in partial saturation conditions," *Journal of Geophysical Research B*, vol. 108, no. 2141, p. 2, 2003.
- [32] K. Spitzer, "A 3-D finite-difference algorithm for DC resistivity modelling using conjugate gradient methods," *Geophysical Journal International*, vol. 123, no. 3, pp. 903–914, 1995.
- [33] K. Aizawa, Y. Ogawa, and T. Ishido, "Groundwater flow and hydrothermal systems within volcanic edifices: delineation by electric self-potential and magnetotellurics," *Journal of Geophysical Research B*, vol. 114, no. 1, Article ID B01208, 2009.

Research Article

Frequency-Dependent Streaming Potential of Porous Media—Part 2: Experimental Measurement of Unconsolidated Materials

P. W. J. Glover,¹ E. Walker,¹ J. Ruel,² and E. Tardif²

¹ Department of Geology and Engineering Geology, Laval University, Québec City, QC, Canada G1K 7P4

² Department of Mechanical Engineering, Laval University, Québec City, QC, Canada G1K 7P4

Correspondence should be addressed to P. W. J. Glover, paglover@ggl.ulaval.ca

Received 3 June 2011; Revised 1 November 2011; Accepted 12 December 2011

Academic Editor: Tsuneo Ishido

Copyright © 2012 P. W. J. Glover et al. This is an open access article distributed under the Creative Commons Attribution License, which permits unrestricted use, distribution, and reproduction in any medium, provided the original work is properly cited.

Frequency-dependent streaming potential coefficient measurements have been made upon Ottawa sand and glass bead packs using a new apparatus that is based on an electromagnetic drive. The apparatus operates in the range 1 Hz to 1 kHz with samples of 25.4 mm diameter up to 150 mm long. The results have been analysed using theoretical models that are either (i) based upon vibrational mechanics, (ii) treat the geological material as a bundle of capillary tubes, or (iii) treat the material as a porous medium. The best fit was provided by the Pride model and its simplification, which is satisfying as this model was conceived for porous media rather than capillary tube bundles. Values for the transition frequency were derived from each of the models for each sample and were found to be in good agreement with those expected from the independently measured effective pore radius of each material. The fit to the Pride model for all four samples was also found to be consistent with the independently measured steady-state permeability, while the value of the streaming potential coefficient in the low-frequency limit was found to be in good agreement with other steady-state streaming potential coefficient data.

1. Introduction

There have only been 10 measurements of the frequency-dependent streaming potential coefficient of porous geological and engineering materials. A review of the existing measurements was carried out by Glover et al. [1]. These previous measurements can be divided into two groups: (i) transient measurements with a percussive source and (ii) harmonic measurements with a vibrating source.

While the first of these approaches mimics many of the possible applications more closely [2–4], it cannot provide the streaming potential coupling coefficient as a function of frequency without using the frequency domain filtering and Fourier techniques. Such techniques can only be used in a linear system. Although the equations that describe the streaming potential coefficient are linear below the transition frequency and there is no evidence that they become non-linear above that frequency, it has not yet been shown that such an approach can be made to work for streaming po-

tential coupling coefficient measurements on rocks. The processing of such data has, however, been discussed at length in Reppert and Morgan [5]; they mention that inertial effects may be seen if the transient signal has strong enough high-frequency components.

The second approach is capable of providing the streaming potential coupling coefficient at each frequency directly. Its disadvantage is that a high-quality harmonic driving pressure is required to create the time-varying flow. Various authors have shown that measurements on a range of materials are possible in the range 1 Hz to 600 Hz [6–10], but before the recent paper of Tardif et al. [11] only one measurement had been made on a geological material [10].

This paper reports research that uses the electromagnetic drive concept proposed by Glover et al. [1] to create an apparatus for measuring the frequency-dependent streaming potential coupling coefficient of unconsolidated materials such as sands, gravels, and soils. Unconsolidated materials were chosen because it is easier to arrange a sample holder

with no need for a sleeve and a sleeve pressure. The experimental data have been analyzed using a number of theoretical models. The first part of this paper is dedicated to describing these models, followed by experimental measurements on samples of sand and glass beads. The theoretical models have been compared with the measured data in order to obtain the transition frequency, which has then been used to calculate the effective pore radius of the sands and glass bead packs using the theory in Glover and Walker [12].

2. Theoretical Models

The steady-state streaming potential coefficient (the streaming potential per driving fluid pressure difference) has long been described by the Helmholtz-Smoluchowski (HS) equation, and is given in the form most convenient for application to rocks (e.g., [13]);

$$C_{so} = \frac{\Delta V}{\Delta P} = \frac{\varepsilon \zeta}{\eta_f \sigma}, \quad \text{where} \quad \sigma = \sigma_f + \frac{2\Sigma_s}{\Lambda}. \quad (1)$$

In this equation ΔP (Pa) is the fluid pressure difference, ε (F/m) is the dielectric constant of the fluid, η_f (Pa.s) is the dynamic viscosity of the fluid, ζ (V) is the zeta potential, ΔV (V) is the streaming potential, σ_f (S/m) is the electrical conductivity of the bulk fluid, Σ_s (S) is the specific electrical conductance of the surface (i.e., that due to the double layer), σ (S/m) is the electrical conductivity of the mobile fluid, and Λ (m) is a characteristic length associated with the microstructure of the pore network [14–18]. The steady-state streaming potential is independent of the sample geometry.

The importance of considering the surface conductance when applying the HS equation to geological materials has been discussed by a number of authors including [1, 14–17]. Recently several modified versions of the classical HS equation have been published that take into account the variability of the streaming potential coupling coefficient as a function of grain size [17, 19–21], pore size [17], and pore throat size [17].

There are several theoretical models for the frequency-dependent streaming potential coupling coefficient. The models fall into three categories: (i) models based only on vibrational mechanics [22], (ii) models based on flow in capillary bundles [6], and (iii) those that have been developed for porous media [23].

2.1. Vibrational Mechanics Models. If we apply the amplitude of the critically damped second-order vibrational behaviour [22] to the frequency-dependent streaming potential coupling coefficient, we get

$$\frac{C_s(\omega)}{C_{so}} = \left(1 + \left(\frac{\omega}{\omega_t}\right)^2\right)^{-1/2}, \quad (2)$$

where $C_s(\omega)$ (in V/MPa) is the streaming potential coupling coefficient at a frequency ω (in Hz), C_{so} (in V/MPa) is the steady-state streaming potential coupling coefficient, and ω_t (in Hz) is the transition frequency. This model only exists in the real domain and is a special case (for $\xi = 1$) of the general

second-order vibrational behaviour with variable damping that is given by

$$\frac{C_s(\omega)}{C_{so}} = \left(\left(1 - \left(\frac{\omega}{\omega_t}\right)^2\right)^2 + \left(2\xi\left(\frac{\omega}{\omega_t}\right)\right)^2 \right)^{-1/2}, \quad (3)$$

for the frequency-dependent streaming potential coupling coefficient. In this equation ξ is the damping factor of the system. This equation provides the modulus or magnitude of the vibration as is usually measured experimentally either by a peak-to-peak or an RMS measurement.

Both equations can be fitted to experimental data where $C_s(\omega)/C_{so}$ is plotted as a function of frequency. For (2) the transition frequency is the only fitting variable, while (3) has two fitting variables: the transition frequency and the damping factor.

These vibrational mechanics models are purely formal and contain no underlying physics. They are interesting in that they can show that a system is behaving in a certain manner, but no inference can be made, for example, about what controls the damping coefficient. This lack of specificity often allows such models to apparently fit the data better than other models which include more of the underlying physics.

2.2. Capillary Tube Models. The capillary tube model was introduced by Packard [6] together with a small number of experimental measurements. It is given by

$$\frac{C_s(\omega)}{C_{so}} = \left(\frac{-2 J_1(kr)}{kr J_0(kr)}\right), \quad (4)$$

where

$$k^2 = \frac{-i\omega\rho_f}{\eta_f}, \quad (5)$$

where $i = \sqrt{-1}$, ρ_f (kg/m³) is the density of the bulk fluid, ω (rad/s) is the angular frequency, r (m) is the radius of the capillary in which the flow takes place, and J_0 and J_1 are Bessel functions of the zeroth and first order, respectively. Note that k has dimensions of inverse length; hence, kr is dimensionless, and the real part of the Bessel function expression $\Re[(2J_1(kr)/krJ_0(kr))]$ varies between unity at low frequencies and zero at high frequencies, and its imaginary part $\Im[(2J_1(kr)/krJ_0(kr))]$ is zero at both low and high frequencies, but attains a peak value at a frequency known as the transition frequency.

Reppert et al. [9] have provided a simplification of (4):

$$\frac{C_s(\omega)}{C_{so}} = \left(1 - \frac{2}{r} \sqrt{\frac{\eta_f}{\omega\rho_f}} \left\{ \frac{1}{\sqrt{2}} - \frac{1}{\sqrt{2}}i \right\}\right), \quad (6)$$

(their Equations 26 and 38). However, a recent study showed that the simplification is incorrect [11]. The correct simplification, which is consistent with the simplified model solution shown in their Figure 4 [9] (T. Ishido, pers. comm., 2011), is

$$\frac{C_s(\omega)}{C_{so}} = \left(1 + \left[\frac{-2}{r} \sqrt{\frac{\eta_f}{\omega\rho_f}} \left\{ \frac{1}{\sqrt{2}} - \frac{1}{\sqrt{2}}i \right\} \right]^{-2} \right)^{-1/2}. \quad (7)$$

When (4) or (7) is fitted to experimental data where the viscosity and density of the process fluid is known, the only fitting variable is the effective capillary radius r .

2.3. Porous Media Models. An extremely important study by Pride [23] has provided a model of streaming potential coupling coefficient for porous media. It takes the form

$$C_s(\omega) = \left(\frac{\varepsilon\zeta}{\eta_f\sigma} \left\{ 1 - 2 \frac{\delta}{\Lambda} \right\} \right) \times \left(1 - i \frac{\omega}{\omega_t} \frac{m^*}{4} \left\{ 1 - 2 \frac{\delta}{\Lambda} \right\}^2 \left\{ 1 - i^{3/2} \delta \sqrt{\frac{\omega\rho_f}{\eta_f}} \right\}^2 \right)^{-1/2}, \quad (8)$$

where

$$\omega_t \equiv \frac{\phi}{\tau_e \kappa_{DC}} \frac{\eta_f}{\rho_f}, \quad (9)$$

and

$$m^* \equiv \frac{\phi\Lambda^2}{\tau_e \kappa_{DC}}. \quad (10)$$

Equation (8) can be rewritten in the same form as the previous models as

$$\frac{C_s(\omega)}{C_{so}} = \left(1 - i \frac{\omega}{\omega_t} \frac{m^*}{4} \left\{ 1 - 2 \frac{\delta}{\Lambda} \right\}^2 \left\{ 1 - i^{3/2} \delta \sqrt{\frac{\omega\rho_f}{\eta_f}} \right\}^2 \right)^{-1/2}, \quad (11)$$

noting that the steady-state term in this model includes an additional factor $C_{so} = \varepsilon\zeta/(\eta_f\sigma)\{1 - 2(\delta/\Lambda)\}$.

In (8)–(11), τ_e (unitless) is the electrical tortuosity of the pore network, ϕ (unitless) is the porosity of the sample, κ_{DC} (m^2) is the steady-state fluid permeability, and δ (m) is the Debye length. The parameter ω_t (rad/s) is the transition frequency, at which the quadrature component of the dispersive system is greatest. While this equation may seem complex, it should be noted that for most geological media the pore fluid is sufficiently saline for the Debye length to be much smaller than the characteristic length scale (i.e., $\delta \ll \Lambda$), which allows significant simplifications to be made.

Recently, such a simplification of (11) has been proposed [19]:

$$\frac{C_s(\omega)}{C_{so}} = \left(1 - i \frac{m^*}{4} \frac{\omega}{\omega_t} \right)^{-1/2}, \quad (12)$$

where

$$\omega_t = \frac{\phi}{\tau_e \kappa_{DC}} \frac{\eta_f}{\rho_f} = \frac{8}{r_{\text{eff}}^2} \frac{\eta_f}{\rho_f}, \quad (13)$$

where r_{eff} (m) is the effective pore radius of the rock. Equation (12) makes the assumption that $\delta \ll \Lambda$, which is valid for the majority of porous rocks that are saturated with

saline fluids with a concentration of 10^{-3} mol/dm³ or more. If we take $m^* = 8/3$ as suggested by [19], we get

$$\frac{C_s(\omega)}{C_{so}} = \left(1 - i \frac{2}{3} \frac{\omega}{\omega_t} \right)^{-1/2}, \quad (14)$$

which is dependent solely on the transition frequency.

If either the full Pride model (11) or its simplifications (12) and (14) are fitted to experimental data where the viscosity and density of the pore fluid and the microstructural parameters ($\delta, \Lambda, \phi, \tau_e, \kappa_{DC}$) of the porous medium are known, the only fitting variable is the transition frequency.

2.4. Physical Interpretation of Theoretical Models. Until recently only the Packard model [6] and its simplification [9] had been tested against data from a few measurements on capillary tubes and filter material [9, 10]. Recently [11] published some data for Ottawa sand which suggested that the vibrational mechanics models [22] fitted their data best. They reported that the best fit of all of the models was a damped second-order vibration mechanics model (3). However, there were errors in their data processing. A correct analysis of their data shows that their data follow the Pride model best, which agrees very well with the results of this study.

Most of the theoretical models have a real and imaginary part. In this paper we have analysed these two contributions separately, comparing the measured data with the overall magnitude and each of the complex components of each model. We have taken an RMS measurement approach which provides the magnitude of the variation and maximises the precision with which it can be measured.

It is interesting to consider the physical meaning of the real and imaginary contributions to the streaming potential coupling coefficient. Currently we do not have sufficient information to answer this question with authority. However, there are some indications. The streaming potential coupling coefficient is defined as the ratio of the streaming potential to the pressure drop across the sample. However, it is the fluid velocity that separates the charge and causes the streaming potential. This implies that the frequency dependence of the streaming potential coupling coefficient depends on the frequency dependence of the dynamic fluid permeability. The dynamic fluid permeability at low frequencies is controlled by viscous flow that is represented by the real part of the dynamic permeability. However, when a critical frequency is reached, the inertial acceleration of the fluid begins to control the flow (e.g., [9, 24]). The inertial acceleration is represented by the imaginary part of the dynamic permeability. Hence, we might expect the real and imaginary parts of the streaming potential coupling coefficient to be influenced by the same transition from viscous-dominated to inertial-dominated fluid flow. In this scenario, the transition frequency is the same as the critical frequency at which viscous-dominated fluid flow becomes inertially dominated. It is becoming clear, however, that the frequency dependence of fluid flow and of the streaming potential coupling coefficient are subtly different. The normalised

dynamic permeability of a bundle of capillary tubes approximately follows a Debye model for all frequencies, while the normalised streaming potential coupling coefficient follows the same Debye model up to the transition frequency then deviates from it considerably [25].

3. Experimental Tests

3.1. Sample Material and Basic Characteristics. Experimental tests were carried out on samples of Ottawa sand and on packs of glass beads using the apparatus described in the associated paper [1]. Their main properties are shown in Table 1.

Ottawa Sand. Ottawa sand was obtained from Fisher Scientific and washed repeatedly in distilled water in order to remove any rock powder before being dried in a vacuum oven prior to use. The pore throat and grain size distributions of the sample material were measured using mercury injection porosimetry and are shown as Figure 1 in [11] together with the grain size distribution obtained by laser diffraction measurements using a Malvern Mastersizer 2000. The porosity of sand samples was also measured using a helium pycnometer. The complex electrical properties of a saturated sample of the sand were measured at 60 frequencies between 1 Hz and 1 MHz using a Solartron 1260A Impedance Analyzer. The absolute value of the complex electrical conductivity at the frequency for which the out-of-phase conductivity was minimum has been used together with the modal grain size from the laser diffraction measurements and the helium porosity in order to calculate the mean pore size of the sand samples using the method of [12].

The quasi-steady-state permeability was obtained by calculating the volume of fluid flowing through the sample per second at 10 Hz using the measured piston displacement and also measuring the pressure required to move this fluid. The permeability at 10 Hz was $\kappa_{10} = 1.19 \times 10^{-10} \text{ m}^2$. We have taken this value to represent the steady-state permeability in the absence of steady-state permeability on the sample.

The measurements shown in this paper are the same as those reported in [11]. However, it should be noted that there were major errors in the analysis of the data in [11] which are corrected in this work. Consequently, this work represents the correct treatment of the Ottawa sand data, while the previous paper should be referred to for a detailed petrophysical description of the material as well as measurements of the petrophysical properties of the Ottawa sand that have been made by other authors.

Glass Beads. Three sizes of soda lime glass bead (nominally 0.5, 1, and 2 mm in diameter) were obtained from Endecotts Ltd.. Samples of the beads were washed repeatedly in distilled water before being dried in a vacuum oven prior to use. No mercury porosimetry was carried out on the beads because they are too expensive to be disposed of after only one use. The grain size distribution was obtained by laser diffraction measurements and using the detailed calibration information provided by Endecotts Ltd., which is based on

a sieve analysis. The porosity of the glass bead samples was measured using a helium pycnometer. The complex electrical properties of a saturated sample of the sand were measured at 60 frequencies between 1 Hz and 1 MHz using a Solartron 1260A Impedance Analyzer, and the results were used to calculate the mean pore size of each bead pack using the Glover and Walker method [12] in the same way as for the Ottawa sand.

The steady-state permeability of each bead pack was measured using a gravitational pressure head. The results are shown in Table 1. These values are in very good agreement with the value predicted from the grain size and electrical measurements using the RGPZ method [26] (their Equation (10)).

Fluids. The fluid used in the experiments was 10^{-3} mol/L NaCl with a measured density of 997 kg/m^3 , which agrees well with the equation of state of NaCl solutions (e.g., [27]) and a viscosity of $8.94 \times 10^{-4} \text{ Pa}\cdot\text{s}$ calculated using the model of [28]. The electrical conductivity of the fluid was measured at $\sigma_f = [1.23 \pm 0.05] \times 10^{-2} \text{ S/m}$ at 25°C before use, which is in good agreement with the model of Sen and Goode [29] at $[1.23 \pm 0.05] \times 10^{-2} \text{ S/m}$. For the Ottawa sand, the conductivity of the fluid emerging from the apparatus during the measurement was extremely close to the original conductivity of the fluid ($[1.21 \pm 0.05] \times 10^{-2} \text{ S/m}$ at 25°C). In the case of the glass beads, the conductivity of the fluid slowly increased to $1.48 \times 10^{-2} \text{ S/m}$, $1.38 \times 10^{-2} \text{ S/m}$, and $1.33 \times 10^{-2} \text{ S/m}$ for 0.5, 1, and 2 mm diameter beads, respectively, while being circulated through the sample for 24 hours before the electrical and electrokinetic measurements were made. This amounts to an increase of concentration from $1 \times 10^{-3} \text{ mol/L}$ to $1.23 \times 10^{-3} \text{ mol/L}$, $1.15 \times 10^{-3} \text{ mol/L}$, and $1.10 \times 10^{-3} \text{ mol/L}$, respectively, which we associate with dissolution of the grains during the attainment of physico-chemical equilibrium between the grains and the fluid. For the Ottawa sand experiment, the pH of the fluid during the measurement was pH 6. In the case of the glass beads, the initial pH of the fluid was pH 6.9, which reduced during the recirculation of the fluids. The pH of the fluid was measured on samples of fluid emerging from the apparatus during the electrokinetic experiment. The stable values were pH 6.4, 6.6, and 6.7 for the 0.5, 1, and 2 mm diameter beads, respectively. We note again that the changes in the fluid conductivity and pH are not as great as some authors have experienced (e.g., Leroy et al. [30]), and we associate this with the repeated washings that we subjected the material to initially. However, we note later that modelling of the steady-state streaming potential coupling coefficient is extremely sensitive to the fluid conductivity and the pH. Hence it is extremely important for these parameters to be measured on the fluid emerging from the experimental apparatus during the electrokinetic measurement.

3.2. Experimental Methodology. The cell was loaded with either a sample of sand or beads in layers of 1 cm with light tamping between the layers in the case of the sand, and with agitation after each layer in the case of the glass beads.

TABLE 1: Physical properties of the sample material.

Property	Unit	Glass beads			Comment
		0.5 mm	1 mm	2 mm	
Modal grain radius (laser diffraction), r_g	μm	—	—	—	Using a Malvern Mastersizer 2000.
Modal grain radius (image analysis), r_g	μm	249 ± 2.32	492 ± 11	995 ± 7	Image analysis using Sigma Scan 4.
Modal grain radius (Hg injection), r_g	μm	—	—	—	Calculated from pressure data using Mayer-Stowe theory.
D10 grain radius (sieving), r_g	μm	251.1 ± 0.200	493 ± 0.838	989.6 ± 0.989	
Effective pore radius, r_p	μm	67.6 ± 16.2	139 ± 3.41	287 ± 4.03	Using the method of Glover and Walker [12].
Effective pore throat radius, r_{pt}	μm	40.7 ± 9.0	84 ± 2.06	173 ± 2.43	Using Glover and D�ery [17], for random packing.
Modal pore throat radius (Hg injection), r_{pt}	μm	38.5 ± 7.5	—	—	Using a Micromeritics AutoPore IV
Porosity (gravimetry)	—	0.314	0.383	0.382	Please see text.
Porosity (helium expansion)	—	0.325	0.391	0.385	Using a real gas expansion pycnometer.
Porosity (mercury injection)	—	0.304	—	—	Using a Micromeritics AutoPore IV.
Measured permeability, κ_{meas}	m^2	1.19×10^{-10}	5.95×10^{-10}	27.2×10^{-10}	The measured permeability at 5 Hz for the Ottawa sand and under steady-state conditions for the glass beads.
Predicted permeability using the RGPZ method, κ_{RGPZ}	m^2	1.22×10^{-10}	5.80×10^{-10}	24.8×10^{-10}	Permeability predicted from electrical data and the grain diameter using the method of Glover et al. [26].
Electrical conductivity, σ	S/m	2.63×10^{-3}	3.33×10^{-3}	3.32×10^{-3}	For a 0.001 mol/L NaCl at 25�C.
Electrical conductivity of the fluid, σ_f	S/m	1.23×10^{-2}	1.38×10^{-2}	1.33×10^{-2}	Measured on the recycled fluid at the sample outlet after equilibration.
Formation factor, F	—	4.676	4.13	4.16	Calculated from the conductivities of the saturated rock and the saturating fluid.
Connectedness, G	—	0.214	0.242	0.241	Calculated from the formation factor [33, 34].
Cementation exponent, m	—	1.372	1.48	1.48	Calculated from the formation factor.
Electrical tortuosity, τ_e	—	1.519	1.583	1.589	Calculated from the porosity and m .
Theta factor, Θ	—	3.705	3.53	3.57	From the method of [12].
Predicted transition frequency, ω_t	Hz	256.48	213.36	57.32	At 24�C using the method of [19].

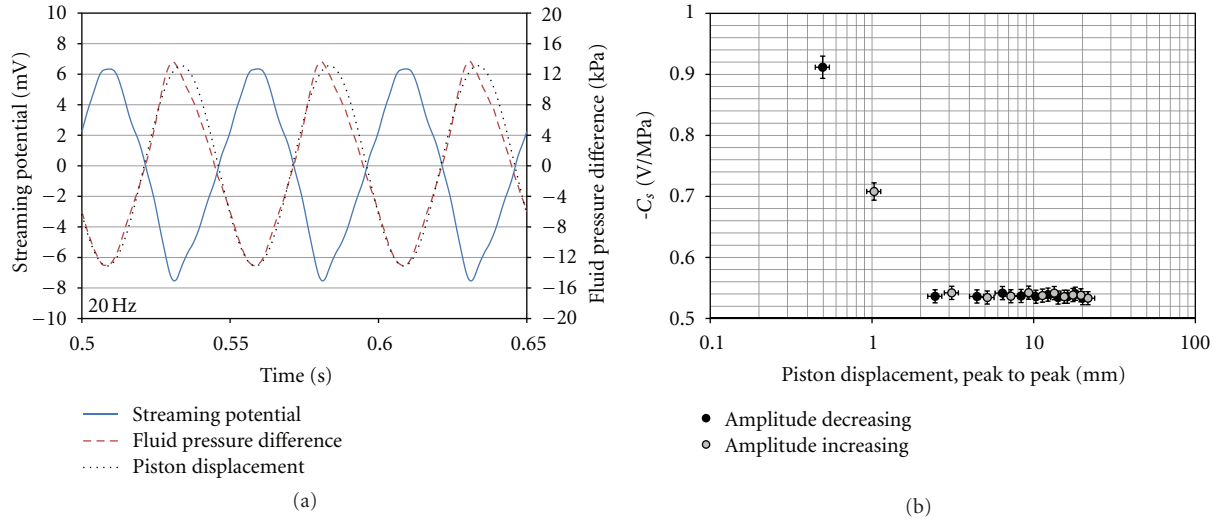


FIGURE 1: (a) The measured waveforms (streaming potential, fluid pressure and piston position (LVDT)) at 20 Hz. (b) The calculated streaming potential coupling coefficient as a function of piston amplitude at 10 Hz for Ottawa sand saturated with 10^{-3} mol/L NaCl solution at 24°C ($\phi = 0.325$, $\kappa_{10} = 1.19 \times 10^{-10} \text{ m}^2$). The errors in the frequency were calculated from the analysis of a train of approximately 500 cycles, while the errors in the streaming potential coupling coefficient were calculated from the errors in the RMS streaming potential and the measured RMS pressure difference (500 cycles).

The system was fully saturated with the process fluid, using back-pressure where necessary to remove all air bubbles. Once saturated, the steady-state permeability of the glass beads was measured using gravity-driven flow. The process fluid was then recycled through the sample for 24 hours to ensure full physicochemical equilibrium. During this time the permeability of the Ottawa sand was measured at a frequency of 10 Hz using the pressure transducers and calculating the flow by measuring the piston displacement with the LVDT.

Figure 1 shows the typical measured waveforms for 20 Hz, noting that there is a tendency that higher frequencies provide better-quality waveforms. High-quality measurements were possible between 5 and 200 Hz for the Ottawa sand and between 10 Hz and 500 Hz for the glass bead packs. Both the streaming potential and the dynamic pressure can be measured with acceptable levels of noise. Figure 1(a) shows that the fluid pressure and piston displacement are in phase with each other and in antiphase with the streaming potential, as theory requires. The compressive part of each cycle is sinusoidal as expected, whereas the backstroke is slightly distorted due to the inflow for new fluid through the check valve. This slight asymmetry might be corrected using digital filtering of the measured data or by imposing a background DC fluid flow and a back-pressure instead of using check valves. This latter approach would also remove any tendency for the fluid to cavitate.

In the case of Ottawa sand, tests were made up to 600 Hz, when the sample tube failed. It was observed that the seal between the piston and the tube let in air at frequencies higher than 200 Hz. Although the data for frequencies greater than 200 Hz seem to behave well, we have not reported them because the presence of air bubbles may make the measurements unreliable. We corrected the air leakage for the

glass bead pack measurements simply by lubricating the piston seal.

This paper contains results for three diameters of glass bead (0.5, 1, and 2 mm). We also attempted to make measurements on glass bead packs with a 0.25 mm and 3.35 mm nominal diameter. Unfortunately we could not generate sufficient pressure to produce a streaming potential of sufficient size to measure the 3.35 mm beads with accuracy, and the experiment with the 0.25 mm beads did not provide data of sufficient quality to report.

The frequency-dependent streaming potential coefficients were calculated using the methods described in Reppert et al. [9] and Reppert and Morgan [5], the most important step being the renormalisation of the data taking into account of the frequency-dependent impedance of the sample and measuring circuit, which is shown for each sample at each of the measurement frequencies in Figure 2. This procedure ensures that the streaming potential coefficient is calculated with the correct sample conductivity, that is, that which relates to the frequency of the data. Without such a step, the data seem to fit better the vibrational mechanics models, as was erroneously reported by us in [11]. Inclusion of the correction results in the data fitting the Pride model [23] better than the other models. This is a satisfying result as the Pride model was specifically conceived for porous media.

3.3. Displacement Tests. One of the characteristics of an electromagnetic shaker is that the piston amplitude decreases with frequency for any set driving current [1]. However, the differential fluid pressure generated by the piston increases with frequency [1]. If the driving current is kept constant throughout a suite of tests at different frequencies, the combination of these two effects is to generate smaller

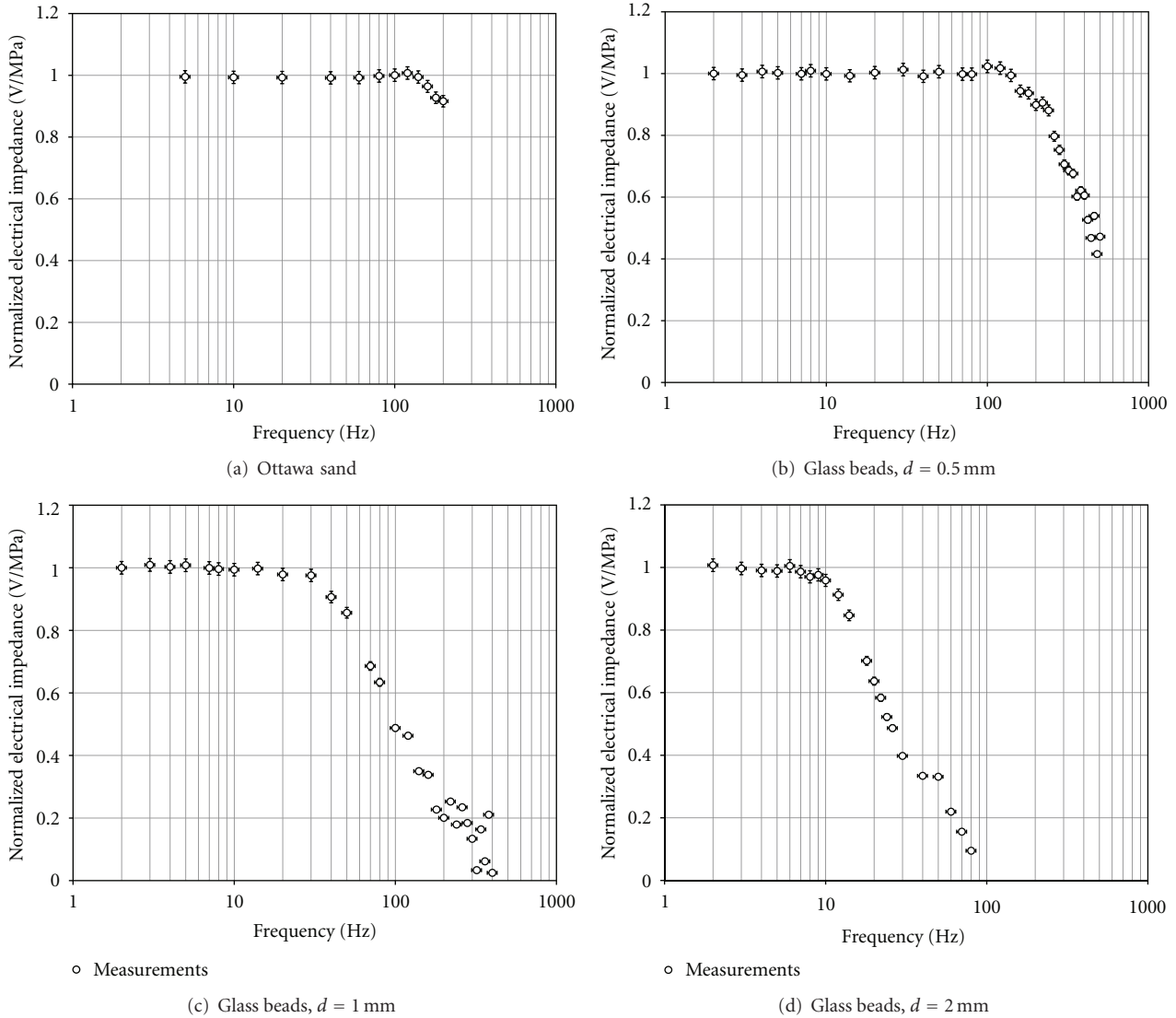


FIGURE 2: Normalised electrical impedance data for (a) Ottawa sand, and glass beads with (b) $d = 0.5$ mm, (c) $d = 1$ mm, and (d) $d = 2$ mm.

differential fluid pressures at high frequencies, lowering the signal-to-noise ratio. One solution to this problem is to vary the drive current in order to generate a differential fluid pressure that can be measured with good signal-to-noise ratio and to keep that differential pressure constant for as great a range of frequencies as possible. Such a procedure implies that the piston amplitude will be different for each frequency. Current understanding of frequency-dependent streaming potentials does not indicate that there is a piston amplitude below which the coupling is not fully developed or any other reason why the streaming potential coupling coefficient should vary with piston amplitude. However, it is important experimentally to know if we will introduce any systematic errors by allowing the piston amplitude to vary and also to know if there is a piston amplitude below which measurements become unreliable due to the signal-to-noise ratio.

We have carried out tests to examine the measured streaming potential as a function of the piston amplitude using a sample of the Ottawa sand and an arbitrary frequency of 10 Hz. Dynamic fluid pressure, dynamic streaming potential, and instantaneous piston position measurements were made while decreasing the shaker driving current in increments (and hence the piston amplitude) until the measured values were below the noise threshold. Measurements were then made while incrementally increasing the driving current until the maximum displacement was reached.

The results are shown in Figure 1(b). The initial peak-to-peak displacement was just over 20 mm, and this decreased incrementally until it was 0.5 mm, then increased again to a maximum about 21.7 mm. In the range about 2 mm to 21.7 mm, the measured streaming potential and the calculated streaming potential coupling coefficient remained stable with $C_s = 0.5374 \pm 0.0029$ V/MPa, which represents a

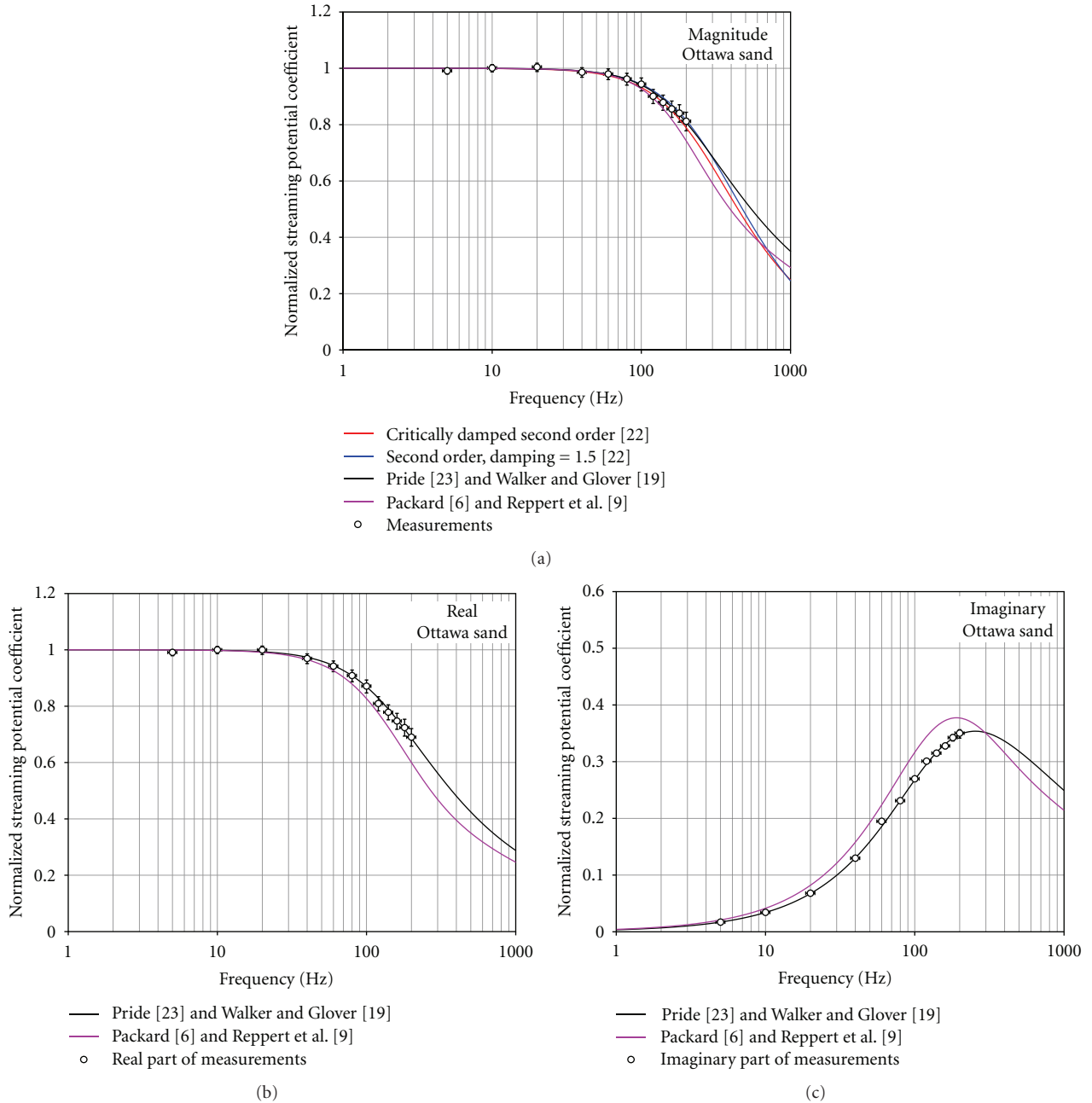


FIGURE 3: The calculated streaming potential coupling coefficient (normalised to the value at 5 Hz, which was 0.518 V/MPa) as a function of frequency for Ottawa sand saturated with 10^{-3} mol/L NaCl solution at 24°C ($\phi = 0.325$, $\kappa_{10} = 1.19 \times 10^{-10}$ m²). (a) Magnitude with six models fitting the data [6, 9, 19, 22, 23], (b) real component for models [6, 9, 19, 23], and (c) imaginary component for models [6, 9, 19, 23].

variability of about 0.5%. The values during reduction and augmentation of piston displacement were $C_s = 0.5369 \pm 0.0026$ V/MPa and 0.5379 ± 0.0032 V/MPa, respectively, so there is no sensitivity to whether the piston amplitude is increasing or decreasing. We can remark, therefore, that in the range 2 mm to 21.7 mm the streaming potential and the calculated streaming potential coupling coefficient measured by this instrument are independent of piston amplitude and direction of piston amplitude change. Hence the piston

amplitude may be varied to optimize the measurement conditions.

The measured streaming potential was affected at piston amplitude less than about 2 mm. Under these conditions the measured pressure difference is very small for our high permeability sample, and it is difficult to distinguish the measurements from the background noise. We believe that the observed increase in the streaming potential coupling coefficient for displacements less than 2 mm is due to the

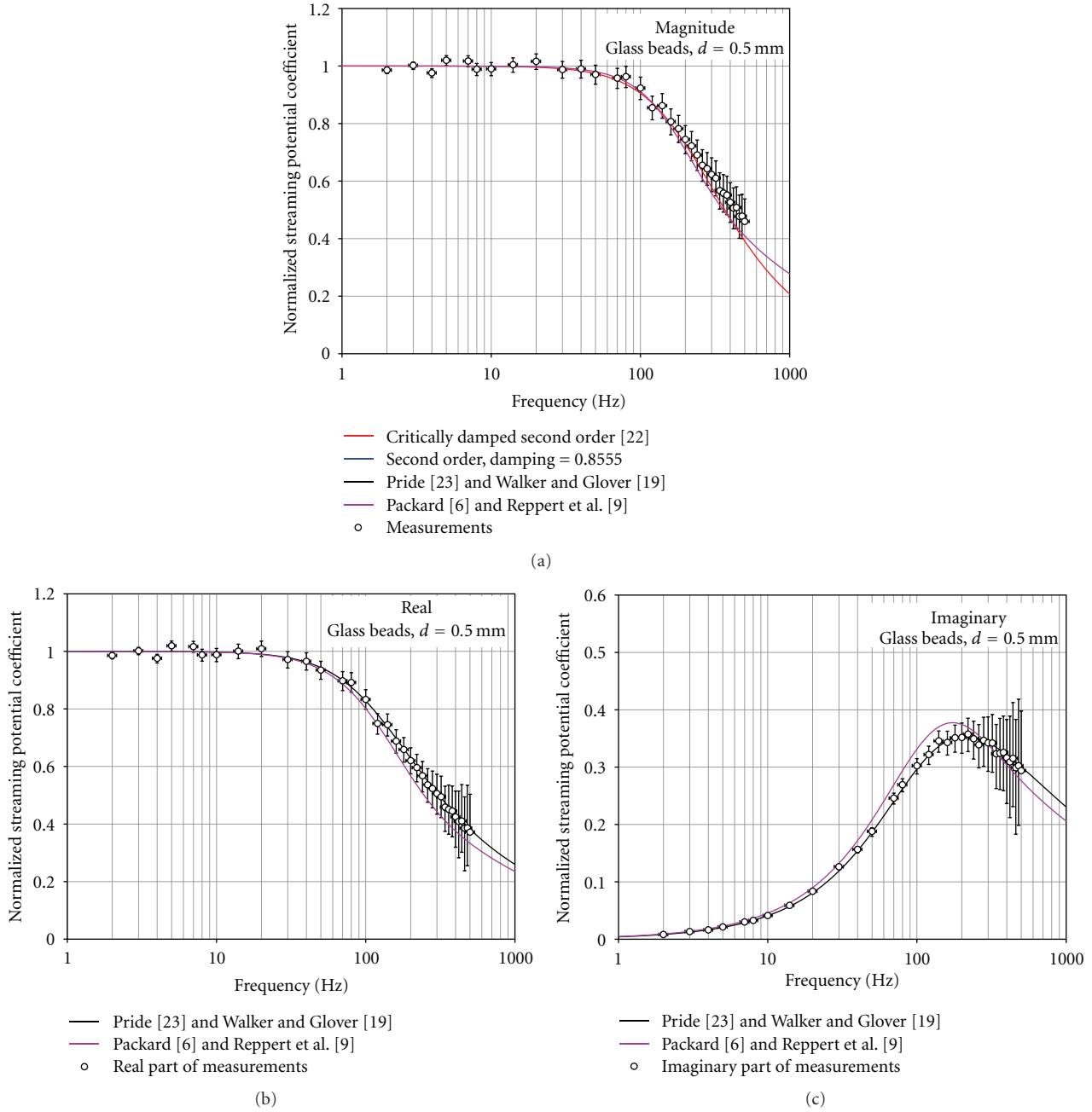


FIGURE 4: The calculated streaming potential coupling coefficient (normalised to the value at 2 Hz, which was 1.37 V/MPa) as a function of frequency for a pack of nominally 0.5 mm diameter glass beads saturated with 10^{-3} mol/L NaCl solution at 24°C ($\phi = 0.383$, $\kappa_{\text{DC}} = 1.62 \times 10^{-10} \text{ m}^2$). (a) Magnitude with six models shown fitting the data [6, 9, 19, 22, 23], (b) real component for models [6, 9, 19, 23], and (c) imaginary component for models [6, 9, 19, 23].

difficulty in measuring these small pressures. There was no evidence for turbulent fluid flow at large piston amplitudes.

3.4. Initial Frequency-Dependent Streaming Potential Coupling Coefficient Results. Figures 3, 4, 5 and 6 show the normalised measured streaming potential coupling coefficient for Ottawa sand and the three grades of glass bead as a function of frequency. The normalised streaming potential coup-

ling coefficient was calculated by dividing the measured streaming potential coupling coefficient at a given frequency by that measured at the lowest frequency available (5 Hz for Ottawa sand and 2 Hz for the glass beads). If one can assume that the streaming potential coupling coefficient at this low frequency approximates to that during steady-state flow, it is possible to say that the data shown in Figures 3–6 represent the right-hand side of (2), (3), (4), (11) and (14), that is, the frequency-dependent terms.

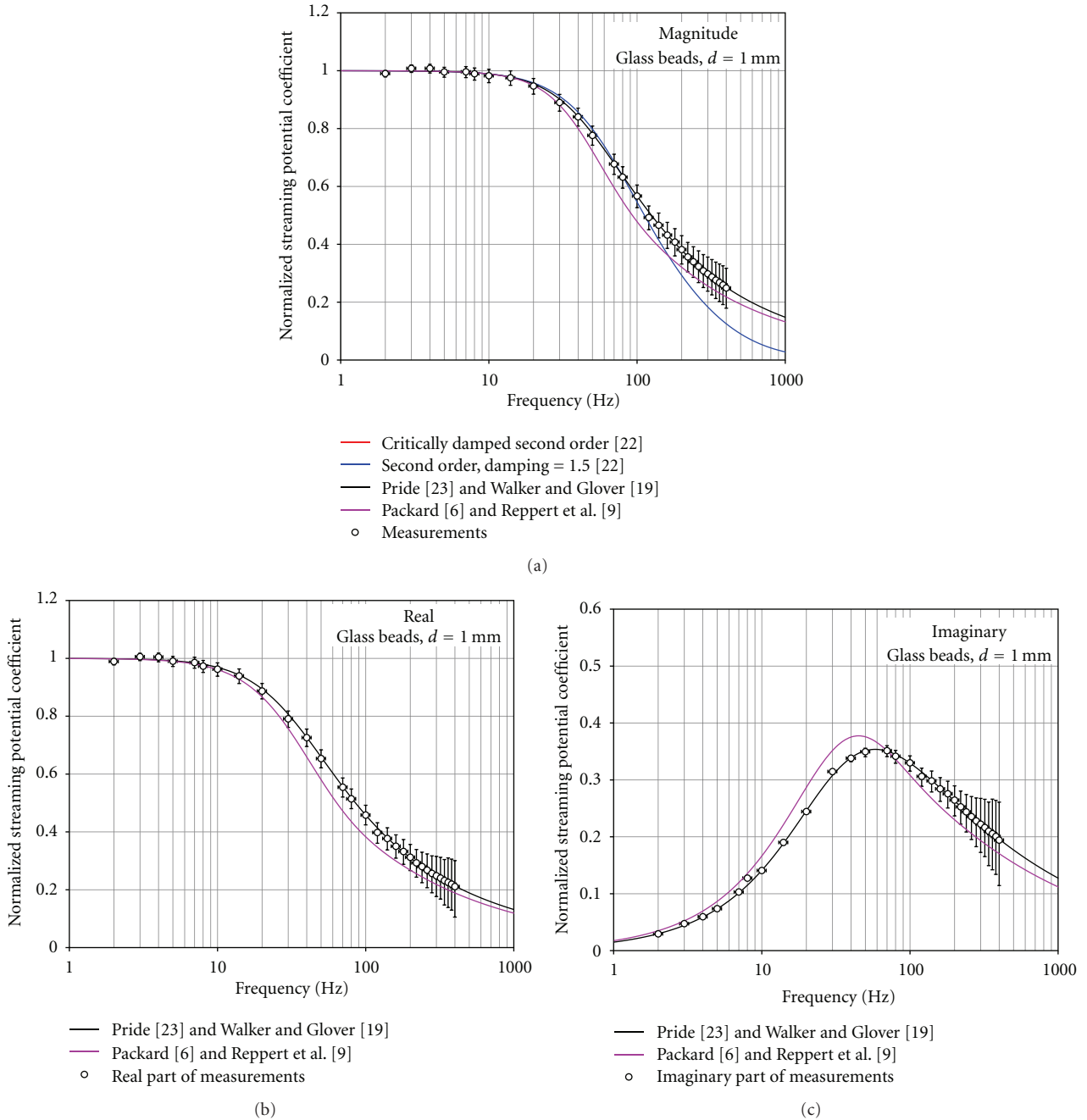


FIGURE 5: The calculated streaming potential coupling coefficient (normalised to the value at 2 Hz, which was 1.61 V/MPa) as a function of frequency for a pack of nominally 1 mm diameter glass beads saturated with 10^{-3} mol/L NaCl solution at 24°C ($\phi = 0.38$, $\kappa_{\text{DC}} = 5.95 \times 10^{-10} \text{ m}^2$). (a) Magnitude with six models shown fitting the data [6, 9, 19, 22, 23], (b) real component for models [6, 9, 19, 23], and (c) imaginary component for models [6, 9, 19, 23].

It should be noted in these figures that the error bars become larger at the higher frequencies. This is due to the difficulty in measuring small streaming potentials at frequencies greater than the transition frequency.

4. Analysis and Modelling of the Experimental Results

4.1. Steady-State Streaming Potential Coupling Coefficient. The majority of the data analysis will concentrate on the fre-

quency-dependent part of the streaming potential coupling coefficient. However, we should say a few words about the steady state streaming potential coupling coefficient. Although this was not measured in our apparatus, we can perhaps use the streaming potential coupling coefficient at the lowest frequency as a reasonable indication of that under true steady-state conditions considering that Figures 3–6 show that these values tend towards the steady-state value. The lowest frequency for the Ottawa sand was 5 Hz while those for the glass beads was 2 Hz. We will call the

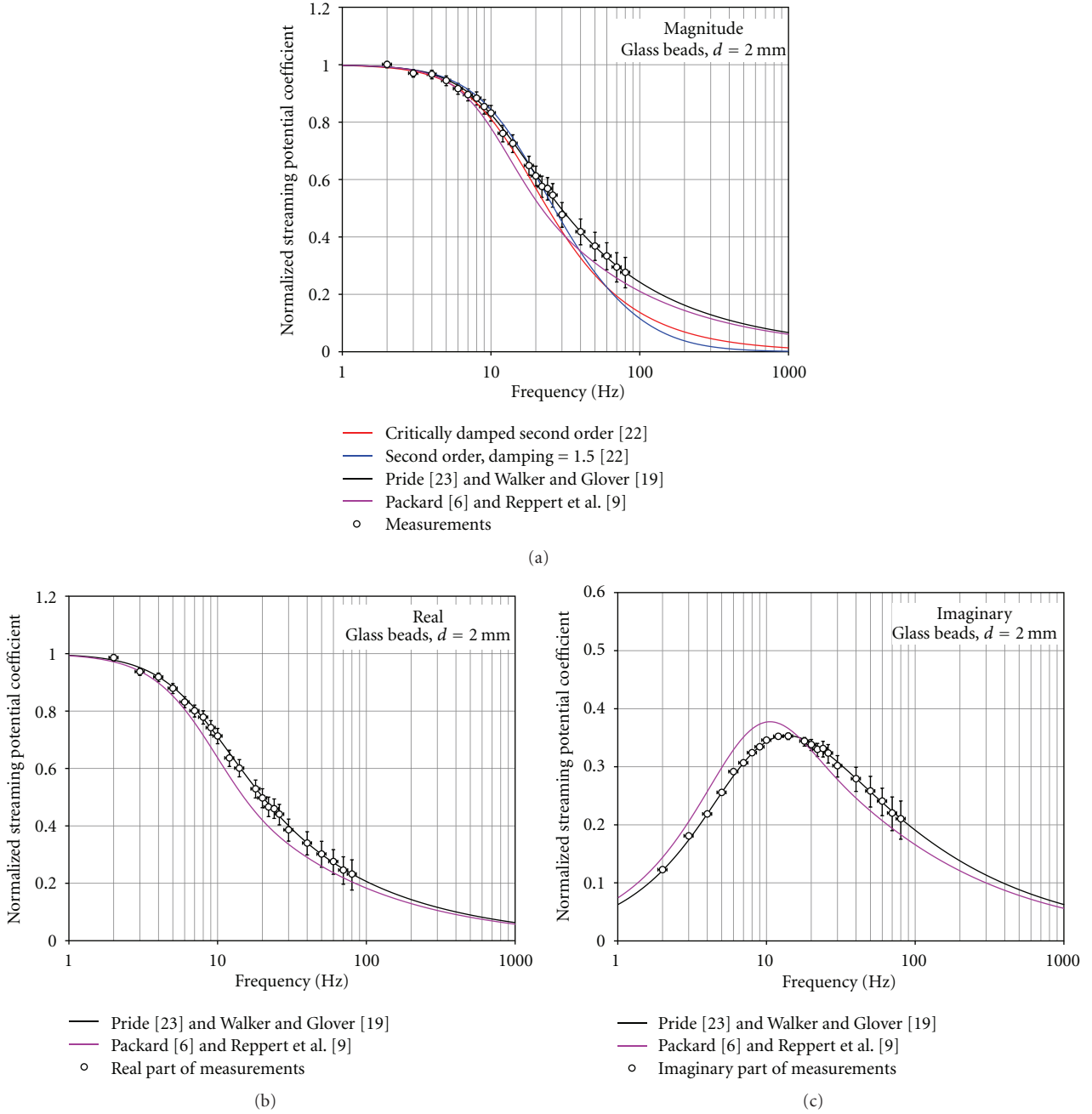


FIGURE 6: The calculated streaming potential coupling coefficient (normalised to the value at 2 Hz, which was 1.80 V/MPa) as a function of frequency for a pack of nominally 2 mm diameter glass beads saturated with 10^{-3} mol/L NaCl solution at 24°C ($\phi = 0.382$, $\kappa_{\text{DC}} = 27.2 \times 10^{-10} \text{ m}^2$). (a) Magnitude with six models shown fitting the data [6, 9, 19, 22, 23], (b) real component for models [6, 9, 19, 23], and (c) imaginary component for models [6, 9, 19, 23].

streaming potential coupling coefficients at these frequencies the quasi-steady-state values. The quasi-steady-state values of the streaming potential coupling coefficient for each of the samples are shown in Table 2. This table also shows some electrokinetic modelling that we have carried out using the same approach as Glover and D ery [17] and Glover et al. [16]. In this modelling we kept the following parameters constant: $\Gamma_o = 5 \text{ sites/nm}^2$, $\text{pK}_{\text{me}} = 7.5$, $\text{pK}_- = 8$, while the formation factor, porosity, cementation exponent, grain

diameter fluid concentration, and pH were set to the values related to each sample (Table 1). It can be seen from Table 2 that the modelled values of the steady-state streaming potential coupling coefficient slightly overestimate the measured values. We need to put the measured and modelled values in the context of the measurements made by others and the experimental errors. Figure 7 shows the measured values and the model curves in the context of a database of other steady-state streaming potential coupling coefficient measurements

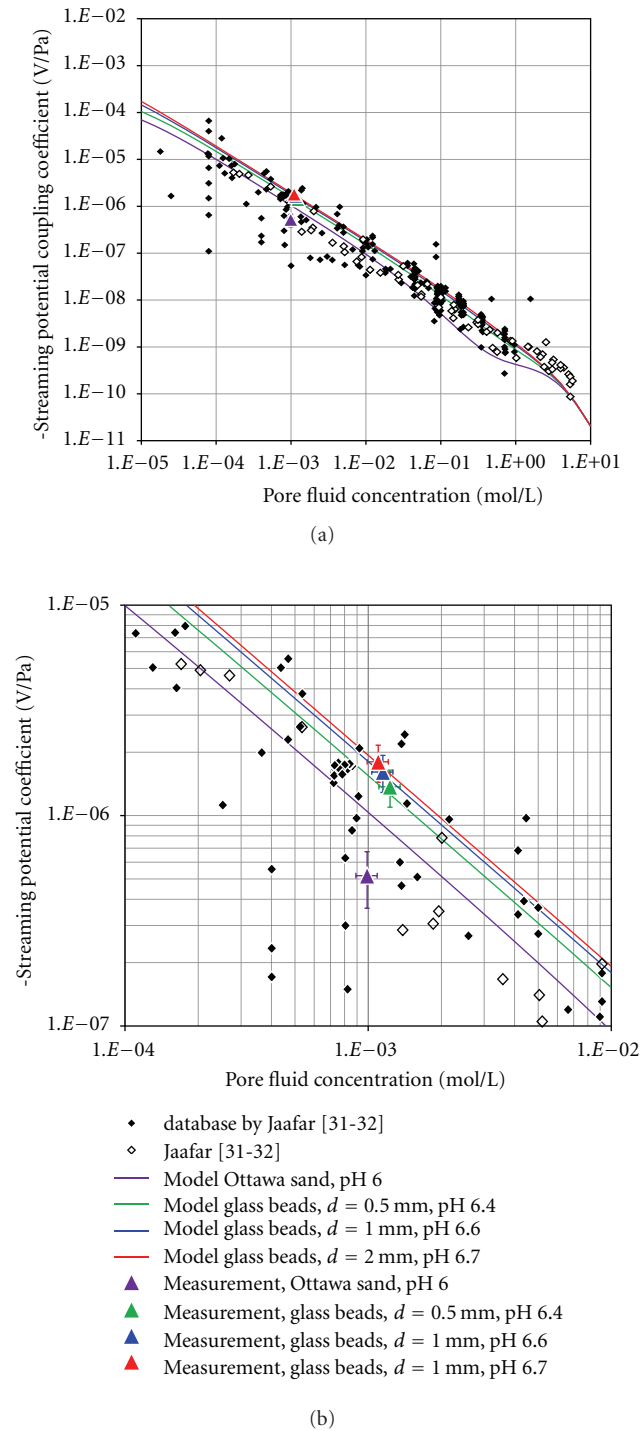


FIGURE 7: (a) The steady-state streaming potential coupling coefficient measured in this work shown with a compilation of silica-based earth materials measured by (open symbols) or compiled by (solid symbols) Jaafar [31, 32]. The lines represent the theoretically modelled streaming potential coupling coefficient using the method of Glover et al. [16] and Glover and Déry [17] and with the parameters $\Gamma_o = 5$ sites/nm², $pK_{me} = 7.5$, $pK_- = 8$, and $T = 24.0^\circ\text{C}$, with the porosity, cementation exponent, grain size, and pH for the individual samples (given in Table 1). (b) The same diagram as (a) on an expanded scale.

(from [31, 32]). It should be noted that the experimental values are plotted here at the fluid concentrations calculated from the fluid electrical conductivity that was measured on the fluid leaving the apparatus during the experiment rather than that of the original stock fluid, which was 0.001 mol/L. The error bars are approximate and represent a conservative assessment of the measurement errors (30% for the streaming potential coupling coefficient and 10% for the pore fluid concentration). It can be seen that the measured values are in fact in extremely good agreement with the existing data and the model. The model is extremely sensitive to the values of fluid concentration and pH used, and hence it is extremely important to have an accurate measurement of the pH value and the electrical conductivity of the fluid that emerges from the experimental apparatus during the experiment in order that the measurements can be compared with the model at an acceptable level of precision.

4.2. Frequency-Dependent Streaming Potential Coupling Coefficient. Figures 3–6 show the experimental data together with theoretical curves that (i) are based on standard equations in vibration mechanics, for example, [22], (ii) have been developed for capillary tubes [6, 9], and (iii) have been derived for porous media [19, 23]. In each figure there are three parts. The first shows the behaviour of the magnitude (absolute value, modulus) of the complex variable, while the other two parts show the real and imaginary components of the complex variable. The vibrational mechanics models [22], the Pride model [23], and its simplification [19] may all be fitted to the data to obtain the transition frequency ω_t , from which the characteristic pore radius of the sand can be calculated using (13), while the Packard model [6] and its simplification [9] may be used to obtain the effective capillary radius of the sand directly. A single curve is included for the Packard capillary tube model [6] and the Reppert et al. simplification [9] because they are indistinguishable at the scale of the figures and which indicates that the corrected Reppert et al. simplification (i.e., (8)) performs extremely well. The Pride model [23] and its simplification by Walker and Glover [19] are also represented by a single curve for the same reason.

Figures 3–6 show that all of the models describe the data fairly well. However, the following discussion shows that some of these fits do not use parameters that are consistent with other physical properties of the samples. The best fit for all the samples is provided by the Pride model [23] and its Walker and Glover simplification [19]. These models are specifically designed for porous media but do not implicitly take into account the surface conduction that occurs naturally in geological porous media. In fitting this model, we used the independently measured quasi-steady-state permeability k_{DC} , the electrical tortuosity τ_e that was calculated from the electrical impedance measurements, and the porosity by helium pycnometry ϕ , all of which are given in Table 1. The fitting variables were the transition frequency and the characteristic length scale of the pore space Λ . The values of the fitting variables are given in Table 2. The transition frequency can be used to derive an effective

TABLE 2: Summary of results.

Property	Unit	Glass beads			Comment
		Ottawa sand	0.5 mm	1 mm	
Steady-state electrokinetic modelling					
Measured steady-state streaming potential coupling coefficient, C_{so}	V/MPa	0.518 ± 0.155	1.37 ± 0.411	1.61 ± 0.483	1.80 ± 0.54
Modelled steady-state streaming potential coupling coefficient, C_{so}	V/MPa	1.05	1.26	1.57	1.76
Modelled zeta potential, ζ	mV	-15.9	-29.6	-29.6	-29.6
pH for electrokinetic modelling	—	6	6.7	6.7	6.7
Transition frequencies					
Transition frequency, critically damped 2nd order vibrational model, ω_t	Hz	230	234	54	13
Transition frequency, 2nd order model with variable damping, ω_t	Hz	748.8	636.9	176.4	41.7
Damping factor, ξ	—	1.5	1.5	1.5	1.5
Transition frequency from the Pride model, ω_t	Hz	256.58	213	58.79	13.85
Transition frequency from the Glover and Walker simplification, ω_t	Hz	256.58	213.36	57.32	12.61
Predicted effective pore radius					
Calculated effective pore radius from independent measurement, r_p	μm	67.6 ± 16.2	70.8 ± 0.70	139 ± 3.41	287 ± 4.03
From the Packard model, equivalent capillary tube radius, r_{eff}	μm	67.5	72	145	302
From the critically damped 2nd order vibrational model	μm	70.46	69.85	145.41	296.35
From the Pride model	μm	66.71	73.21	139.36	287.11
From the Glover and Walker simplification	μm	66.71	73.15	141.13	300.90
Characteristic length scale, Λ	μm	62.40	67.76	131.45	280.24
Predicted permeabilities					
Measured permeability, κ_{meas}	m^2	1.19×10^{-10}	1.62×10^{-10}	5.95×10^{-10}	27.2×10^{-10}
Predicted permeability using the RGPZ method, κ_{RGPZ}	m^2	1.22×10^{-10}	1.52×10^{-10}	5.80×10^{-10}	24.8×10^{-10}
From the critically damped 2nd order vibrational model	m^2	1.33×10^{-10}	1.48×10^{-10}	6.32×10^{-10}	26.4×10^{-10}
From the Pride model	m^2	1.19×10^{-10}	1.62×10^{-10}	5.80×10^{-10}	24.8×10^{-10}
From the Glover and Walker simplification	m^2	1.19×10^{-10}	1.62×10^{-10}	5.95×10^{-10}	27.2×10^{-10}

pore size for the sample r_{eff} using (13), which is also given in Table 2. When this is done, it is clear that both Λ and r_{eff} agree well with the independently obtained pore size of the sample r_p (Tables 1 and 2). We conclude that the Pride model and its simplification perform extremely well when compared to experimental data.

While not as effective as the Pride model and its simplification, the Packard model [6] and its Reppert et al. simplification [9] also provide a fairly good fit to the data. However, the discrepancies between these models and the data clearly show that a model which is based on a bundle of capillary tubes is not as effective as the Pride model in describing a porous medium when the fluid flow and electrical flow have a tortuosity which is significantly different from unity such as in our samples where the electrical tortuosity is approximately 1.5 (see Table 1). Many rocks have tortuosities much higher than this. Hence, one would expect the Packard model and Reppert et al. models to perform worse for these rocks, overestimating the effective capillary radius and hence the predicted permeability of the sample. The advantage with these models is that when used with a single pore fluid at a constant temperature and pressure, they use a single variable: the effective capillary radius, which is shown in Table 2 for comparison with the independently measured value r_p .

The critically damped second-order vibrational mechanics model also provides a reasonable fit to the data, giving transition frequencies and effective pore radii that are consistent with the independently obtained measurements (Table 2). However, the variably damped second-order vibrational mechanics model has difficulty fitting the data. Here there are two fitting parameters, the transition frequency and the damping coefficient. A large number of different combinations of these parameters provide curves that seem to fit the experimental data approximately. Figures 3–6 show one particular combination where the damping coefficient $\xi = 1.5$ and the transition frequencies are given in Table 2. The transition frequencies are clearly much too large and predict effective pore radii that are badly underestimated. Increasing the damping coefficient further allows the frequency roll-off to approach the experimental data, but only at the expense of even higher predicted transition frequencies. We conclude, therefore, that this model is of no practical use when describing frequency-dependent streaming potential coefficients of porous media.

4.3. Sensitivity of the Pride Model to Steady-State Permeability.

The full Pride model calculates the transition frequency from the sample porosity, electrical tortuosity, and permeability as well as the density and viscosity of the pore fluid (9). It also calculates a parameter which we have called m^* (10) from the porosity, characteristic length scale of the pores Λ , the electrical tortuosity, and the permeability of the sample. It became clear in our modelling that the fit to the experimental data depends strongly on the value of m^* , which in turn depends upon the steady-state permeability of the rock k_{DC} , its electrical tortuosity τ_e , and its porosity ϕ as well as the characteristic length scale of its pores Λ . While τ_e , ϕ , and Λ vary from sample to sample, they can

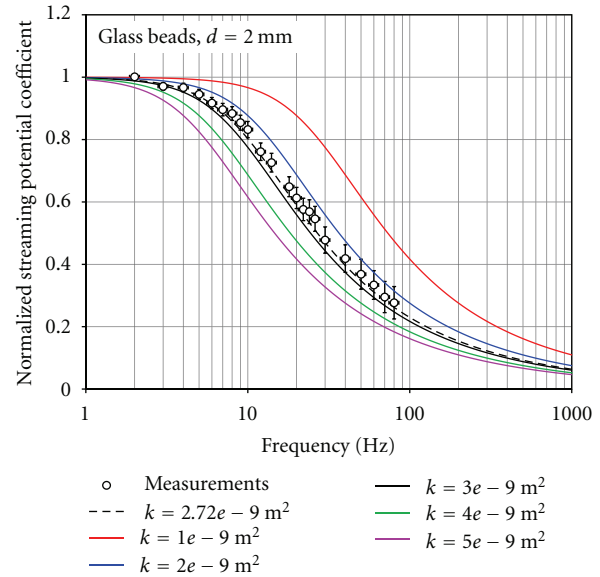


FIGURE 8: The calculated streaming potential coupling coefficient (normalised to the value at 2 Hz, which was 1.80 V/MPa) as a function of frequency using the Pride model [23] for a pack of nominally 2 mm diameter glass beads saturated with 10^{-3} mol/L NaCl solution at 24°C ($\phi = 0.382$, $\kappa_{\text{DC}} = 27.2 \times 10^{-10} \text{ m}^2$). Each solid curve shows the results of the model for a different value of permeability. The dashed line is for the permeability of the sample that was measured independently.

be measured independently. This is also true of the steady-state permeability of the rock. However, the steady-state permeability of the rock can vary over many orders of magnitude which makes the Pride model extremely sensitive to this parameter. Figure 8 shows the Pride model for a range of different permeabilities from $1 \times 10^{-9} \text{ m}^2$ to $5 \times 10^{-9} \text{ m}^2$ and the other parameters matching those for our 2 mm glass bead dataset. It is worthwhile noting that this is a very small permeability range considering (i) the precision that is usual when measuring permeability in the laboratory and (ii) the natural variability of permeability from sample to sample even in isotropic, homogeneous clean reservoir rocks. While this sensitivity might be considered to be a problem when forward modelling, it is a huge advantage when backward modelling as it should allow the predicted permeability to have a very high precision. Hence, although these measurements are currently difficult to make, they have the potential of providing an extremely precise method of obtaining the permeability of porous media.

4.4. Transition Frequencies and Pore Sizes. The transition frequencies and capillary radii calculated from each of the 5 models are given in Table 2. All of the transition frequencies, except those from the second order vibrational mechanics model with variable damping, are in broad agreement and vary according to the pore size of the sample. Figure 9 shows all the existing data as compiled by Tardif et al. [11] together with the Ottawa sand data of [11] and the new glass bead data presented in this paper. The dashed lines represent the

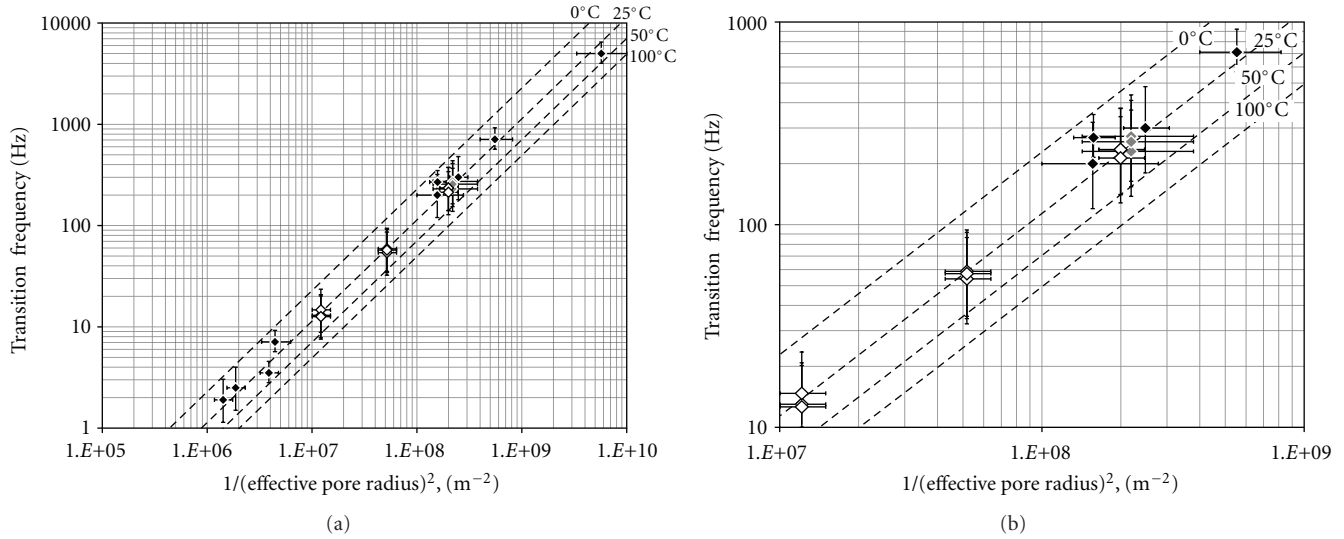


FIGURE 9: The electrokinetic transition frequency as a function of the inverse square characteristic pore size (a) in full and (b) at expanded scale. Black symbols, previous data for capillary tubes, filters frits, and rocks, Figure 6 of [19]; grey symbols, Ottawa sand measured at $24.0^\circ\text{C} \pm 0.8^\circ\text{C}$; open symbols, glass bead packs. The dashed lines represent the theoretical result [19] at four different temperatures.

result of (13) [19] using the fluid viscosities and densities for the pore fluid at various different temperatures. It is clear that the new data are compatible with the independently obtained effective pore radius measurements.

The transition frequency can be used to predict the effective pore radius of each sample using (13). Table 2 shows that all the predictions are in good agreement with the value of effective pore radius derived from the measured grain diameter using the method of Glover and Walker [12] and with the equivalent capillary radius derived from the Packard model [6].

The transition frequency can be used to predict the steady-state permeability of the sample using (13). Table 2 shows that all the predictions are in good agreement with the measured values of permeability and the permeability predicted using the RGPZ method [26]. It should be noted that the predictions for the porous media models [19, 23] are exact because the permeability is an input to these models. Hence, these models can only be used to predict permeability if they are fitted to the experimental data with the permeability as a variable parameter.

5. Conclusions

We have used the electromagnetic drive approach to create an experimental apparatus to measure the dynamic streaming potential coupling coefficient of disaggregated porous media between 1 Hz and 1 kHz. The apparatus has been used to measure samples of Ottawa sand and glass bead packs. Measurements were made on Ottawa sand between 5 Hz and 200 Hz, and on glass bead packs between 2 Hz and 500 Hz. In most cases the full variation either side of the transition frequency was captured. Measurements were possible up to

1 kHz, but in practice the streaming potential values became so small at high frequencies that they were unreliable; only those with reasonably small errors have been included in this paper.

Analysis of the steady-state part of the measured data, shows that the measured steady-state streaming potential coupling coefficient is compatible with the latest theoretical models of electrokinetics.

The dynamic experimental data, in the form of normalised streaming potential coupling coefficient, have been fitted with five theoretical models that were derived (i) from vibrational mechanics theory, (ii) for bundles of capillary tubes, and (iii) for porous media. The Pride model and its simplification, which were developed for porous media, fitted the data best and provided transition frequencies, characteristic length scales, and effective pore radii that were consistent with independently measured values for the samples. The Packard model and its simplification, which were developed for capillary tubes, also performed well. The second order vibrational mechanics model with variable damping only fitted the data when unreasonable transition frequencies were used, but the critically damped second order vibrational model performed reasonably well.

We found that the Pride model and its simplification models are extremely sensitive to the steady-state permeability which may cause difficulties in forward modelling given that this parameter is rarely known precisely and that there is often a large range of permeabilities even in isotropic, homogeneous, clean reservoir rock. However, the sensitivity is an advantage in reverse modelling as it should allow precise permeability determinations to be made by fitting this model to experimental dynamic streaming potential coupling coefficient data.

Acknowledgments

This work has been made possible thanks to funding by the Natural Sciences and Engineering Research Council of Canada (NSERC) Discovery Grant Programme. The authors would also like to thank Guillaume Lalonde and the members of the mechanical engineering workshop for their help.

References

- [1] P. W. J. Glover, J. Ruel, and E. Tardif, "Frequency-dependent streaming potential of porous media: 1. Experimental approaches and apparatus design," *International Journal of Geophysics*. In press.
- [2] C. Bordes, L. Jouniaux, S. Garambois, M. Dietrich, J. P. Pozzi, and S. Gaffet, "Evidence of the theoretically predicted seismo-magnetic conversion," *Geophysical Journal International*, vol. 174, no. 2, pp. 489–504, 2008.
- [3] C. Bordes, L. Jouniaux, M. Dietrich, J. P. Pozzi, and S. Garambois, "First laboratory measurements of seismo-magnetic conversions in fluid-filled Fontainebleau sand," *Geophysical Research Letters*, vol. 33, no. 1, Article ID L01302, 2006.
- [4] R. Chandler, "Transient streaming potential measurements on fluid-saturated porous structures: an experimental verification of biot's slow wave in the quasi-static limit," *Journal of the Acoustical Society of America*, vol. 70, no. 1, pp. 116–121, 1981.
- [5] P. M. Reppert and F. D. Morgan, "Streaming potential collection and data processing techniques," *Journal of Colloid and Interface Science*, vol. 233, no. 2, pp. 348–355, 2001.
- [6] R. G. Packard, "Streaming potentials across glass capillaries for sinusoidal pressure," *The Journal of Chemical Physics*, vol. 21, no. 2, pp. 303–307, 1953.
- [7] C. E. Cooke, "Study of electrokinetic effects using sinusoidal pressure and voltage," *The Journal of Chemical Physics*, vol. 23, no. 12, pp. 2299–2303, 1955.
- [8] A. R. Sears and J. N. Groves, "The use of oscillating laminar flow streaming potential measurements to determine the zeta potential of a capillary surface," *Journal of Colloid and Interface Science*, vol. 65, no. 3, pp. 479–482, 1978.
- [9] P. M. Reppert, F. D. Morgan, D. P. Lesmes, and L. Jouniaux, "Frequency-dependent streaming potentials," *Journal of Colloid and Interface Science*, vol. 234, no. 1, pp. 194–203, 2001.
- [10] P. M. Reppert, *Electrokinetics in the earth*, Ph.D. thesis, Massachusetts Institute of Technology, 2000.
- [11] E. Tardif, P. W. J. Glover, and J. Ruel, "Frequency-dependent streaming potential of Ottawa sand," *Journal of Geophysical Research B*, vol. 116, no. 4, Article ID B04206, 2011.
- [12] P. W. J. Glover and E. Walker, "A grain-size to effective pore-size transformation derived from electrokinetic theory," *Geophysics*, vol. 74, no. 1, pp. E17–E29, 2009.
- [13] F. D. Morgan, E. R. Williams, and T. R. Madden, "Streaming potential properties of Westerly granite with applications," *Journal of Geophysical Research B*, vol. 94, no. 9, pp. 12449–12461, 1989.
- [14] P. M. Reppert and F. D. Morgan, "Temperature-dependent streaming potentials: 1. Theory," *Journal of Geophysical Research B*, vol. 108, no. 11, pp. 3–12, 2003.
- [15] P. M. Reppert and F. D. Morgan, "Temperature-dependent streaming potentials: 2. Laboratory," *Journal of Geophysical Research B*, vol. 108, no. 11, pp. 4–13, 2003.
- [16] P. W. J. Glover, E. Walker, and M. D. Jackson, "Streaming-potential coefficient of reservoir rock: A theoretical model," *Geophysics*, vol. 77, no. 2, pp. D17–D43, 2012.
- [17] P. W. J. Glover and N. Déry, "Streaming potential coupling coefficient of quartz glass bead packs: dependence on grain diameter, pore size, and pore throat radius," *Geophysics*, vol. 75, no. 6, pp. F225–F241, 2010.
- [18] D. L. Johnson, J. Koplik, and R. Dashen, "Theory of dynamic permeability and tortuosity in fluid-saturated porous media," *Journal of Fluid Mechanics*, vol. 176, pp. 379–402, 1987.
- [19] E. Walker and P. W. J. Glover, "Characteristic pore size, permeability and the electrokinetic coupling coefficient transition frequency in porous media," *Geophysics*, vol. 75, no. 6, pp. E235–E246, 2010.
- [20] A. Revil and L. M. Cathles III, "Permeability of shaly sands," *Water Resources Research*, vol. 35, no. 3, pp. 651–662, 1999.
- [21] A. Revil, P. A. Pezard, and P. W. J. Glover, "Streaming potential in porous media 1. Theory of the zeta potential," *Journal of Geophysical Research B*, vol. 104, no. 9, pp. 20021–20031, 1999.
- [22] W. T. Thomson and M. D. Dahleh, *Theory of Vibration with Applications*, Prentice Hall, 1998.
- [23] S. Pride, "Governing equations for the coupled electromagnetics and acoustics of porous media," *Physical Review B*, vol. 50, no. 21, pp. 15678–15696, 1994.
- [24] E. Charlaix, A. P. Kushnick, and J. P. Stokes, "Experimental study of dynamic permeability in porous media," *Physical Review Letters*, vol. 61, no. 14, pp. 1595–1598, 1988.
- [25] P. W. J. Glover and E. Walker, "Modelling the frequency dependence of hydraulic flow and streaming potential coupling coefficients in capillary bundles and porous rocks," in *Proceedings of the Annual Congress of European Geosciences Union*, paper A-02892, Vienna, Austria, April 2008.
- [26] P. W. J. Glover, I. I. Zadjali, and K. A. Frew, "Permeability prediction from MICP and NMR data using an electrokinetic approach," *Geophysics*, vol. 71, no. 4, pp. F49–F60, 2006.
- [27] S. N. Lvov and R. H. Wood, "Equation of state of aqueous NaCl solutions over a wide range of temperatures, pressures and concentrations," *Fluid Phase Equilibria*, vol. 60, no. 3, pp. 273–287, 1990.
- [28] S.L. Phillips, H. Ozbek, and R.J. Otto, "Basic energy properties of electrolytic solutions database," in *Proceedings of the 6th International CODATA Conference*, Santa Flavia, Italy, May 1978, <http://www.osti.gov/bridge/purl.cover.jsp;jsessionid=3954E775156A8BC0FA35DB5CE5B402D4?purl=/6269880-iPJPhB/DB5CE5B402D4?purl=/6269880-iPJPhB/>.
- [29] P. N. Sen and P. A. Goode, "Influence of temperature on electrical conductivity on shaly sands," *Geophysics*, vol. 57, no. 1, pp. 89–96, 1992.
- [30] P. Leroy, A. Revil, A. Kemna, P. Cosenza, and A. Ghorbani, "Complex conductivity of water-saturated packs of glass beads," *Journal of Colloid and Interface Science*, vol. 321, no. 1, pp. 103–117, 2008.
- [31] M. Z. Jaafar, J. Vinogradov, and M. D. Jackson, "Measurement of streaming potential coupling coefficient in sandstones saturated with high salinity NaCl brine," *Geophysical Research Letters*, vol. 36, no. 21, Article ID L21306, 2009.
- [32] J. Vinogradov, M. Z. Jaafar, and M. D. Jackson, "Measurement of streaming potential coupling coefficient in sandstones saturated with natural and artificial brines at high salinity," *Journal of Geophysical Research B*, vol. 115, no. 12, Article ID B12204, 2010.

- [33] P. W. J. Glover, "What is the cementation exponent? A new interpretation," *The Leading Edge*, vol. 28, no. 1, pp. 82–85, 2009.
- [34] P. W. J. Glover, "A generalized Archie's law for n phases," *Geophysics*, vol. 75, no. 6, pp. E247–E265, 2010.

Review Article

Electrokinetics in Earth Sciences: A Tutorial

L. Jouniaux¹ and T. Ishido²

¹*Institut de Physique du Globe de Strasbourg, Uds-CNRS UMR 7516, Université de Strasbourg, 5 rue René Descartes, 67084 Strasbourg, France*

²*Geological Survey of Japan, National Institute of Advanced Industrial Science and Technology (AIST), Tsukuba, Ibaraki 305-8567, Japan*

Correspondence should be addressed to L. Jouniaux, laurence.jouniaux@unistra.fr

Received 1 June 2011; Accepted 14 October 2011

Academic Editor: Rudolf A. Treumann

Copyright © 2012 L. Jouniaux and T. Ishido. This is an open access article distributed under the Creative Commons Attribution License, which permits unrestricted use, distribution, and reproduction in any medium, provided the original work is properly cited.

We describe in this paper the theoretical background for the electrokinetics in rocks and in porous media, to be included in the special issue “Electrokinetics in Earth Sciences” of International Journal of Geophysics. We describe the methodology used for self-potential (SP) and for seismoelectromagnetic measurements, for both field and laboratory experiments and for modelling. We give a large bibliography on the studies performed in hydrology to detect at distance the water flow, to deduce the thickness of the aquifer and to predict the hydraulic conductivity. The observation of SP has also been proposed to detect fractures in boreholes, to follow the hydraulic fracturing, and to predict the earthquakes. Moreover, we detail the studies on geothermal applications.

1. Introduction

The electrokinetic phenomena are induced by the relative motion between the fluid and the rock matrix. In a porous medium, the electric current density, linked to the ions within the fluid, is coupled to the fluid flow [1] so that the streaming potentials are generated by fluids moving through porous media [2].

The SP method consists in measuring the natural electric field on the earth's surface. Usually, the electric field is measured by a high-input impedance multimeter, using impolarizable electrodes [3, 4], and its interpretation needs filtering techniques [5]. Moreover, for long-term observations, the monitoring of the magnetic field is also needed for a good interpretation [6]. The classical interpretation of the self-potential (SP) observations is that they originate from electrokinetic effect as water flows through aquifer or fractures. Surface observations of SP anomalies have been reported from numerous tectonically active areas in the world, at different scales from centimetric to kilometric, at the earth surface or in boreholes.

The SP method has been used to characterize active volcanic areas, usually showing positive anomalous electric signals [7–13]. These anomalous signals are commonly

attributed to electrokinetic processes induced by upward hydrothermal flow. The SP sources have been localized at depth using multiscale wavelet tomography [14, 15]. However, numerical modeling showed that these SP anomalies can be induced by meteoric flow in the nonsaturated zone and are linked to the spatial distribution of the electrical conductivity [16–18]. Moreover, a recent study showed that air convection can also be present if the porous medium is highly permeable [19], leading to the conclusion that the effect of water-content on the electrokinetic processes should be better known [20–24].

Monitoring the SP has been proposed as a possible means for predicting earthquakes [25, 26]. Indeed, the electrokinetic effects may be produced by fluid percolation in the crust, driven by a pore pressure gradient related to precursory deformation [25]. In this case, dilatancy prior to the earthquake [27, 28] is assumed to enhance the permeability of the medium and allows the fluid to flow in the vicinity of the fault [29]. It has also been proposed a long-distance elastic effect near the electrodes of measurement [30]. Bernard [31] proposed an electrokinetic model based on the triggering of fluid instabilities at the measurement site responding nonlinearly to precursory strain. However, the long-distance effects are still controversial, as their

observation requires the coincidence of very favorable circumstances to take into account a reasonable precursory strain and the fact that no coseismic electrical anomalies are observed. Another interpretation was proposed on the basis of laboratory observations showing that the electrokinetic coupling of a rock was enhanced by fracturing [32, 33], when stresses rise to over 75% of the yield stress that ruptures the seismic zone. Moreover, the oscillatory nature of some observations has been attributed to an electrokinetic effect associated with unsteady fluid flow during failure of faults. Fenoglio et al. [34] suggested that the stop-and-go fracture propagation associated with rapid fluid flow in a shear fracture 17 km deep could generate electric and magnetic signals measurable at the surface as a result of electrokinetic effects.

Some anomalous electric signals were interpreted as due to the change of the self-potential of the fractured fault rock in which one electrode was fixed, the other electrode being at a constant potential serving as a reference [35]. The detection of fractures and cracks is possible through streaming potential response to a pressure pulse in a borehole [36]. The propagation of hydraulic fracturing could also be detected at distant by measuring the electrical field. The hydraulic fracturing can induce streaming potentials as the fracture propagates, if the fracture remains fulfilled with water. Laboratory experiments on hydraulic fracturing on granite samples showed that the streaming potential varies linearly with the injection of pressure, with an exponential trend when approaching the breakdown pressure [37]. The modeling of the streaming potential induced by an advancing crack showed that the streaming electric current is maximum at the tip of the fracture and decays exponentially in front of the tip [38]. Hydraulic stimulation is often used to stimulate fluid flow in geothermal reservoirs, and surface electrical potential has been monitored around geothermal wells [39]. An anomalous potential of about 5 mV at the Soultz Hot Dry Rock site (France) was interpreted as an electrokinetic effect at 5 km depth and measured at the surface because of the conductive well casing [40]. The SP anomaly was essentially related to water-flows after the earliest stage of injection [41–44]. The observed SP decay after shut-in was interpreted as related to large fluid-flow persisting after the end of stimulation and correlated to the microseismic activity [45]. Another field experiment was performed with periodic pumping tests (injection/production) and showed that the attenuation of SP amplitude with distance was roughly similar to the pressure attenuation [46], leading to the conclusion that the hydraulic diffusivity could be inferred from SP observations.

The distribution of SP can be used to map ground water flow features. Time-varying fluid flow has been identified through SP measurements, showing clearly both rainfall and evaporation events [47]. Modelling of such observations confirmed that SP measurements allow effectively to estimate the direction of water flux at the scale of the electrode separation (usually several decimetres), that is, at a much larger scale than tensiometric measurements [41]. It has been proposed to use SP observations to infer water-table variations and some observations of SP can yield an estimate of aquifer hydraulic properties. It has been proposed to deduce not

only the equivalent electric sources, but also the geometry and flow rate, using a forward and inverse modeling in the wavelet domain [48]. The hydraulic conductivity and the thickness of the aquifer can also be estimated using an inversion scheme for surface SP generated by flow pumping, taking into account the conducting steel casing [49]. Electric potential variations have also been associated with lake level variations, showing a magnitude of 2 mV per meter of water level change between a one km wide ridge separating two lakes [50]. The detection of changes in the flow rate of expelled fluids in accretionary prisms by monitoring of electric and magnetic fields has been discussed. The modeling of electrokinetics at the Nankai trough showed that fluid flow rate variations of 20% could be detected by a variation of 3 mV and about 2 nT at 600 m depth in a borehole [51]. Moreover, recent modeling has shown that SP could detect at distance the propagation of a water-front in a reservoir [52].

The interpretation of all these observations has been possible through developments of the theory, direct modellings, and inverse problems. The interpretation of SP observations needs to resolve the poisson equation for the electric streaming potential, considering a total electric potential [53–56]. Direct modelling has been developed [51, 57, 58]. Moreover, SP observations have been interpreted in the wavelet domain in order to identify location and intensity of the source of the underground hydraulic flows [14, 15, 59, 60]. Gibert & Sailhac [61] have commented on Patella's correlation approach to demonstrate that the so-called probability of tomography defines images of SP data in the wavelet domain that must not be interpreted as underground images of SP sources. They pointed out that an appropriate inversion is necessary to achieve underground images. Numerous recent studies showed that these inverse problems still need further developments [62–65].

Because of similarity between the electrical potential with the pressure behavior, it has been proposed also to use SP measurements as an electrical flow-meter [66]. Moreover, the electrokinetic properties have been used to predict the permeability. Li et al. [67] defined an electrokinetic permeability which can be deduced from the rock conductivity, the electroosmosis coefficient, and the streaming potential coefficient. Recently, Glover et al. [68] proposed a new prediction for the permeability by comparing an electrical model derived from the effective medium theory to an electrical model for granular medium. And, it has also been proposed to deduce the permeability of the Nojima fault (Japan) using the self-potential observations in surface when water is injected into a well of 1800 m depth [69].

The origin of seismoelectromagnetic conversions is also the electrokinetic effect, which is in this case induced by a seismic wave propagation. Two kinds of mechanical to electromagnetic conversions exist: (1) The electrokinetic signal which travels with the acoustic wave; (2) The interfacial conversion occurring at contrasts of physical properties such as permeability.

The second kind of conversion can be used to detect contrasts in physical properties in the crust. A seismic source placed at the surface can induce a seismic wave propagation downward up to the interface (Figure 1). There is a charge

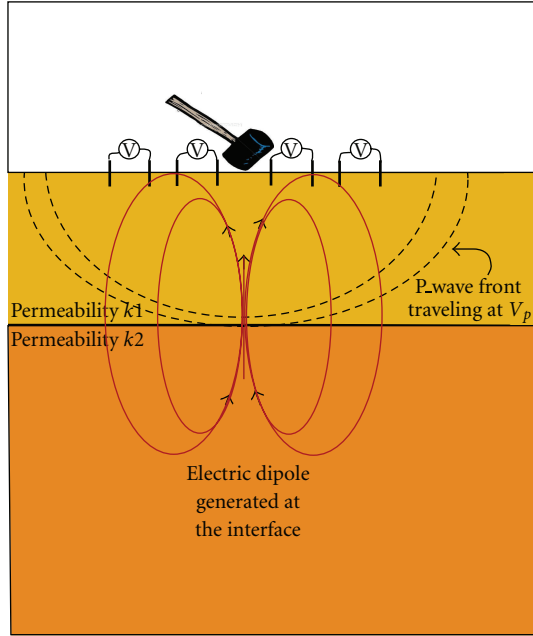


FIGURE 1: The seismic waves (induced by a hammer strike) propagate up to the interface where an electric dipole is generated because of the contrast in permeability (or in other physical properties). This electromagnetic wave can be detected at the surface by measuring the difference of the electrical potential V between electrodes. Picking the time arrival allows to know the depth of the interface.

inbalance that causes a charge separation on both sides of the interface because of the difference in the physical properties. This acts as an electric dipole which emits an electromagnetic wave that travels with the speed of the light in the medium and that can be detected at the surface (Figure 2). The velocity of the seismic wave propagation is deduced by surface measurements of the soil velocity. Then the depth of the interface can be deduced by picking the time arrival of the electromagnetic wave. The amplitude of the seismoelectric signals is usually low from $100 \mu\text{V}$ to mV . Then signal processing needs filtering techniques such as Butler & Russell [70, 71]. The advantage of this method is to detect the contrasts in physical properties at depth from few meters to few hundreds of meters [72–76].

The aim of this paper is to give the background needed to understand this special issue on “Electrokinetics in Earth Sciences”. We detail the theoretical background for the electrical double-layer and for the transport equations used to study the streaming potential and the seismoelectromagnetic conversions. We specially point out the use of self-potential for geothermal applications.

2. Electrokinetics: Theoretical Background

2.1. Electrical Double Layer. Fluid flow in porous media can lead to electrokinetic effects. Indeed the presence of ions within the fluid can induce electric currents when water flows. This effect is directly related to the existence of an electrical double layer between the rock and the fluid.

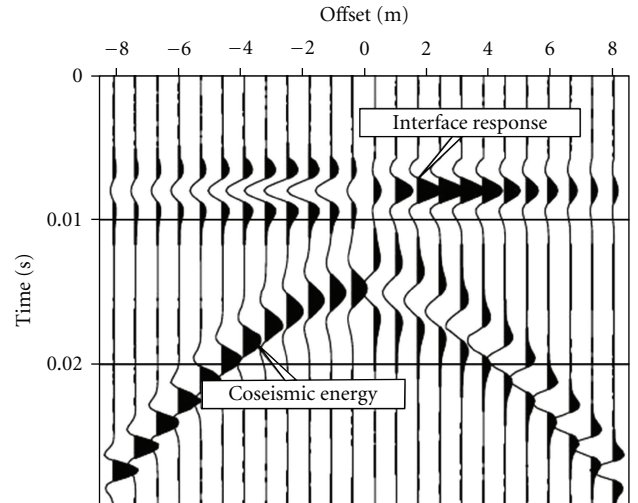


FIGURE 2: Model of the seismoelectric response to a hammer strike on the surface at position zero (from Haines [77]). The seismoelectric signal is shown as measured at the surface along a line centered on the seismic source. The interfacial signal is related to a contrast between properties of the media, such as the permeability.

Minerals forming the rock develop an electric double-layer when in contact with an electrolyte, usually resulting from a negatively charged mineral surface. An electric field is created perpendicular to the surface of the mineral which attracts counterions (usually cations) and repels anions in the vicinity of the pore matrix interface. The electric double layer (Figure 3) is made up of the Stern layer, where cations are adsorbed on the surface and the Gouy diffuse layer, where the number of counterions exceeds the number of anions [78–80].

The fluid contains M_i ionic species with valence z_i ($i = 1, \dots, M_i$) and number density N_i^b (the number of species- i ions per unit volume) in the bulk solution far from any charged surface. The distribution of the electrical potential ϕ within the electrical double layer perpendicular to the solid surface can be calculated resolving the following Poisson’s equation:

$$\nabla^2 \phi = -\frac{\rho}{\epsilon_f}, \quad (1)$$

where ϵ_f is the dielectric constant of the fluid, and the charge density ρ can be expressed using a Boltzmann distribution for the ionic species within the fluid

$$\rho = \sum_{i=1}^M e z_i N_i^b \exp\left(-\frac{e z_i \phi}{kT}\right), \quad (2)$$

where k is the Boltzmann constant, $-e$ is the charge of an electron, and T is the temperature. It is often assumed that the Poisson-Boltzmann equation governing the equilibrium charge clouds can be linearized. Assuming $e\phi/kT \ll 1$, the Poisson’s equation becomes

$$\nabla^2 \phi = \kappa^2 \phi, \quad (3)$$

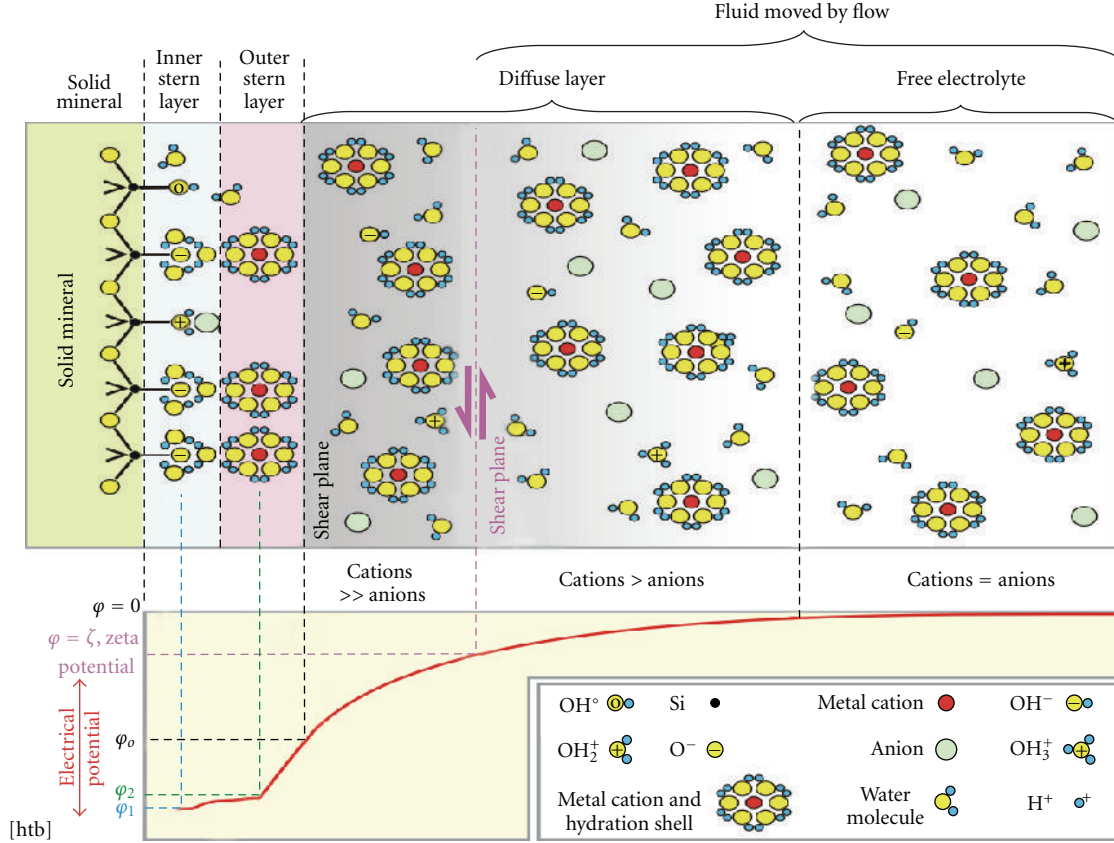


FIGURE 3: Electric double layer, first published in [81]. The solid mineral presented is the case of silica. At pH above the isoelectric point, the cations are adsorbed within the Stern layer; there is an excess of cations in the diffuse layer. The zeta potential is defined at the shear plane. The fluid flow creates a streaming current which is balanced by the conduction current, leading to the streaming potential.

with κ^{-1} is the Debye length, which is a measure of the thickness of the double diffuse layer, typically of the order of a few nm

$$\frac{1}{\kappa^{-2}} = \sum_{i=1}^M \frac{e^2 z_i^2 N_i^b}{\epsilon_f k T}. \quad (4)$$

The electrical potential ϕ at a distance x from a charged surface is therefore

$$\phi(x) = \zeta \exp(-\kappa x), \quad (5)$$

and ζ is called the zeta potential and is the electrical potential at the shear plane (for further details see Pride [82]).

The charge density at the surface of the minerals results from surface complexation reactions. The quartz surface can be modelled with silanol $>SiOH$ group [79]. The potential-determining ions OH^- and H^+ are adsorbed onto the surface of the mineral and determine the charge density on the inner plane (see Figure 3). The surface charge is therefore dependent on the pH. There exists a pH for which the total surface charge is zero; this is the point of zero charge and pH is called pH_{pzc} [83, 84]. The charge is positive for $pH < pH_{pzc}$ and negative for $pH > pH_{pzc}$. In this case, this electrokinetic

effect is zero. The pH_{pzc} for quartz is in the range $2 < pH_{pzc} < 4$ [85, 86]. The calcite surface can be modelled with $>CaOH$ and $>CO_3H$ groups. Carbonate ions and Ca^{2+} are the determining potential ions. The electrokinetic behavior on carbonates is more complicated. The pH_{pzc} varies from 7 to 10.8 according to the authors [87]. It is possible to model simple interfaces and to calculate zeta potential in simple cases [88]. This modeling can be performed assuming the triple-layer model (TLM) which distinguishes three planes to describe the electric double layer: the inner Helmholtz plane for counter ions directly bound to the mineral (assumed to be chemically adsorbed), the outer Helmholtz plane for weakly bound counter ions (assumed to be physically adsorbed), and a d -plane associated with the smallest distance between the mineral surface and the counter ions in the diffuse layer. It has been proposed that the slipping plane lies near the distance of closest approach of dissociated ions, and that the ζ potential can be calculated as the potential on this plane [83].

The streaming current is due to the motion of the diffuse layer induced by a fluid pressure difference along the interface. This streaming current is then balanced by the conduction current, leading to the streaming potential.

2.2. *Theoretical Background for Streaming Potentials.* The different flows (fluid flow, electrical flow, heat flow, concentration flow) are governed by the general equation

$$\mathbf{J}_i = \sum_{j=1}^N \mathcal{L}_{ij} \mathbf{X}_j, \quad (6)$$

which links the forces \mathbf{X}_j to the macroscopic fluxes \mathbf{J}_i , through transport coupling coefficients \mathcal{L}_{ij} [89].

Considering the coupling between the hydraulic flow and the electric flow, assuming a constant temperature and no concentration gradients, the electric current density \mathbf{J}_e [$\text{A} \cdot \text{m}^{-2}$] and the flow of fluid \mathbf{J}_f [$\text{m} \cdot \text{s}^{-1}$] can be written as the following coupled equation:

$$\mathbf{J}_e = -\sigma_0 \nabla V - \mathcal{L}_{ek} \nabla P, \quad (7)$$

$$\mathbf{J}_f = -\mathcal{L}_{ek} \nabla V - \frac{k_0}{\eta_f} \nabla P, \quad (8)$$

where P is the pressure that drives the flow [Pa], V is the electrical potential [V], σ_0 is the bulk electrical conductivity [$\text{S} \cdot \text{m}^{-1}$], k_0 the bulk permeability [m^2], η_f the dynamic viscosity of the fluid [$\text{Pa} \cdot \text{s}$], and \mathcal{L}_{ek} the electrokinetic coupling [$\text{A Pa}^{-1} \text{m}^{-1}$]. Therefore, the first term in (7) is the Ohm's law, and the second term in (8) is the Darcy's law. The coupling coefficient is the same in (7) and (8) because the coupling coefficients must satisfy the Onsager's reciprocal relation in the steady state. This reciprocity has been verified on porous materials [90, 91] and on natural materials [92].

Without direct electric current source, the conservation of the total current density implies

$$\nabla \cdot \mathbf{J}_e = 0, \quad (9)$$

which is the Poisson's equation for the electrical potential V . If the medium is heterogeneous, (9) has to be computed taking into account the sources located at boundaries formed by electrical conductivities and streaming coefficients contrasts [93]. In the case of an homogeneous medium (9) leads to the simplified Poisson's equation

$$\nabla^2 V = C \nabla^2 P. \quad (10)$$

The streaming potential coefficient C_{s0} [$\text{V} \cdot \text{Pa}^{-1}$] is defined when the electric current density \mathbf{J}_e is zero, leading to

$$\frac{\Delta V}{\Delta P} = -\frac{\mathcal{L}_{ek}}{\sigma_0} = C_{s0}. \quad (11)$$

This coefficient can be measured by applying a driving pore pressure ΔP to a porous medium and by detecting the induced electric potential difference ΔV . The driving pore pressure induces a streaming current (second term in (7)) which is balanced by the conduction current (first term in (7)) which leads to the electric potential difference ΔV that can be measured. In the case of a unidirectional flow through a cylindrical saturated porous rock, this coefficient can be expressed as [32, 94]

$$C_{s0} = \frac{\epsilon_f \zeta}{\eta_f \sigma_{\text{eff}}}. \quad (12)$$

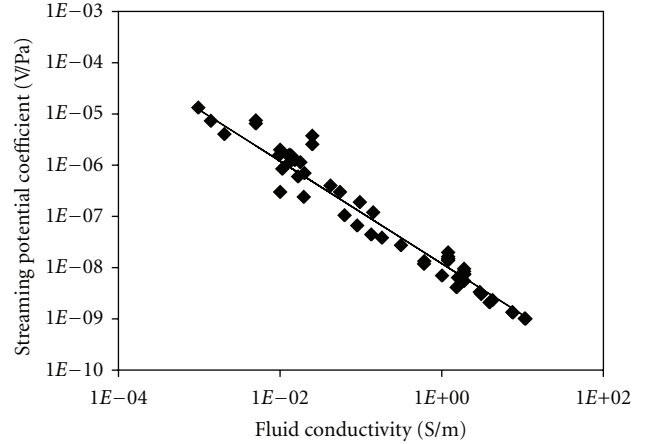


FIGURE 4: Streaming potential coefficient from data collected (in absolute value) on sands and sandstones at pH 7-8 (when available) from Ahmad [100]; Li et al. [67]; Jouniaux and Pozzi [101]; Lorne et al. [86]; Pengra et al. [102]; Guichet et al. [21]; Perrier and Froidefond [103]; Guichet et al. [88]; Ishido and Mizutani [96]; Jaafar et al. [98]. The regression (black line) leads to $C_{s0} = -1.2 \times 10^{-8} \sigma_f^{-1}$. A zeta potential of -17 mV can be inferred from these collected data from Allègre [24].

with the fluid electrical permittivity ϵ_f [$\text{F} \cdot \text{m}^{-1}$], the effective electrical conductivity σ_{eff} [$\text{S} \cdot \text{m}^{-1}$] defined as $\sigma_{\text{eff}} = F \sigma_0$ with F the formation factor and σ_0 the rock conductivity which can include a surface conductivity. The potential ζ [V] is the zeta potential described as the electrical potential inside the EDL at the slipping plane or shear plane (i.e., the potential within the double-layer at the zero-velocity surface).

The streaming coefficient is described by the well-known Helmholtz-Smoluchowski equation [95] when the surface conductivity can be neglected compared to the fluid conductivity ($F \sigma_0 = \sigma_f$)

$$C_{s0} = \frac{\epsilon_f \zeta}{\eta_f \sigma_f}. \quad (13)$$

The assumptions are a laminar fluid flow, identical hydraulic, and electric tortuosity. The influencing parameters on this streaming potential coefficient are therefore the dielectric constant of the fluid, the viscosity of the fluid, the fluid conductivity and the zeta potential itself depending on rock, fluid composition, and pH [86, 88, 94, 96–99]. At a given pH, the most influencing parameter is the fluid conductivity. Numerous measurements of the streaming potential on sand have been published, that can lead to the relation $C_{s0} = -1.2 \times 10^{-8} \sigma_f^{-1}$ (Figure 4). A zeta potential of -17 mV can be inferred from these collected data, assuming all the other parameters constant.

2.3. *Theoretical Background for Seismoelectromagnetics.* The origin of the seismoelectromagnetic conversion is also the electrokinetic effect, which is in this case induced by seismic wave propagation. The relative motion between the fluid and the rock matrix is induced by the seismic wave propagation. The reciprocal process also occurs; the electromagnetic waves

couple to displacement fields and they generate seismic waves at electrical/mechanical interfaces [104, 105]. In this case, the electrokinetic coefficient depends on the frequency ω as the dynamic permeability $k(\omega)$ [106]. Pride [82] developed the theory for the coupled electromagnetics and acoustics of porous media, coupling the electric field in Maxwell's relations to the displacement fields in Biot's equations. The transport relations ([82, equations (250) and (251)]) are

$$\begin{aligned} \mathbf{J}_e &= \sigma(\omega)\mathbf{E} + \mathcal{L}_{ek}(\omega)(-\nabla p + \omega^2\rho_f\mathbf{u}_s), \\ -i\omega\mathbf{J}_f &= \mathcal{L}_{ek}(\omega)\mathbf{E} + \frac{k(\omega)}{\eta}(-\nabla p + \omega^2\rho_f\mathbf{u}_s). \end{aligned} \quad (14)$$

The electrical fields and mechanical forces which induce the electric current density \mathbf{J}_e and the fluid flow \mathbf{J}_f are, respectively, \mathbf{E} and $(-\nabla p + i\omega^2\rho_f\mathbf{u}_s)$, where p is the pore-fluid pressure, \mathbf{u}_s is the solid displacement, \mathbf{E} is the electric field, ρ_f is the pore-fluid density, and ω is the angular frequency. The electrokinetic coupling $\mathcal{L}_{ek}(\omega)$ is now complex and frequency-dependent and describes the coupling between the seismic and electromagnetic fields [82, 107]

$$\begin{aligned} \mathcal{L}_{ek}(\omega) &= \mathcal{L}_{ek} \left[1 - i\frac{\omega}{\omega_c} \frac{m}{4} \left(1 - 2\frac{d}{\Lambda} \right)^2 \right. \\ &\quad \left. \times \left(1 - i^{3/2}d\sqrt{\frac{\omega\rho_f}{\eta}} \right)^2 \right]^{-1/2}, \end{aligned} \quad (15)$$

where m and Λ are geometrical parameters of the pores (Λ is defined in Johnson et al. [108] and m is in the range 4–8), d is the Debye length. The transition frequency ω_c defined in the Biot's theory separates the viscous and inertial flow domains and depends on the permeability k_0 . The frequency-dependence of the streaming potential coefficient has been studied [107, 109–115] mainly on synthetic samples and recently on sand [116]. Both models [117–123] and laboratory experiments [116, 124–129] have been developed on these seismoelectromagnetic conversions. Over the past decades, seismoelectromagnetic phenomena have been observed in the field [130–132], and increasing successful field experiments have been reported in recent years [73, 75, 119, 133–136].

3. Geothermal Applications

3.1. Self-Potential Associated with Natural Hydrothermal Circulation. The SP method has attracted increasing interest in geothermal prospecting. Among the various mechanisms which can cause SP in geothermal areas, the most important appear to be streaming potentials [96, 137–139]. Electrokinetic effects are almost certainly responsible for the production-induced changes in SP which take place after a field is developed [57]. Repetitive SP surveying of geothermal fields during exploitation represents a promising tool for geothermal field monitoring and resource management.

During the past two decades, numerical modeling of SP generation has been undertaken in geothermal and hydrological studies [55, 57, 58, 140]. The method proposed

by Ishido and Pritchett [57] applies the so-called “EKP-postprocessor” to the results of an unsteady thermohydraulic reservoir simulation. First, it calculates the distributions of pertinent parameters such as the electrokinetic coupling \mathcal{L}_{ek} , the electrical conductivity, and the drag current density using the results from the reservoir simulation. Next, the postprocessor calculates the electric potential distribution by solving the Poisson's equation within a finite-difference grid with appropriate boundary conditions.

Figure 5 shows the SP distribution expected to arise from natural hydrothermal convection. A positive SP anomaly is present above the central upflow region. This is produced by positive-charge accumulation due to the large reduction in the streaming potential coefficient along the upflow path. Contrasting large negative anomalies appear in the peripheral regions where meteoric water flows downward. This is produced by the descending meteoric water which removes positive charge from the neighborhood of the ground surface. The peripheral negative anomalies are larger in magnitude than the central positive anomaly due to relatively low electrical conductivity. A representative flow rate (Darcy velocity) is 10^{-8} m/s in this case. In cases with higher flow rate, the magnitudes of both the positive and negative anomalies will be increased. However, the magnitude of central positive anomaly will not become significantly larger than 100 mV since the driving force for the upflow is usually less than several percent of the hydrostatic pressure gradient [141], and the electrical conductivity of upflowing fluid is relatively high due to dissolved species.

Figure 6 shows the measured SP profile across the Nigorikawa caldera [142]. SP is high within the caldera where upflows take place, but the surrounding area is characterized by more distinct negative SP anomalies. These features are well reproduced by the above calculation (Figure 5(d) using “EKP-postprocessor” Ishido & Pritchett [57]). Similar SP features were observed at the mud volcano area in Yellowstone [137], the Kirishima field in Japan [143], the Mokai and Rotokawa fields in New Zealand [144], and so forth.

The results of the calculation shown in Figure 5 confirmed the results of “semiquantitative” modeling by Ishido [142] (an outline of which is given in Ishido et al. [145]; Zlotnicki & Nishida [146]). In the case of source-free fluid flow driven by buoyancy, the primary conduction current source (which causes the SP at the earth's surface) appears at the boundary between regions of different electrokinetic coupling (\mathcal{L}_{ek}). The magnitude of the conduction current source is given by the difference in the coupling coefficient across the boundary multiplied by the pressure gradient perpendicular to the boundary. Ishido [142] assumed that the coupling coefficient depends both on temperature and on pore-water chemistry based upon the experimental results of Ishido & Mizutani [96].

Better understanding of the zeta potential and/or streaming potential coefficient is fundamentally important in quantitative modeling of electrokinetic potentials associated with subsurface fluid flow. Recent laboratory measurements under high-temperature conditions [147–149], high-salinity conditions [98], and liquid/gas two-phase conditions [21, 22] are particularly relevant to modeling studies for geothermal and

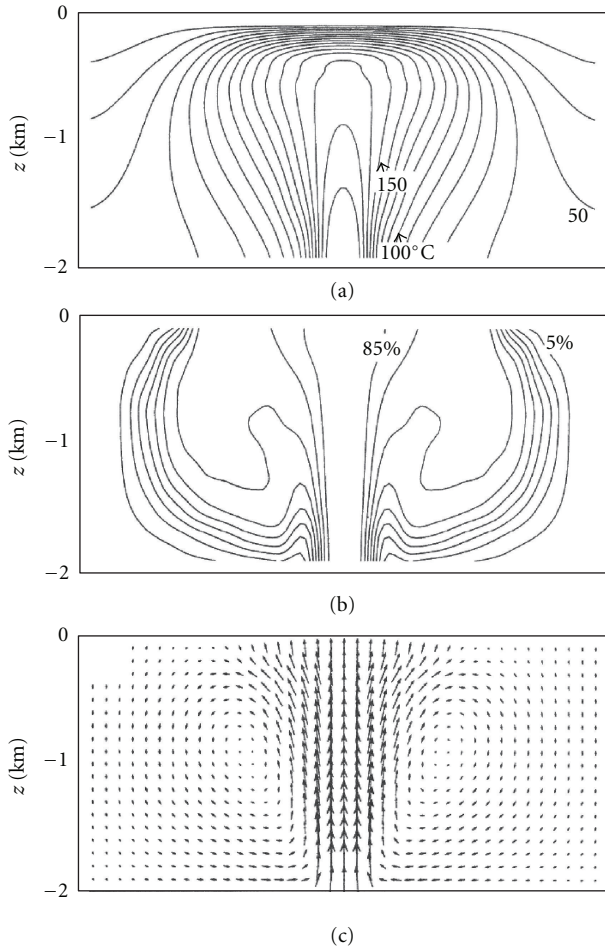


FIGURE 5: Results of reservoir simulation: natural-state distributions of (a) temperature (contour interval 10°C), (b) mass fraction of “source fluid”, and (c) fluid mass flux. Earth-surface SP distributions computed by the so-called “EKP postprocessor” for this natural state (solid curve), and for a subsequent exploited state (broken curve), are shown in (d), after [57].

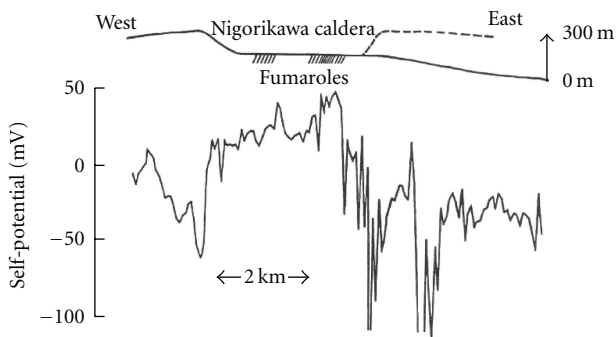
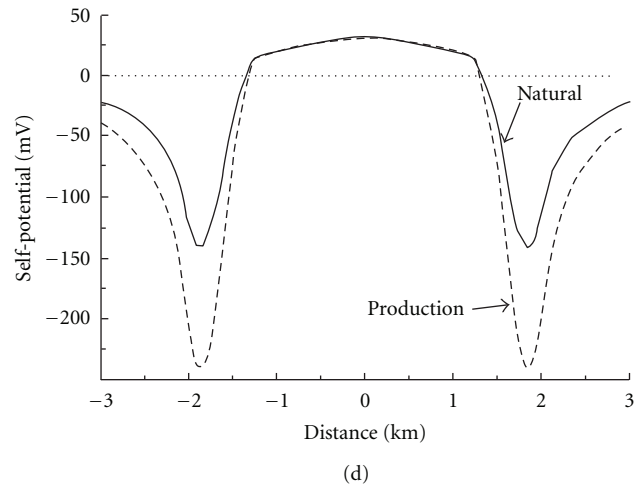


FIGURE 6: Topographic section and self-potential profile across the Nigorikawa caldera measured in 1978, after [142].

volcanic areas. In addition to measuring the coupling coefficients of representative rock samples from survey areas (e.g., Jouniaux et al. [94]; Hase et al. [150]; Aizawa et al. [151]; Onizawa et al. [18]), basic phenomenological measurements such as the determination of the dependency of the



streaming potential coefficient upon pore size [152] are essential.

3.2. “W”-Shaped SP Profiles across Volcanoes. Numerous SP surveys of active volcanoes have been carried out during the past thirty years. Obvious positive-polarity SP anomalies have often been observed around volcanic craters or vents; for example, Kilauea [153], Akita Yake-yama [145], Unzen [154], Miyake-jima [155, 156], Izu-Oshima [16], La Fournaise [157], Mt. Fuji [158], Misti [12], and Mt. Aso [13]. In addition to these, various other types of SP anomalies were reported on active volcanoes [11, 146, 159, 160]. In cases like Miyake-jima, Izu-Oshima, Mt. Fuji, Mt. Aso, Misti and La Fournaise [9], SP first decreases several hundred millivolts, sometimes more than one volt, as one climbs the slopes of the volcano, then rapidly recovers to the level measured on the flank of volcano as the summit crater is approached. Consequently, the entire SP profile along a survey line starting from the foot, passing near the summit, and reaching the foot on the opposite side often has the shape of the letter “W”.

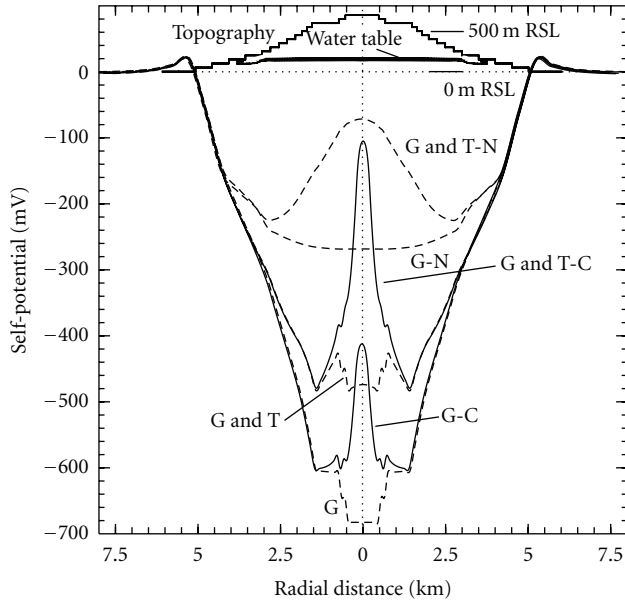


FIGURE 7: Self-potential distributions computed from numerical simulation results of thermohydraulic processes within a volcanic body, after [17]. Cases “G-” and “G and T-” correspond to the conditions of “steady-state of topography-driven groundwater flow” and “100 years after continuous heating of central conduit below sea level”, respectively. For cases “-C”, a shallow conductor above the water table is assumed. For cases “-N”, the drag current in the unsaturated zone is neglected. The “W”-shaped SP profile observed at Izu-Oshima volcano is reproduced by case “G and T-C”. The sketch in the upper part of the figure illustrates the earth surface topography and the water table elevation.

Numerical simulations by Ishido [17], which were based on a conceptual model of Izu-Oshima volcano, show that the primary cause of the “W”-shaped SP distribution is a combination of the electrokinetic drag current associated with the downward liquid flow in the unsaturated and underlying saturated layers and the presence of a shallow conductor near the volcano summit. If the shallow conductor contacts a deep conductive layer, this conductive structure provides a current path between the low-potential shallow and high-potential deep regions, resulting in substantial increase in SP around the summit (Figure 7). The calculated W-shaped profile is stable even with periodic groundwater recharge, which is consistent with field observations.

Assuming a plausible value of zeta potential and liquid-saturation dependency of drag current, the terrain-related SP is calculated as about -1 mV/m, which is typical of the magnitudes observed at a number of volcanoes. Two ways have been proposed to interpret SP generation due to gravity-driven water flow; the first considers only downward percolation of vadose-zone water to the water table [8], and the second considers situations where the effects of water flow in the deeper saturated zone predominate [161, 162]. In the simulation results shown in Figure 7, gravity-driven water flows in both the unsaturated and underlying saturated zones contribute to generate the terrain-related SP. Concerning SP generation in the unsaturated zone, a vertical potential gradient

of -1 to -2 mV/m was observed by multiple Ag/AgCl electrodes installed in a 100 m research hole drilled in the eastern part of the caldera floor at Izu-Oshima (N. Matsushima, personal communication). A similar vertical SP gradient averaging -1.35 mV/m was observed for the upper 488 m interval above the water table in a research hole at Kilauea’s summit [163]. This potential gradient is thought to be produced by a substantial downward flow of meteoric water in the unsaturated zone, which is suggested by uniform temperatures near 25°C in the subsurface region above the water table [163].

The effect of drag current associated with hydrothermal upflow is shown minor compared to the effect of the heterogeneous conductivity structure, especially if the fluid circulates to great depth and is highly saline. Upflows of vapor or volcanic gas to the summit crater can reduce the drag current associated with meteoric water downflow within the volcanic conduit [16] and will also provide a secondary contribution to the increased SP near the summit (Figure 7). Onizawa et al. [18] carried out 3-D numerical simulations of groundwater flow due to meteoric water infiltration and the resulting induced SP to understand the fundamental groundwater flow regime and the causes of the SP observed at Izu-Oshima. They reproduced the overall pattern of the observed SP distribution by incorporating a heterogeneous resistivity structure derived from Audio Magneto Telluric (AMT) measurements.

Aizawa et al. [164] found that 2-D resistivity sections obtained by AMT surveys in five large Japanese stratovolcanoes (Iwate, Iwaki, Nasu, Nantai, and Nikko-Shirane) correlate closely with SP measurements [160]. Extensive conductors extend downward from shallow levels on slopes that lack SP anomalies, whereas the top of the conductor is relatively deep on slopes where large SP minima are observed. They confirmed the plausibility of the proposed conceptual model based on numerical simulations of a hydrothermal system with sealing layers and meteoric water recharge and reproduced the observed relationship between the SP and resistivity data.

The calculated high SP amplitude near the summit is sensitive to the conductivity structure, which is thought to change over time due to volcanic activities such as magma ascent, degassing, and development of hydrothermal convection [165, 166]. This is thought to be at least partly responsible for the temporal SP variations observed at Kilauea [153], Unzen [154] and other volcanoes.

3.3. SP Changes Induced by Geothermal Fluid Production and Reinjection. When a sink or source of fluid is present within a reservoir as a result of production or reinjection of geothermal fluids, a surface electric potential anomaly can be produced through electrokinetic coupling if the following conditions are satisfied. First, there must be a boundary separating regions of differing streaming potential coefficient C_{s0} (denoted as C hereafter); second, there must be a nonzero component of pressure gradient parallel to this boundary [53, 167]. A temperature boundary, a boundary between regions of different pore water chemistry, and/or a contact of different rock formations are the most likely causes for discontinuities in the value of C in a geothermal reservoir

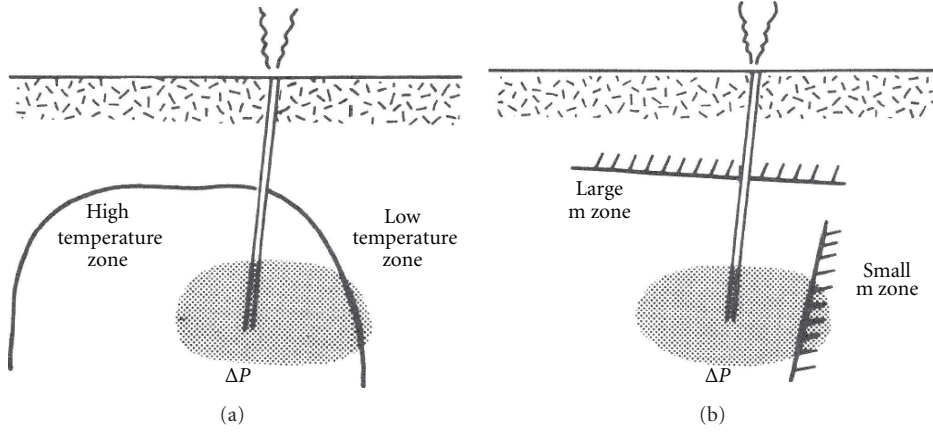


FIGURE 8: Models for production-induced SP change, after [145]. (a) High-low temperature interface, or (b) large-small pore hydraulic radius (m) interface acts as a boundary between regions of differing streaming potential coefficient. Shaded region: zone of production-induced pressure disturbance.

(Figure 8). When a propagating pressure disturbance induced by production and/or injection of fluids reaches a boundary between regions of differing C in the reservoir, an SP change will appear at the earth's surface [145].

A quantitative and physically reasonable method for calculating SP anomalies near C boundaries was described by Fitterman [53] based on earlier work by Nourbehech [167]. A total electric potential is defined by

$$\psi = V - CP, \quad (16)$$

such that the current flow is given by

$$\mathbf{J}_e = -\sigma_0 \nabla \psi. \quad (17)$$

In the absence of current sources, $\nabla \cdot \mathbf{J}_e = 0$ and for homogeneous regions,

$$\nabla^2 \psi = 0, \quad (18)$$

with boundary conditions of continuity of normal current flow

$$\sigma_0 \mathbf{n} \nabla \psi|_1^2 = 0 \quad (19)$$

and discontinuity of total electric potential at interfaces equal to the difference in C times the pressure

$$\psi|_1^2 = -C|_1^2 P = S, \quad (20)$$

where S is a generalized source function ($X|_1^2$ means the jump in X across the boundaries). The discontinuity of ψ is the result of V and P being continuous while C is discontinuous. The ψ distribution can be calculated as the potential produced by a surface distribution of current dipoles with surface dipole density $\sigma_0 S$ along the interface [168]. If the boundary is nearly vertical, the SP anomaly will be dipolar in waveform. When P is negative (positive), this dipole source points towards the side of larger (smaller) C . If the boundary condition at the earth's surface is $P =$

constant or the pressure change is confined at depth, the SP anomaly is brought about solely by this dipole source; therefore no SP anomaly will appear at the earth's surface if the C distribution is homogeneous. This is also true for gravity-driven groundwater flow if the fluid density is constant in the entire region. For example, SP depends only on ground surface elevation for a fully saturated region of homogeneous C [169]; this is true even if the permeability distribution is heterogeneous and thus pressure gradient normal to a permeability boundary is discontinuous.

The Mori geothermal power plant was built in the Nigori-kawa caldera in 1982 and has been in continuous operation since. Comparing the results of SP surveys in 1978, 1981, and 1984, Ishido et al. [145] found a production-induced SP change (Figure 9). The dipolar change in SP appears over the principal zone of fluid production. This observed change is believed to be generated by underground fluid flows resulting from the production (and reinjection) of geothermal fluids through electrokinetic coupling and partly reproduced in the modeling results shown Figure 5. The upflowing hot water in the central region is relatively saline, so the magnitude of the local streaming potential coefficient $|C_{\text{res}}|$ is thought to be smaller than for the fresh water in the peripheral region $|C_{\text{per}}|$ (so that $C_{\text{per}} < C_{\text{res}} < 0$). So, the dipole source for ψ appearing along the nearly vertical C boundary is thought to point into the central region, resulting in increase and decrease in SP in the central and peripheral areas, respectively.

This is one of the possible interpretations. Another candidate for a boundary between regions of differing C is thought to be the interface between the reservoir and overlying caprock. Yasukawa et al. [170] carried out modeling studies to interpret the observed SP changes associated with a short-term field-wide shut-in of production and reinjection wells at the Mori power plant. In their model, the streaming potential coefficient is assumed as $C_{\text{res}} < C_{\text{cap}} < 0$ (here, C_{res} and C_{cap} are the streaming potential coefficient of reservoir and caprock regions, resp.). So the observed central increase and peripheral decrease in SP, which are also reproduced

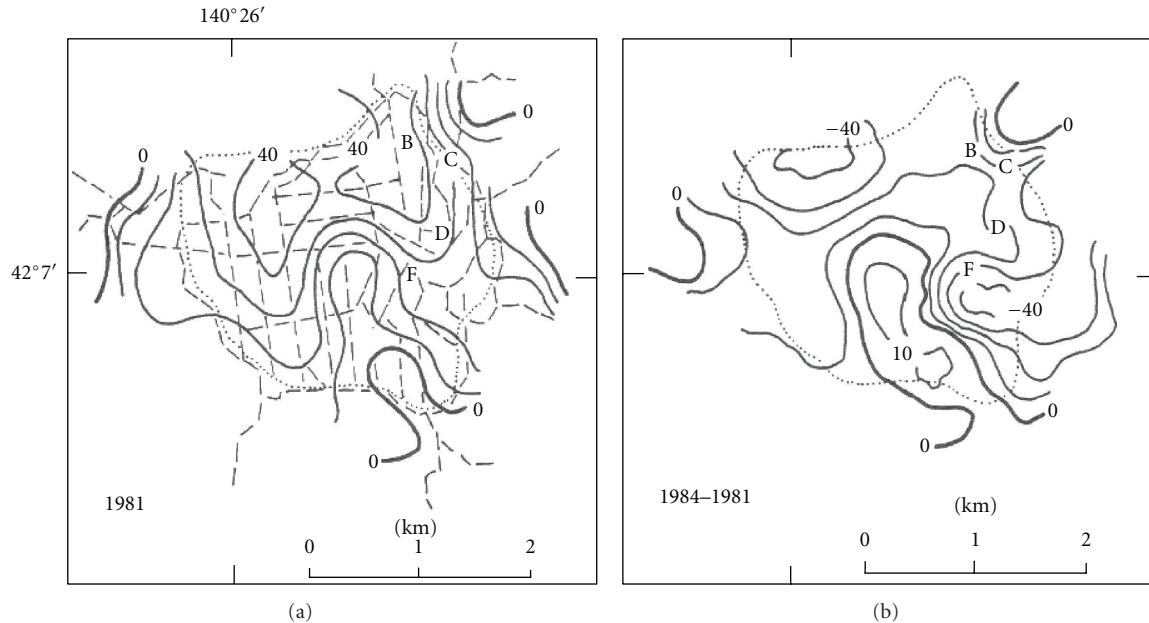


FIGURE 9: Self-potential distributions in the Nigorikawa caldera (a) measured in 1981 and (b) difference in SP distribution between 1981 and 1984, after [145]. Contour interval is 10 mV. Broken lines shown in (a) denote survey lines used for 1981 and 1984 surveys (the data sampling intervals are 100 m). The edge of the caldera floor is indicated by the dotted lines. B, C, D, and F represent well sites.

in the numerical modeling, are interpreted as induced by pressure decrease (due to production) and increase (due to reinjection), respectively, along the interface.

In many geothermal reservoirs, substantial production-induced expansion of the vapor-dominated zone (due to reservoir pressure decline) takes place during the early stages of field operation. Just below the vapor zone, vigorous boiling occurs and counterflows of vapor (upward) and liquid (downward) are produced. This downward flow of the liquid phase carries drag current with it and brings about a negative SP change on the ground surface [57]. Preliminary modeling studies [171, 172] show that the observed SP changes at the Okuaizu field in Japan (Figure 10) can be explained by this process. An interpretation based on the total electric potential is also available for this process [57]. At Okuaizu, fractured reservoirs develop along nearly vertical faults within country rocks of very low permeability. The magnitude of the streaming potential coefficient of the country rocks (C_{ctr}) is thought to be substantially smaller than that of the reservoir rocks (C_{res}) [32, 97]. So the $C_{res} < C_{ctr} < 0$ inequality will not change, irrespective of C_{res} change caused by increasing vapor saturation, so long as the liquid phase remains mobile. Then, pressure decline due to a vertically-extensive boiling zone brings about a negative SP change at the earth's surface.

Since the possibility always exists that production-induced SP changes overlap the natural SP distribution associated with the undisturbed state, care must be exercised in interpreting SP data from areas where fluid production is taking place. Furthermore, sources of noise associated with newly drilled wells, deployed pipelines, and so forth need to be evaluated. At the Sumikawa field in Japan, SP surveys were carried out twice before the startup of the geothermal power

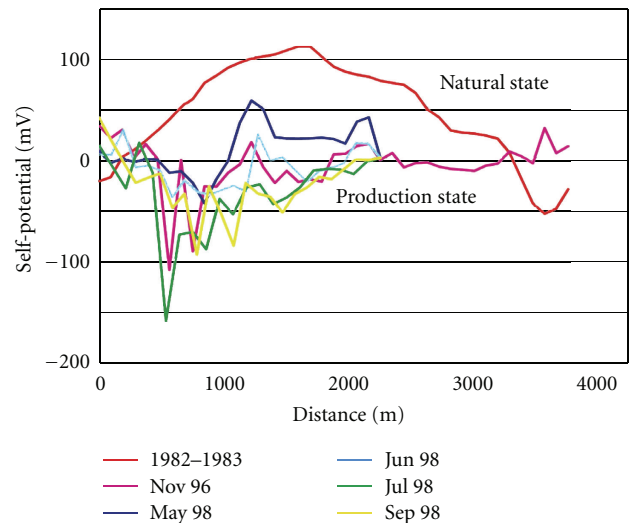


FIGURE 10: SP profile along a survey line passing through the central part of the Okuaizu geothermal field in Japan. The red line shows the SP profile under natural state conditions, measured in 1982-83. The survey in November 1996 was carried out about 1.5 years after start-up of the Yanaizu-Nishiyama power station. The repeated surveys in 1998 were carried out after 2 months shut-in of production wells in April and May 1998, after [171, 172].

station in 1995 and again three times afterwards [173]. Unfortunately, no data free from "artificial" noise are available except that from the first survey in 1983. Negative potentials of up to several hundred millivolts are present near metallic artifacts such as well casings and pipelines.

The pipelines, which were deployed after 1983 along the principal survey lines used in the 1983 survey, are connected to the wellheads and are in electrical contact with the ground surface at various locations. Continuous SP measurements near the wellheads and pipelines show that temporal potential changes correspond to temporal temperature variations near the surfaces of the metallic structures, which could be explained by a simple “redox” model [174]. Other important noise sources to be taken into account for field measurements are discussed by Corwin and Hoover [139].

To estimate magnetic fields associated with fluid flows in geothermal reservoirs, “EKP postprocessor” calculations were carried out applying the Biot-Savart law to the distributions of drag and conduction current densities [175]. Their results suggest that magnetic anomaly magnitudes caused solely by electrokinetic coupling are too weak to be observed, either for natural or exploited conditions. However, this does not rule out the appearance of observable magnetic fields due to electrokinetic coupling in other situations where significant fluid flow takes place in a region with heterogeneous and/or anisotropic rock properties (e.g., Mizutani & Ishido [176]; Zlotnicki & Mouel [177]).

In addition to electrokinetic (EK) coupling, several other effects such as thermoelectric coupling and chemical diffusion potential cannot be ruled out as possible causes of self-potential anomalies in geothermal fields. However, EK phenomena are almost certainly responsible for the production-induced changes in SP that take place after a field is developed. No other effects will play significant roles, since production-induced changes in the distributions of fluid chemistry and temperature will be minor compared to flow pattern changes, especially in the early stages of exploitation. SP monitoring such as that carried out at Okuaizu [171, 178] is thought to be useful for history matching studies, particularly to improve mathematical models of fractured reservoirs [172, 179, 180].

4. Conclusion

A lot of observations have been performed these last decades, both Self-Potential and seismoelectromagnetics observations. We detailed the theoretical background needed to interpret these observations and pointed out the use of self-potentials for geothermal applications. We tried to provide an extensive overview and to mention the related key publications. We hope that this tutorial is useful to better understand the papers published in the special issue “Electrokinetics in Earth Sciences” of International Journal of Geophysics. Further improvement should come from studies on signal processing, on inverse problems, and from technical development.

Acknowledgments

This paper was supported by the French National Scientific Center (CNRS) and by REALISE the “Alsace Region Research Network in Environmental Sciences in Engineering” and the Alsace Region. The paper on geothermal applications was supported by the Geological Survey of Japan and the Institute

for Geo-Resources and Environment, the National Institute of Advanced Industrial Science and Technology.

References

- [1] J. T. G. Overbeek, “Electrochemistry of the double layer,” in *Colloid Science, Irreversible Systems*, H. R. Kruyt, Ed., vol. 1, pp. 115–193, Elsevier, 1952.
- [2] L. Jouniaux, A. Maineult, V. Naudet, M. Pessel, and P. Sailhac, “Review of self-potential methods in hydrogeophysics,” *Comptes Rendus Geoscience*, vol. 341, no. 10-11, pp. 928–936, 2009.
- [3] G. Petiau and A. Dupis, “Noise, temperature coefficient, and long time stability of electrodes for telluric observations,” *Geophysical Prospecting*, vol. 28, no. 5, pp. 792–804, 1980.
- [4] G. Petiau, “Second generation of Lead-lead chloride electrodes for geophysical applications,” *Pure and Applied Geophysics*, vol. 157, no. 3, pp. 357–382, 2000.
- [5] F. Moreau, D. Gibert, and G. Saracco, “Filtering non-stationary geophysical data with orthogonal wavelets,” *Geophysical Research Letters*, vol. 23, no. 4, pp. 407–410, 1996.
- [6] F. E. Perrier, G. Petiau, G. Clerc et al., “A one-year systematic study of electrodes for long period measurements of the electric field in geophysical environments,” *Journal of Geomagnetism and Geoelectricity*, vol. 49, pp. 1677–1696, 1997.
- [7] M. Aubert and G. Kieffer, “Underground water circulation within volcanic structures of mount Etna southern flank. Results of PS measurements,” *Comptes Rendus de l’Academie des Sciences*, vol. 296, pp. 1003–1006, 1984.
- [8] M. Aubert and Q. Y. Atangana, “Self-potential method in hydrogeological exploration of volcanic areas,” *Ground Water*, vol. 34, no. 6, pp. 1010–1016, 1996.
- [9] J.-F. Lénat, D. Fitterman, D. B. Jackson, and P. Labazuy, “Geoelectrical structure of the central zone of Piton de la fournaise volcano (Reunion),” *Bull Volcanol*, vol. 62, no. 2, pp. 75–89, 2000.
- [10] A. Finizola, F. Sortino, J.-F. Lénat, and M. Valenza, “Fluid circulation at Stromboli volcano (Aeolian Islands, Italy) from self-potential and CO₂ surveys,” *Journal of Volcanology and Geothermal Research*, vol. 116, no. 1-2, pp. 1–18, 2002.
- [11] A. Finizola, F. Sortino, J.-F. Lénat, M. Aubert, M. Ripepe, and M. Valenza, “The summit hydrothermal system of Stromboli. new insights from self-potential, temperature, CO₂ and fumarolic fluid measurements, with structural and monitoring implications,” *Bulletin of Volcanology*, vol. 65, no. 7, pp. 486–504, 2003.
- [12] A. Finizola, J. F. Lénat, O. Macedo, D. Ramos, J. C. Thouret, and F. Sortino, “Fluid circulation and structural discontinuities inside Misti volcano (Peru) inferred from self-potential measurements,” *Journal of Volcanology and Geothermal Research*, vol. 135, no. 4, pp. 343–360, 2004.
- [13] H. Hase, T. Hashimoto, S. Sakanaka, W. Kanda, and Y. Tanaka, “Hydrothermal system beneath Aso volcano as inferred from self-potential mapping and resistivity structure,” *Journal of Volcanology and Geothermal Research*, vol. 143, no. 4, pp. 259–277, 2005.
- [14] G. Saracco, P. Labazuy, and F. Moreau, “Localization of self-potential sources in volcano-electric effect with complex continuous wavelet transform and electrical tomography methods for an active volcano,” *Geophysical Research Letters*, vol. 31, no. 12, Article ID L12610, 5 pages, 2004.
- [15] G. Mauri, G. Williams-Jones, and G. Saracco, “Depth determinations of shallow hydrothermal systems by self-potential and multi-scale wavelet tomography,” *Journal of Volcanology*

- and *Geothermal Research*, vol. 191, no. 3-4, pp. 233–244, 2010.
- [16] T. Ishido, T. Kikuchi, N. Matsushima et al., “Repeated self-potential profiling of Izu-Oshima volcano, Japan,” *Journal of Geomagnetism and Geoelectricity*, vol. 49, pp. 1267–1278, 1997.
- [17] T. Ishido, “Electrokinetic mechanisms for the “W”-shaped self-potential profile on volcanoes,” *Geophysical Research Letters*, vol. 31, no. 15, Article ID L15616, 5 pages, 2004.
- [18] S. Onizawa, N. Matsushima, T. Ishido, H. Hase, S. Takakura, and Y. Nishi, “Self-potential distribution on active volcano controlled by three-dimensional resistivity structure in Izu-Oshima, Japan,” *Geophysical Journal International*, vol. 178, no. 2, pp. 1164–1181, 2009.
- [19] R. Antoine, D. Baratoux, M. Rabinowicz et al., “Thermal infrared image analysis of a quiescent cone on Piton de la Fournaise volcano: Evidence of convective air flow within an unconsolidated soil,” *Journal of Volcanology and Geothermal Research*, vol. 183, no. 3-4, pp. 228–244, 2009.
- [20] F. Perrier and P. Morat, “Characterization of electrical daily variations induced by capillary flow in the non-saturated zone,” *Pure and Applied Geophysics*, vol. 157, no. 5, pp. 785–810, 2000.
- [21] X. Guichet, L. Jouniaux, and J.-P. Pozzi, “Streaming potential of a sand column in partial saturation conditions,” *Journal of Geophysical Research B*, vol. 108, article 2141, 12 pages, 2003.
- [22] A. Revil, N. Linde, A. Cerepi, D. Jougnot, S. Matthäi, and S. Finsterle, “Electrokinetic coupling in unsaturated porous media,” *Journal of Colloid and Interface Science*, vol. 313, no. 1, pp. 315–327, 2007.
- [23] V. Allègre, L. Jouniaux, F. Lehmann, and P. Sailhac, “Streaming potential dependence on water-content in Fontainebleau sand,” *Geophysical Journal International*, vol. 182, no. 3, pp. 1248–1266, 2010.
- [24] V. Allègre, L. Jouniaux, F. Lehmann, and P. Sailhac, “Streaming potential dependence on water-content in fontainebleau sand,” *Geophysical Journal International*, vol. 186, no. 1, pp. 115–117, 2011, Reply to the comment by A. Revil and N. Linde.
- [25] H. Mizutani, T. Ishido, T. Yokokura, and S. Ohnishi, “Electrokinetic phenomena associated with earthquakes,” *Geophysical Research Letters*, vol. 3, pp. 365–368, 1976.
- [26] R. F. Corwin and H. F. Morrison, “Self potential variations preceding earthquakes in central California,” *Geophysical Research Letters*, vol. 4, no. 4, pp. 171–174, 1977.
- [27] A. Nur, “Dilatancy, pore fluids, and premonitory variations of ts/tp travel times,” *Bulletin of the Seismological society of America*, vol. 62, pp. 1217–1222, 1972.
- [28] C. H. Scholz, L. R. Sykes, and Y. P. Aggarwal, “Earthquake prediction: a physical basis,” *Science*, vol. 181, no. 4102, pp. 803–810, 1973.
- [29] H. Murakami, H. Mizutani, and S. Nabetani, “Self-potential anomalies associated with an active fault,” *Journal of Geomagnetism & Geoelectricity*, vol. 36, no. 9, pp. 351–376, 1984.
- [30] I. Dobrovolsky, N. Gershenzon, and M. Gokhberg, “Theory of electrokinetic effects occurring at the final stage in the preparation of a tectonic earthquake,” *Physics of the Earth and Planetary Interiors*, vol. 57, no. 1-2, pp. 144–156, 1989.
- [31] P. Bernard, “Plausibility of long distance electrotelluric precursors to earthquakes,” *Journal of Geophysical Research*, vol. 97, pp. 17531–17546, 1992.
- [32] L. Jouniaux and J. P. Pozzi, “Streaming potential and permeability of saturated sandstones under triaxial stress: consequences for electrotelluric anomalies prior to earthquakes,” *Journal of Geophysical Research*, vol. 100, no. 6, pp. 10197–10209, 1995.
- [33] B. Lorne, F. Perrier, and J. P. Avouac, “Streaming potential measurements 2. Relationship between electrical and hydraulic flow patterns from rock samples during deformation,” *Journal of Geophysical Research B*, vol. 104, no. 8, pp. 17879–17896, 1999.
- [34] M. Fenoglio, M. Johnston, and J. Byerlee, “Magnetic and electric fields associated with changes in high pore pressure in fault zones: application to the loma prieta ULF emissions,” *Journal of Geophysical Research*, vol. 100, pp. 12951–12958, 1995.
- [35] J. Miyakoshi, “Anomalous time variation of the self-potential in the fractured zone of an active fault preceding the earthquake occurrence,” *Journal of Geomagnetism and Geoelectricity*, vol. 38, pp. 1015–1030, 1986.
- [36] C. W. Hunt and M. H. Worthington, “Borehole electrokinetic responses in fracture dominated hydraulically conductive zones,” *Geophysical Research Letters*, vol. 27, no. 9, pp. 1315–1318, 2000.
- [37] J. Moore and S. Glaser, “Self-potential observations during hydraulic fracturing,” *Journal of Geophysical Research*, vol. 112, no. 2, Article ID B02204, 2007.
- [38] N. Cuevas, J. Rector, J. Moore, and S. Glaser, “Electrokinetic coupling in hydraulic fracture propagation,” *SEG Technical Program Expanded Abstracts*, vol. 28, no. 1, pp. 1721–1725, 2009.
- [39] T. Ishido, H. Mizutani, and K. Baba, “Streaming potential observations, using geothermal wells and in situ electrokinetic coupling coefficients under high temperature,” *Tectonophysics*, vol. 91, no. 1-2, pp. 89–104, 1983.
- [40] G. Marquis, M. Darnet, P. Sailhac, A. K. Singh, and A. Gérard, “Surface electric variations induced by deep hydraulic stimulation: an example from the Soultz HDR site,” *Geophysical Research Letters*, vol. 29, article 1662, 4 pages, 2002.
- [41] M. Darnet and G. Marquis, “Modelling streaming potential (SP) signals induced by water movement in the vadose zone,” *Journal of Hydrology*, vol. 285, no. 1–4, pp. 114–124, 2004.
- [42] A. Maineult, Y. Bernabé, and P. Ackerer, “Detection of advected, recating redox fronts from self-potential measurements,” *Journal of Contaminant Hydrology*, vol. 86, pp. 32–52, 2006.
- [43] A. Maineult, M. Darnet, and G. Marquis, “Correction to on the origins of self-potential (SP) anomalies induced by water injections into geothermal reservoirs,” *Geophysical Research Letters*, vol. 33, Article ID L20319, 2006.
- [44] A. Maineult, L. Jouniaux, and Y. Bernabé, “Influence of the mineralogical composition on the self-potential response to advection of kcl concentration fronts through sand,” *Geophysical Research Letters*, vol. 33, Article ID L24311, 2006.
- [45] M. Darnet, G. Marquis, and P. Sailhac, “Hydraulic stimulation of geothermal reservoirs: fluid flow, electric potential and microseismicity relationships,” *Geophysical Journal International*, vol. 166, no. 1, pp. 438–444, 2006.
- [46] A. Maineult, E. Strobach, J. Renner et al., “Self-potential signals induced by periodic pumping,” *Journal of Geophysical Research*, vol. 113, Article ID B01203, 12 pages, 2008.
- [47] C. Doussan, L. Jouniaux, and J.-L. Thony, “Variations of self-potential and unsaturated water flow with time in sandy loam and clay loam soils,” *Journal of Hydrology*, vol. 267, no. 3-4, pp. 173–185, 2002.
- [48] P. Sailhac and G. Marquis, “Analytic potentials for the forward and inverse modeling of SP anomalies caused by

- subsurface fluid flow," *Geophysical Research Letters*, vol. 28, no. 9, pp. 1851–1854, 2001.
- [49] M. Darnet, G. Marquis, and P. Sailhac, "Estimating aquifer hydraulic properties from the inversion of surface streaming potential (SP) anomalies," *Geophysical Research Letters*, vol. 30, article 1679, 2003.
- [50] F. Perrier, M. Trique, B. Lorne, J.-P. Avouac, S. Hautot, and P. Tarits, "Electric potential variations associated with yearly lake level variations," *Geophysical Research Letters*, vol. 25, no. 10, pp. 1955–1958, 1998.
- [51] L. Jouniaux, J.-P. Pozzi, and J. Berthier, "Detection of fluid flow variations at the Nankai trough by electric and magnetic measurements in boreholes or at the seafloor," *Journal of Geophysical Research B*, vol. 104, no. 12, pp. 29293–29309, 1999.
- [52] J. H. Saunders, M. D. Jackson, and C. C. Pain, "Fluid flow monitoring in oilfields using downhole measurements of electrokinetic potential," *Geophysics*, vol. 73, no. 5, pp. E165–E180, 2008.
- [53] D. Fitterman, "Electrokinetic and magnetic anomalies associated with dilatant regions in a layered earth," *Journal of Geophysical Research*, vol. 83, pp. 5923–5928, 1978.
- [54] C. Fournier, *Méthodes géoélectriques appliquées à l'hydrogéologie en région volcanique; Développement de la méthode des potentiels spontanés en hydrogéologie*, Ph.D. thesis, University of Clermont-Ferrand, 1983.
- [55] W. Sill, "Self-potential modeling from primary flows," *Geophysics*, vol. 48, no. 1, pp. 76–86, 1983.
- [56] C. Fournier, "Spontaneous potentials and resistivity surveys applied to hydrogeology in a volcanic area: case history of the Chaîne des Puys (France)," *Geophysical Prospecting*, vol. 37, pp. 647–668, 1988.
- [57] T. Ishido and J. Pritchett, "Numerical simulation of electrokinetic potentials associated with subsurface fluid flow," *Journal of Geophysical Research B*, vol. 104, no. 7, pp. 15247–15259, 1999.
- [58] M. Sheffer and D. Oldenburg, "Three-dimensional modelling of streaming potential," *Geophysical Journal International*, vol. 169, no. 3, pp. 839–848, 2007.
- [59] D. Gilbert and M. Pessel, "Identification of sources potential fields with the continuous wavelet transform: application to self-potential profiles," *Geophysical Research Letters*, vol. 28, no. 9, pp. 1863–1866, 2001.
- [60] P. Sailhac, M. Darnet, and G. Marquis, "Electrical streaming potential measured at the ground surface: forward modeling and inversion issues for monitoring infiltration and characterizing the vadose zone," *Vadose Zone Journal*, vol. 3, pp. 1200–1206, 2004.
- [61] D. Gibert and P. Sailhac, "Comment on: self-potential signals associated with preferential groundwater flow pathways in sinkholes," *Journal of Geophysical Research*, vol. 113, Article ID B03210, 2008, by A. Jardani, J. P. Dupont, A. Revil.
- [62] B. Minsley, J. Sogade, and F. Morgan, "Three-dimensional modelling source inversion of self-potential data," *Journal of Geophysical Research*, vol. 112, Article ID B02202, 13 pages, 2007.
- [63] V. Naudet, J. Fernandez-Martinez, E. Garcia-Gonzalo, and J. Fernandez-Alvarez, "Estimation of water table from self-potential data using particle swarm optimization (psa)," *SEG Expanded Abstracts*, vol. 27, pp. 1203–1207, 2008.
- [64] H. El-Kaliouby and M. Al-Garni, "Inversion of self-potential anomalies caused by 2D inclined sheets using neural networks," *Journal of Geophysics and Engineering*, vol. 6, no. 1, pp. 29–34, 2009.
- [65] J. Fernandez-Martinez, E. Garcia-Gonzalo, and V. Naudet, "Particle swarm optimization applied to solving and appraising the streaming-potential inverse problem," *Geophysics*, vol. 75, no. 4, pp. WA3–WA15, 2010.
- [66] P. Pezard, S. Gautier, T. L. Borgne, B. Legros, and J. L. Deltombe, "MuSET: a multiparameter and high precision sensor for downhole spontaneous electrical potential measurements," *Comptes Rendus Geoscience*, vol. 341, no. 10–11, pp. 957–964, 2009.
- [67] S. Li, D. Pengra, and P. Wong, "Onsager's reciprocal relation and the hydraulic permeability of porous media," *Physical Review E*, vol. 51, no. 6, pp. 5748–5751, 1995.
- [68] P. W. J. Glover, I. I. Zadjali, and K. A. Frew, "Permeability prediction from MICP and NMR data using an electrokinetic approach," *Geophysics*, vol. 71, no. 4, pp. F49–F60, 2006.
- [69] H. Murakami, T. Hashimoto, N. Oshiman, S. Yamaguchi, Y. Honkura, and N. Sumitomo, "Electrokinetic phenomena associated with a water injection experiment at the Nojima fault on Awaji Island, Japan," *The Island Arc*, vol. 10, no. 3–4, pp. 244–251, 2001.
- [70] K. E. Butler and R. D. Russell, "Subtraction of powerline harmonics from geophysical records," *Geophysics*, vol. 58, no. 6, pp. 898–903, 1993.
- [71] K. E. Butler and R. D. Russell, "Cancellation of multiple harmonic noise series in geophysical records," *Geophysics*, vol. 68, no. 3, pp. 1083–1090, 2003.
- [72] D. Beamish, "Characteristics of near surface electrokinetic coupling," *Geophysical Journal International*, vol. 137, no. 1, pp. 231–242, 1999.
- [73] A. Thompson, S. Hornbostel, J. Burns et al., "Field tests of electroseismic hydrocarbon detection," *SEG Technical Program Expanded Abstracts*, vol. 24, p. 565, 2005.
- [74] J. C. Dupuis, K. E. Butler, and A. W. Kepic, "Seismoelectric imaging of the vadose zone of a sand aquifer," *Geophysics*, vol. 72, no. 6, pp. A81–A85, 2007.
- [75] M. H. P. Strahser, W. Rabbel, and F. Schildknecht, "Polarisation and slowness of seismoelectric signals: a case study," *Near Surface Geophysics*, vol. 5, no. 2, pp. 97–114, 2007.
- [76] S. S. Haines, A. Guitton, and B. Biondi, "Seismoelectric data processing for surface surveys of shallow targets," *Geophysics*, vol. 72, no. 2, pp. G1–G8, 2007.
- [77] S. Haines, *Seismoelectric imaging of shallow targets*, Ph.D. dissertation, Stanford University, 2004.
- [78] A. W. Adamson, *Physical Chemistry of Surfaces*, John Wiley & Sons, New York, NY, USA, 1976.
- [79] J. A. Davis, R. O. James, and J. Leckie, "Surface ionization and complexation at the oxide/water interface. I. Computation of electrical double layer properties in simple electrolytes," *Journal of Colloid And Interface Science*, vol. 63, no. 3, pp. 480–499, 1978.
- [80] R. Hunter, *Zeta Potential in Colloid Science: Principles and Applications*, Academic, New York, NY, USA, 1981.
- [81] P. Glover and M. Jackson, "Borehole electrokinetics," *The Leading Edge*, vol. 29, no. 6, pp. 724–728, 2010.
- [82] S. Pride, "Governing equations for the coupled electromagnetics and acoustics of porous media," *Physical Review B*, vol. 50, no. 21, pp. 15678–15696, 1994.
- [83] J. Davis and D. Kent, "Surface complexation modeling in aqueous geochemistry," in *Mineral Water Interface Geochemistry*, M. F. Hochella and A. F. White, Eds., Mineralogical Society of America, 1990.
- [84] G. Sposito, *The Chemistry of Soils*, Oxford University, Oxford, UK, 1989.

- [85] G. Parks, "The isoelectric points of solid oxides, solid hydroxides, and aqueous hydroxo complex systems," *Chemical Reviews*, vol. 65, no. 2, pp. 177–198, 1965.
- [86] B. Lorne, F. Perrier, and J.-P. Avouac, "Streaming potential measurements: 1. Properties of the electrical double layer from crushed rock samples," *Journal of Geophysical Research B*, vol. 104, no. 8, pp. 17857–17877, 1999.
- [87] P. Van Cappellen, L. Charlet, W. Stumm, and P. Wersin, "A surface complexation model of the carbonate mineral-aqueous solution interface," *Geochimica et Cosmochimica Acta*, vol. 57, no. 15, pp. 3505–3518, 1993.
- [88] X. Guichet, L. Jouniaux, and N. Catel, "Modification of streaming potential by precipitation of calcite in a sand-water system: laboratory measurements in the pH range from 4 to 12," *Geophysical Journal International*, vol. 166, no. 1, pp. 445–460, 2006.
- [89] L. Onsager, "Reciprocal relations in irreversible processes. I," *Physical Review*, vol. 37, no. 4, pp. 405–426, 1931.
- [90] D. Miller, "Thermodynamics of irreversible processes: the experimental verification of the onsager reciprocal relations," *Chemical Reviews*, vol. 60, no. 1, pp. 15–37, 1960.
- [91] J. Auriault and T. Strzelecki, "On the electro-osmotic flow in a saturated porous medium," *International Journal of Engineering Science*, vol. 19, no. 7, pp. 915–928, 1981.
- [92] K. Beddiar, Y. Berthaud, and A. Dupas, "Experimental verification of the onsager's reciprocal relations for electro-osmosis and electro-filtration phenomena on a saturated clay," *Comptes Rendus Mécanique*, vol. 330, no. 12, pp. 893–898, 2002.
- [93] V. Allègre, F. Lehmann, P. Ackerer, L. Jouniaux, and P. Sailhac, "Modelling the streaming potential dependence on water content during drainage: 1. A 1D modelling of SP using finite element method," *Geophysical Journal International*. In press.
- [94] L. Jouniaux, M.-L. Bernard, M. Zamora, and J.-P. Pozzi, "Streaming potential in volcanic rocks from Mount Peleé," *Journal of Geophysical Research B*, vol. 105, no. 4, pp. 8391–8401, 2000.
- [95] S. S. Dukhin and B. V. Derjaguin, *Surface and Colloid Science*, John Wiley & Sons, New York, NY, USA, 1974, Edited by E. Matijevic.
- [96] T. Ishido and H. Muzutani, "Experimental and theoretical basis of electrokinetic phenomena in rock-water systems and its applications to geophysics," *Journal of Geophysical Research*, vol. 86, no. 3, pp. 1763–1775, 1981.
- [97] L. Jouniaux and J.-P. Pozzi, "Permeability dependence of streaming potential in rocks for various fluid conductivities," *Geophysical Research Letters*, vol. 22, no. 4, pp. 485–488, 1995.
- [98] M. Z. Jaafar, J. Vinogradov, and M. D. Jackson, "Measurement of streaming potential coupling coefficient in sandstones saturated with high salinity NaCl brine," *Geophysical Research Letters*, vol. 36, no. 21, Article ID L21306, 2009.
- [99] J. Vinogradov, M. Jaafar, and M. D. Jackson, "Measurement of streaming potential coupling coefficient in sandstones saturated with natural and artificial brines at high salinity," *Journal of Geophysical Research B*, vol. 115, no. 12, Article ID B12204, 2010.
- [100] M. Ahmad, "A laboratory study of streaming potentials," *Geophysical Prospecting*, vol. 12, no. 1, pp. 49–64, 1964.
- [101] L. Jouniaux and J.-P. Pozzi, "Laboratory measurements anomalous 0.1–0.5 Hz streaming potential under geochemical changes: implications for electrotelluric precursors to earthquakes," *Journal of Geophysical Research B*, vol. 102, no. 7, pp. 15335–15343, 1997.
- [102] D. B. Pengra, S. X. Li, and P.-Z. Wong, "Determination of rock properties by low-frequency AC electrokinetics," *Journal of Geophysical Research B*, vol. 104, no. 12, pp. 29485–29508, 1999.
- [103] F. Perrier and T. Froidefond, "Electrical conductivity and streaming potential coefficient in a moderately alkaline lava series," *Earth and Planetary Science Letters*, vol. 210, no. 1–2, pp. 351–363, 2003.
- [104] S. Pride and M. W. Haartsen, "Electroseismic wave properties," *Journal of the Acoustical Society of America*, vol. 100, no. 3, pp. 1301–1315, 1996.
- [105] B. White and M. Zhou, "Electroseismic prospecting in layered media," *SIAM Journal on Applied Mathematics*, vol. 67, no. 1, pp. 69–98, 2006.
- [106] D. Smeulders, R. Eggels, and M. van Dongen, "Dynamic permeability: reformulation of theory and new experimental and numerical data," *Journal of Fluid Mechanics*, vol. 245, pp. 211–227, 1992.
- [107] P. M. Reppert, F. D. Morgan, D. P. Lesmes, and L. Jouniaux, "Frequency-dependent streaming potentials," *Journal of Colloid and Interface Science*, vol. 234, no. 1, pp. 194–203, 2001.
- [108] D. L. Johnson, J. Koplik, and R. Dashen, "Theory of dynamic permeability in fluid saturated porous media," *Journal of Fluid Mechanics*, vol. 176, pp. 379–402, 1987.
- [109] R. G. Packard, "Streaming potentials across glass capillaries for sinusoidal pressure," *The Journal of Chemical Physics*, vol. 21, pp. 303–307, 1953.
- [110] C. E. Cooke, "Study of electrokinetic effects using sinusoidal pressure and voltage," *The Journal of Chemical Physics*, vol. 23, no. 12, pp. 2299–2303, 1955.
- [111] J. Groves and A. Sears, "Alternating streaming current measurements," *Journal of Colloid And Interface Science*, vol. 53, no. 1, pp. 83–89, 1975.
- [112] A. Sears and J. Groves, "The use of oscillating laminar flow streaming potential measurements to determine the zeta potential of a capillary surface," *Journal of Colloid And Interface Science*, vol. 65, no. 3, pp. 479–482, 1978.
- [113] R. Chandler, "Transient streaming potential measurements on fluid-saturated porous structures: an experimental verification of Biot's slow wave in the quasi-static limit," *Journal of the Acoustical Society of America*, vol. 70, no. 1, pp. 116–121, 1981.
- [114] F. Schoemaker, D. Smeulders, and E. Slob, "Simultaneous determination of dynamic permeability and streaming potential," *SEG Technical Program Expanded Abstracts*, vol. 26, no. 1, pp. 1555–1559, 2007.
- [115] F. C. Schoemaker, D. M. J. Smeulders, and E. C. Slob, "Electrokinetic effect: theory and measurement," *SEG Technical Program Expanded Abstracts*, vol. 27, no. 1, pp. 1645–1649, 2008.
- [116] E. Tardif, P. Glover, and J. Ruel, "Frequency-dependent streaming potential of Ottawa sand," *Journal of Geophysical Research B*, vol. 116, no. 4, Article ID B04206, 2011.
- [117] M. W. Haartsen and S. R. Pride, "Electroseismic waves from point sources in layered media," *Journal of Geophysical Research B*, vol. 102, no. b11, pp. 24745–24769, 1997.
- [118] M. W. Haartsen, W. Dong, and M. N. Toksöz, "Dynamic streaming currents from seismic point sources in homogeneous poroelastic media," *Geophysical Journal International*, vol. 132, no. 2, pp. 256–274, 1998.
- [119] S. Garambois and M. Dietrich, "Seismoelectric wave conversions in porous media: field measurements and transfer function analysis," *Geophysics*, vol. 66, no. 5, pp. 1417–1430, 2001.

- [120] S. Garambois and M. Dietrich, "Full waveform numerical simulations of seismoelectromagnetic wave conversions in fluid-saturated stratified porous media," *Journal of Geophysical Research B*, vol. 107, no. 7, Article ID 2148, 2002.
- [121] C. Pain, J. H. Saunders, M. H. Worthington et al., "A mixed finite-element method for solving the poroelastic Biot equations with electrokinetic coupling," *Geophysical Journal International*, vol. 160, no. 2, pp. 592–608, 2005.
- [122] M. Schakel and D. Smeulders, "Seismoelectric reflection and transmission at a fluid/porous-medium interface," *Journal of the Acoustical Society of America*, vol. 127, no. 1, pp. 13–21, 2010.
- [123] Y. Gao and H. Hu, "Seismoelectromagnetic waves radiated by a double couple source in a saturated porous medium," *Geophysical Journal International*, vol. 181, no. 2, pp. 873–896, 2010.
- [124] Z. Zhu, M. W. Haartsen, and M. N. Toksöz, "Experimental studies of electrokinetic conversions in fluid-saturated borehole models," *Geophysics*, vol. 64, no. 5, pp. 1349–1356, 1999.
- [125] B. Chen and Y. Mu, "Experimental studies of seismoelectric effects in fluid-saturated porous media," *Journal of Geophysics and Engineering*, vol. 2, no. 3, pp. 222–230, 2005.
- [126] C. Bordes, L. Jouniaux, M. Dietrich, J.-P. Pozzi, and S. Garambois, "First laboratory measurements of seismomagnetic conversions in fluid-filled fontainebleau sand," *Geophysical Research Letters*, vol. 33, Article ID L01302, 5 pages, 2006.
- [127] G. I. Block and J. G. Harris, "Conductivity dependence of seismoelectric wave phenomena in fluid-saturated sediments," *Journal of Geophysical Research B*, vol. 111, no. 1, Article ID B01304, 12 pages, 2006.
- [128] C. Bordes, L. Jouniaux, S. Garambois, M. Dietrich, J.-P. Pozzi, and S. Gaffet, "Evidence of the theoretically predicted seismo-magnetic conversion," *Geophysical Journal International*, vol. 174, no. 2, pp. 489–504, 2008.
- [129] M. Schakel, D. Smeulders, E. Slob, and H. Heller, "Seismoelectric interface response: experimental results and forward model," *Geophysics*, vol. 76, no. 4, pp. N29–N36, 2011.
- [130] R. R. Thompson, "The seismic-electric effect," *Geophysics*, vol. 1, no. 3, pp. 327–335, 1936.
- [131] S. T. Martner and N. R. Sparks, "The electroseismic effect," *Geophysics*, vol. 24, no. 2, pp. 297–308, 1959.
- [132] L. T. Long and W. K. Rivers, "Field measurement of the electroseismic response," *Geophysics*, vol. 40, no. 2, pp. 233–245, 1975.
- [133] M. Strahser, L. Jouniaux, P. Sailhac, P.-D. Matthey, and M. Zillmer, "Dependence of seismoelectric amplitudes on water content," *Geophysical Journal International*, vol. 187, no. 3, pp. 1378–1392, 2011.
- [134] J. C. Dupuis, K. E. Butler, A. W. Kepic, and B. D. Harris, "Anatomy of a seismoelectric conversion: measurements and conceptual modeling in boreholes penetrating a sandy aquifer," *Journal of Geophysical Research B*, vol. 114, Article ID B10306, 9 pages, 2009.
- [135] S. S. Haines, S. R. Pride, S. L. Klemperer, and B. Biondi, "Seismoelectric imaging of shallow targets," *Geophysics*, vol. 72, no. 2, pp. G9–G20, 2007.
- [136] J. C. Dupuis and K. E. Butler, "Vertical seismoelectric profiling in a borehole penetrating glaciofluvial sediments," *Geophysical Research Letters*, vol. 33, no. 16, Article ID L16301, 2006.
- [137] A. Zohdy, L. Anderson, and L. Muffler, "Resistivity, self-potential, and induced polarization surveys of a vapor dominated geothermal system," *Geophysics*, vol. 38, no. 6, pp. 1130–1144, 1973.
- [138] L. Anderson and G. Johnson, "Application of the self-potential method to geothermal exploration in Long Valley, California," *Journal of Geophysical Research*, vol. 81, no. 8, pp. 1527–1532, 1976.
- [139] R. Corwin and D. Hoover, "The self-potential method in geothermal exploration," *Geophysics*, vol. 44, no. 2, pp. 226–245, 1979.
- [140] B. Wurmstich and F. Morgan, "Modeling of streaming potential responses caused by oil well pumping," *Geophysics*, vol. 59, no. 1, pp. 46–56, 1994.
- [141] M. Grant, I. Donaldson, and P. Bixley, *Geothermal Reservoir Engineering*, vol. 72, Academic press, 1982.
- [142] T. Ishido, "Streaming potential associated with hydrothermal convection in the crust: a possible mechanism of self-potential anomalies in geothermal areas," *Journal of the Geothermal Research Society of Japan*, vol. 3, pp. 87–100, 1981.
- [143] T. Ishido, T. Kikuchi, Y. Yano, M. Sugihara, and S. Nakao, "Hydrogeology inferred from the self-potential distribution, Kirishima geothermal field, Japan," *Geothermal Resources Council Transactions*, vol. 14, no. 2, pp. 916–926, 1990.
- [144] M. Hochstein, I. Mayhew, and R. Villarosa, "Self-potential surveys of the Mokai and Rotokawa high temperature fields (NZ)," in *Proceedings of the 12th New Zealand Geothermal Workshop*, vol. 17, pp. 87–89, 1990.
- [145] T. Ishido, T. Kikuchi, and M. Sugihara, "Mapping thermally driven upflows by the self-potential method," in *Hydrogeological Regimes and Their Subsurface Thermal Effects*, vol. 47 of *Geophysical Monograph*, pp. 151–158, 1989.
- [146] J. Zlotnicki and Y. Nishida, "Review on morphological insights of self-potential anomalies on volcanoes," *Surveys in Geophysics*, vol. 24, no. 4, pp. 291–338, 2003.
- [147] P. Reppert and F. Morgan, "Temperature-dependent streaming potentials: 2. Laboratory," *Journal of Geophysical Research B*, vol. 108, no. 11, Article ID 2547, 13 pages, 2003.
- [148] T. Tosha, N. Matsushima, and T. Ishido, "Zeta potential measured for an intact granite sample at temperatures to 200°C," *Geophysical Research Letters*, vol. 30, no. 6, Article ID 1295, 4 pages, 2003.
- [149] T. Ishido and N. Matsushima, "Streaming potential measured for an intact rock sample at temperatures to 200°C," in *Proceedings of the 32nd Workshop on Geothermal Reservoir Engineering*, Stanford University, 2007.
- [150] H. Hase, T. Ishido, S. Takakura, T. Hashimoto, K. Sato, and Y. Tanaka, "Zeta potential measurement of volcanic rocks from Aso caldera," *Geophysical Research Letters*, vol. 23, no. 30, Article ID 2210, 2003.
- [151] K. Aizawa, M. Uyeshima, and K. Nogami, "Zeta potential estimation of volcanic rocks on 11 island arc-type volcanoes in Japan: implication for the generation of local self-potential anomalies," *Journal of Geophysical Research*, vol. 113, no. 2, Article ID B02201, 2008.
- [152] P. Glover and N. Déry, "Streaming potential coupling coefficient of quartz glass bead packs: dependence on grain diameter, pore size, and pore throat radius," *Geophysics*, vol. 75, no. 6, pp. F225–F241, 2010.
- [153] C. Zablocki, "Mapping thermal anomalies on an active volcano by the self-potential method, Kilauea, Hawaii," in *Proceedings of the 2nd U.N. Symposium on the Development and Use of Geothermal Resources*, vol. 2, pp. 1299–1309, San Francisco, Calif, USA, 1976.
- [154] T. Hashimoto and Y. Tanaka, "A large self-potential anomaly on Unzen volcano, Shimabara Peninsula, Kyushu Island, Japan," *Geophysical Research Letters*, vol. 22, no. 3, pp. 191–194, 1995.

- [155] Y. Nishida, N. Matsushima, A. Goto et al., "Self-potential studies in volcanic areas (3) Miyake-jima, Esan and Usu," *Journal of the Hokkaido University Series 7*, vol. 10, no. 1, pp. 63–77, 1996.
- [156] Y. Sasai, J. Zlotnicki, Y. Nishida et al., "Electromagnetic monitoring of Miyake-jima volcano, Izu-Bonin arc, Japan: A preliminary report," *Journal of Geomagnetism and Geoelectricity*, vol. 49, no. 11-12, pp. 1293–1316, 1997.
- [157] S. Michel and J. Zlotnicki, "Self-potential and magnetic surveying of la Fournaise volcano (Reunion Island): correlations with faulting, fluid circulation, and eruption," *Journal of Geophysical Research B*, vol. 103, no. 8, pp. 17845–17857, 1998.
- [158] K. Aizawa, "A large self-potential anomaly and its changes on the quiet Mt. Fuji, Japan," *Geophysical Research Letters*, vol. 31, no. 5, Article ID L05612, 4 pages, 2004.
- [159] P. Bedrosian, M. Unsworth, and M. Johnston, "Hydrothermal circulation at mount St. Helens determined by self-potential measurements," *Journal of Volcanology and Geothermal Research*, vol. 160, no. 1-2, pp. 137–146, 2007.
- [160] K. Aizawa, "Classification of self-potential anomalies on volcanoes and possible interpretations for their subsurface structure," *Journal of Volcanology and Geothermal Research*, vol. 175, no. 3, pp. 253–268, 2008.
- [161] C. Fournier, "Spontaneous potentials and resistivity surveys applied to hydrogeology in a volcanic area: case history of the Chaîne des Puys (Puy-de-Dôme, France)," *Geophysical Prospecting*, vol. 37, no. 6, pp. 647–668, 1989.
- [162] A. Revil, V. Naudet, J. Nouzaret, and M. Pessel, "Principles of electrography applied to self-potential electrokinetic sources and hydrogeological applications," *Water Resources Research*, vol. 39, no. 5, Article ID 1114, 15 pages, 2003.
- [163] C. Zablocki, R. Tilling, D. Peterson, and R. Christiansen, "A deep research drill hole at the summit of an active volcano, kilauea, Hawaii," *Geophysical Research Letters*, vol. 1, no. 7, pp. 323–326, 1974.
- [164] K. Aizawa, Y. Ogawa, and T. Ishido, "Groundwater flow and hydrothermal systems within volcanic edifices: delineation by electric self-potential and magnetotellurics," *Journal of Geophysical Research*, vol. 114, no. 1, Article ID B01208, 2009.
- [165] T. Ishido, *Volcano Monitoring Using Self-Potential Technique*, EGU General Assembly, Vienna, Austria, 2006, Abstract EGU06-A-00975.
- [166] T. Ishido, *Self-Potential Changes Caused by Magma Ascent and Degassing*, AGU Fall Meeting, San Francisco, Calif, USA, 2009, Abstract V33F-03.
- [167] B. Nourbehecht, *Irreversible thermodynamic effects in inhomogeneous media and their applications in certain geoelectric problems*, Ph.D. thesis, MIT Press, Cambridge, Mass, USA, 1963.
- [168] D. Fitterman, "Correction to theory of electrokinetic-magnetic anomalies in a fault halfspace," *Journal of Geophysical Research*, vol. 86, pp. 9585–9588, 1981.
- [169] T. Ishido, "Self-potential generation by subsurface water flow through electrokinetic coupling," in *Detection of Subsurface Flow Phenomena, Lecture Notes in Earth Sciences*, vol. 27, pp. 121–131, 1989.
- [170] K. Yasukawa, T. Ishido, and I. Suzuki, "Geothermal reservoir monitoring by continuous self-potential measurements, Mori geothermal field, Japan," *Geothermics*, vol. 34, no. 5, pp. 551–567, 2005.
- [171] T. Toshi, T. Ishido, N. Matsushima, and Y. Nishi, "Self-potential variation at the Yanaizu-Nishiyama geothermal field and its interpretation by the numerical simulation," in *Proceedings of the World Geothermal Congress*, vol. 3, pp. 1871–1876, Beppu-Morioka, Japan, 2000.
- [172] Y. Nishi and T. Ishido, "Self-potential measurements for reservoir monitoring at the Okuaizu geothermal field," *Journal of the Geothermal Research Society of Japan*. In press.
- [173] N. Matsushima, T. Kikuchi, T. Toshi et al., "Repeat SP measurements at the Sumikawa geothermal field, Japan," in *Proceedings of the World Geothermal Congress*, pp. 2725–2730, Beppu-Morioka, Japan, 2000.
- [174] T. Ishido, *Changes in Self-Potential Caused by Redox Reaction*, SGEPPS, Sendai, Japan, 2008, Abstract A003–07.
- [175] T. Ishido and J. Pritchett, "Prediction of magnetic field changes induced by geothermal fluid production and reinjection," *Geothermal Resources Council Transactions*, vol. 25, pp. 645–649, 2001.
- [176] H. Mizutani and T. Ishido, "A new interpretation of magnetic field variation associated with the Matsushiro earthquakes," *Journal of Geomagnetism and Geoelectricity*, vol. 28, pp. 179–188, 1976.
- [177] J. Zlotnicki and J. L. Mouel, "Possible electrokinetic origin of large magnetic variations at La Fournaise volcano," *Nature*, vol. 343, no. 6259, pp. 633–636, 1990.
- [178] Y. Nishi, T. Ishido, M. Sugihara et al., "Reservoir monitoring in the Okuaizu geothermal field using multi-geophysical survey techniques," in *Proceedings of the World Geothermal Congress*, Antalya, Turkey, 2005.
- [179] T. Ishido, K. Goko, T. Toshi, M. Adachi, J. Ishizaki, and Y. Nishi, "Reservoir monitoring using multi-geophysical survey techniques," *Geothermal Resources Council Transactions*, vol. 27, pp. 827–831, 2003.
- [180] T. Ishido, K. Goko, M. Adachi et al., "System integration of various geophysical measurements for reservoir monitoring," in *Proceedings of the World Geothermal Congress*, Antalya, Turkey, April 2005.

Research Article

Characterization of Fractured Reservoirs Using a Combination of Downhole Pressure and Self-Potential Transient Data

Yuji Nishi and Tsuneo Ishido

GSJ, National Institute of Advanced Industrial Science and Technology (AIST), Tsukuba Central 7, Tsukuba, Ibaraki 305-8567, Japan

Correspondence should be addressed to Tsuneo Ishido, ishido-t@aist.go.jp

Received 1 July 2011; Revised 11 October 2011; Accepted 8 November 2011

Academic Editor: Laurence Jouniaux

Copyright © 2012 Y. Nishi and T. Ishido. This is an open access article distributed under the Creative Commons Attribution License, which permits unrestricted use, distribution, and reproduction in any medium, provided the original work is properly cited.

In order to appraise the utility of self-potential (SP) measurements to characterize fractured reservoirs, we carried out continuous SP monitoring using multi Ag-AgCl electrodes installed within two open holes at the Kamaishi Mine, Japan. The observed ratio of SP change to pressure change associated with fluid flow showed different behaviors between intact host rock and fractured rock regions. Characteristic behavior peculiar to fractured reservoirs, which is predicted from numerical simulations of electrokinetic phenomena in MINC (multiple interacting continua) double-porosity media, was observed near the fractures. Semilog plots of the ratio of SP change to pressure change observed in one of the two wells show obvious transition from intermediate time increasing to late time stable trends, which indicate that the time required for pressure equilibration between the fracture and matrix regions is about 800 seconds. Fracture spacing was estimated to be a few meters assuming several micro-darcies (10^{-18} m²) of the matrix region permeability, which is consistent with geological and hydrological observations.

1. Introduction

Geothermal reservoirs are frequently found in fractured rock formations which are otherwise nearly impermeable. The fractures serve as conduits for the geothermal fluids, and the relatively low-permeability country rock provides the reservoir storage capacity. The spacing between the discontinuities (faults/fractures/joints) is obviously an important parameter in any mathematical description of fluid flow through fissured rocks. Apart from major fault zones which is necessary to be modeled individually, the spacing (λ) of the discontinuities is usually small compared to the reservoir dimensions (L). Hence, the fissured rock mass can be treated as a continuum on an intermediate length scale (l), with $\lambda < l < L$ [1].

One continuum description of such a system is provided by the so-called “double-porosity model” (e.g., [2, 3]), in which the fractures and the porous matrix blocks are regarded as two separate but overlapping continua. But this approach is of limited utility in geothermal reservoir engineering mainly due to employment of analytical approximations for mass and energy exchange between the two

continua. Pruess and Narasimhan [4] developed the “MINC” (multiple interacting continua) model, which circumvents the difficulties associated with the estimation of mass and energy exchange between the fracture and matrix regions. The “MINC” method was successfully applied to explain, for example, “excess enthalpy” phenomena [5]; when a well is drilled into the fractured reservoir and fluid is withdrawn, the enthalpy of the stable fluid discharge is often anomalously high—sometimes the well discharges steam alone even though the reservoir is initially filled with almost liquid water. Pritchett and Garg [1] showed that two time constants are key parameters in characterizing two-phase flow in fractured reservoirs: the time required for pressure equilibration (τ_{pe}) and temperature equilibration (τ_{tc}) between the fracture and matrix regions, both of which are proportional to the square of fracture spacing (λ^2).

In the problem of cold water injection into a geothermal reservoir, the cold water advancement in a fractured reservoir that is represented as “MINC” double-porosity medium will be very different from that in a reservoir that can be represented by equivalent porous medium. In the fractured

reservoir, the cold water will advance along the fracture zones, gradually extract heat from the adjacent rock matrix, and eventually arrive at the production wells. If the representative time scale t_R is shorter than τ_{hc} , the cold water has not fully heated up by then, which brings about undesired effects on heat recovery from decreasing fluid enthalpies. To achieve more complete heat recovery from the matrix rocks, we need to reduce the injection rate so as that the representative time scale is sufficiently longer than $\tau_{hc} \propto \lambda^2$ (e.g., [6, 7]).

It is highly desirable to know the time constants τ_{pe} and τ_{hc} in advance for prediction of two-phase flow behavior and/or cold water advancement in fractured geothermal reservoirs. Ishido and Pritchett [8] extended the so-called EKP-postprocessor [9] to apply it to fractured reservoirs represented by MINC media. They carried out pressure-transient simulations and calculated associated “self-potential transients” by using the extended EKP-postprocessor and showed that much more pronounced differences will be brought about in the self-potential transients between competing “fractured/MINC” and “porous-medium” descriptions of the same reservoir than is the case for pressure transients. They suggested that combining continuous pressure and SP measurements may therefore provide a means for better characterizing fractured geothermal reservoirs. This prediction motivated us to carry out flow tests at the Kamaishi Mine in Japan.

Self-potential (SP) observations associated with flow tests of boreholes have been conducted in various fields by now (e.g., [13–17]). Among them, SP observations designed for hydraulic characterization of groundwater aquifers were also conducted; the SP signals, which complement piezometric observations, were used to estimate the transmissivity of aquifers (e.g., [18–21]).

In the present study, we focus on the characterization of fractured reservoirs. First, SP transient signals expected for fractured reservoirs are explained based upon the results of numerical simulations [8, 10], and then SP data obtained from experiments at the Kamaishi Mine are described and interpretation of the data is discussed.

2. SP Transients in Fractured Reservoirs

2.1. Electrokinetic Coupling. The flow of a fluid through a porous medium will generate an electrical potential gradient (called the electrokinetic or streaming potential) along the flow path by the interaction of the moving pore fluid with the electrical double layer at the pore surface. This process is known as electrokinetic coupling. The general relations between the electric current density \mathbf{I} and fluid volume flux \mathbf{J} and the electric potential gradient $\nabla\phi$ and pore pressure gradient $(\nabla P - \rho\mathbf{g})$ forces are

$$\mathbf{I} = -L_{ee}\nabla\phi - L_{ev}(\nabla P - \rho\mathbf{g}), \quad (1)$$

$$\mathbf{J} = -L_{ve}\nabla\phi - L_{vv}(\nabla P - \rho\mathbf{g}), \quad (2)$$

where the L_{ij} are phenomenological coefficients (e.g., [22]). The first term on the right-hand side in (1) represents Ohm’s law, and the second term in (2) represents Darcy’s law.

The cross-coupling terms (with the L_{ev} and L_{ve} coefficients) represent the electrokinetic effect, $L_{ev} = L_{ve}$ according to Onsager’s reciprocal relations. See the tutorial of this special issue for more details (Jouniaux and Ishido, this issue).

Based upon a capillary model, the above coefficients may be written as follows (e.g., [20]):

$$L_{ev} = -\frac{\eta\varepsilon\zeta R_{ev}G}{\tau\mu}, \quad (3)$$

$$L_{ee} = \frac{\eta(\sigma + m^{-1}\Sigma_s)}{\tau}, \quad (4)$$

where η = porosity, ε = liquid-phase dielectric permittivity, ζ = zeta-potential, R_{ev} = “electrical relative permeability” for liquid/gas two-phase flow, G = correction factor which becomes less than unity only if the hydraulic radius is comparable to the thickness of the electrical double layer, τ = square of tortuosity ($\tau = t^2$), μ = liquid-phase viscosity, σ = electrical conductivity of pore fluid (two-phase mixture), m = hydraulic radius of pores and/or cracks, which equals half of radius and aperture for pores with circular and slit-like cross-sections, respectively, and Σ_s = surface conductance.

Equation (1) describes the total current density, composed of a drag (convection) current density \mathbf{I}_{drag} caused by charges moved by fluid flow and a conduction current density \mathbf{I}_{cond} caused by electric conduction; hence,

$$\mathbf{I} = \mathbf{I}_{cond} + \mathbf{I}_{drag}, \quad (5)$$

where

$$\begin{aligned} \mathbf{I}_{cond} &= -L_{ee}\nabla\phi, \\ \mathbf{I}_{drag} &= -L_{ev}(\nabla P - \rho\mathbf{g}). \end{aligned} \quad (6)$$

In the absence of external current sources, $\nabla \cdot \mathbf{I} = 0$, so from (5),

$$\nabla \cdot \mathbf{I}_{cond} = -\nabla \cdot \mathbf{I}_{drag}. \quad (7)$$

Equation (7) represents sources of conduction current that are required for the appearance of electrical potential.

In a homogeneous region with a homogeneous density (ρ), (7) can be written as

$$\nabla^2\phi = C\nabla^2(P - \rho g z), \quad (8)$$

where C is called the streaming potential coefficient, which is given as follows in case of liquid single-phase flow (and $G = 1$),

$$C = -\frac{L_{ev}}{L_{ee}} = \frac{\varepsilon\zeta}{(\sigma + m^{-1}\Sigma_s)\mu}. \quad (9)$$

If the pore pressure change occurs within a finite homogeneous volume, the following relation between changes in ϕ (streaming potential) and $(P - \rho g z)$ (pressure) prevails:

$$\Delta\phi = C\Delta(P - \rho g z). \quad (10)$$

2.2. *EKP Postprocessor.* The cross-coupling term in (2) may be safely neglected for typical geologic situations, and Darcy's law alone may be used to model the hydraulic problem; it is not necessary to solve (1) and (2) simultaneously. A "postprocessor" may then be used to calculate the drag current (\mathbf{I}_{drag}) from the results of an unsteady thermohydraulic reservoir simulation.

The "EKP-postprocessor" [9, 23] simulates electric potentials caused by subsurface fluid flow by a two-step process. First, it calculates the distribution of L_{ev} , L_{ee} , and \mathbf{I}_{drag} from the reservoir-simulation results using the same spatial grid used for the reservoir simulation calculation (called the RSV grid hereafter). Next, the postprocessor calculates the electric potential (ϕ) distribution by solving the above Poisson equation (7) within a finite-difference grid that is usually much greater in spatial extent than the RSV grid (hereafter called the SP grid).

Within that portion of the SP grid overlapped by the RSV grid, the distribution of electrical conductivity is obtained directly from RSV grid values. Elsewhere within the SP grid, the electrical conductivity distribution is user specified and time invariant. Ordinarily, boundary conditions on the potential are zero normal gradients (Neumann condition) on the ground surface (upper surface) and zero potential (Dirichlet condition) along the bottom and vertical sides of the SP grid. Equation (7) is solved numerically using a Gauss-Seidel iteration procedure incorporating intermittent automatic optimization of the overrelaxation factor.

2.3. *Model for Drag Current in MINC Media.* The model which Ishido and Pritchett [8] adopted to calculate the drag current density in "MINC" media [4] amounts to the following:

$$\mathbf{I}_{\text{drag}} = \mathbf{I}_f + \mathbf{I}_m, \quad (11)$$

with

$$\begin{aligned} \mathbf{I}_f &= \left[\frac{\varepsilon \zeta \eta R_{ev} G(\nabla P - \rho \mathbf{g})}{\tau \mu} \right]_f \times \psi, \\ \mathbf{I}_m &= \left[\frac{\varepsilon \zeta \eta R_{ev} G(\nabla P - \rho \mathbf{g})}{\tau \mu} \right]_m \times (1 - \psi), \end{aligned} \quad (12)$$

where \mathbf{I}_{drag} = total drag current density vector, \mathbf{I}_f = drag current density due to fracture zone effects, \mathbf{I}_m = drag current density due to matrix region effects, ψ = fracture zone volume/total volume, and where subscript "f" denotes conditions in the fracture zone, and subscript "m" denotes "averaged" conditions in the matrix region (see [8] for further details). We detail now the SP transients related to a continuous injection, first for the MINC double-porosity media, and secondly for the reservoir model taking into account individual fractures and a borehole. We show that the characteristic behavior of SP predicted by the first model is present in the second model only if a skin zone with a lower streaming potential coefficient is assumed.

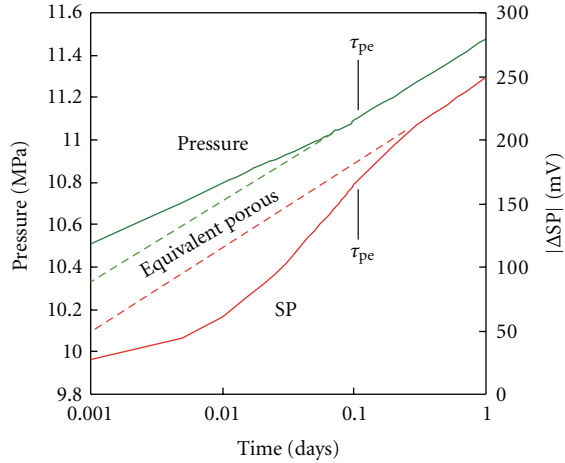
2.4. *Pressure and SP Transients in MINC Media.* Ishido and Pritchett [8] performed a pressure-transient simulation for

a two-dimensional axisymmetric horizontal reservoir model. The formation is represented by an "MINC" double-porosity medium with the following properties: global permeability: $k = 10^{-14} \text{ m}^2$, fracture zone volume fraction: $\psi = 0.1$, fracture zone porosity: $\eta_f = 0.1$, matrix region porosity: $\eta_m = 0.1$, matrix region permeability: $k_m = 10^{-17} \text{ m}^2$, and fracture spacing: $\lambda = 10 \text{ m}$. (In the present parameter setting, the fracture zone permeability is $k/\psi = 10^{-13} \text{ m}^2$, which is due to fractures occupying 10% volume of the fracture zone. The rest 90% volume is assumed to be of impermeable rock matrix.) The time required ($\tau_{pe} = \eta_m \mu C_t \lambda^2 / 10 k_m$) for pressure equilibration between the fracture and matrix regions is $\sim 10^4 \text{ sec}$ (here C_t : total system (fluid plus rock) compressibility). The initial thermodynamic state is uniform (temperature = 200°C and pressure = 10 MPa). For the corresponding SP calculations shown in Figure 1, the reservoir fluid's NaCl concentration is assumed to be 0.02 mol/L, and the formation conductivity L_{ee} is assumed to be 0.03 S/m (homogeneous).

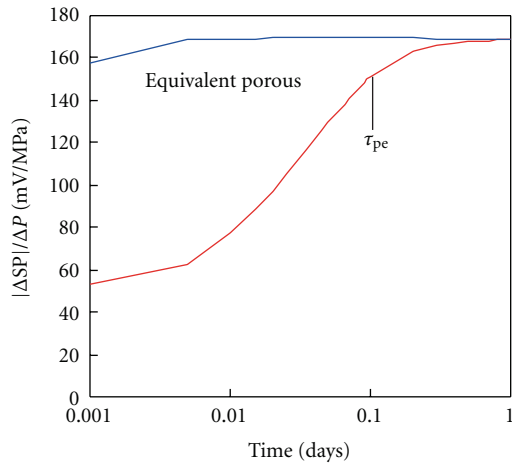
Figure 1(a) shows semilog plots of changes in pressure and in SP due to continuous injection at 0.5 tons per hour per meter of reservoir thickness. The pressure transient at a point near the injection well shows behavior typical of a double-porosity medium; the late-time slope develops after the time required for pressure equilibrium within the matrix region τ_{pe} has elapsed.

The SP transient exhibits three segments. The drag current contribution through the matrix region is small at early times (up to ~ 0.01 day), so the slope is smaller than that at late times (after ~ 0.1 day), by the factor ψ (=0.1). At intermediate times, SP changes rapidly with increasing involvement of matrix region. The time τ_{pe} can be clearly identified at the intersection of the intermediate-time and late-time semilog straight lines (In Figure 1, the "observation" point is not located within the borehole, but ~ 5 meters away from the injection well. The reason for this is that in the case of "open hole," the SP change within the borehole does not show the typical behavior like that shown in Figure 1 since the pressure in the matrix region coincides with the borehole pressure even in early times as approaching the borehole. This topic will be explained in the next Section 2.5).

Figure 1(b) shows the ratio of SP changes to pressure changes for the results shown in Figure 1(a). In the case of the equivalent porous medium, relationship (10) is satisfied for the entire period, resulting in an almost constant ratio. In this plot, the difference between double-porosity and equivalent porous medium behavior is much more apparent and the time τ_{pe} is more evident than in a plot of SP change itself shown in Figure 1(a). The change-ratio plot has the additional advantage that, in real situations, pressure transient data suffer from fluctuations in the sandface flow-rate, so it is often difficult to discern the three segments such as those shown in Figure 1(a). By contrast, the ratio of SP change to pressure change is insensitive to flow-rate fluctuations, so a combination of pressure and SP measurements is expected to provide a more robust and reliable technique for fractured reservoir characterization.



(a)



(b)

FIGURE 1: Results from the MINC double-porosity model. (a) Changes in pressure and SP at a point ~ 5 m away from the injection well (open hole) during injection test for fractured medium (after [8]). The pressure and SP changes for the equivalent porous medium are shown by broken curves. (b) Plot of the ratio of SP change to pressure change converted from the pressure and SP changes shown in (a).

2.5. Near-Field Effects. In the calculations described in the previous section, the “near-field” effects around a borehole were not considered. Ishido et al. [10] constructed a reservoir model to treat a borehole and individual fractures explicitly instead of using the MINC double-porosity representation (Figure 2). The model is axisymmetric, eight meters thick, and of 1 km horizontal extent (radius). Five equally spaced horizontal fractures intersect the borehole located along the axis of symmetry (only two fractures are drawn schematically in Figure 2). Sufficiently fine block spacing was adopted near the borehole (radius of 0.075 meter) to represent the well casing. Fine block spacing was also used for the host rock (matrix) region close to the fracture zone so as to resolve the high electrical potential gradients there. Here, only the

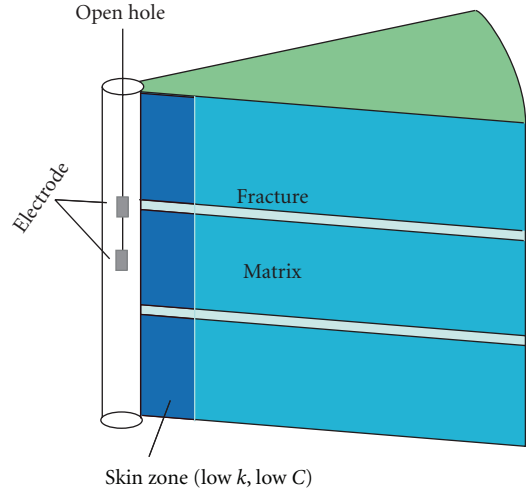


FIGURE 2: “Open hole” model used for numerical simulation of SP transient near a borehole (after [10]). In “open (skin)” case, a skin zone of low permeability and low magnitude of streaming potential coefficient is assumed for the matrix region.

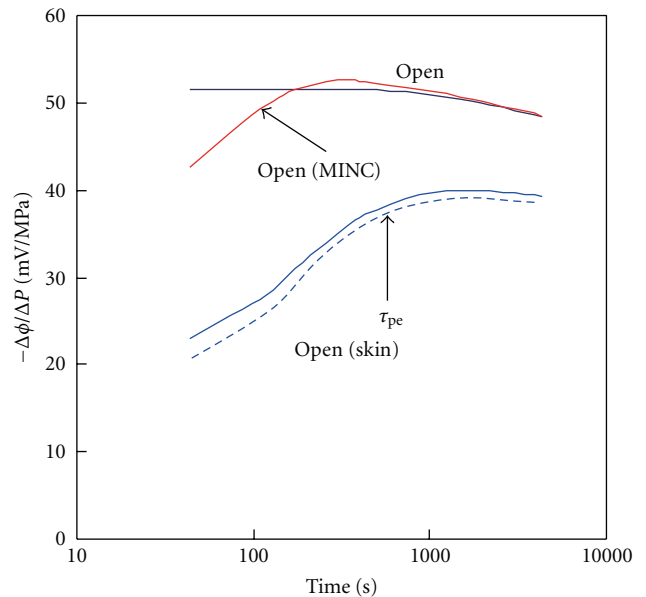


FIGURE 3: The ratio of SP change to pressure change as a function of time (after [10]). Results from the reservoir model, for (a) open hole homogeneous case “open” and (b) open hole with a skin-zone case “open (skin)”; (c) Result from the equivalent MINC double-porosity model “open (MINC).”

results for open hole cases are explained. See [10] for the results of cased wells.

The formation properties are: fracture zone permeability: $k_f = 10^{-12} \text{ m}^2$, fracture zone thickness = 0.01 m, fracture zone porosity: $\eta_f = 0.5$, host rock porosity: $\eta_m = 0.01$, host rock permeability: $k_m = 10^{-18} \text{ m}^2$, and fracture spacing: $\lambda = 1 \text{ m}$. The time required (τ_{pe}) for pressure equilibration between the fracture and host rock regions is ~ 500 sec. The initial thermodynamic state is uniform (temperature = 45°C

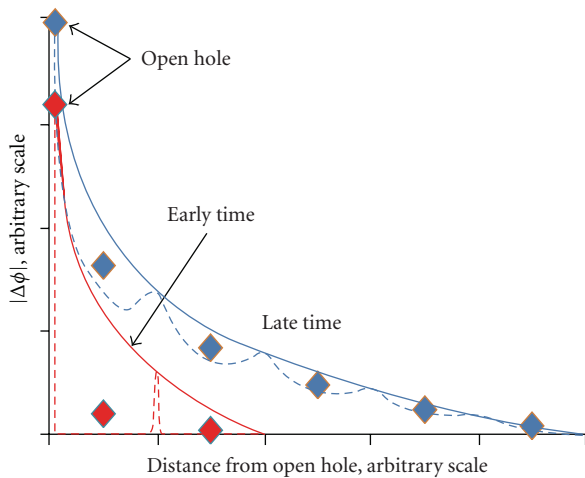


FIGURE 4: Results from the reservoir model taking into account individual fractures and a borehole. Schematic diagram showing the distribution of “microscopic” potential in the fracture (solid lines) and matrix (broken lines) regions in the reservoir, which is equal to change in local pressure multiplied by the streaming potential coefficient C (here homogeneous C is assumed for simplicity). “Macroscopic” potential (\blacklozenge) calculated for MINC-medium blocks corresponds to an averaged potential over the fracture and matrix regions (after [10]).

and pressure = 10 MPa). Fluid production takes place from the borehole with a constant pressure drawdown of 1 MPa. For the corresponding SP calculations, the reservoir fluid’s NaCl concentration is assumed to be 0.005 mol/L, and the streaming potential coefficient is uniform throughout the fracture and host rock regions.

In the “open hole” cases, the SP change that would be measured by electrode(s) installed within the borehole (Figure 2) is calculated, and then the ratio of SP change to pressure change is plotted as a function of time (Figure 3). As Figure 3 shows, the “open” ratio is almost constant with time, which is similar to the “equivalent porous medium” behavior shown in Figure 1(b) and does not exhibit any characteristic fractured reservoir behavior.

But if a skin zone in which the streaming potential coefficient is much smaller than that of the outer matrix region is present, the typical double-porosity behavior appears in the plot (“open (skin)” curves in Figure 3). Although the SP change magnitude is independent of the location of the electrode for the case without a skin zone, the SP change is slightly smaller at the electrode located at the matrix region for the case with skin zone as shown by the broken line in Figure 3.

In Figure 3, also shown (in red) is the result for a case in which the reservoir is represented by “equivalent” MINC double-porosity medium. In this “open (MINC)” case, the SP/pressure change ratio exhibits similar behavior as that of “open” case. This is because the present scheme used by the EKP postprocessor to calculate SP in an MINC medium gives an “averaged” potential over the fracture and matrix regions.

Figure 4 illustrates the spatial distribution of “microscopic” potential, which is the streaming potential coefficient

multiplied by local pressure change, in the fracture and matrix regions around an open hole. Along the wall of the open hole, the local pressures in both the fracture and matrix regions are equal to the borehole pressure, so the microscopic potentials in both the regions converge as the borehole is approached. This is the reason why the SP change is in proportion to the pressure change within the borehole in the “open” case. However, in the “open (skin)” case, substantial drag current is not induced in the matrix region, while a large pressure gradient remains within the skin zone. So, SP change within the borehole is brought about solely by the drag current induced in the fracture zone, resulting in smaller SP change magnitude at early times.

3. Field Experiments at the Kamaishi Mine

The Kamaishi Mine had been one of the largest mines in Japan, which produced copper and iron ore over 130 years since 1857 (see the inset of Figure 5 for its location). The total amount of ore mined during this period is about 70 million tons. The galleries of ~ 140 km in total length were made mainly in hard rocks composed of Kitakami Paleozoic granitic rocks, Mesozoic granitic intrusions, and skarn ore deposits formed at the contacts of the intrusions. During the last more than two decades, the mine has been diversifying from mining into underground research sites for developing new methods of geological and geophysical studies and for rock mechanics, hydrology, and so forth (e.g., [24]). In this section, we describe the experiments performed by inducing a fluid flow from horizontal wells, which causes pressure disturbance along the entire borehole both in the fracture and host rock matrix regions.

3.1. Outline of Measurements. We carried out flow tests and pressure and SP measurements in two open holes (KF-1 and KF-3) which were drilled nearly horizontally from the wall of one of the levels into the surrounding granodiorite body (both wells were drilled in the direction $\sim 15^\circ$ from the direction of the tunnel on the horizontal plane as shown in Figure 5). Both wells maintain stable pressures of about five bars under shut-in conditions, so that flow tests may be carried out by simply opening and closing the wellhead valves. After preliminary experiments in 2005 and 2006 [25], we installed twelve custom-made silver-silver chloride electrodes in each of the two wells in 2007 [26].

To reduce flow effects on measuring electrodes, each silver-silver chloride electrode was installed in a container made of hard plastic tube, the upstream and downstream ends of which were closed and open (via sponge), respectively (Figure 6). The voltages between each electrode and the reference (the location of which is shown in Figure 5) and the pressure and flow rate of the two wells were recorded with two data loggers Campbell Scientific’s CR5000. The valve operation of wells KF-1 and KF-3 was automatically controlled, and all measuring equipments were powersupplied by a few car batteries, which were fully charged at maintenance time. One unit of the experiment was carried out in two days; KF-1 was opened for one hour on the first

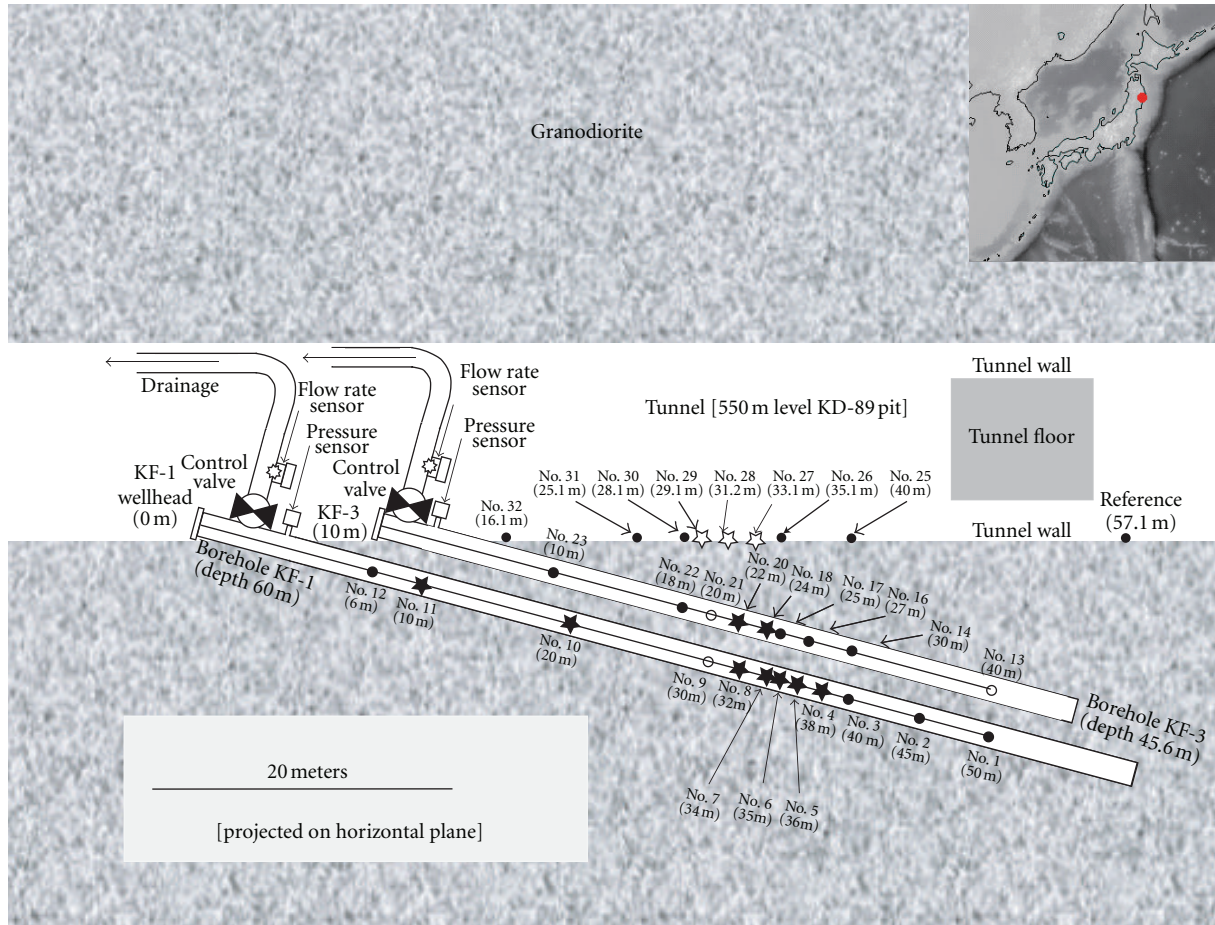


FIGURE 5: Plan view of experimental setup of pressure and SP measurements at the Kamaishi Mine in April–June 2007. Ag–AgCl electrodes No. 1 to 12 and No. 13 to 24 were installed in wells KF-1 and KF-3, respectively. Ag–AgCl electrodes were also installed on the tunnel floor at eight points No. 25 to 32 and at the reference point. Locations of the borehole electrodes near permeable fractures which showed distinguishable behaviors from those of other electrodes are shown by solid asterisks. Locations of tunnel floor electrodes which showed SP changes corresponding to the flow from KF-1 or KF-3 are shown by open asterisks. Locations of other electrodes are shown by solid or open circles (open circles show the locations of electrodes which were sometimes unstable during the period from April to June 2007).

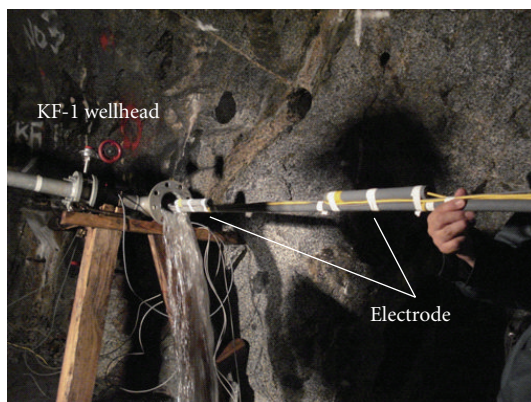


FIGURE 6: Photo of installation of custom-made Ag–AgCl electrode which is contained in a plastic tube into well KF-1.

day, and then KF-3 was opened for one hour on the second day. We repeated this procedure as many as possible with various valve openings in April through June 2007.

Examples of the test results are shown in Figure 7. In Figure 7(a), the results are shown for an experiment when well KF-1 was flowing on May 13. The two wells are connected to each other through permeable fractures, so KF-3 pressure also substantially decreased. Corresponding to the pressure decreases, SP in both wells KF-1 and KF-3 increased several millivolts. Concerning the SP changes on the tunnel (level) floor, their appearance is restricted to an interval of ~5 meters near the fracture zones; only three electrodes nos. 27, 28, and 29 (see Figure 5 for the locations) showed a few millivolts decrease and increase corresponding to the start and stop of the flow, respectively (in Figure 7, the data of nos. 27 and 29 showing substantial changes and the data of no. 25

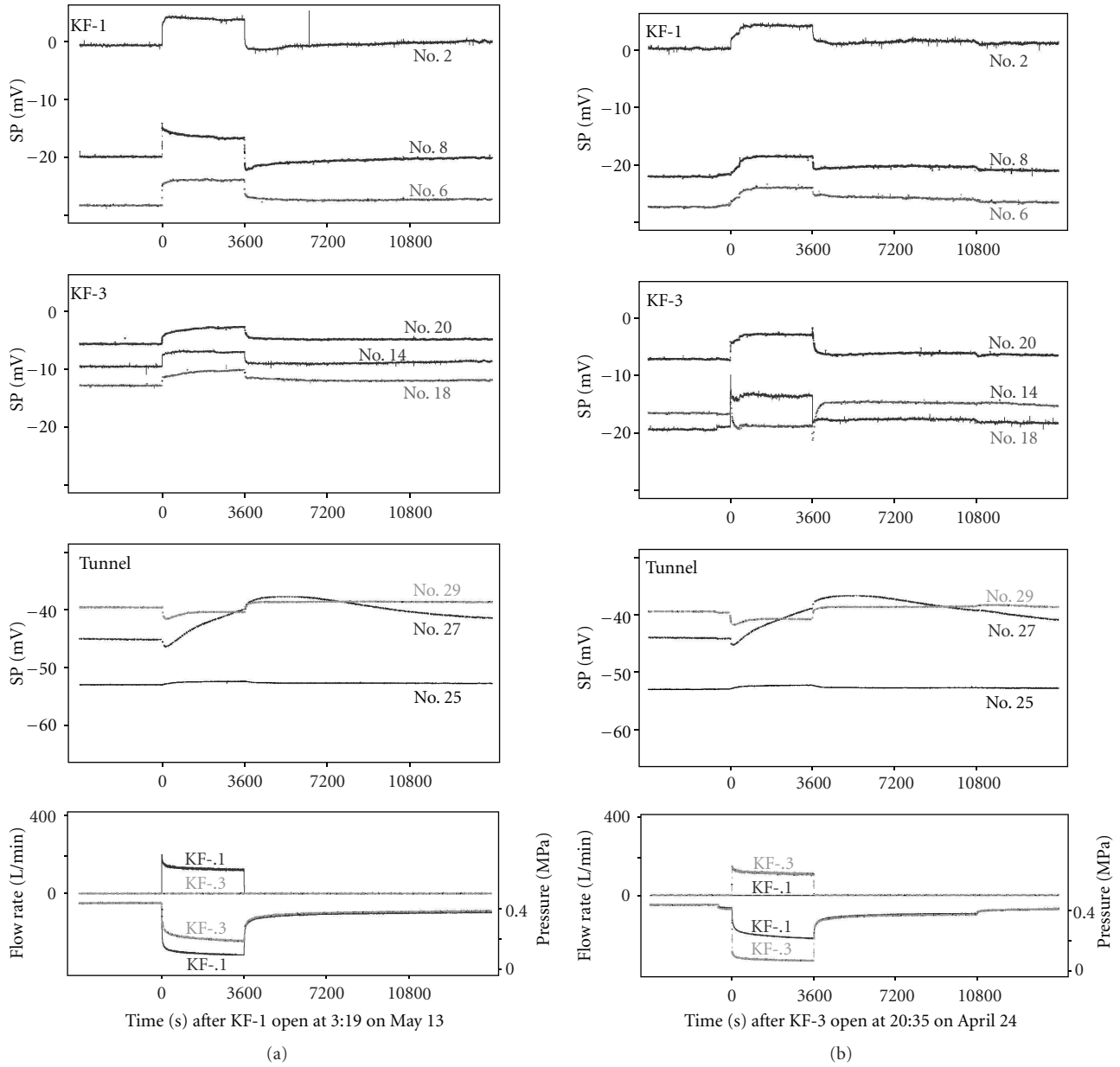


FIGURE 7: Recorded data during one cycle of valve operation. Changes in SP in wells KF-1 and KF-3 and on the tunnel floor are shown for the valve opening of KF-1 (a) and KF-3 (b). Also shown are the recorded pressure and flow rate of wells KF-1 and KF-3 (bottom).

showing only a tiny fluctuation are shown). In Figure 7(b), the results are shown for an experiment when well KF-3 was flowing on April 24. Similar SP changes to those when KF-1 was flowing were observed.

As seen in Figure 7, some of the electrodes installed in the flowing well showed spike-like changes at the start and stop of the flow, which seem to correlate with sudden flow rate changes and influence the successive SP changes. So hereafter, we focus on the SP data measured in “observation” wells, that is, KF-3 and KF-1 corresponding to the flow of KF-1 and KF-3 respectively, which are thought to be less influenced by the flow effects on the electrodes. In the next section, three KF-3

observations associated with KF-1 valve opening (70% for one hour on April 23, May 3, and May 13 and three KF-1 observations associated with KF-3 valve opening (70% for one hour on April 24, May 4, and May 14 will be shown. Among these, the data from experiments on April 24 and May 13 are the same as those shown in Figure 7.

3.2. Results. Figure 8 shows three records (with one-second sampling interval) from each of four electrodes in KF-3 (observation well) associated with KF-1 valve opening on April 23, May 3, and May 13. As seen in the figure, the

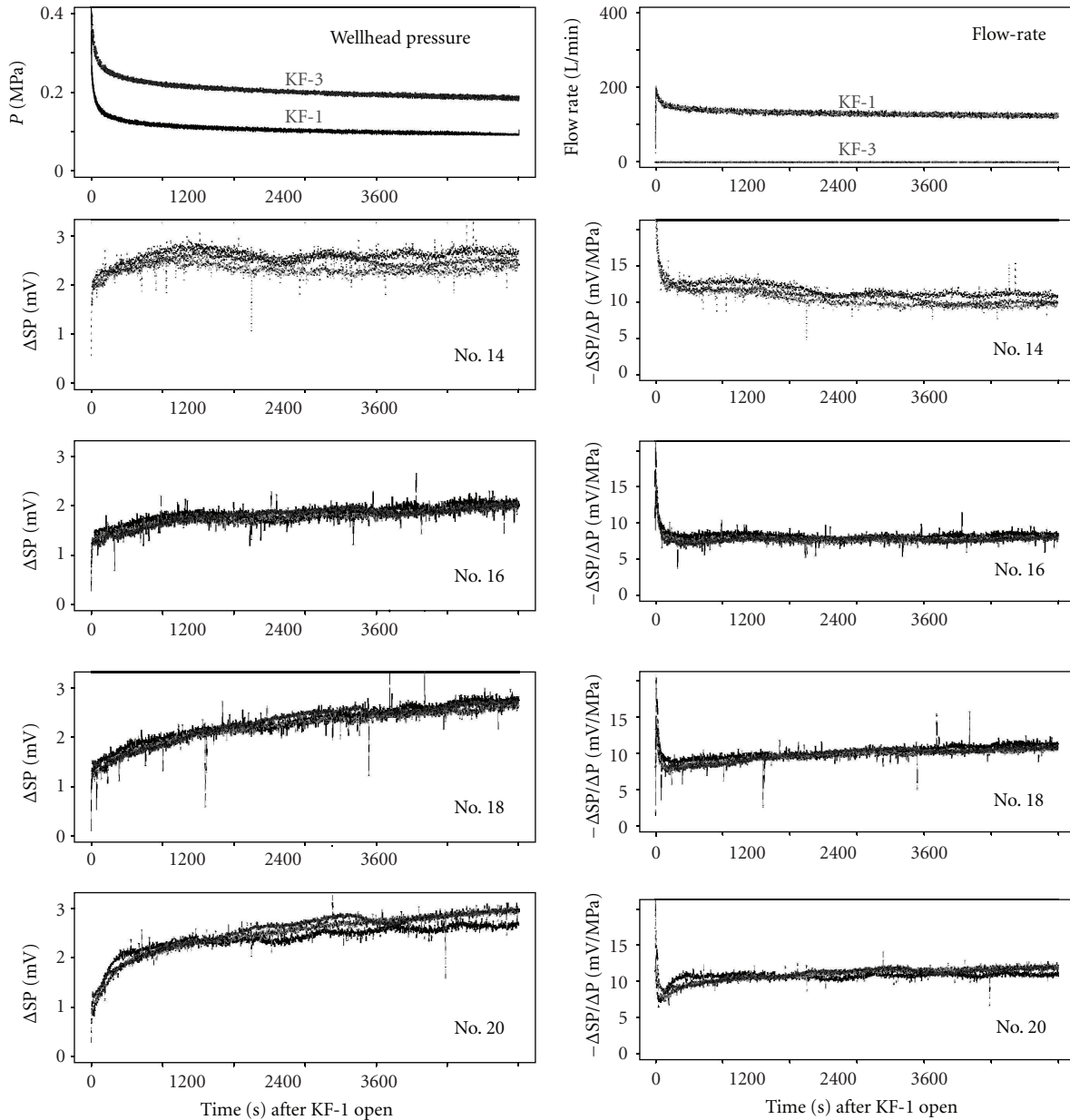


FIGURE 8: Changes in SP in KF-3 (observation well) for three repeated KF-1 valve operations. Ratio of SP change to pressure change is also shown on the right. Both of ΔSP and $\Delta SP/\Delta P$ are fairly reproducible.

differences among the three records are not so small compared to those of pressure and flow rate histories, but overall trends are fairly reproducible both for SP change (ΔSP) and the ratio of SP change to pressure change ($\Delta SP/\Delta P$). The $\Delta SP/\Delta P$ corresponds to the streaming potential coefficient, which is estimated to be around -10 mV/MPa from the records at later times. During the first ~ 100 seconds, the magnitude of $\Delta SP/\Delta P$ rapidly decreased from the initial values of around 20 mV/MPa to ~ 10 mV/MPa. This rapid change is thought to be caused by (1) electrode drifts induced by the flow start, which were small in the observation well but not negligible compared to the small signals at early times and (2) uncertainty involved in the evaluation of SP

values just before the valve opening. We usually determined “static” SP values from the average values over intervals between 25 and 15 minutes before the valve opening. In Figure 9, comparison between the results using this average “static” value and an instantaneous “static” value just at the valve opening is shown. The differences between the two curves are relatively minor even for earlier times than 100 seconds. However, in cases such as the experiment on April 24 shown in Figure 7, a small pressure down occurred before 10 minutes before the flow start, which was caused by a faint unexpected opening of the automatically controlled wellhead valve when power was supplied for operational preparation. In such cases, SP was disturbed from 10 minutes before the

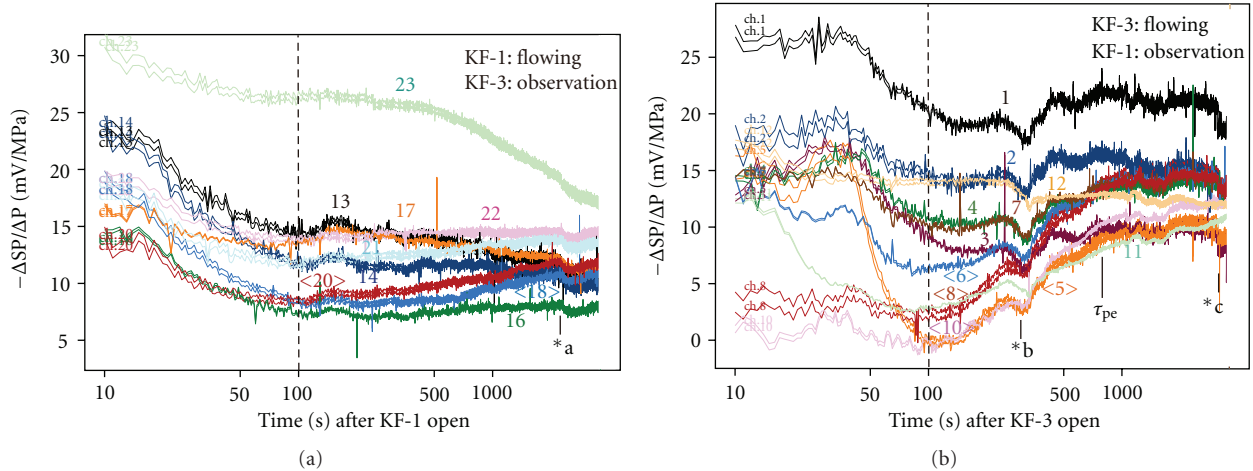


FIGURE 9: Ratio of SP change to pressure change as a function of time for KF-3 observation on May 13, 2007 (a) and KF-1 observation on May 14, 2007 (b). Two records for each electrode are drawn with different “static” SP values: one is with an average value over interval between 25 and 15 minutes before the valve opening and another is with an instantaneous value just at the valve opening at time zero. The differences between the two curves are relatively small even for earlier times than 100 seconds in the results shown here. At times pointed by *a, *b, and *c, all electrodes in wells KF-1 and KF-3 were suffered from a shift or a short-term disturbance. If the “double-porosity” model is applied to the KF-1 observation, the time required for pressure equilibration between the fracture and matrix regions is estimated as $\tau_{pe} \sim 800$ seconds.

flow start at $t = 0$, and the difference between the two results with “static” values determined from the instantaneous (at $t = 0$) and average (between $t = -25$ and -15 minutes) values became significant for early times. While the SP changes remained below ~ 1 mV, these uncertainties would easily bring about factor 2 to 3 uncertainty in $\Delta SP/\Delta P$ values. So we will disregard the first 100 seconds of $-\Delta SP/\Delta P$ plots in the following discussion.

In Figures 9 and 10, $\Delta SP/\Delta P$ is plotted as a function of logarithm of time. Figure 10 shows the records of selected electrodes for three KF-3 observations on the left and three KF-1 observations on the right. As seen in the figure, the results for KF-3 observations are fairly reproducible. Three different behaviors are recognized: the first one shows a stable or small decreasing trend observed at electrodes located at host rock zone without permeable fractures (no. 14 and no. 16), the second one shows an increasing trend observed at electrodes located near permeable fractures (no. 18 and no. 20), and the third one shows a high magnitude at early times and decreasing trend after ~ 400 seconds observed at the shallowest electrode no. 23.

In contrast to the KF-3 observations, the reproducibility is not good for the KF-1 observations. This is mainly due to a shift (equivalent to ~ 1 mV positive SP change) appearing around 300–400 seconds for all electrodes except the shallowest electrode no. 12 in the first and second observations. A “V”-shaped change appeared also around 300–400 seconds for all electrodes in the third observation. Such shift or rapid change did not appear for the electrodes installed on the tunnel floor (eight electrodes nos. 25–32), and the occurrence time was not correlated with time of a day (the first, second, and third ones were at 20:40 on April 24, at 12:08 on May 4, and at 3:35 on May 14, resp.), and a possibility of external noise source due to working

activity of the mine is low. In addition, no anomalous change is present in pressure and flow rate histories in the three observations (see Figure 7 for April 24 data). We have not understood the cause of these anomalous changes yet. However, comparing the earlier records than 300–400 seconds of the three observations, the changing patterns are quite similar to each other. This is also true for the later records than 300–400 seconds.

Records of all electrodes for the third KF-1 observation are shown in Figure 9. The behaviors can be divided into three groups; the difference between the earlier and later portions than 300–400 seconds is relatively small for the first group to which electrodes located at host rock zone without permeable fractures belong (nos. 1, 2, 3, and 12). The magnitude is small at early times, increasing up to ~ 800 seconds, and stable afterwards for the second group to which electrodes located near permeable fractures belong (nos. 5, 6, 8, and 10). The third group (electrodes nos. 4, 7, and 11) shows an intermediate behavior between those of the first and second groups. The observed $\Delta SP/\Delta P$ is almost constant with time in the host rock zone but exhibits temporal variation near the fractures, which looks like the “double-porosity behavior” predicted by Ishido and Pritchett [8]. If their prediction is applied, the time required for pressure equilibration (τ_{pe}) between the fracture and matrix regions will be identified at the intersection of the intermediate time increasing and late-time stable trends seen in the change-ratio plots; τ_{pe} is estimated to be about 800 seconds for KF-1 observations.

3.3. Interpretation. Figure 11 shows the resistivity distribution around wells KF-1 and KF-3 [11]. The main permeable fracture zone located around 30 meters depth of KF-1

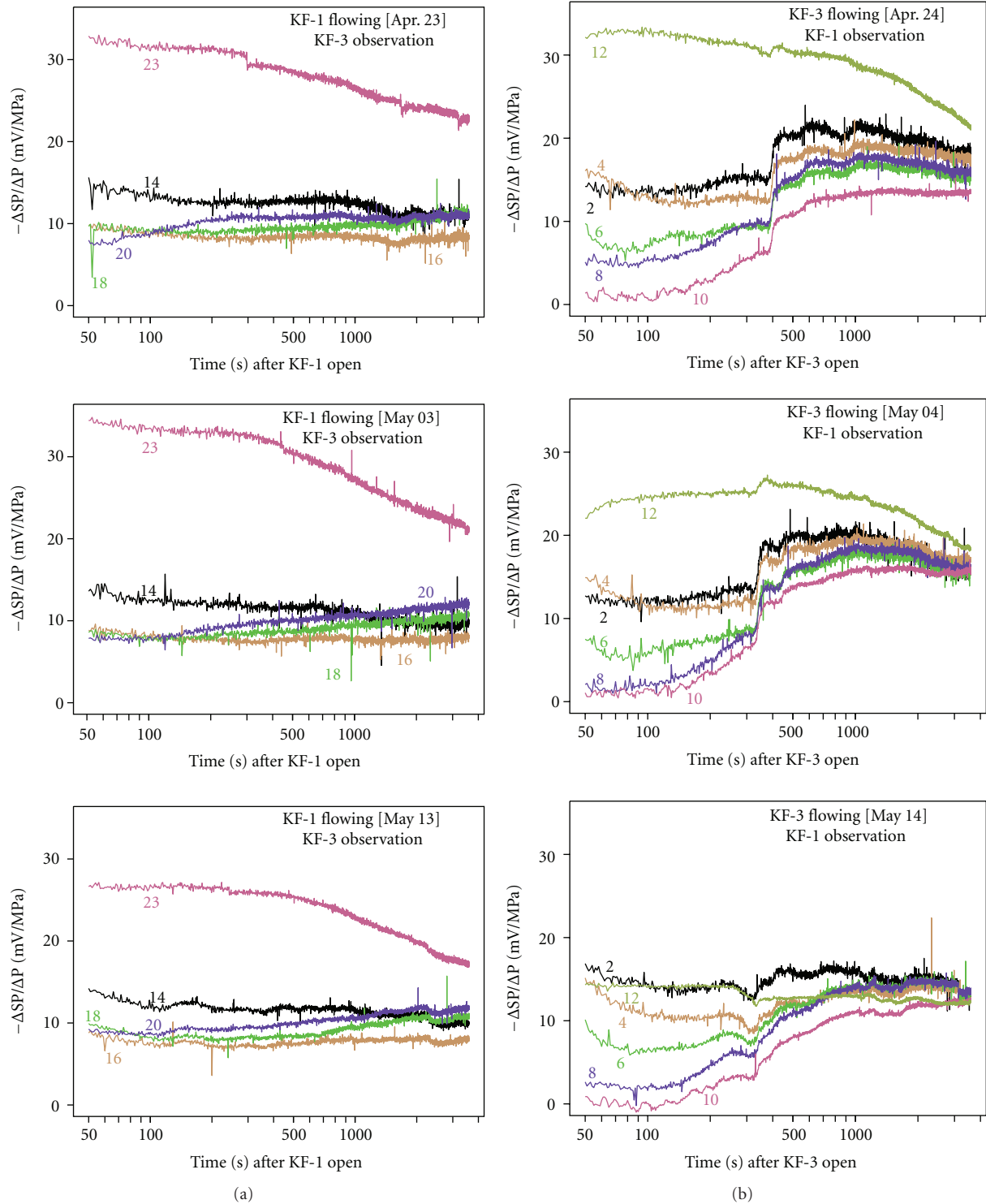


FIGURE 10: Ratio of SP change to pressure change as a function of time for KF-3 observations associated with three KF-1 valve opening (a) and for KF-1 observations associated with three KF-3 valve opening (b). The start of pressure drop is at time zero.

[12] is clearly delineated as a relatively low-resistivity zone ($\sim 800 \Omega\text{m}$) within high-resistive ($\sim 4000 \Omega\text{m}$) rocks. The extent of this low-resistive zone is well correlated with low-velocity zone revealed by seismic tomography measurements [27]. The locations of KF-1 electrodes of the first, second,

and third groups mentioned above are indicated by circle, yellow-filled asterisk, and white-filled asterisk, respectively, in Figure 11. The locations of KF-3 electrodes showing increasing trend and other KF-3 electrodes are indicated by white-filled asterisk and circle, respectively, in Figure 11.

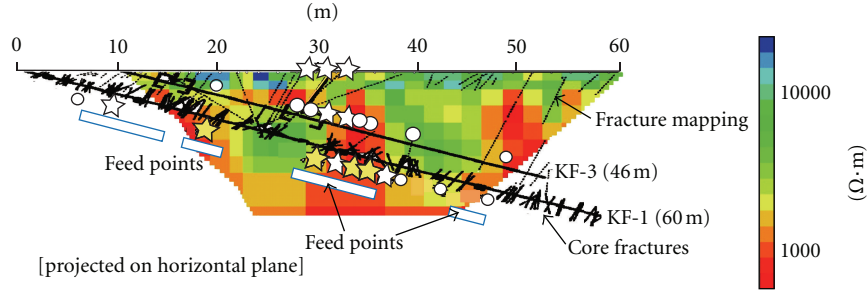


FIGURE 11: Electrical resistivity distribution around wells KF-1 and KF-3 (after [11]). Also shown are traces of major fractures, directions of core fractures, and locations of fluid feed points for KF-1 (e.g., [12]). Locations of KF-1 electrodes (nos. 5, 6, 8, and 10) showing typical fractured rock behavior in Figures 9 and 10 are denoted by yellow-filled asterisks, and those of KF-3 electrodes (nos. 18, 20) showing increasing trend are shown by white-filled asterisks. Locations of electrodes showing almost constant $\Delta SP/\Delta P$ with time are shown by circles.

Different $\Delta SP/\Delta P$ behaviors observed at low-permeability host rock and permeable fractured rock regions can be explained by a conceptual model shown in Figure 12. After valve opening of KF-1 (KF-3), pressure drawdown immediately propagates to nearby observation well KF-3 (KF-1) through permeable fractures. Due to substantial pressure drawdown, radial fluid flow toward the wellbore also takes place in host rocks surrounding the observation well (point “A” in Figure 12), which makes $\Delta SP/\Delta P$ equal to the streaming potential coefficient (C) from early times. In fractured rocks, pressure within the matrix region remains near the initial pressure at early times. So large pressure gradient is created in the matrix region near the fractures and/or the wellbore (point B in Figure 12). As shown in Section 2.5, the magnitude of $\Delta SP/\Delta P$ is modeled to be quite large from early times and constant with time thereafter if the matrix region’s C is assumed to be homogeneous. But if C in the near surface skin zone is assumed significantly smaller in magnitude than that in the interior of the matrix region, $|\Delta SP/\Delta P|$ is modeled to remain at quite small value at early times.

As shown in Figure 11, quite large contrast of resistivity is present between the main fracture and the surrounding host rock regions. This might bring about difference in the streaming potential coefficient between the fracture and host rock regions. We need to take into account the presence of such heterogeneity in addition to that from EDZ (excavation-damaged zone), which is thought to have ~ 1 m thickness around the tunnel wall (e.g., [24]), in future studies.

If we apply the “double-porosity” model mentioned in Section 2 to the KF-1 observations shown in Figure 9, the fracture spacing is estimated to be a few meters based on the τ_{pe} value of ~ 800 seconds and the matrix rock permeability of several microdarcies (10^{-18} m²) deduced by testing core samples. This is in the range of spacing of permeable fractures estimated for the fracture zone of KF-1 from detailed geological and hydrological observations (e.g., [12, 28]). The ratio of SP change to pressure change corresponds to the streaming potential coefficient C and is $-7 \sim -20$ mV/MPa as seen in Figure 9 for the nonfractured host rock region. This value is in the range of C measured for an intact granite sample in dilute solutions [29]. As for

the fracture zone, the final asymptotic value is also about -10 mV/MPa. This suggests that the contribution of drag current through the matrix region dominates under steady-state conditions.

We measured the zeta potential (-20 mV) for a crushed sample of granodiorite rock cored near the wellheads of KF-1 and KF-3 under room temperatures using the water discharged from the wells ($T \sim 11^\circ\text{C}$, $\text{pH} \sim 9$ and electrical conductivity $\sim 0.85 \times 10^{-4}$ S/m at sampling site; major chemical components are $\text{Na}^+ \sim 6$, $\text{Ca}^{++} \sim 9$, $\text{Cl}^- \sim 2.5$, $\text{HCO}_3^- \sim 33$, and $\text{SO}_4 \sim 7$ mg/L). If we assume the zeta potential of in situ intact host rock is also around -20 mV, we can estimate the in situ streaming potential coefficient by using (9). Unfortunately, we do not know the surface conductivity, but its contribution must be significant since the in situ bulk conductivity ($1/800 \sim 1/4000$ S/m) is even higher than the pore fluid conductivity itself. If we use the observed bulk conductivity in (9), the streaming potential coefficient is given as $C = (\eta/\tau)(\epsilon\zeta/\mu)/L_{ee}$. By substituting $\zeta = -0.02$ V, $\epsilon = 83.6 \times 8.85 \times 10^{-12}$ F/m, $\mu = 0.00127$ Pa-s, and $L_{ee} = 2.5 \times 10^{-4}$ S/m into this equation, $C = -(\eta/\tau) \times 4.7 \times 10^4$ mV/MPa. If we assume term η/τ ($=F^{-1}$, here F is the electrical formation factor) to be 0.0002, which is thought to be in the range of F^{-1} for intact crystalline rocks (e.g., [29]), C becomes about -10 mV/MPa, which is comparable to the observed “in situ” values: $-7 \sim -20$ mV/MPa. Using this value for F^{-1} , we can also estimate the surface conductivity ($m^{-1}\Sigma_s$) in (4) or (9) to be around 1.25 S/m.

4. Concluding Remarks

We have carried out continuous pressure and SP monitoring in KF-1 and KF-3 wells at the Kamaishi Mine by inducing a fluid flow from these wells, which caused pressure disturbance in the surrounding formation along the entire borehole. The observed ratio of SP change to pressure change associated with the fluid flow showed different behaviors between intact host rock and fractured rock regions. In open holes, the appearance of double-porosity behavior is modeled to depend on whether or not a skin zone or some heterogeneity in the streaming potential coefficient is present. It may be that skin zones will be found in most open

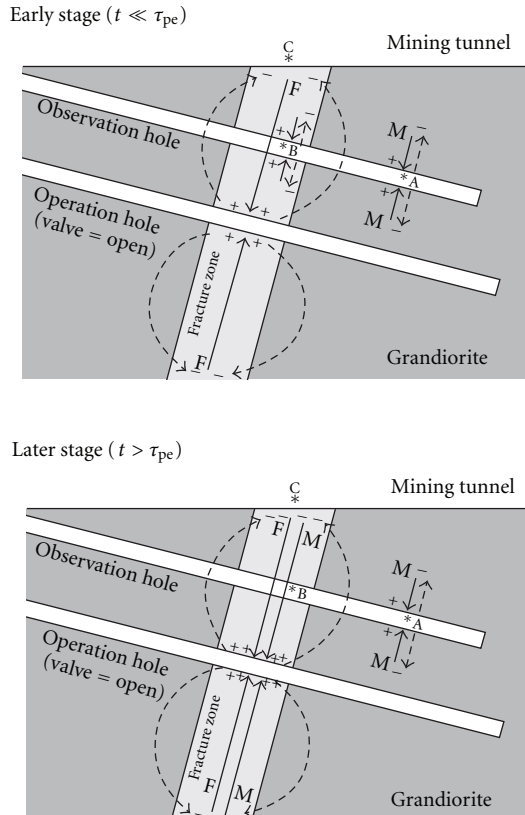


FIGURE 12: A conceptual model for different behaviors of SP changes at the country rock (A) and fractured rock (B) regions, and on the tunnel wall/floor (C). The drag current (solid line) flows only through the fracture (F) region at early times and through both of the fracture (F) and matrix (M) regions at later times than the time required for pressure equilibrium between the fracture and matrix regions. The conduction current (broken line) flows to compensate the resulting charge separation. The model is drawn for a case that KF-3 and KF-1 are observation and flowing wells, respectively; but the model is also applicable to a case that KF-1 and KF-3 are observation and flowing wells, respectively.

hole completions, so measurements of this type in open holes are likely to be useful to deduce the time required for pressure equilibrium between the fractures and the rock matrix.

When the observation is carried out using cased wells, the hydraulic communication between the borehole and the formation should be restricted to the fracture region. Direct hydraulic contact between the borehole and matrix region is prevented by solid casing and cementing [10]. To detect microscopic $\Delta SP/\Delta P$, an electrode array installed outside the insulated casing is desirable. Such observations were reported from an oil field [17]. Downhole SP measurement is thought to be a promising monitoring technique in various applications (e.g., [30, 31]). How to equip observation and/or production/injection wells with appropriate electrodes is very important for these applications. To detect macroscopic $\Delta SP/\Delta P$ such as predicted by Ishido and Pritchett [8], the conductive casing itself (with electrical

continuity extending over a distance longer than the typical fracture spacing) can be used as an electrode. Surface SP measurements (e.g., [14, 21]) detected SP changes which were generated at the reservoir depths and transferred to the earth's surface through the conductive well casing. Thus surface SP measurement around a wellhead is also promising to detect macroscopic $\Delta SP/\Delta P$ if the hydraulic communication between the borehole and the formation is restricted to the fracture region.

Acknowledgments

The present study was supported by basic research fund from The Institute for Geo-Resources and Environment, AIST. The authors greatly acknowledge the generous courtesy received from Kamaishi Mine Co., Ltd. and Nittetsu Mining Consultants Co., Ltd. during the field experiments. They express special thanks to the Kamaishi city where they stayed during the field surveys. They also wish the city recovers as soon as possible from the tsunami damages caused by the 2011 off the Pacific Coast of Tohoku Earthquake. The associate editor L. Jouniaux and two anonymous reviewers are acknowledged for helpful comments to improve the paper.

References

- [1] J. W. Pritchett and S. K. Garg, "On similitude, heat conduction, and two-phase flow in fractured porous media," in *Proceedings of the 15th Stanford Workshop on Geothermal Reservoir Engineering*, 1990.
- [2] J. E. Warren and P. J. Root, "The behavior of naturally fractured reservoirs," *Society of Petroleum Engineers Journal*, vol. 3, pp. 245–255, 1963.
- [3] H. Kazemi, "Pressure transient analysis of naturally fractured reservoirs with uniform fracture distribution," *Society of Petroleum Engineers Journal*, vol. 9, pp. 451–462, 1969.
- [4] K. Pruess and T. N. Narasimhan, "A practical method for modeling fluid and heat flow in fractured porous media," in *Proceedings of the the Reservoir Simulation Symposium of the Society of Petroleum Engineers*, New Orleans, La, USA, 1982, Also see SPE Journal, pp.14–26, 1985.
- [5] K. Pruess and T. N. Narasimhan, "On fluid reserves and the production of superheated steam from fractured, vapor-dominated geothermal reservoirs," *Journal of Geophysical Research*, vol. 87, no. 11, pp. 9329–9339, 1982.
- [6] J. W. Pritchett, "Efficient numerical simulation of nonequilibrium mass and heat transfer in fractured geothermal reservoirs," in *Proceedings of the 22nd Stanford Workshop on Geothermal Reservoir Engineering*, pp. 287–293, 1997.
- [7] T. Ishido, *Geothermal Reservoir Engineering*, Japan Geothermal Energy Association, 2002.
- [8] T. Ishido and J. W. Pritchett, "Characterization of fractured reservoirs using continuous self-potential measurements," in *Proceedings of the 28th Stanford Workshop on Geothermal Reservoir Engineering*, pp. 158–165, 2003.
- [9] T. Ishido and J. W. Pritchett, "Numerical simulation of electrokinetic potentials associated with subsurface fluid flow," *Journal of Geophysical Research B*, vol. 104, no. 7, pp. 15247–15259, 1999.

- [10] T. Ishido, Y. Nishi, and J. W. Pritchett, "Application of self-potential measurements to geothermal reservoir engineering: characterization of fractured reservoirs," in *Proceedings of the 35th Stanford Workshop on Geothermal Reservoir Engineering*, 2010.
- [11] S. Takakura, Y. Nishi, and T. Ishido, "Resistivity monitoring during an air injection experiment to fractured rocks," in *Proceedings of the 123rd Meeting of SEGJ Extended Abstract*, pp. 225–228, 2010.
- [12] T. Negi, Y. Yoneda, and T. Senba, "Application of streaming potential method for detection of fractures in granite rock (part II)," in *Proceedings of the 97th Meeting of SEGJ Extended Abstract*, pp. 274–278, 1997.
- [13] V. V. Bogoslovsky and A. A. Ogilvy, "Deformation of natural electric fields near drainage structures," *Geophysical Prospecting*, vol. 21, no. 4, pp. 716–723, 1973.
- [14] T. Ishido, H. Mizutani, and K. Baba, "Streaming potential observations, using geothermal wells and in situ electrokinetic coupling coefficients under high temperature," *Tectonophysics*, vol. 91, no. 1-2, pp. 89–104, 1983.
- [15] M. Darnet, A. Mainault, and G. Marquis, "On the origins of self-potential (SP) anomalies induced by water injections into geothermal reservoirs," *Geophysical Research Letters*, vol. 31, no. 19, article L19609, 2004.
- [16] M. Darnet, A. Mainault, and G. Marquis, "On the origins of self-potential (SP) anomalies induced by water injections into geothermal reservoirs," *Geophysical Research Letters*, vol. 31, no. 19, article L19609, 2004.
- [17] M.-Y. Chen, B. Raghuraman, I. Bryant, and M. Supp, "Streaming potential applications in oil fields," in *Proceedings of SPE Annual Technical Conference and Exhibition*, vol. 2, pp. 24–27, 2006, Paper SPE 102106.
- [18] E. Rizzo, B. Suski, A. Revil, S. Straface, and S. Troisi, "Self-potential signals associated with pumping tests experiments," *Journal of Geophysical Research B*, vol. 109, no. 10, article B10203, 2004.
- [19] S. Straface, C. Fallico, S. Troisi, E. Rizzo, and A. Revil, "An inverse procedure to estimate transmissivity from heads and SP signals," *Ground Water*, vol. 45, no. 4, pp. 420–428, 2007.
- [20] A. Mainault, E. Strobach, and J. Renner, "Self-potential signals induced by periodic pumping tests," *Journal of Geophysical Research B*, vol. 113, no. 1, Article ID B01203, 2008.
- [21] M. Darnet, G. Marquis, and P. Sailhac, "Hydraulic stimulation of geothermal reservoirs: fluid flow, electric potential and microseismicity relationships," *Geophysical Journal International*, vol. 166, no. 1, pp. 438–444, 2006.
- [22] T. Ishido and J. Muzutani, "Experimental and theoretical basis of electrokinetic phenomena in rock-water systems and its applications to geophysics," *Journal of Geophysical Research*, vol. 86, no. 3, pp. 1763–1775, 1981.
- [23] T. Ishido and J. W. Pritchett, "Numerical simulation of electrokinetic potentials associated with subsurface fluid flow," in *Proceedings of the 21st Stanford Workshop on Geothermal Reservoir Engineering*, pp. 143–149, 1996.
- [24] K. Yokoi, Y. Noguchi, H. Choh, and S. Hamabe, "Geophysical methods applied in underground investigation programs at the Kamaishi Mine," *Busuri-Tansa*, vol. 44, no. 6, pp. 350–361, 1991.
- [25] Y. Nishi, T. Ishido, and T. Negi, "Field experiments to characterize hydrological properties of fractured rock using continuous borehole self-potential measurement," *Transactions of Geothermal Resources Council*, vol. 30, pp. 835–838, 2006.
- [26] Y. Nishi, T. Ishido, and T. Negi, "Continuous borehole self-potential measurement—a new approach to characterize hydrological properties of fractured rock," *Busuri-Tansa*, vol. 61, pp. 285–299, 2008.
- [27] Y. Yoneda, H. Takahara, N. Nakamura, S. Akiyama, T. Moriya, and T. Negi, "Investigation of geological environment of deeper granitic rock at the Kamaishi Mine (H9)," Report PNC TJ 1380 98-002, Power Reactor and Nuclear Fuel Development, 1998.
- [28] Y. Yoneda and T. Negi, "Geological surveys of fracture zone of deeper granitic rock at the Kamaishi Mine (H7)," PNC TJ 1380 96-001, Power Reactor and Nuclear Fuel Development, 1996.
- [29] T. Ishido and N. Matsushima, "Streaming potential measured for an intact granite sample at temperatures to 200°C," in *Proceedings of the 32nd Stanford Workshop on Geothermal Reservoir Engineering*, 2007.
- [30] J. W. Pritchett and T. Ishido, "Numerical simulation of underground electrical signals caused by hydrofracturing operations," in *Proceedings of the World Geothermal Congress*, Bali, Indonesia, 2010.
- [31] J. H. Saunders, M. D. Jackson, and C. C. Pain, "Fluid flow monitoring in oilfields using downhole measurements of electrokinetic potential," *Geophysics*, vol. 73, no. 5, pp. E165–E180, 2008.

Research Article

Changes in Electrokinetic Coupling Coefficients of Granite under Triaxial Deformation

Osamu Kuwano and Shingo Yoshida

Earthquake Research Institute, University of Tokyo, 1-1-1 Yayoi, Bunkyo-ku, Tokyo 113-0032, Japan

Correspondence should be addressed to Osamu Kuwano, kuwano@eri.u-tokyo.ac.jp

Received 30 June 2011; Revised 21 September 2011; Accepted 29 October 2011

Academic Editor: Tsuneo Ishido

Copyright © 2012 O. Kuwano and S. Yoshida. This is an open access article distributed under the Creative Commons Attribution License, which permits unrestricted use, distribution, and reproduction in any medium, provided the original work is properly cited.

Electrokinetic phenomena are believed to be the most likely origin of electromagnetic signals preceding or accompanying earthquakes. The intensity of the source current due to the electrokinetic phenomena is determined by the fluid flux and the electrokinetic coupling coefficient called streaming current coefficient; therefore, how the coefficient changes before rupture is essential. Here, we show how the electrokinetic coefficients change during the rock deformation experiment up to failure. The streaming current coefficient did not increase before failure, but continued to decrease up to failure, which is explained in terms of the elastic closure of capillary. On the other hand, the streaming potential coefficient, which is the product of the streaming current coefficient and bulk resistivity of the rock, increased at the onset of dilatancy. It may be due to change in bulk resistivity. Our result indicates that the zeta potential of the newly created surface does not change so much from that of the preexisting fluid rock interface.

1. Introduction

Electrokinetic phenomena occur when an electrolyte flows along charged solid surfaces. For several decades, these phenomena have been of interest to geophysicists in many subfields. Observed self-potential has been associated with geothermal fields (e.g., [1, 2]), volcanic activity and topography (e.g., [3–6]), and shallow ground water flow (e.g., [7, 8]). In numerical modelings, quantitative interpretation of self-potential observed in geothermal and volcanic areas and modelings in hydrogeophysics have been studied (e.g., [9–13]). Electrokinetic phenomena are also believed to be the most likely origin of the observed electromagnetic signals preceding or accompanying earthquakes. Mizutani et al. [14] first proposed a model: during dilatancy stage, which is assumed to precede earthquakes [15, 16], pore pressure in the dilatant region decreases and water flows into this region from the surrounding area, generating electromagnetic precursors to earthquakes due to electrokinetic phenomena.

To provide an appropriate interpretation of field observations, a better understanding of the physics of electrokinetic

effect at the level of the rock-fluid interface and at the level of the rock sample is required. In laboratory experiments, zeta potential and streaming potential coefficients, fundamental quantities that characterize the electrokinetic effect, were measured for crushed rocks (e.g., [5, 17–21]) and for natural intact rocks (e.g., [22–29]) to determine the electrokinetic parameters as a function of pH, resistivity, permeability, or temperature. Jouniaux and Pozzi [23] measured the streaming potential coefficients of Fontainebleau sandstones under triaxial stress up to failure. They reported a large increase of the streaming potential coefficient beginning at about 75% of the yield stress. Yoshida [27] measured electric current and electric potential during rock deformation and found that the streaming current flowed before main failure, showing good correlation with dilatancy rate and water flow rate. In his study, however, changes of coupling coefficient (streaming potential coefficient or streaming current coefficient) during deformation were not measured.

Jouniaux and Pozzi [23] suggested that the increase of the streaming potential coefficient is due to an increase of zeta potential. An increase of the streaming potential coefficient,

however, is also caused by an increase of bulk resistivity. In this study, by measuring not only the streaming potential coefficient but also the streaming current coefficient which has different dependence on bulk resistivity, we investigate what causes changes in the coupling coefficient during rock deformation.

2. Electrokinetic Phenomena

It is well known that when in contact with an electrolyte, the surface of rock-forming minerals are charged and surrounded by an equivalent amount of ionic charge of opposite sign from the electrolyte. The overall arrangement of the electric charge on the solid surface together with the balancing charge in the bulk liquid phase is often referred to as an electric double layer. Electrokinetic phenomena are induced by the relative motion between the fluid and the rock which develops an electric double layer. When the fluid in such a system moves due to a pressure gradient, the charges in the fluid are transported in the direction of fluid motion, resulting in an electric current. In a porous medium the electric current density \mathbf{i} (in A/m²) and fluid flux \mathbf{j} (i.e., flow velocity, in m/s) are described by the following relations [30, 31]:

$$\begin{aligned}\mathbf{i} &= -\frac{\sigma_f + \sigma_s}{F} \text{grad } \phi + \frac{\epsilon \zeta}{\mu F} \text{grad } P_p, \\ \mathbf{j} &= \frac{\epsilon \zeta}{\mu F} \text{grad } \phi - \frac{k}{\mu} \text{grad } P_p,\end{aligned}\quad (1)$$

where σ_f and σ_s are the electrical bulk and surface conductivities, ϵ is the dielectric constant of the fluid, ζ is the zeta potential (the potential at the slipping plane near the boundary), k is the permeability, μ is the viscosity of the fluid, P_p is the pressure of the fluid, and ϕ is the streaming potential. The first term of (1) represents Ohm's law, and the second term represents streaming current which can be derived by considering the product of the charge density (proportional to $\epsilon \zeta$) with the flow velocity of the viscous fluid (proportional to $\text{grad } P_p / \mu$). The first term of (1) shows the macroscopic conductivity of rock (reciprocal of bulk-resistivity), which is expressed as

$$\sigma_R = \frac{\sigma_f + \sigma_s}{F}. \quad (2)$$

Considering the capillary model [17, 32], we define formation factor F as

$$F = \frac{\sigma_{\text{eff}}}{\sigma_R} = \frac{T^2}{\eta}, \quad (3)$$

where η is the porosity, T is the tortuosity, and σ_{eff} is the effective conductivity defined as

$$\sigma_{\text{eff}} = \sigma_f + \sigma_s. \quad (4)$$

The surface conductivity σ_s (in S/m) is related to the specific surface conductance Σ_s (in S) by $\sigma_s = 2\Sigma_s/m$, where m is

hydraulic radius for the capillary model. The permeability of the capillary model is represented as

$$k = \frac{\eta}{T^2} \frac{m^2}{b}, \quad (5)$$

where b is a constant related to the shape of pore; $b = 8$ for capillaries with a circular cross-section. We refer to $-\mathbf{i}/\text{grad } P_p$ under $\text{grad } \phi = 0$ in (1) as the streaming current coefficient C_c :

$$C_c = \frac{\epsilon \zeta}{\mu F} = \frac{\eta}{T^2} \frac{\epsilon \zeta}{\mu}. \quad (6)$$

Both C_c and k are functions of the fluid path network, and the dependence of C_c and k on η and T are the same. However, dependencies on m are different for C_c and k . The difference by m^2 can be understood if we note that the volume flow rate of a viscous fluid through a tube is proportional to the square of the cross-sectional area of the tube, while the amount of the transport electric charges distributed along the boundary are proportional to circumference length (i.e., proportional to the radius) and the flow velocity around the boundary is also proportional to the radius.

If there are no external current sources and no leaking current, the streaming current (due to $\text{grad } P_p$) would be balanced by the conduction current (due to $\text{grad } \phi$), so

$$\Delta \phi = \frac{\epsilon \zeta}{\sigma_{\text{eff}} \mu} \Delta P_p, \quad (7)$$

which is the Helmholtz-Smoluchowski equation. The ratio $\Delta \phi / \Delta P_p$ is referred to as the streaming potential coefficient,

$$C_p = \frac{\Delta \phi}{\Delta P_p} = \frac{\epsilon \zeta}{\sigma_{\text{eff}} \mu} = \frac{C_c}{\sigma_{\text{eff}} / F} = \frac{C_c}{\sigma_R}. \quad (8)$$

In general geometry, divergence of the total current is zero, but the zero total current condition (7) is not always satisfied.

3. Experimental Methods

In this study, we measured the streaming current (or streaming potential), permeability, and dilatancy of the rock specimen simultaneously and continuously during rock deformation test. We used the triaxial apparatus which was specially designed to investigate the electrical behavior during rock deformation and failure [27]. In this apparatus, the rock specimen is electrically isolated from the surroundings by inserting alumina plates. The pore fluid tubes of stainless steel inside the vessel are also isolated from the outside fluid tubes by using insulating tubes through the vessel closure as shown in Figure 1. This apparatus has two options for force loading: hydraulic loading with servo valves and a screwed pump with a servo motor. In the present experiment, we used the screwed pump for deformation test at a strain rate of approximately $10^{-7}/\text{s}$. This apparatus is equipped with up to 11 feedthroughs that Nishizawa [33] developed on the basis of Bridgeman's self-sealing mechanism. During the

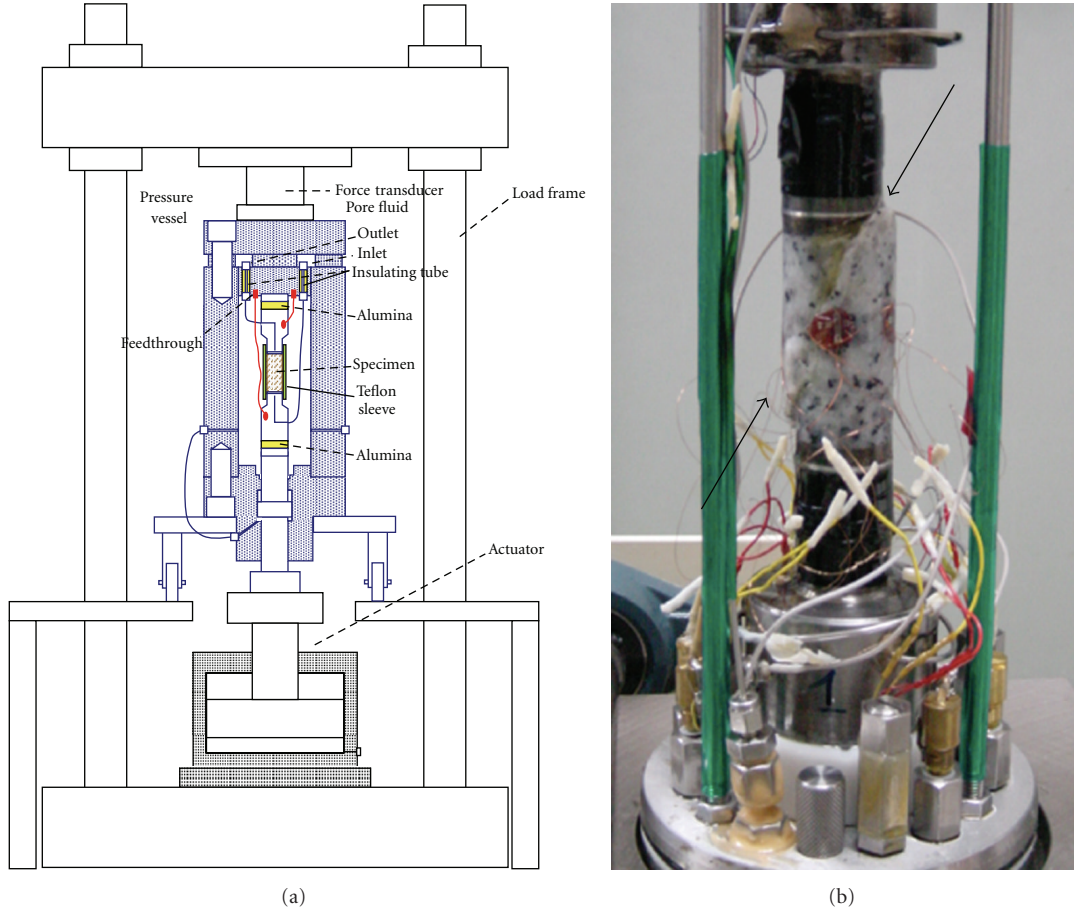


FIGURE 1: (a) Schematic diagram of apparatus. A rock specimen is electrically isolated by inserting alumina plates and by using insulating tubes of pore water through vessel closure. (b) Picture of the specimen after experiment. A failure plane is indicated by black arrows.

experiment, we measured differential axial stress, axial piston displacement, pore fluid volume, pore pressure change, electric signals (either current or potential), and local strains of the specimen, at a sampling rate of 10 Hz.

In the present study, we used coarse grained Inada granite (from a locality in Ibaraki, Japan), which has been often used as a standard specimen in rock mechanics (e.g., [27, 29, 34]). We used two specimens which were cored cylindrically 24 mm in diameter and 60 mm in length. One specimen was used in the electric potential measurement and denoted G01. The other was used in the electric current measurement and denoted G02. The porosity of both specimens was approximately 1%. The rock specimens were air-dried and degassed under a vacuum for 12 hours before being saturated with 10^{-3} M KCl solution for 2 days. The conductivity of the fluid was 14 mS/m. Then, the specimens were placed between the stainless steel end plugs and jacketed in a Teflon sleeve.

To measure the axial strain e_z and the circumferential strain e_h , strain gauges were mounted at four positions on the cylindrical surface of the Teflon sleeve. A volume change of the specimen ΔVol is estimated as $\Delta \text{Vol} = \text{Vol}^0 (\tilde{e}_z + 2\tilde{e}_h)$, where \tilde{e}_z and \tilde{e}_h are averaged strains for four positions, and Vol^0 is the initial volume of the specimen. The cross-section of the specimen is assumed to remain circular. This

assumption is not satisfied when a fault plane is formed and large localized deformation occurs. A volume change due to dilatancy is obtained by subtracting elastic deformation from the volume change.

To measure the permeability continuously during the deformation experiments [35], we adopted the sinusoidal oscillation method [36–39]. The method is based on the measurement of an attenuation and a phase retardation of an oscillation of the pore-fluid pressure as it propagates through the specimen. In its application, a sinusoidal pressure oscillation is imposed at one end of the specimen and a pressure response is monitored at the other end as illustrated in Figure 2. The permeability is calculated from the measured attenuation factor R between downstream and upstream pore-fluid-pressure sinusoidal waves, and the phase lag δ , using the following relation (calculations detailed in [37]),

$$P_{p1} = R P_{p2} \sin(\omega t - \delta),$$

$$R \cdot \exp(i\delta) = \frac{1}{\cosh[\psi(1+i)] + \gamma \psi(1+i) \sinh[\psi(1+i)]}, \quad (9)$$

where P_{p1} and P_{p2} are upstream and downstream pore fluid pressure, respectively, R is the attenuation factor, δ is the

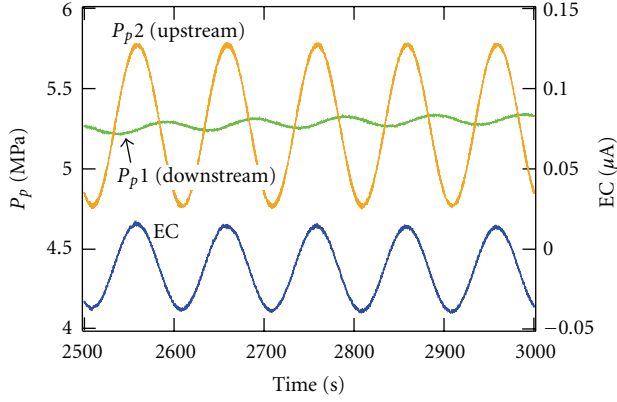


FIGURE 2: An example of measurement using the sinusoidal oscillation method. Upstream and downstream fluid pressure are shown as orange and green lines, respectively. In this example, electric current measured using stainless-steel end plugs equipped at each end of specimen as electrode is also shown (blue line). The streaming current coefficient is calculated from the amplitude of fluid-pressure difference ($P_{p1} - P_{p2}$) and the amplitude of the electric current.

phase lag, ω is an angular frequency, and i is the imaginary unit. From the measurements of R and δ , the value of dimensionless parameters ψ and γ can be evaluated, and then we obtain permeability k ,

$$k = \frac{\pi \mu f B_d L}{A \psi^2 \gamma}, \quad (10)$$

where f is a frequency of oscillation, A is the cross-sectional area, L is the length of the specimen, and B_d is the storage of the downstream reservoir ($B_d = 0.0038 \text{ cm}^3/\text{MPa}$ in our apparatus). During the experiments, the upstream pore-fluid pressure (P_{p2}) was sinusoidally oscillated at a frequency of 0.01 Hz by computer-controlled servo-mechanism. The amplitude of the sinusoidal pressure variation was 0.5 MPa. The upper specimen face is connected to the downstream reservoir of a volume of 9.52 cm^3 . To calculate the permeability from the measured attenuation factor and phase lag, we used a custom-made code following Takahashi [35].

To reveal the physical mechanism causing the observed changes of electrokinetic properties of rock-water system, it is convenient to measure both of the two coupling coefficients, namely, the streaming potential coefficient and the streaming current coefficient, because the streaming potential coefficient involves bulk resistivity and the source current. We measured electric current or potential between the upper and bottom faces of the specimen with an electrometer (Keithley 6517) by using the stainless-steel end plugs placed at the both ends of the specimen as electrodes. Electric potential was measured in the experiment using specimen G01 and electric current was measured in another experiment using specimen G02, respectively, because an electric potential and an electric current could not be measured at the same time. The sinusoidal oscillation method [29] enables us to measure the streaming potential (or current) induced by pore-fluid movement continuously

during a rock deformation test. Figure 2 shows a typical data obtained by the oscillation test at a frequency of 0.01 Hz. The resultant electric current showed sinusoidal variations. By reading the amplitude of the sinusoidal variation of the electric current (ΔI_s) and the amplitude of the sinusoidal variation of the fluid pressure difference ($\Delta P_p = P_{p1} - P_{p2}$), we evaluated the generated current per unit change in the fluid pressure $\Delta I_s / \Delta P_p$. The streaming current coefficient C_c was obtained using the relation

$$C_c = \frac{\Delta I_s / S}{\Delta P / L} = \frac{\Delta I_s L}{\Delta P S} \text{ [A/mMPa]}. \quad (11)$$

Similarly, from measurements of the amplitude of electric potential variation ($\Delta \phi$), we estimated the streaming potential coefficient as

$$C_p = \frac{\Delta \phi}{\Delta P_p} \text{ [V/MPa]}. \quad (12)$$

Frequency effect on the coupling coefficient [40–42] for the Inada granite with the present experiment system has been reported in [27]. Coupling coefficient does not depend on frequency in such a low frequency range (0.01–1 Hz) for the intact Inada granite. Although we cannot rule out the possibility of the changes of frequency dependence on the coupling coefficient during deformation, we focus on the continuous measurement during deformation to fix the frequency to 0.01 Hz and do not discuss the frequency dependence in the present study.

4. Results

Here, we show the results of the two experiments. Experimental conditions for G01 and G02 were the same. The confining pressure P_c was kept at 15 MPa. The pore-fluid pressure at each end of the specimen was set to 5.3 MPa at the beginning of the experiment. Then, pore fluid pressure of the bottom face of the specimen was sinusoidally oscillated at a frequency of 0.01 Hz with an amplitude of 0.5 MPa throughout the rest of the experiment. Experiments were conducted under room temperature ($25 \pm 1^\circ \text{C}$).

Figure 3 shows the results of the run G01, in which electric potential was monitored. The axial loading rate was $5.1 \times 10^{-7} \text{ s}$. A shear failure plane was found in the postexperimental sample (Figure 1(b)). From Figure 3(a) showing the differential axial stress and the displacement, it can be seen that dynamic failure occurred at $t = 37,323 \text{ s}$. Some small releases of axial stress occurred around $t = 6,000$ and $17,000 \text{ s}$. These small stress releases may be due to poor initial setting of the apparatus. Thus, we do not analyze the data before these stress changes ($t \sim 20,000 \text{ s}$). The pore-fluid pressure P_{p1} and P_{p2} are shown in Figure 3(b). The pore-fluid pressure of the bottom face of the specimen appears to be a thick line in this scale because it is sinusoidally oscillated at a frequency of 0.01 Hz and amplitude of 0.5 MPa. Figure 3(e) shows the volume change of the specimen obtained from strain measurements and the dilatancy calculated by subtracting the elastic deformation from the volume change. In Figure 3(b), the volume change

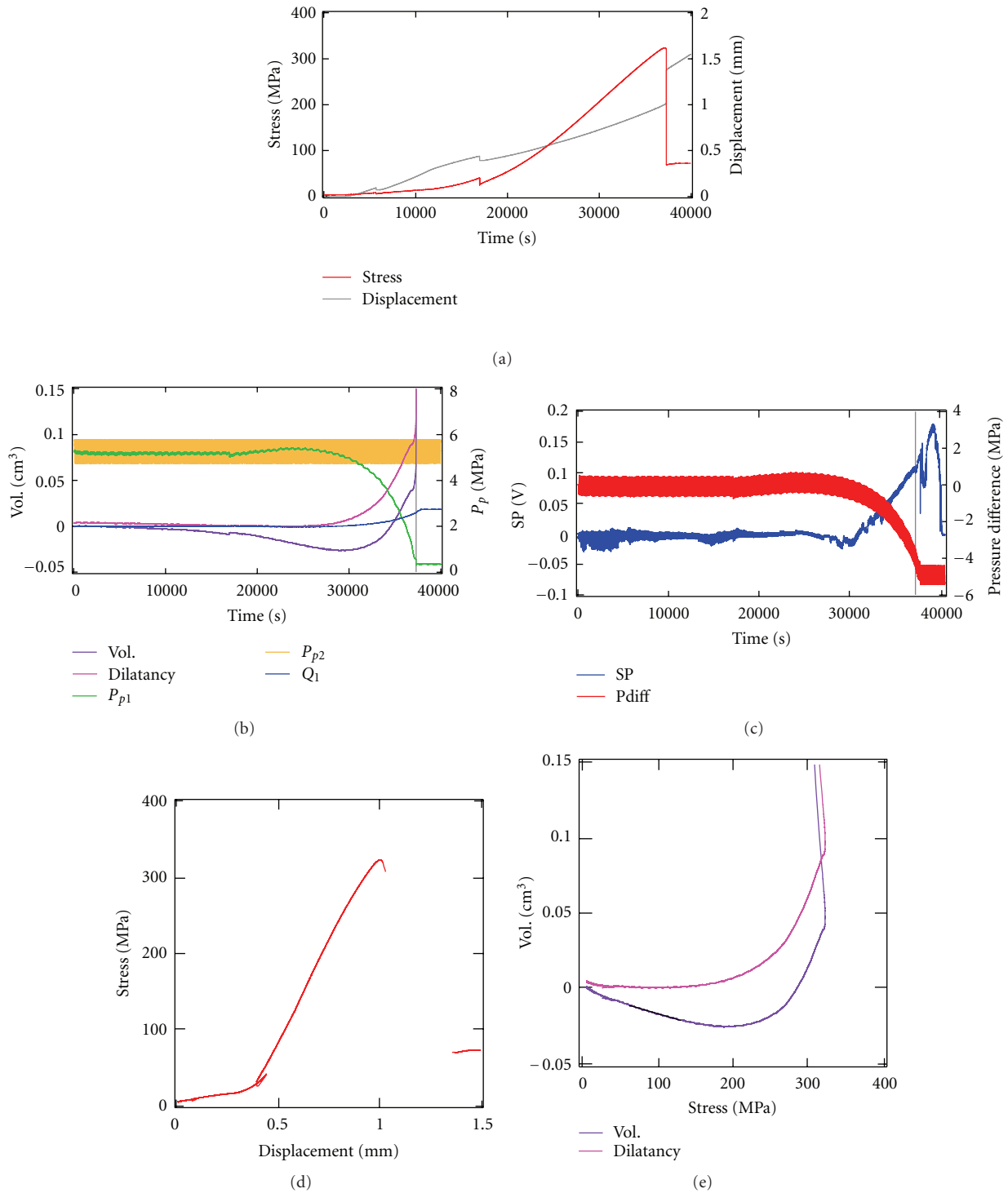


FIGURE 3: Result of deformation test for initially intact Inada granite (G01) at $P_c = 15$ MPa, $P_p = 5$ MPa. (a) Differential stress and displacement. (b) Volume change of the specimen obtained from the average of the strain measurements at four positions, dilatancy, pore fluid pressures, and water volume. (c) Streaming potential (SP) and pore-fluid pressure difference between bottom and top faces of the specimen. (d) Axial stress versus axial displacement. In this experiment, failure stress was 324 MPa and Young's modulus was 32 MPa. (e) Volume change of the specimen and dilatancy versus the axial stress. The elastic deformation is indicated by the thick black line in this figure.

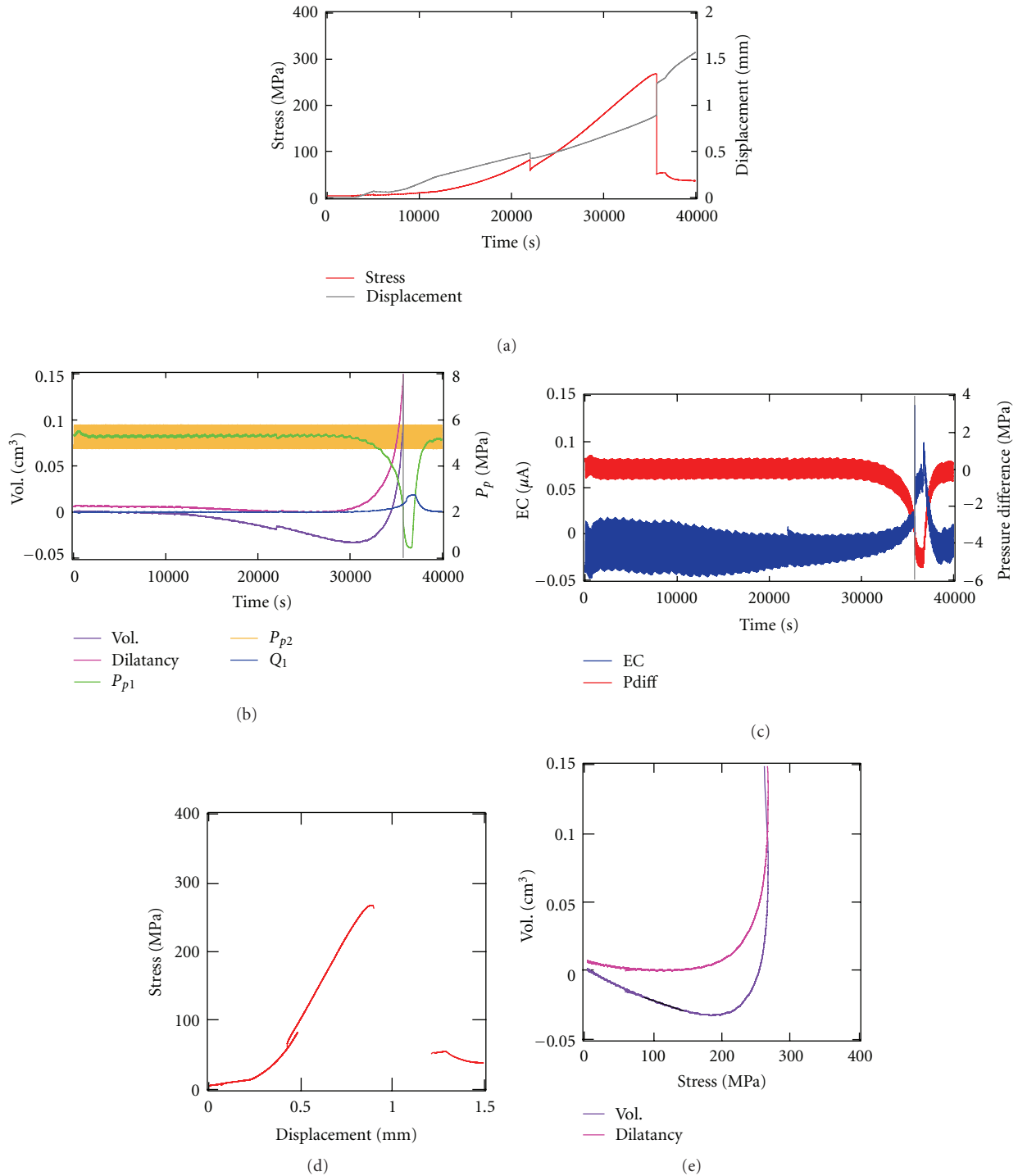


FIGURE 4: Result of deformation test for initially intact Inada granite (G02) at $P_c = 15$ MPa, $P_p = 5$ MPa. In this experiment, streaming current was measured instead of potential. This result also shows good correlation between the pressure difference and the streaming current. Failure stress was 268 MPa and Young's modulus was 29 MPa.

and the dilatancy are plotted. When dilatancy began (around $t = 27,000$ s), the downstream pore pressure P_{p1} began to drop, indicating that the pore pressure in the specimen dropped and water flowed into the specimen. From the change of P_{p1} , we calculated the water volume Q_1 , which

flows into the specimen from the downstream reservoir, as $Q_1 = -B_d(P_{p1} - P_{p0})$, where P_{p0} is an initial pore pressure. Although we attempted to estimate the water volume Q_2 , which flows into the specimen from the upstream side, using the displacement of the piston of the pore water

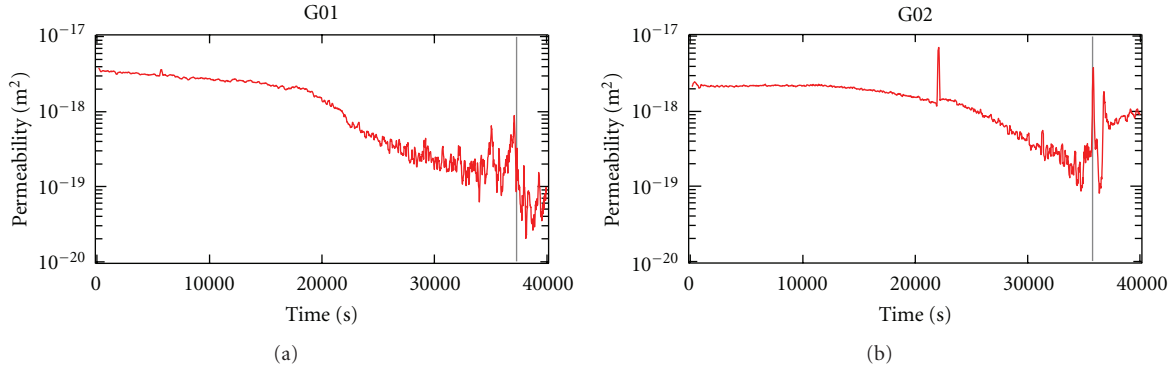


FIGURE 5: Permeability calculated from measured amplitude ratio and phase lag between upstream and downstream pore pressure (P_{p2} , P_{p1}). Vertical gray lines indicate the time of failure.

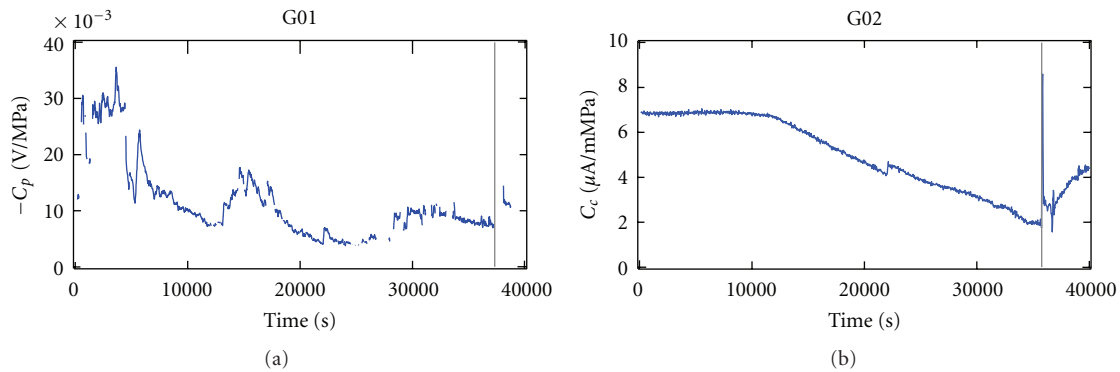


FIGURE 6: Coupling coefficients, C_p (G01) and C_c (G02), calculated from measured amplitude ratio of potential (or current) to pore pressure difference. Vertical gray lines indicate the time of failure.

intensifier, we could not estimate Q_2 due to the leakage of the water at the upstream side. Therefore, we show only Q_1 in Figure 3(b). In Figures 3(b) and 3(c), we can see good correlation among the trends of dilatancy, the pore pressure difference, and the streaming potential (SP). Details of this “DC” relation are discussed later. Here, we focus on the results of “AC” measurement based on the imposed sinusoidal oscillation of the pore pressure.

Figure 4 shows the other run (G02) in which the electric current was measured. A similar result with the run G01 was obtained, showing good correlation among dilatancy, pore pressure difference, and the streaming current (EC). The axial loading rate was $5.5 \times 10^{-7}/s$. As in G01, a discrete shear plane was found in the postexperimental sample, indicating that the main failure (around $t = 35,788$ s) involved the formation of such a failure plane. When dilatancy began (around $t = 28,650$ s), the pore pressure of the downstream P_{p1} began to decrease. Some small stress releases were also observed at about $t = 6,000$ and $22,000$ s due to the setting of the apparatus similarly to the former experiment.

Figure 5 shows the permeability of G01 and G02. The permeability was initially of the order of 10^{-18} m^2 . With the increase of the axial loading, the permeability decreased to 10^{-19} m^2 . Then, just before the failure, the permeability increased to $\sim 10^{-18} \text{ m}^2$ in the both experiments. There are a

lot of studies dealing with permeability-porosity relationship and permeability-stress relationship (e.g., [43–45]). In our experiment, permeability reduction is approximately an exponential function of effective mean stress [45] and mainly attributed to elastic crack closure [43]. The permeability increase indicates enhanced connection of cracks. Although the dilatancy should involve the creation of microcracks, the permeability continued to decrease with progressive loading, indicating that microcracks were not fully interconnected or not fully saturated with pore fluid.

5. Discussion

The coupling coefficients C_p (or C_c) were calculated from amplitude of pore pressure difference and potential (or current). The polarity of obtained coupling coefficients were negative in the present experiments, indicating negative zeta potential, as expected for granites. The values of the coupling coefficients are shown in absolute values hereafter. Figure 6 shows the coupling coefficients of G01 and G02. To remove the data which are not suitable for calculating streaming potential coefficient, we evaluated a signal quality by $P(0.01 \text{ Hz})/\sum P(f)$, where $P(f)$ is the power spectrum of potential variation. The data with the signal quality lower than 0.98 were not used. We can see variations of C_p around

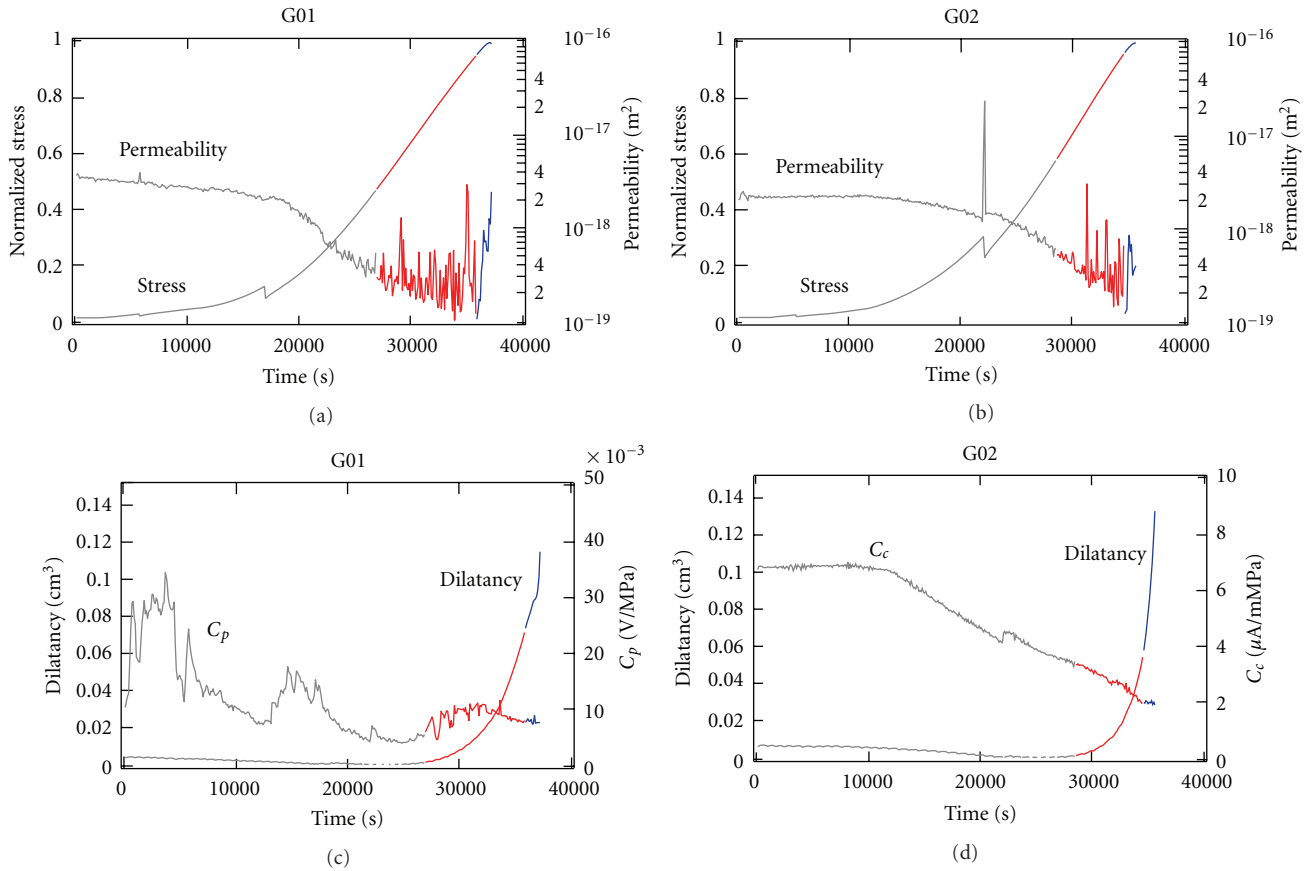


FIGURE 7: Normalized stress, permeability, dilatancy, and coupling coefficient versus time. The gray, red, and blue lines indicate the stages A, B, and C, respectively. Three stages which are divided by the beginning of dilatancy (G01 $t = 27,000$ s, G02 $t = 28,650$ s) and the beginning of permeability increase (G01 $t = 36,000$ s, G02 $t = 34,750$ s).

$t = 6,000$ and $17,000$ s in Figure 6(b). These variations were due to small stress releases resulting from the setting of the apparatus as mentioned before. A fluctuation of C_c around $t = 22,000$ s was due to the same reason. The streaming potential coefficient C_p decreased with loading (Figure 6) and then increased by a factor of two at the onset of dilatancy (around $t = 27,000$ s). Note that C_p did not continue to increase with dilatancy increase but C_p increased just at the onset of the dilatancy. In contrast, the streaming current coefficient C_c continued to decrease during the loading until the time of failure, not particularly affected by dilatancy. It is noted that the observed change in C_c indicates that the source current density did not increase during the deformation, and therefore observed increase in C_p is attributed to bulk resistivity (see (8)).

The estimation of the zeta potential is done from the measured streaming current coefficient. The streaming current coefficient C_c of Inada granite before loading is approximately $7\mu A/mMPa$. The formation factor F of Inada granite under atmospheric pressure was estimated to be 1100 from the measurement of the resistance of the rock sample saturated with KCl solution with a high conductivity (0.2–1.1 S/m). Inserting these values into (6), we obtained the zeta potential as -11 mV, which is slightly smaller than the previously reported value of granite [17, 18, 29].

To investigate the evolution of the coupling coefficients in detail, we divide experiments into three stages; stage A: from the start of experiment to the beginning of dilatancy, stage B: from the beginning of dilatancy to the beginning of permeability increase, stage C: from the beginning of permeability increase to the failure. Figure 7 indicates these stages in different colors. We defined the normalized stress as the stress normalized by the failure stress. Figure 8(a) shows the streaming potential coefficient C_p and the dilatancy of G01 as a function of the normalized stress. We can see that the dilatancy and increase of streaming potential coefficient began at 47% of yield stress. Figure 8(b) shows the relation between the streaming potential coefficient and the dilatancy. Increase of the streaming potential coefficient (5 V/MPa to 10V/MPa) occurred at the onset of the dilatancy. Figure 8(c) shows C_c and the dilatancy of G02 as a function of the normalized stress. We can see the dilatancy began at 58% of the failure stress. The streaming current coefficient C_c continued to decrease at an approximately constant rate unrelated to the dilatancy. Relation between the C_c and the dilatancy is shown in Figure 8(d). When the permeability increase (stage C) began, C_c stopped to decrease and remained roughly constant during the stage C up to failure.

Figure 9 shows the relation between the streaming current coefficients and the permeability. The streaming current

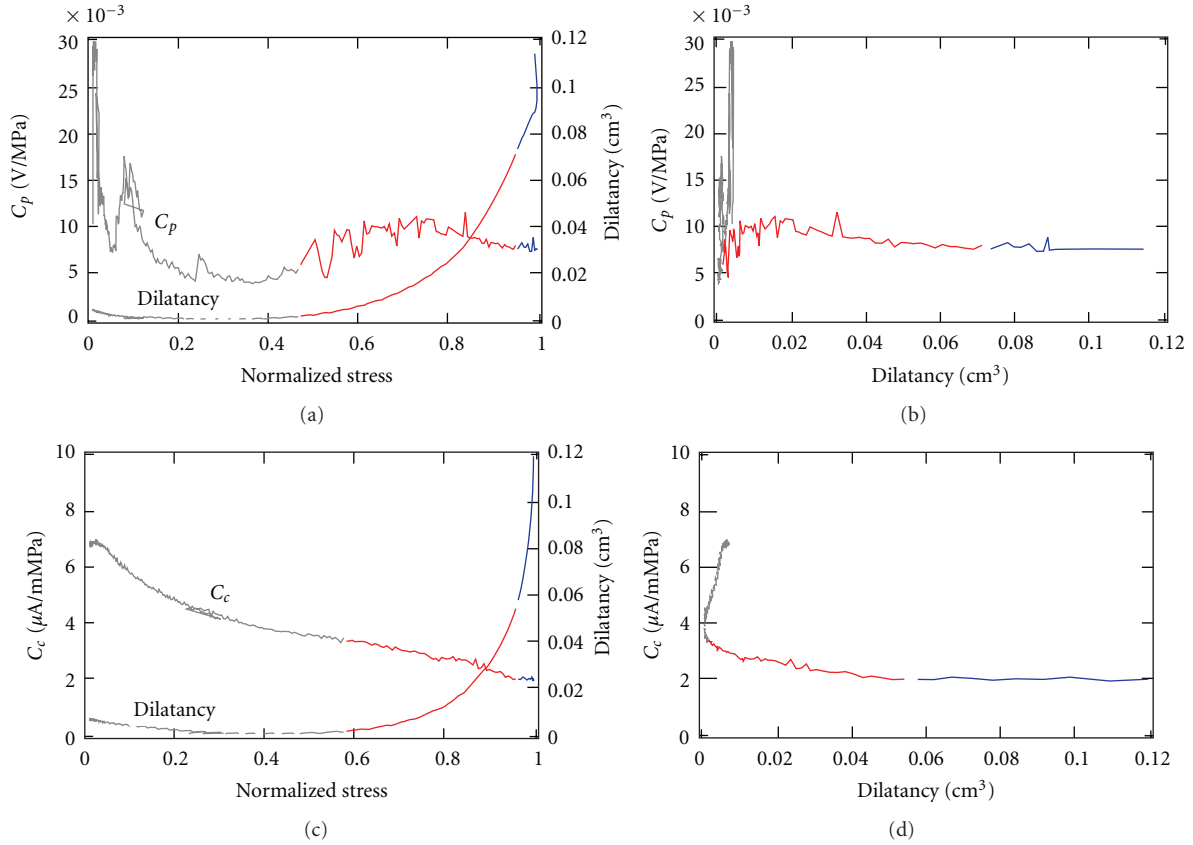


FIGURE 8: (a) C_p and dilatancy versus normalized stress. (b) C_p versus dilatancy. (c) C_c and dilatancy versus normalized stress. (d) C_c versus dilatancy.

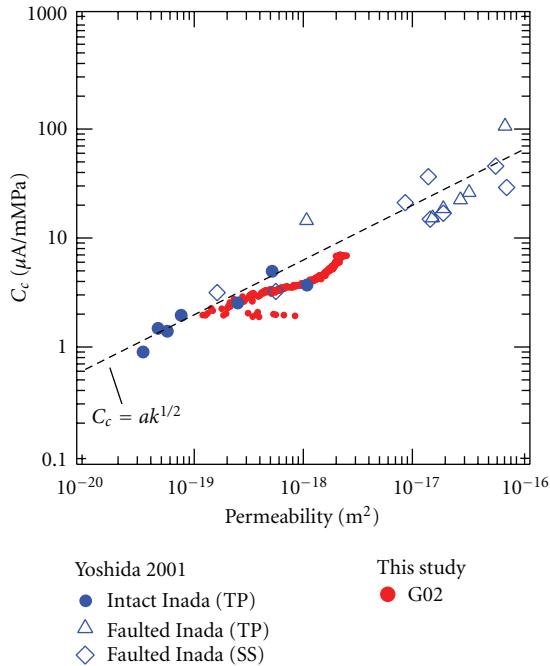


FIGURE 9: The streaming current coefficients C_c as a function of the permeability. Blue symbols are data of Inada granite obtained by Yoshida [27].

coefficient C_c was approximately proportional to the square root of the permeability. This dependence can be explained by assuming that m^2 is proportional to $1/F = \eta/T^2$ in (5) and (6) for the capillary model [17, 27, 32]. This assumption is supported by the experimental results that $\log k$ is linearly related to $\log F$ with slope of ~ -2 for granite reported by Walsh and Brace [32].

The fact that the streaming current coefficient did not increase indicates that the zeta potential did not increase throughout the deformation test. Furthermore, there is a possibility of decrease of the zeta potential, because C_c does not increase with the permeability increase in stage C. If bulk resistivity increases at the onset of the dilatancy, the streaming potential coefficient C_p , which is the product of C_c and bulk resistivity (see (8)), will increase. Figures 3(b) and 4(b) show the volume of water flow from the downstream Q_1 , which is much smaller than dilatancy. The ratio of Q_1 to dilatancy is approximately 0.1 to 0.2, indicating the possibility of the undersaturation of the pore, although the water flow from the upstream is not included. We mention the possibility of bulk-resistivity change here. To understand the observed change of C_p , we would require measurements of the bulk-resistivity changes during the deformation. On the basis of recent studies (e.g., [46–48]), however, the magnitude of C_p decreases with decreasing water saturation S_w in most situations even though substantial increase of bulk-resistivity takes place at the same time.

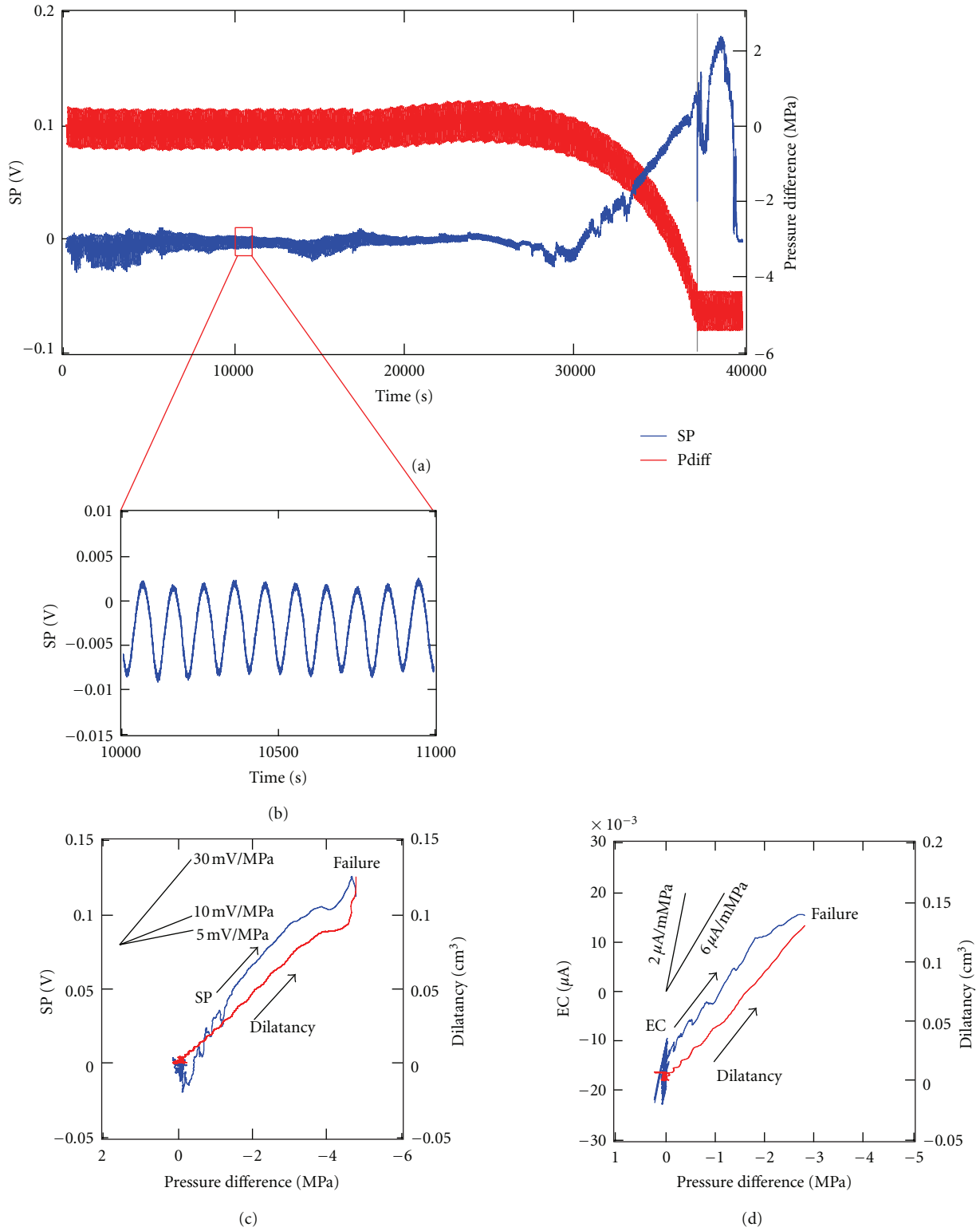


FIGURE 10: The streaming potential (SP) and the pore pressure difference (Pdiff). Long-term trend of these values are used in the “DC” measurements of electrokinetic phenomena (a). Amplitude and phase of the sinusoidal variation caused by imposed pore pressure oscillation are used for the “AC” measurements of electrokinetic phenomena (b). The DC coupling coefficients and the dilatancy as a function of the pressure difference for G01 (c) and G02 (d). Blue and red lines indicate coupling coefficients and dilatancy, respectively.

The S_w dependence of the coupling coefficients is important also for modeling of field self-potential data related to unsaturated flow in volcanic areas (e.g., [49, 50]) and shallow groundwater systems. We need further study to clarify the S_w change during dilatancy stage and its effect on the coupling coefficients of low-permeability rocks such as granite used in this study.

Here we compare the coupling coefficients obtained from the AC measurements and those obtained from the DC measurements. We can see the DC electrokinetic effect in Figure 10(a). Figure 10(b) shows the AC electrokinetic effect discussed earlier. The DC coupling coefficients and the dilatancy are shown as a function of the pressure difference in Figures 10(c), 10(d). The dilatancy showed a linear relation with the pressure difference in both experiments. The magnitude of the DC streaming current coefficient C_c was approximately $6 \mu\text{A}/\text{mMPa}$ before dilatancy began and then decreased to $2 \mu\text{A}/\text{mMPa}$ after dilatancy began. These values agree well with the C_c obtained from the AC measurement (see Figure 7). On the other hand, the magnitude of the DC streaming potential coefficient C_p during dilatancy was approximately $30 \text{ mV}/\text{MPa}$, which was three-times as large as that from the AC measurement (see Figure 7). At the present stage, we do not fully understand the discrepancy between AC and DC streaming potential coefficients. We need further study including a frequency dependence of the specific resistivity of the rock specimen.

6. Conclusions

Jouniaux and Pozzi [23] suggested that the onset of increase in the streaming potential coefficient corresponded to the onset of shear localization and that this increase was due to an increase of the zeta potential in the shear zone as new surfaces were created and connected. Although Jouniaux and Pozzi [23] suggested a possibility of the enhancement in the zeta potential on the newly created surface, there exists some uncertainties. They measured the streaming potential, which was the product of the streaming current density and the specific resistivity of the specimen. Therefore, one cannot deny a possibility that the observed increase of the streaming potential was due to an increased bulk resistivity rather than an enhanced zeta potential.

In our experiment, the C_p increased but the C_c did not increase, indicating that the source current density did not increase during the deformation. Such an increase in C_p due to increase in bulk resistivity cannot be the source of the electric signals unless the increase in bulk resistivity occurs broadly in the observation field. Variation of the zeta potential according to the deformation stage makes it difficult to interpret the self-potential data quantitatively. Results of the present experiments, however, indicate the zeta potential does not vary so much throughout all the deformation stage of the rock up to failure.

Acknowledgments

The authors thank the Editor T. Ishido and the anonymous reviewers for constructive comments which greatly improved

the paper. This paper was partially supported by JSPS KAKENHI(05J11788).

References

- [1] R. F. Corwin and D. B. Hoover, "Self-potential method in geothermal-exploration," *Geophysics*, vol. 44, no. 2, pp. 226–245, 1979.
- [2] T. Ishido, H. Mizutani, and K. Baba, "Streaming potential observations, using geothermal wells and in situ electrokinetic coupling coefficients under high temperature," *Tectonophysics*, vol. 91, no. 1-2, pp. 89–104, 1983.
- [3] T. Ishido, T. Kikuchi, N. Matsushima et al., "Repeated self-potential profiling of izu-oshima volcano, Japan," *Journal of Geomagnetism and Geoelectricity*, vol. 49, no. 11-12, pp. 1267–1278, 1997.
- [4] J. Zlotnicki, Y. Sasai, P. Yvetot et al., "Resistivity and self-potential changes associated with volcanic activity: the July 8, 2000 Miyake-jima eruption (Japan)," *Earth and Planetary Science Letters*, vol. 205, no. 3-4, pp. 139–154, 2003.
- [5] H. Hase, T. Ishido, S. Takakura, T. Hashimoto, K. Sato, and Y. Tanaka, "Zeta potential measurement of volcanic rocks from Aso caldera," *Geophysical Research Letters*, vol. 30, no. 23, pp. 2–4, 2003.
- [6] K. Aizawa, "A large self-potential anomaly and its changes on the quiet Mt. Fuji, Japan," *Geophysical Research Letters*, vol. 31, no. 5, article L05612, p. 4, 2004.
- [7] F. Perrier, M. Trique, B. Lorne, J. P. Avouac, S. Hautot, and P. Tarits, "Electric potential variations associated with yearly lake level variations," *Geophysical Research Letters*, vol. 25, no. 10, pp. 1955–1958, 1998.
- [8] M. Trique, F. Perrier, T. Froidefond, J. P. Avouac, and S. Hautot, "Fluid flow near reservoir lakes inferred from the spatial and temporal analysis of the electric potential," *Journal of Geophysical Research B*, vol. 107, no. 10, pp. 1–28, 2002.
- [9] W. R. Sill, "Self-potential modeling from primary flows," *Geophysics*, vol. 48, no. 1, pp. 76–86, 1983.
- [10] T. Ishido and J. W. Pritchett, "Numerical simulation of electrokinetic potentials associated with subsurface fluid flow," *Journal of Geophysical Research B*, vol. 104, no. 7, pp. 15247–15259, 1999.
- [11] A. Revil, H. Schwaeger, L. M. Cathles, and P. D. Manhardt, "Streaming potential in porous media 2. Theory and application to geothermal systems," *Journal of Geophysical Research B*, vol. 104, no. 9, pp. 20033–20048, 1999.
- [12] S. R. Pride, F. Moreau, and P. Gavrilenko, "Mechanical and electrical response due to fluid-pressure equilibration following an earthquake," *Journal of Geophysical Research B*, vol. 109, no. 3, article B03302, p. 10, 2004.
- [13] M. R. Sheffer and D. W. Oldenburg, "Three-dimensional modelling of streaming potential," *Geophysical Journal International*, vol. 169, no. 3, pp. 839–848, 2007.
- [14] H. Mizutani, T. Ishido, T. Yokokura, and S. Ohnishi, "Electrokinetic phenomena associated with earthquakes," *Geophysical Research Letters*, vol. 3, no. 7, pp. 365–368, 1976.
- [15] A. Nur, "Dilatancy, pore fluids, and premonitory variations of T_s - T_p travel times," *Bulletin of the Seismological Society of America*, vol. 62, no. 5, pp. 1217–1222, 1972.
- [16] C. H. Scholz, L. R. Sykes, and Y. P. Aggarwal, "Earthquake prediction: a physical basis," *Science*, vol. 181, no. 4102, pp. 803–810, 1973.

- [17] T. Ishido, "Experimental and theoretical basis of electrokinetic phenomena in rock-water systems and its applications to geophysics," *Journal of Geophysical Research*, vol. 86, no. 3, pp. 1763–1775, 1981.
- [18] F. D. Morgan, E. R. Williams, and T. R. Madden, "Streaming potential properties of Westerly granite with applications," *Journal of Geophysical Research*, vol. 94, no. 9, pp. 12449–12461, 1989.
- [19] L. Jouniaux and J. P. Pozzi, "Permeability dependence of streaming potential in rocks for various fluid conductivities," *Geophysical Research Letters*, vol. 22, no. 4, pp. 485–488, 1995.
- [20] B. Lorne, F. Perrier, and J. P. Avouac, "Streaming potential measurements: 1. Properties of the electrical double layer from crushed rock samples," *Journal of Geophysical Research B*, vol. 104, no. 8, pp. 17857–17877, 1999.
- [21] F. Perrier and T. Froidefond, "Electrical conductivity and streaming potential coefficient in a moderately alkaline lava series," *Earth and Planetary Science Letters*, vol. 210, no. 1–2, pp. 351–363, 2003.
- [22] L. Jouniaux, S. Lallemand, and J. P. Pozzi, "Changes in the permeability, streaming potential and resistivity of a claystone from the Nankai prism under stress," *Geophysical Research Letters*, vol. 21, no. 2, pp. 149–152, 1994.
- [23] L. Jouniaux and J. P. Pozzi, "Streaming potential and permeability of saturated sandstones under triaxial stress: consequences for electrotelluric anomalies prior to earthquakes," *Journal of Geophysical Research*, vol. 100, no. 6, pp. 10197–10209, 1995.
- [24] S. Yoshida, O. C. Clint, and P. R. Sammonds, "Electric potential changes prior to shear fracture in dry and saturated rocks," *Geophysical Research Letters*, vol. 25, no. 10, pp. 1577–1580, 1998.
- [25] B. Lorne, F. Perrier, and J. P. Avouac, "Streaming potential measurements 2. Relationship between electrical and hydraulic flow patterns from rock samples during deformation," *Journal of Geophysical Research B*, vol. 104, no. 8, pp. 17879–17896, 1999.
- [26] L. Jouniaux, M. L. Bernard, M. Zamora, and J. P. Pozzi, "Streaming potential in volcanic rocks from Mount Pelée," *Journal of Geophysical Research B*, vol. 105, no. 4, pp. 8391–8401, 2000.
- [27] S. Yoshida, "Convection current generated prior to rupture in saturated rocks," *Journal of Geophysical Research B*, vol. 106, no. 2, pp. 2103–2120, 2001.
- [28] P. M. Reppert and F. D. Morgan, "Temperature-dependent streaming potentials: 2. Laboratory," *Journal of Geophysical Research B*, vol. 108, no. 11, pp. 4–13, 2003.
- [29] T. Toshi, N. Matsushima, and T. Ishido, "Zeta potential measured for an intact granite sample at temperatures to 200°C," *Geophysical Research Letters*, vol. 30, no. 6, pp. 28–1, 2003.
- [30] S. R. de Groot and P. Mazur, *Non-Equilibrium Thermodynamics*, North-Holland, Amsterdam, The Netherlands; Interscience Publishers, New York, NY, USA, 1962.
- [31] S. Pride, "Governing equations for the coupled electromagnetics and acoustics of porous media," *Physical Review B*, vol. 50, no. 21, pp. 15678–15696, 1994.
- [32] J. B. Walsh and W. F. Brace, "The effect of pressure on porosity and the transport properties of rock," *Journal of Geophysical Research*, vol. 89, no. 11, pp. 9425–9431, 1984.
- [33] O. Nishizawa, "New multi-wire type and co-axial type feedthroughs for an oil pressure medium vessel," *Bulletin of the Geological Survey of Japan*, vol. 48, pp. 431–438, 1997.
- [34] T. Ishido and O. Nishizawa, "Effects of Zeta potential on microcrack growth in rock under relatively low uniaxial compression," *Journal of Geophysical Research*, vol. 89, no. 6, pp. 4153–4159, 1984.
- [35] M. Takahashi, "Permeability change during experimental fault smearing," *Journal of Geophysical Research B*, vol. 108, no. 5, pp. 1–15, 2003.
- [36] R. L. Kranz, J. S. Saltzman, and J. D. Blacic, "Hydraulic diffusivity measurements on laboratory rock samples using an oscillating pore pressure method," *International Journal of Rock Mechanics and Mining Sciences*, vol. 27, no. 5, pp. 345–352, 1990.
- [37] G. J. Fischer, "The determination of permeability and storage capacity: pore pressure oscillation method," in *Fault Mechanics and Transport Properties of Rocks*, B. Evan and T. F. Wong, Eds., pp. 187–211, Academic Press, San Diego, Calif, USA, 1992.
- [38] G. J. Fischer and M. S. Paterson, "Measurement of permeability and storage capacity in rocks during deformation at high temperature and pressure," in *Fault Mechanics and Transport Properties of Rocks*, B. Evan and T. F. Wong, Eds., pp. 213–252, Academic Press, San Diego, Calif, USA, 1992.
- [39] I. Song and J. Renner, "Analysis of oscillatory fluid flow through rock samples," *Geophysical Journal International*, vol. 170, no. 1, pp. 195–204, 2007.
- [40] R. G. Packard, "Streaming potentials across glass capillaries for sinusoidal pressure," *The Journal of Chemical Physics*, vol. 21, no. 2, pp. 303–307, 1953.
- [41] P. M. Reppert, F. D. Morgan, D. P. Lesmes, and L. Jouniaux, "Frequency-dependent streaming potentials," *Journal of Colloid and Interface Science*, vol. 234, no. 1, pp. 194–203, 2001.
- [42] P. M. Reppert and F. D. Morgan, "Streaming potential collection and data processing techniques," *Journal of Colloid and Interface Science*, vol. 233, no. 2, pp. 348–355, 2001.
- [43] W. F. Brace, J. B. Walsh, and W. T. Frangos, "Permeability of granite under high pressure," *Journal of Geophysical Research*, vol. 73, no. 6, pp. 2225–2236, 1968.
- [44] Y. Bernabé, U. Mok, and B. Evans, "Permeability-porosity relationships in rocks subjected to various evolution processes," *Pure and Applied Geophysics*, vol. 160, no. 5–6, pp. 937–960, 2003.
- [45] W. Zhu, L. G. J. Montési, and T. F. Wong, "A probabilistic damage model of stress-induced permeability anisotropy during cataclastic flow," *Journal of Geophysical Research B*, vol. 112, no. 10, Article ID B10207, 2007.
- [46] X. Guichet, L. Jouniaux, and J. P. Pozzi, "Streaming potential of a sand column in partial saturation conditions," *Journal of Geophysical Research B*, vol. 108, no. 3, article 2141, p. 12, 2003.
- [47] N. Linde and A. Revil, "Inverting self-potential data for redox potentials of contaminant plumes," *Geophysical Research Letters*, vol. 34, no. 14, Article ID L14302, 2007.
- [48] A. Revil, N. Linde, A. Cerepi, D. Jougnot, S. Matthäi, and S. Finsterle, "Electrokinetic coupling in unsaturated porous media," *Journal of Colloid and Interface Science*, vol. 313, no. 1, pp. 315–327, 2007.
- [49] T. Ishido, "Electrokinetic mechanisms for the "W"-shaped self-potential profile on volcanoes," *Geophysical Research Letters*, vol. 31, no. 15, article L15616, p. 5, 2004.
- [50] S. Onizawa, N. Matsushima, T. Ishido, H. Hase, S. Takakura, and Y. Nishi, "Self-potential distribution on active volcano controlled by three-dimensional resistivity structure in Izu-Oshima, Japan," *Geophysical Journal International*, vol. 178, no. 2, pp. 1164–1181, 2009.

Research Article

Electric Signals on and under the Ground Surface Induced by Seismic Waves

Akihiro Takeuchi,¹ Kan Okubo,² and Nobunao Takeuchi³

¹ Earthquake Prediction Research Center, Institute of Oceanic Research and Development, Tokai University, 3-20-1 Orido, Shimizu-ku, Shizuoka 424-8610, Japan

² Division of Information and Communications Systems Engineering, Tokyo Metropolitan University, 6-6 Asahigaoka, Hino 191-0065, Japan

³ Research Center for Prediction of Earthquakes and Volcanic Eruptions, Graduate School of Science, Tohoku University, 6-6 Aza-aoba, Aramaki, Aoba-ku, Sendai 980-8578, Japan

Correspondence should be addressed to Akihiro Takeuchi, atakeuchi@sems-tokaiuniv.jp

Received 31 May 2011; Revised 2 November 2011; Accepted 18 November 2011

Academic Editor: Laurence Jouniaux

Copyright © 2012 Akihiro Takeuchi et al. This is an open access article distributed under the Creative Commons Attribution License, which permits unrestricted use, distribution, and reproduction in any medium, provided the original work is properly cited.

We constructed three observation sites in northeastern Japan (Honjo, Kyowa, and Sennan) with condenser-type large plate electrodes ($4 \times 4 \text{ m}^2$) as sensors supported 4 m above the ground and with pairs of reference electrodes buried vertically at 0.5 m and 2.5 m depth (with a ground velocity sensor at Sennan only). Electrical signals of an earthquake (M6.3) in northeastern Japan were detected simultaneously with seismic waves. Their waveforms were damped oscillations, with greatly differing signal amplitudes among sites. Good positive correlation was found between the amplitudes of signals detected by all electrodes. We propose a signal generation model: seismic acceleration vertically shook pore water in the topsoil, generating the vertical streaming potential between the upper unsaturated water zone and the lower saturated water zone. Maximum electric earth potential difference was observed when one electrode was in the saturated water zone, and the other was within the unsaturated water zone, but not when the electrodes were in the saturated water zone. The streaming potential formed a charge on the ground surface, generating a vertical atmospheric electric field. The large plate electrode detected electric signals related to electric potential differences between the electrode and the ground surface.

1. Introduction

Many researchers throughout the world have explored abnormal electromagnetic phenomena preceding earthquakes, such as electromagnetic emissions [1] and ionospheric disturbances [2]. However, most such reports describe methods that are retrospective. Scientific proof of the precursors is apparently still elusive. Earthquake prediction by detection of such precursors cannot be realized easily at this stage. To make steady progress in the scientific study of seismo-electromagnetic precursors, we believe that it is important to prove, first of all, the existence of phenomena that occur at the occurrence of earthquakes and at the arrival of seismic waves and to evaluate these phenomena quantitatively.

First, the piezoelectric effects of quartz and electrokinetic effects of pore water will be regarded as the matter that couples seismic waves and electromagnetic phenomena. However, Ogawa and Utada previously simulated an electric signal induced by seismic waves in a piezoelectric body lying at shallow depth and concluded that the signals would be weak unless the ground motion was unusually strong [3]. On the other hand, Pride proposed, theoretically, coupling of electromagnetics and acoustics of porous media saturated with electrolyte [4] although the purpose of that study was not earthquake prediction. Bordes and coworkers confirmed such coupled phenomena using an experimental apparatus built in an ultrashielded chamber in a deep underground laboratory [5]. Garambois and Dietrich detected electric signals induced by a dynamite shot in the field and analyzed

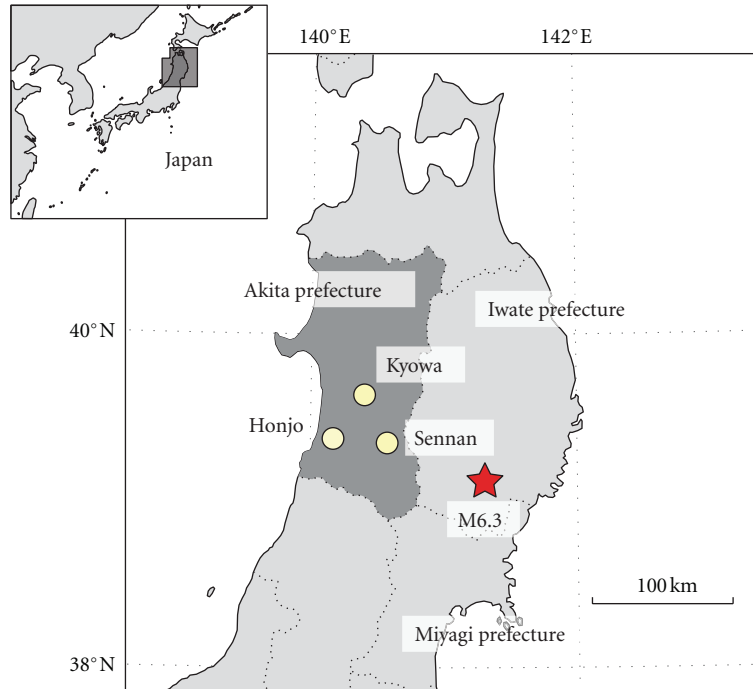


FIGURE 1: Location of three observation sites (Honjo, Kyowa, and Sennan) and the epicenter of an earthquake (M6.3) in northeastern Japan.

them in light of Pride's theory [6]. Consequently, it is expected that electromagnetic phenomena appear under the ground surface at the arrival of "natural" seismic waves, which are driven by the electrokinetic effect of pore water.

We have conducted observations of seismo-electromagnetic phenomena under the ground surface using electrodes buried in the ground. Additionally, we used condenser-type plate electrodes supported above the ground surface. This paper describes the simultaneous detection of electrical signals by electrodes of both types at the arrival of natural seismic waves and discusses their generation models based on their streaming potential under several underground environmental circumstances, although results remain qualitative at this stage.

2. Observation Sites and System

Our first observation sites were in Miyagi Prefecture in northeastern Japan [7, 8]. These sites had sensors of two types: (i) condenser-type electrodes supported above the ground surface by insulator pillars and (ii) reference electrodes buried horizontally and vertically under the ground surface. They detected electric signals at the arrival of seismic waves. The next site was located in Akita Prefecture in northeastern Japan [9]. This site had a similar set of sensors that also detected electric signals. We expected a relation between the signals and pore water in the ground and proposed a prototype model to explain the signals induced by the arrival of seismic waves. However, we had never detected a signal simultaneously at more than two sites until 2001. Therefore, we were unable to discuss a detailed model that was probably strongly related to the observation conditions.

In 2003, we prepared three new observation sites in Akita Prefecture in northeastern Japan. Figure 1 depicts the locations of the three observation sites.

- (1) The Honjo observation site (N39°23', E140°04') was located in a green belt on the Honjo Campus of Akita Prefectural University. To construct the campus, a hill surrounded by rice fields was leveled. The topsoil in this area was brown forest soil or gley soil with silt stones and conglomerates. No tall building existed near this site.
- (2) The Kyowa observation site (N39°40', E140°23') was located in a garden yard of a small recreation house of Akita Prefectural University on a flat land in the middle of mountains. The topsoil in this area was brown forest soil with acid tuff and sandstone. The area around this site was dotted with low-rise houses.
- (3) The Sennan observation site (N39°23', E140°30') was located on the sports ground of a former primary school surrounded by rice fields. The topsoil in this area was gley soil or sand-rich sediments. No tall building existed around this site.

Figure 2 presents a schematic of the observation system. They basically had sensors of two types: (i) a pair of reference electrodes (RE-5; M. C. Miller Co. Inc.) to detect the vertical component of the earth potential difference (EPD), and (ii) a large plate electrode to detect the signal related to the vertical component of the atmospheric electricity (AE). No tall building existed around the large plate electrodes. Therefore, we can reduce the atmospheric electricity disturbing because of such buildings. Only the Sennan observation site also

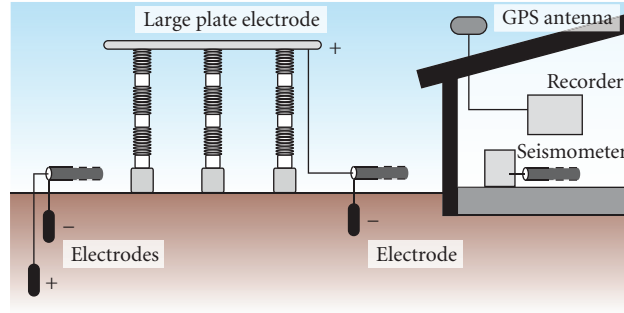


FIGURE 2: Schematic of the observation system. The pair of reference electrodes measured the vertical component of the earth potential difference (EPD). The positive electrode was buried 2.5 m deep; the negative one was buried 0.5 m deep. The aluminum large plate electrode measured signals related to the vertical component of the atmospheric electricity (AE). The plate area was $4 \times 4 \text{ m}^2$. It was supported by five insulators at a height of about 4 m. The velocity sensor (only at Sennan), which was fixed on the concrete base of a barn near the sensors, measured the up-down component of the ground surface velocity.

had a velocity sensor (L-22D; Mark Products LLC) to detect the up-down ground motion. All sensors were connected to a data recorder (DR-1021; DKK-TOA Corp.) with coaxial cables. A PC controlled the recorder and stored the data on its HD at 4 Hz sampling at the Honjo site and at 10 Hz sampling at the Kyowa and Sennan sites. The data clock was synchronized to within 1 ms of the time accuracy using a GPS unit.

Results confirmed that no disturbance appeared in EPD data by minute displacement of the electrodes buried in the ground or by movement of the coaxial cables. Based on our observation experiences [7, 8], we selected the electrode pairs buried vertically rather than horizontally, which can minimize the effects of artificial noise superimposed on the natural telluric currents flowing horizontally. The large plate electrodes were tested under various weather conditions such as heavy snow from August 2000. Thereafter, ordinary observations in the three sites started in May 2001. Although the system worked well during 2001–2006, it became too old to use in 2007: it was difficult to maintain and repair. Therefore, we dismantled the system in 2009.

3. Observation Results

Small earthquakes occurred in and around Akita Prefecture, sometimes causing weak electric signals at the Sennan observation site at the arrival of seismic waves [9]. When a major earthquake occurred in Iwate Prefecture (Figure 1), it caused electric signals at all three sites. We specifically examine this earthquake, which was the only major earthquake occurring around this area during 2001–2006. It occurred at 22:02 JST (= UT + 9 hr) on December 2, 2001. Its magnitude was 6.3 on the Japan Meteorological Agency (JMA) scale. The epicenter was (N39°23', E141°16'), with focal depth of 130 km. The focal depth of this earthquake was so great that the hypocentral distances of the three sites were almost identical. In general, local seismic intensity depends strongly on the site environments and the propagation paths of seismic waves. However, JMA seismometers around our three observation sites indicated the local seismic intensity of 3–4

on the JMA scale that is classified into 10 ranks. Therefore, we can assume that the local seismic intensities at the sites were similar.

Figure 3 portrays plots of raw data before and after the arrival of seismic waves at each site. The upper rows show raw EPD, the middle ones show raw AE, and the lower one shows the raw ground velocity at the Sennan site. The time range is 22:00–22:05 JST. Dotted lines show the time of origin of the earthquake. Vibrating waveforms are confirmed, although some are small against background variations. These background variations were probably the result of local variations of atmospheric electricity, power line noise, and wind. To clarify the waveforms that are of interest for this study, we adopted the moving average method. In this study, the time period of 1 s was used for calculation of the moving average. The 1 s moving averages were subtracted from the original data, yielding the remnant waveforms as shown in Figure 4. The result clarifies that the damped oscillations are induced simultaneously in EPD and AE at the arrival of seismic waves, although some of them still include background noise, probably from power lines. Spectrum analyses show that both signals have a peak at about 1 Hz. The outline waveforms of the induced EPD and AE signals are similar to that of the ground velocity at the Sennan site. Those at Honjo and Kyowa will be also similar to those of the ground velocity at each site.

Figure 5 shows the relation between the average amplitudes of the induced EPD and AE signals ($\overline{\text{EPD}}$ and $\overline{\text{AE}}$, resp.). They are defined as shown below

$$\begin{aligned} \text{average} &= \sqrt{\frac{1}{30(\text{s})} \sum_{\text{peak time } (t=0(\text{s}))}^{t=30(\text{s})} (\text{induced signal} + \text{background}(t))^2} \\ &\quad - \sqrt{\frac{1}{30(\text{s})} \sum_{\text{no propagation } (t'=0(\text{s}))}^{t'=30(\text{s})} (\text{background}(t'))^2}. \end{aligned} \quad (1)$$

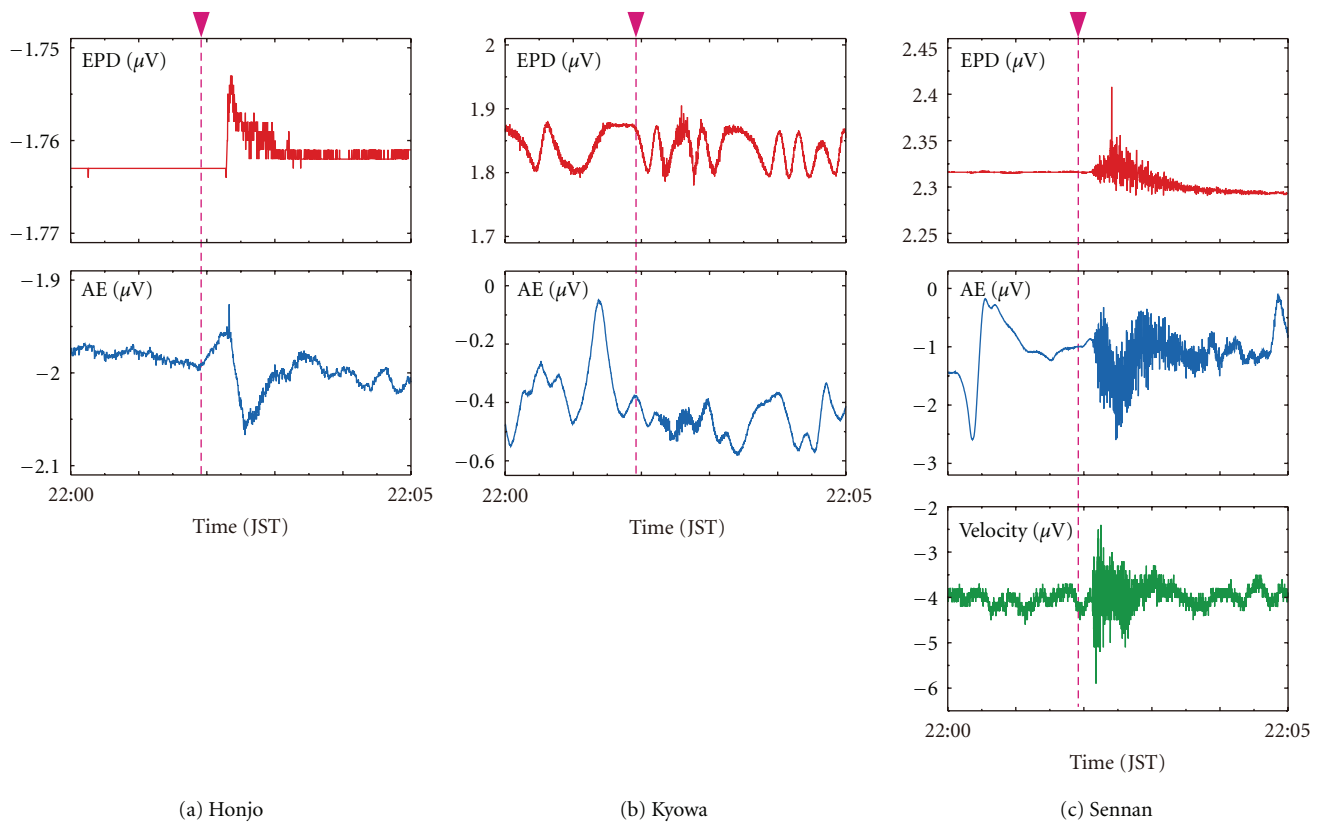


FIGURE 3: Raw data recorded before and after the arrival of seismic waves from a M6.3 earthquake: (a) at Honjo, (b) at Kyowa, and (c) at Sennan. Upper row graphs show raw data of the earth potential difference (EPD). Middle ones show raw data of the signals related to the atmospheric electricity (AE). Lower one shows raw data of the ground velocity (only at Sennan). Broken lines show the origin time. The time is in JST (= UT + 9 hr).

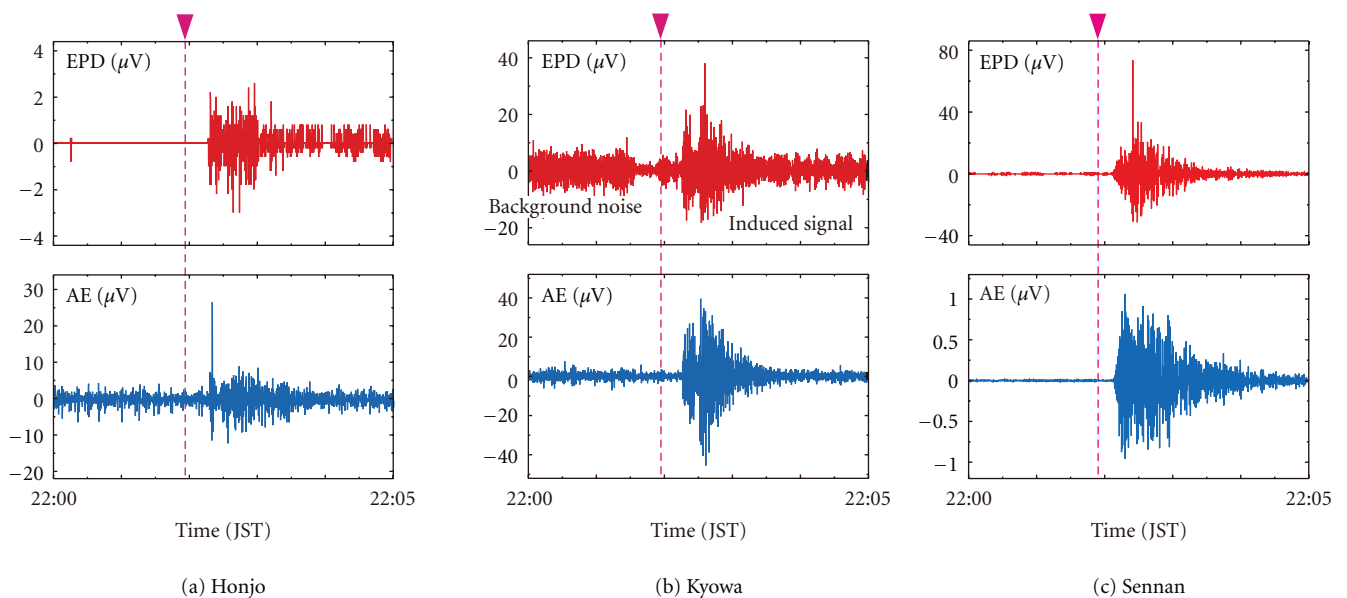


FIGURE 4: Waveforms extracted from raw data presented in Figure 3 using the 1 s moving average method: (a) at Honjo, (b) at Kyowa, and (c) at Sennan. Broken lines mean the origin time. The time is in JST (= UT + 9 hr).

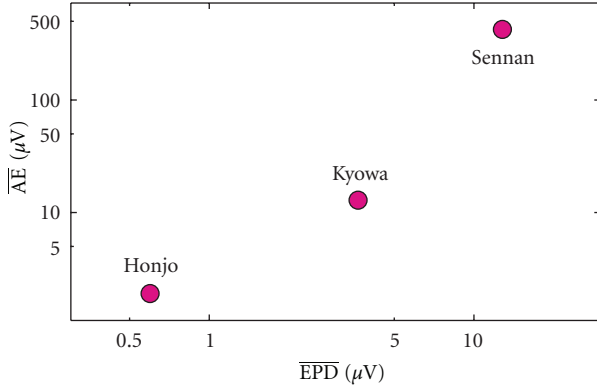


FIGURE 5: Positive correlation between the average of the induced earth potential difference ($\overline{\text{EPD}}$) and the average of the induced atmospheric electricity ($\overline{\text{AE}}$).

The summation in the first root is over a period of 30 s after the peak time of the induced EPD and AE signals; another in the second root is over a period of 30 s when no seismic wave propagated. Figure 5 depicts a positive relation between $\overline{\text{EPD}}$ and $\overline{\text{AE}}$. Although the local seismic intensity is probably similar among the three sites as described above, the $\overline{\text{EPD}}$ and $\overline{\text{AE}}$ at the Honjo site are smaller; those at the Sennan site are larger.

4. Discussion

4.1. Generation Mechanism of the Induced EPD Signals. We can list two effects as possible mechanisms generating the induced EPD signals. The first is a piezoelectric effect of quartz grains involved in the topsoil under the large plate electrodes. However, all observation sites were located on the topsoil, which was wet sometimes. Electric polarizations at each small quartz grain will be quite small. Moreover, polarization vectors will be random. Therefore, the vector summation is almost negligible. Furthermore, as described in the Introduction, an early simulation by Ogawa and Utada indicated that an electric signal induced by piezoelectric effect is expected to be weak [3]. In conclusion, the possibility of piezoelectricity is discounted. The second is an electrokinetic effect of pore water in the topsoil under the large plate electrodes. Our earlier observation data detected by similar sensors at a different site in Miyagi Prefecture and at Sennan site revealed a linear relation in log-log plots between the local seismic intensity and $\overline{\text{EPD}}$ [7, 9]. Moreover, in those observations, the EPD waveform resembles that of the ground acceleration. Therefore, the force applied to pore water varies similarly to the EPD waveform. These results show that $\overline{\text{EPD}}$ increases proportionally with the pressure difference in pore water. In this paper, we specifically examine the streaming potential caused by electrokinetic effect of pore water under seismic pressure.

From the viewpoint of geohydraulics, the water content generally increases with increased depth in the topsoil to be with pores. The upper is called the unsaturated water zone. The lower is called the saturated water zone [10, 11]. Next,

we consider only the vertical component. As portrayed in Figure 6(a), we assume the network of pores in the topsoil as a bundle of tubes connecting the air and the saturated water zone, as is often assumed also for the study of electric fields induced by the vertical fluid flow [12, 13]. The upper part is a fine tube; the lower is a capillary tube. The lower part of the capillary tubes holds the pore water, called the capillary saturated water zone. The lower part is the saturated water zone, where the network of pore water is mutually and completely connected. It is noteworthy that such a bundle of tubes is not generated by seismic waves, but is instead a representation of the network of pores. Here, we assume that positive ions are predominant in water in the capillary tubes, although negative ions adhere to the tube inner walls. Maldistribution of positive and negative ions engenders the formation of electric potential difference between the center and wall of the tubes, called the zeta potential. Because this maldistribution depends on the soil type and the pore water pH [12, 14], positive ions will adhere to the walls under different conditions.

Based on field observations and theoretical studies, it is well known that the seismic acceleration is coupled with the pore pressure [15, 16]. This coupled dynamics must be valid in our geohydraulic system depicted in Figure 6(a). The wavelength of the seismic waves is much longer than the tube dimensions. Therefore, we can assume that the acceleration is uniform in our geohydraulic system. As indicated in Figure 6(b), when acceleration is inflicted upward in this system, the water in the capillary tubes flows upward along the tubes. In the real soil layer, soil grains function also as obstacles to the vertical water flow, so that a portion of the flow will bend in horizontal directions. Such horizontal flows deviated from each vertical flow will cancel each other. As a result, the vertical component of the flow remains. The tubes in our model represent the flow routes of the remnant vertical flow of pore water. Pride used a similar assumption to derive the coupled electromagnetics and acoustics of porous media from first principles [4].

The number of cations exceeds the number of anions in the diffuse layer of the electrical double layer in this system. Therefore, upward flow of the water engenders a positive electrification in the upper range of the tubes. However, the lower range of the tubes is negatively charged. Consequently, the vertical electric dipoles are formed and an electric potential difference (called streaming potential) appears between the upper level of the water flowing up and the saturated water zone. Because no more charge occurs above the upper level of the water, the electric potential in this range is almost constant or decreases because of a small amount of pore water in this range. When the positive and negative terminals of electrodes are buried, respectively, in the saturated water zone and the unsaturated water zone, they will detect a negative induced EPD signal. As Figure 6(c) shows, when acceleration is inflicted downward in this system, the opposite phenomena occur: the electrode will detect a positive induced EPD signal. Consequently, when seismic waves vertically oscillate this geohydraulic system, the electrodes detect an induced EPD signal that also oscillates.

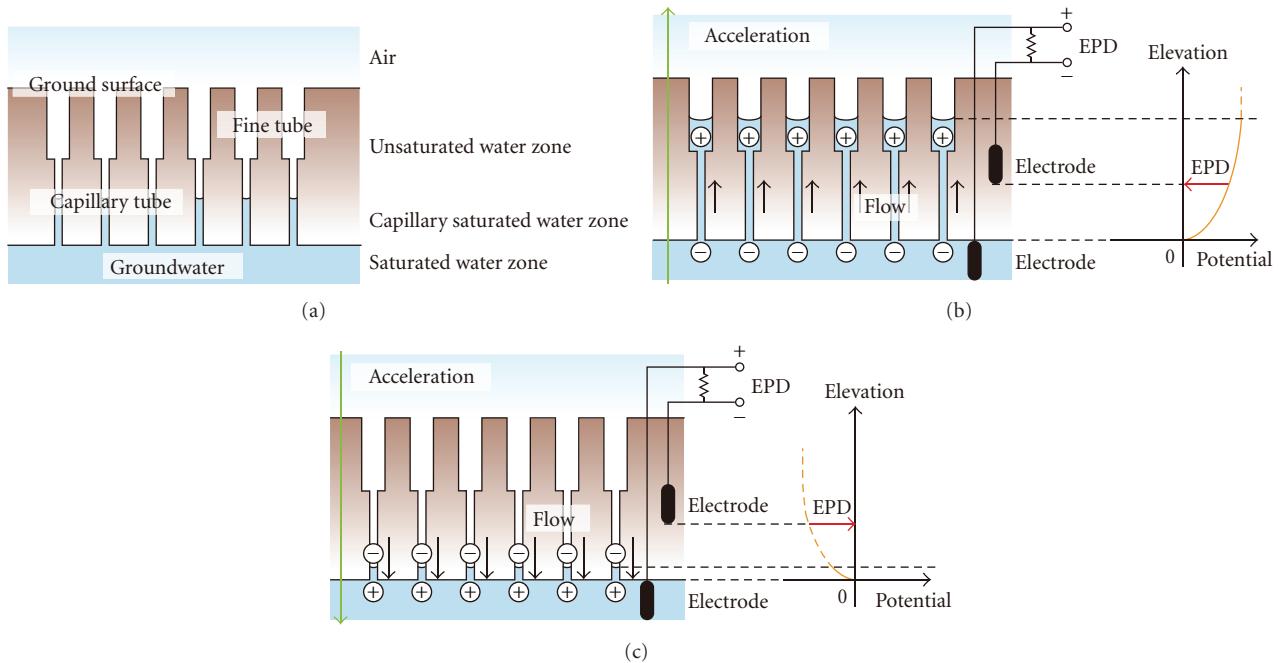


FIGURE 6: Generation model of the induced earth potential difference (EPD). (a) Model of the topsoil from the viewpoint of water saturation/unsaturation. (b) Generation of a negative EPD signal induced by streaming potential because of the upward flow of water along the tubes. (c) Generation of a positive EPD signal induced by streaming potential because of the downward flow of water along the tubes.

It is known that there are the underground electric fields produced by electric dipoles existing at the boundary between the capillary saturated water zone and the saturated water zone (the so-called water table) [17]. The dipoles are perpendicular to the boundary, and their polarity and amplitude depend, respectively, on the zeta potential and the conductivity of the saturated water zone. However, they do not reflect a transient effect, but a DC effect. Therefore, the transient movement of a seismic wave cannot move this boundary at this time scale. Consequently, the underground electric field produced by these dipoles will not contribute to the induced EPD signals in our observation system.

The amplitude of EPD signals will depend on the electrode positions in this geohydraulic system. Next we assume the six cases presented in Figure 7.

- (a) When both electrodes are located mutually parallel in the unsaturated water zone (Figure 7(a)), the induced EPD signals will be slight. Even if the streaming potential appears at the electrodes, the potential difference between them will be small. For example, in our previous similar observations at a different site [7], the vertical induced EPD signal was 10 times larger than the horizontal one, in which each electrode was separated by 2 m.
- (b) When one electrode is located in the unsaturated water zone and another is in the saturated water zone (Figure 7(b)), the induced EPD signals will be large. The electrode pair is located at both ends of electric polarization. Therefore, the electrodes detect the

potential difference most effectively. Consequently, the amplitude becomes the maximum.

- (c) When both electrodes are located in the saturated water zone (Figure 7(c)), the induced EPD signals will be slight. Because the pore water network is completely connected, this zone is sufficiently conductive. Most of the streaming potential will be canceled. For example, in our previous similar observation at a different site [7], two electrodes were buried at depths of 10 m and 12 m, probably in the saturated water zone. They detected only very small induced EPD signals.
- (d) When one electrode is located deep in the unsaturated water zone and another is deep in the saturated water zone (Figure 7(d)), the induced EPD signals will be large. This case resembles case (b). For example, in our previous similar observations at a different site [8], a pair of electrodes was buried at depths of 7 m and 10 m. A borehole survey confirmed that the upper level of the saturated water zone was at 9 m depth. This site detected sufficiently large induced EPD signals against background variations.
- (e) When both electrodes are located in the unsaturated water zone far from the deep saturated water zone (Figure 7(e)), the induced EPD signals will be very small. No pore water flows up in the upper range of the thick unsaturated water zone. Therefore, little potential difference appears between the electrodes.
- (f) When one electrode is in the unsaturated water zone and another is near or above the saturated water zone

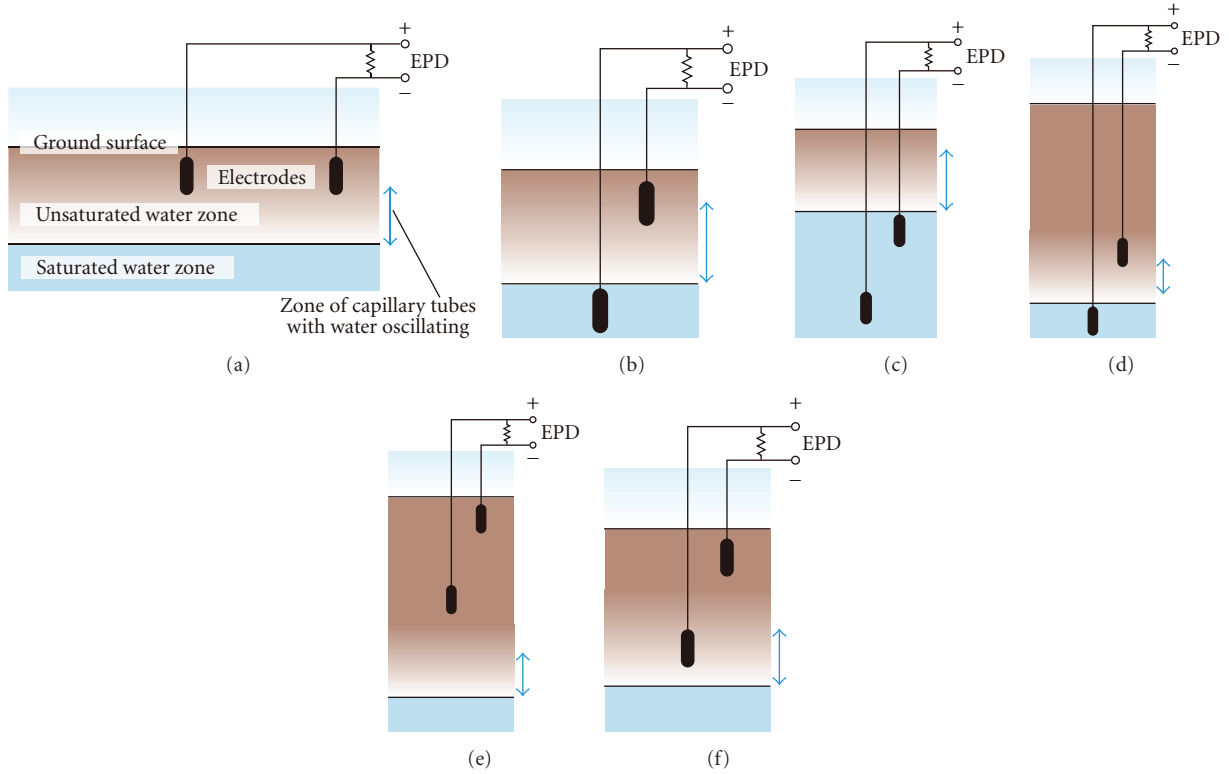


FIGURE 7: Various cases of locations with the electrode pair buried and with saturated/unsaturated water zone levels. (a) Both electrodes are mutually parallel in the unsaturated water zone. (b) One electrode is buried in the unsaturated water zone; another is buried in the saturated water zone. (c) Both electrodes are buried in the saturated water zone. (d) One electrode is deeply buried in the unsaturated water zone; another is buried deeply in the saturated water zone. (e) Both electrodes are buried in the unsaturated water zone far from the deep saturated water zone. (f) One electrode is buried in the unsaturated water zone; another is buried near but above the saturated water zone.

(Figure 7(f)), the induced EPD signals will be not so large. Until the lower electrode is buried in the water flowing up, no sufficient potential difference appears between the electrodes.

Because this model is based on streaming potential, \overline{EPD} depends on the zeta potential, that is, the soil type. However, as described above, the topsoil is fortunately similar among site areas: brown forest soil or gley soil. Therefore, we need not be so sensitively concerned about the soil type in this study. Nevertheless, according to reports of earlier studies, the apparent electrokinetic coefficient of a (un-)saturated medium reaches the maximum under the 70% saturation state, not under a perfectly saturated state [18]. This fact is concordant with our six models presented in Figure 7 because our model for the induced EPD signal is based on the electrokinetic effect, which is strongly related to the electrokinetic coefficient. For example, the saturated state of case (c) is 100%. Therefore, the apparent electrokinetic coefficient is less than that in case (b). This engenders a decrease of \overline{EPD} in case (c). Here, we can expect that the significant difference of the \overline{EPD} among the three sites mainly results from differences in the position of the buried electrodes and saturated water zone.

- (1) The Honjo observation site was located 6 m above the surrounding rice fields. The saturated water zone is

expected to be a few meters deeper than the fields. Therefore, this site corresponds to case (e): the \overline{EPD} was small.

- (2) The Kyowa observation site was located on a flat land in the middle of mountains. Therefore, this site will correspond to case (f): the \overline{EPD} was not so large.
- (3) The Sennan observation site was located on the same level as the surrounding rice fields. The saturated water zone will be a few meters deeper than the fields. Therefore, this site will correspond to case (b): the \overline{EPD} was large.

In case (b), the \overline{EPD} will be roughly equal to the streaming potential, as defined simply by

$$\frac{\overline{EPD}}{L} = \left| C \frac{P_{\text{bottom}} - P_{\text{top}}}{L} \right|, \quad (2)$$

where L (ca. 1-2 m) is the capillary water height, C signifies the apparent electrokinetic coefficient, P_{bottom} denotes the seismic pressure applied at the bottom of the capillary water, and P_{top} stands for the pressure at the top. The value of C is obtained as

$$C = \frac{\epsilon_r \epsilon_0 \zeta}{\eta \sigma}, \quad (3)$$

where ε_r denotes the relative permittivity of capillary water, ε_0 ($= 8.8 \times 10^{-12}$ F/m) represents the permittivity of vacuum, ζ is the zeta potential, η stands for the viscosity of capillary water, and σ signifies the electric conductivity of the capillary water. We have no concrete values for these parameters for our observation sites except σ of approximately 0.01 S/m. Therefore, we simply apply standard values that are often used for order estimation: ε_r of about 80, $|\zeta|$ of about 10^{-2} V, and η of approximately 10^{-4} Pa s [19]. Using these values, we obtain $|C|$ of approximately 10^{-5} V/Pa. Moreover, Allègre and coworkers made a compilation that $|C|$ is of approximately 10^{-6} V/Pa in the case of sands and sand stones at pH 7-8 [18]. Therefore, we adopt $|C|$ of approximately 10^{-6} – 10^{-5} V/Pa for this study. On the other hand, the P_{bottom} is obtained from

$$P_{\text{bottom}} = \frac{ma}{S}, \quad (4)$$

where m ($= m^*SL$, with $m^* = 10^3$ kg/m³) represents the mass of the capillary water, a is the seismic acceleration, and S denotes the cross section of the capillary tube. The local seismic intensity 3 in the JMA scale has a of about 10^{-1} m/s² at ca. 1 Hz. Consequently, we obtain P_{bottom} of ca. 10^2 Pa. By contrast, P_{top} is approximately 0 Pa because nothing is on the top surface of the capillary water. Finally, we obtain $\overline{\text{EPD}}$ of about 10^{-4} – 10^{-3} V, which is not so different from the value obtained from the observations at Sennan site.

4.2. Generation Mechanism of the Induced AE Signals. As shown in Figure 4, the induced AE signals appear in combination with the induced EPD signals. Moreover, as shown in Figure 5, a good positive correlation exists between $\overline{\text{AE}}$ and $\overline{\text{EPD}}$. Therefore, the generation mechanism of the induced AE signals must be coupled with that of EPD: both mechanisms are strongly related to streaming potential. Figure 8 presents a schematic diagram of a possible generation model of the induced AE signals in case (b) shown in Figure 7. As described in Figure 6, oscillation of the streaming potential appears in the unsaturated water zone. This is equivalent to oscillation of the electric dipoles vertical to the ground immediately under the ground surface. Their electric charges on the ground surface generate an atmospheric electric field vertical to the ground. Results show the appearance of oscillation of the electric potential difference between the large plate electrode and the ground surface. Electric charges move between the electrode and the ground through the recorder to cancel the potential oscillation. This movement is detected as oscillation of the induced AE signal.

Here, it is noteworthy that the recorded signal is not equal to the potential difference between the large plate electrode and the ground surface; the electric potential superimposed on the background variation is caused by a transient current passing through the internal resistance of the recorder. To obtain the original waveform of the induced AE signals, we need the integral of the recorded waveforms using different coefficients for each frequency. However, obtaining the coefficients is difficult. We have no concrete values to calculate the original AE signals at the present stage.

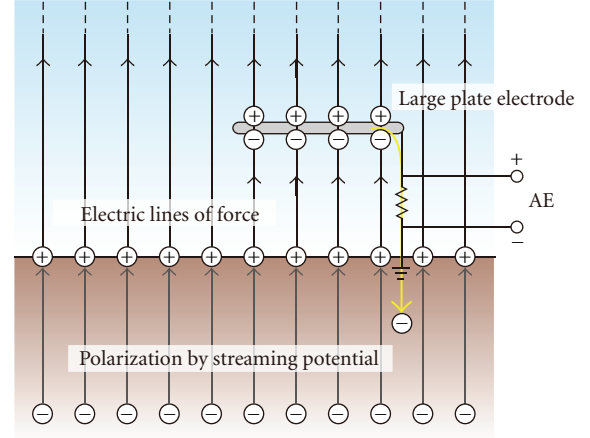


FIGURE 8: Generation model of induced atmospheric electricity (AE) coupled with generation of streaming potential in the topsoil.

Therefore, we must compare only the outwards of the signal amplitudes, as described in Section 3.

According to our model presented in Figure 8, a greater acceleration and a larger electrokinetic coefficient engender the higher charge density on the ground surface under certain good underground conditions such as those in case (b) of Figure 7. This engenders the larger atmospheric electricity. The Sennan observation site will correspond to this case. If this surface charge is sufficiently large, say ca. 5×10^{-5} C/m² [20], to cause dielectric breakdown of the air on the ground surface under a certain special condition, a dim light of corona discharge might appear in the atmosphere. This might be a possible mechanism of luminous phenomena accompanied with earthquakes, so-called earthquake lightning. If this field can be sufficiently large, say ca. 1 kV/m [21, 22], in an extensive area under a certain special condition, then it might disturb plasma in the ionosphere. However, the charge density on the ground surface cannot be large in case (e) of Figure 7 because a portion of the electric field vertical to the ground will be absorbed in the thick upper unsaturated (but not dry) water zone. This engenders a decrease of the charge density on the ground surface. Consequently, only the small induced AE signal appears. The Honjo observation site corresponds to this case.

5. Conclusions

The Honjo, Kyowa, and Sennan observation sites in north-eastern Japan detected the induced earth potential difference (EPD) signal and the induced atmospheric electricity (AE) signals at the arrival of seismic waves from a M6.3 earthquake near the sites. The signal waveforms were damped oscillations in combination with the seismic waves. Although the signal amplitudes were different at each site, good positive correlation was found between the averaged amplitudes of EPD ($\overline{\text{EPD}}$) and AE ($\overline{\text{AE}}$) signals. According to our coupled generation model of the electric signals based on streaming potential, the amplitude of the vertical atmospheric electric field is influenced strongly by the depth of the saturated

water zone and the location of electric polarization because of electrokinetic effects. This model can explain the site dependence of EPD and AE. According to this model, no guarantee exists that the amplitude of the vertical atmospheric electric field is strongest at the epicenter.

Although only one major earthquake simultaneously shook the observation sites during operations, this observation advanced our prototype generation model. The model proposed in this paper presents consideration of the actual underground environmental circumstances. Although it remains merely qualitative, we believe that it is a great step up to steady progress in the study of seismoelectromagnetic precursors. The next step is elucidation of the dynamic electric fields in the ground and accompanying magnetic fields, which are both induced by seismic waves. To do so, observation sites in the ground [23–26] that can detect three-dimensional dynamic electric/magnetic signals are also needed.

Acknowledgments

The authors thank Mr. Hiromi Ishikawa of Yurtec Corp., Akita, Japan, for his support in designing and constructing the large plate electrodes. They also thank two anonymous reviewers for their valuable comments on the paper.

References

- [1] M. Hayakawa, Y. Kasahara, T. Nakamura et al., “A statistical study on the correlation between lower ionospheric perturbations as seen by subionospheric VLF/LF propagation and earthquakes,” *Journal of Geophysical Research A*, vol. 115, no. 9, Article ID A09305, 2010.
- [2] K. I. Oyama, Y. Kakinami, J. Y. Liu, M. Kamogawa, and T. Kodama, “Reduction of electron temperature in low-latitude ionosphere at 600 km before and after large earthquakes,” *Journal of Geophysical Research A*, vol. 113, no. 11, Article ID A11317, 2008.
- [3] T. Ogawa and H. Utada, “Electromagnetic signals related to incidence of a teleseismic body wave into a subsurface piezoelectric body,” *Earth, Planets and Space*, vol. 52, no. 4, pp. 253–260, 2000.
- [4] S. Pride, “Governing equations for the coupled electromagnetics and acoustics of porous media,” *Physical Review B*, vol. 50, no. 21, pp. 15678–15696, 1994.
- [5] C. Bordes, L. Jouniaux, S. Garambois, M. Dietrich, J. P. Pozzi, and S. Gaffet, “Evidence of the theoretically predicted seismomagnetic conversion,” *Geophysical Journal International*, vol. 174, no. 2, pp. 489–504, 2008.
- [6] S. Garambois and M. Dietrich, “Seismoelectric wave conversions in porous media: field measurements and transfer function analysis,” *Geophysics*, vol. 66, no. 5, pp. 1417–1430, 2001.
- [7] N. Takeuchi, N. Chubachi, and K. Narita, “Observations of earthquake waves by the vertical earth potential difference method,” *Physics of the Earth and Planetary Interiors*, vol. 101, no. 1–2, pp. 157–161, 1997.
- [8] N. Takeuchi, N. Chubachi, K. Narita, N. Honma, and T. Takahashi, “Characteristics of vertical earth potential difference signals,” *Transactions of IEE Japan*, vol. 117-C, no. 5, pp. 554–560, 1997 (Japanese).
- [9] K. Okubo, M. Takayama, and N. Takeuchi, “Electrostatic field variation in the atmosphere induced by earth potential difference variation during seismic wave propagation,” *IEEE Transactions on Electromagnetic Compatibility*, vol. 49, no. 1, pp. 163–169, 2007.
- [10] G. N. Smith, *Elements of Soil Mechanics for Civil and Mining Engineers*, Collins, London, UK, 5th edition, 1982.
- [11] D. F. McCarthy, *Essentials of Soil Mechanics and Foundations: Basic Geotechnics*, Prentice Hall, Upper Saddle River, NJ, USA, 7th edition, 2006.
- [12] T. Ishido and J. Muzutani, “Experimental and theoretical basis of electrokinetic phenomena in rock-water systems and its applications to geophysics,” *Journal of Geophysical Research*, vol. 86, no. B3, pp. 1763–1775, 1981.
- [13] M. D. Jackson, “Multiphase electrokinetic coupling: insights into the impact of fluid and charge distribution at the pore scale from a bundle of capillary tubes model,” *Journal of Geophysical Research*, vol. 115, Article ID B07206, 17 pages, 2010.
- [14] X. Guichet, L. Jouniaux, and N. Catel, “Modification of streaming potential by precipitation of calcite in a sand-water system: laboratory measurements in the pH range from 4 to 12,” *Geophysical Journal International*, vol. 166, no. 1, pp. 445–460, 2006.
- [15] R. Muir-Wood and G. C. P. King, “Hydrological signatures of earthquake strain,” *Journal of Geophysical Research*, vol. 98, no. 12, pp. 22,035–22,068, 1993.
- [16] R. Yan, Y. Chen, F. W. Gao, and F. Q. Huang, “Calculating Skempton constant of aquifer from volume strain and water level response to seismic waves at Changping seismic station,” *Acta Seismologica Sinica*, vol. 21, no. 2, pp. 148–155, 2008.
- [17] A. Revil, V. Naudet, J. Nouzaret, and M. Pessel, “Principles of electrography applied to self-potential electrokinetic sources and hydrogeological applications,” *Water Resources Research*, vol. 39, no. 5, pp. SBH31–SBH315, 2003.
- [18] V. Allègre, L. Jouniaux, F. Lehmann, and P. Sailhac, “Streaming potential dependence on water-content in Fontainebleau sand,” *Geophysical Journal International*, vol. 182, no. 3, pp. 1248–1266, 2010.
- [19] H. Mizutani, T. Ishido, T. Yokokura, and S. Ohnishi, “Electrokinetic phenomena associated with earthquakes,” *Geophysical Research Letters*, vol. 3, no. 7, pp. 365–368, 1976.
- [20] D. A. Lockner, M. J. S. Johnston, and J. D. Byerlee, “A mechanism to explain the generation of earthquake lights,” *Nature*, vol. 302, no. 5903, pp. 28–33, 1983.
- [21] S. A. Pulinet, K. A. Boyarchuk, V. V. Hegai, V. P. Kim, and A. M. Lomonosov, “Quasielectrostatic model of atmosphere-thermosphere-ionosphere coupling,” *Advances in Space Research*, vol. 26, no. 8, pp. 1209–1218, 2000.
- [22] Y. Rapoport, V. Grimalsky, M. Hayakawa et al., “Change of ionospheric plasma parameters under the influence of electric field which has lithospheric origin and due to radon emanation,” *Physics and Chemistry of the Earth*, vol. 29, no. 4–9, pp. 579–587, 2004.
- [23] K. Okubo, S. Sato, T. Ishii, and N. Takeuchi, “Observation of atmospheric electricity variation signals during underground seismic wave propagation,” *Transactions on Electrical and Electronic Engineering*, vol. 1, no. 2, pp. 182–187, 2006.
- [24] K. Okubo, N. Takeuchi, M. Utsugi, K. Yumoto, and Y. Sasai, “Direct magnetic signals from earthquake rupturing: Iwate-Miyagi earthquake of M 7.2, Japan,” *Earth and Planetary Science Letters*, vol. 305, no. 1–2, pp. 65–72, 2011.

- [25] A. Takeuchi, K. Okubo, S. Watanabe, Y. Nakamura, and N. Takeuchi, "Electric and ionic environmental circumstances interacting at Hosokura underground mine in northeast Japan," *IEEJ Transactions on Fundamentals and Materials*, vol. 129, no. 12, pp. 870–874, 2009.
- [26] A. Takeuchi, Y. Futada, K. Okubo, and N. Takeuchi, "Positive electrification on the floor of an underground mine gallery at the arrival of seismic waves and similar electrification on the surface of partially stressed rocks in laboratory," *Terra Nova*, vol. 22, no. 3, pp. 203–207, 2010.

Research Article

The Self-Potential Anomaly Produced by a Subsurface Flow at the Contact of Two Horizontal Layers and Its Quantitative Interpretation

Georgios Aim. Skianis

*Department of Geography and Climatology, Faculty of Geology and Geoenvironment,
National and Kapodistrian University of Athens, Panepistimiopolis, 15784 Athens, Greece*

Correspondence should be addressed to Georgios Aim. Skianis, skianis@geol.uoa.gr

Received 24 May 2011; Revised 26 September 2011; Accepted 7 November 2011

Academic Editor: Laurence Jouniaux

Copyright © 2012 Georgios Aim. Skianis. This is an open access article distributed under the Creative Commons Attribution License, which permits unrestricted use, distribution, and reproduction in any medium, provided the original work is properly cited.

In the present paper the problem of a polarized cylinder with a small cross-section, which is located at the contact of two horizontal layers with different resistivities, is studied. Such a polarization geometry simulates the self-potential (SP) field produced by a horizontal flow at the contact between the two layers. First, the expression of the self potential at the space domain is derived, applying the image technique. Then, the expression for the Fourier transform of the SP anomaly is found and the behavior of the amplitude spectrum is studied. Based on this study, a direct interpretation method at the spatial frequency domain is proposed, in order to calculate the depth of the flow and the reflection coefficient of the stratified medium. Experimentation with a synthetic model shows that the method works well (small deviations between true and calculated values). When the SP curve contains noise, deviations between calculated and true depths are smaller than those between calculated and true reflection coefficients. The proposed method, which is also applied on SP data from a geothermal system (Mauri et al., 2010), may be useful in detecting underground water or heat flows.

1. Introduction

The self-potential (SP) method has been extensively used to detect groundwater and hydrothermal flows. During the last decade, a variety of applications of the SP method have been developed, such as detecting ground water and hydrothermal flows at volcanic areas [1–4], mapping infiltration in a karstic environment [5], monitoring evolving plumes at subsoil [6] and studying landslides [7]. Recent experimental work has also been done to study the electrokinetic and hydraulic parameters, which influence the SP anomaly [8–10]. A thorough review on the applications of the self-potential method in the detection and monitoring of subsurface flows is made by Jouniaux et al. [11].

According to Schiavone and Quarto [12], a horizontal groundwater flow at the contact of two layers is expected to produce a self-potential anomaly of electrokinetic origin, at ground surface. The geometry of the subsurface flow in the

stratified medium is presented in Figure 1. The two layers have different electrokinetic coupling coefficients C_1 (upper layer) and C_2 (lower layer) and electrical resistivities ρ_1 and ρ_2 , respectively. In Figure 2 a profile of the SP anomaly at ground surface is presented. The direction of the profile is perpendicular to that of the subsurface flow. The SP anomaly is expected to be positive for $(C_1 - C_2) P > 0$ and negative for $(C_1 - C_2) P < 0$. P is the pressure difference between the contact of the layers, where the flow takes place, and the ambient. Electric potential drops are expected to be produced along the direction of the water flow, but they do not affect the polarity of the SP anomaly across the water flow. The polarity could be affected by the presence of a vertical component of the flow, which does not exist in the model under consideration.

Considerable research has been made to model the electrokinetic self-potential anomaly in terms of its production mechanism (water flow in a porous medium) and its

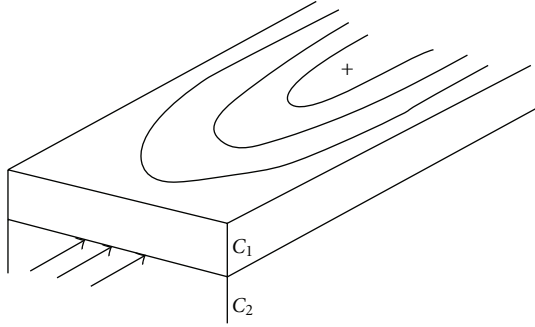


FIGURE 1: Representation of a self-potential anomaly that is produced by a horizontal subsurface flow at the contact of two layers (Schiavone and Quarto [12]).

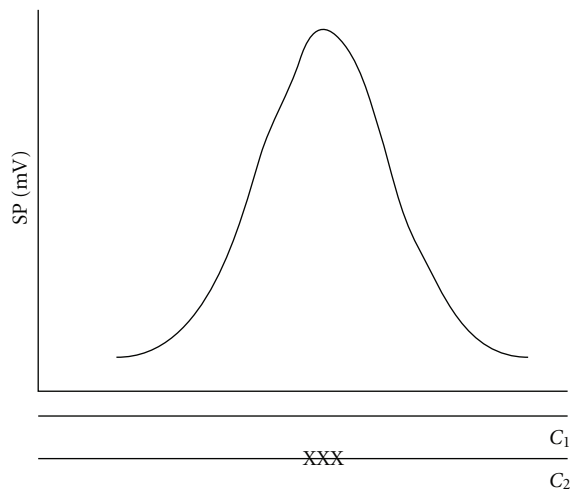


FIGURE 2: A profile of the self-potential anomaly produced by a horizontal flow perpendicular to the paper. The location of the flow is indicated by the symbols XXX (Schiavone and Quarto [12]).

dependence on the resistivity distribution of the ground [13–15]. On the other hand, in order to invert the measured SP anomaly, which means to calculate the depth of the horizontal flow, it is important to have in mind that the physical system of the subsurface flow at the contact of the two layers is equivalent to a system of dipoles oriented perpendicularly to the contact, as Ogilvy et al. [16] have pointed out. Therefore, the inverse problem consists in determining the location of the underground dipole current sources.

If the width of the underground current flow is small relatively to its depth from ground surface, the source of the SP anomaly may be represented by a system of two elongated horizontal lines with an opposite charge. This elongated dipole is usually called polarized cylinder of a small radius R and depth b (see Figure 3). A first approach to the inverse problem is to assume an electrically homogeneous ground and calculate the depth of the cylinder by one of the several direct quantitative interpretation methods which have been developed, such as those of Bhattacharya and Roy [17] or Murty and Haricharan [18]. A serious drawback of

these approaches is that if the electrical inhomogeneity of the ground is not taken into account, considerable errors in the depth calculation of the polarized body may be made [19, 20].

An alternative approach on the inversion problem is to fit the SP curve measured at ground surface by an automated trial and error process, assuming different distributions of electric current sources at a nonhomogeneous ground for each iteration, till a satisfactory fit is achieved [21, 22]. Such a process may work well if the resistivity distribution of the ground is known a priori.

The self-potential tomography, which has been first developed by Patella [23, 24], solves the inverse problem without any a priori knowledge of the resistivity distribution, using correlation integrals and defining probability of tomography. However, Gibert and Sailhac [25] demonstrated that the so-called probability of tomography defines images of SP data in the wavelet domain that must not be interpreted as underground images of SP sources. They pointed out that an appropriate inversion is necessary to achieve underground image. An alternative methodology of self-potential tomography, based on the wavelet transform, has been developed by Gibert and Pessel [26].

In the present paper, a direct interpretation method of SP anomalies is proposed in order to calculate the depth of the horizontal subsurface flow at the contact between two horizontal layers, as well as the resistivity contrast of the ground, which is expressed as reflection coefficient. The flow is simulated by a horizontal polarized cylinder. The quantitative interpretation is carried out at the spatial frequency domain of the self-potential field. The potential advantage of the proposed method, which may be useful in detecting horizontal groundwater or geothermal flows at a stratified ground, is that although it takes into account the ground electrical inhomogeneity, it works with no a priori information about the resistivity distribution.

2. The SP Anomaly at Space Domain

In Figure 3 the geometry of the problem of the horizontal polarized cylinder at the contact of two horizontal layers is presented. The polarized cylinder is the equivalent of a horizontal subsurface flow at the same location, which produces a self-potential anomaly $V(x)$ at ground surface. The intersection of the cylinder (see solid circle in Figure 3) has a small radius R and its center is at depth b below ground surface. b is also the thickness of the upper layer.

For a vertically polarized horizontal cylinder at depth b in an electrically homogeneous medium of resistivity ρ , the SP anomaly $V(x)$ is given by [17, 18]

$$V(x) = \frac{4MRb}{x^2 + b^2}. \quad (1)$$

M is the polarization of the body and it is given by [17, 18]

$$M = \frac{I\rho}{2\pi}. \quad (2)$$

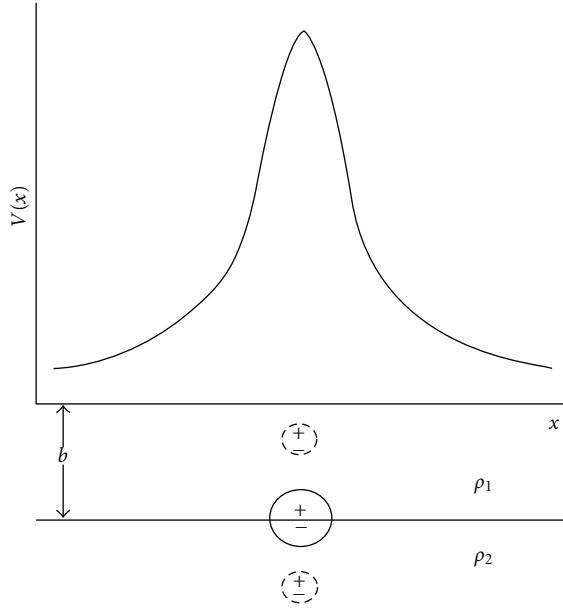


FIGURE 3: Representation of the SP anomaly produced by a polarized cylinder at the contact of two horizontal layers with different resistivities.

I is the current intensity per unit length, at the poles of the cylinder. It can be positive or negative, according to the polarity of the SP anomaly (positive or negative, resp.).

If the resistivity ρ_1 of the upper layer is different from the resistivity ρ_2 of the bedrock and the cylinder is located at depth h greater than b (see the lower dashed circle in Figure 3), then the expression for the self-potential anomaly $V_2(x)$ can be found by the image technique [27], which gives

$$V_2(x) = 4M_2R(1-k) \sum_{n=0}^{\infty} k^n \frac{h+2nb}{x^2+(h+2nb)^2}. \quad (3)$$

Polarization M_2 is given by

$$M_2 = \frac{I\rho_2}{2\pi}. \quad (4)$$

k is the reflection coefficient, which is defined by

$$k = \frac{\rho_2 - \rho_1}{\rho_2 + \rho_1}. \quad (5)$$

If the cylinder is located at depth h smaller than b (see the upper dashed circle in Figure 3), then the expression for the self-potential anomaly $V_1(x)$ is given by

$$V_1(x) = 4M_1R \left[\sum_{n=0}^{\infty} k^n \frac{2nb+h}{x^2+(2nb+h)^2} + \sum_{n=1}^{\infty} k^n \frac{2nb-h}{x^2+(2nb-h)^2} \right]. \quad (6)$$

Polarization M_1 is given by

$$M_1 = \frac{I\rho_1}{2\pi}. \quad (7)$$

The SP anomaly $V(x)$, which is produced by a polarized cylinder at the contact between the two layers, may be seen as the limit of the potentials V_1 and V_2 for $h \rightarrow b^-$ and $h \rightarrow b^+$, respectively. Taking into account the relations (3), (4), (6) and (7), it can be easily proved that the limits of V_1 and V_2 are equal and $V(x)$ is

$$V(x) = \lim_{h \rightarrow b^-} V_1(x) = \lim_{h \rightarrow b^+} V_2(x) = \frac{4I\rho_1\rho_2R}{\pi(\rho_1 + \rho_2)} \sum_{n=0}^{\infty} k^n \frac{(2n+1)b}{x^2 + [(2n+1)b]^2}. \quad (8)$$

The self-potential field produced by a horizontal flow at the contact of the two layers is described by relation (8). Taking the Fourier transform of this expression, it is possible to study the SP anomaly at spatial frequency domain.

3. Derivation of the Fourier Transform of the SP Anomaly

The Fourier transform $U(u)$ of the SP anomaly $V(x)$ is defined by

$$U(u) = \int_{-\infty}^{\infty} V(x) \cdot e^{-iux} dx, \quad (9)$$

u is the spatial frequency. Every u is related to a certain x value by $u = 2\pi/x$.

The following tabulated integral [28] may be used in order to find the Fourier transform of $V(x)$

$$\int_{-\infty}^{\infty} \frac{1}{x^2 + b^2} \cdot e^{-iux} dx = \frac{\pi}{b} \cdot e^{-bu}. \quad (10)$$

Based on relation (10), it can be easily shown that

$$\int_{-\infty}^{\infty} \frac{k^n(2n+1)b}{x^2 + [(2n+1)b]^2} \cdot e^{-iux} dx = \pi k^n \cdot e^{-(2n+1)bu}. \quad (11)$$

Combining (8), (9), and (11) gives

$$U(u) = \frac{4I\rho_1\rho_2R}{\pi(\rho_1 + \rho_2)} \sum_{n=0}^{\infty} \pi k^n e^{-(2n+1)bu}. \quad (12)$$

Summing the terms of the series of relation (12), the following expression for $U(u)$ is obtained:

$$U(u) = K \cdot \frac{e^{-bu}}{1 - ke^{-2bu}}. \quad (13)$$

K is given by

$$K = \frac{4I\rho_1\rho_2R}{\rho_1 + \rho_2}. \quad (14)$$

The amplitude spectrum $A(u)$ of U is defined as the absolute value of U , so

$$A(u) = |U(u)| = |K| \cdot \frac{e^{-bu}}{1 - ke^{-2bu}}. \quad (15)$$

Using tabulated integrals, it can be also proved that the function $A(u)$ is continuous at $u = 0$.

In Figure 4 the amplitude spectrum of the SP anomaly is presented. Studying the behavior of $A(u)$, certain simple mathematical expressions may be derived, in order to develop a method to calculate the quantities b and k .

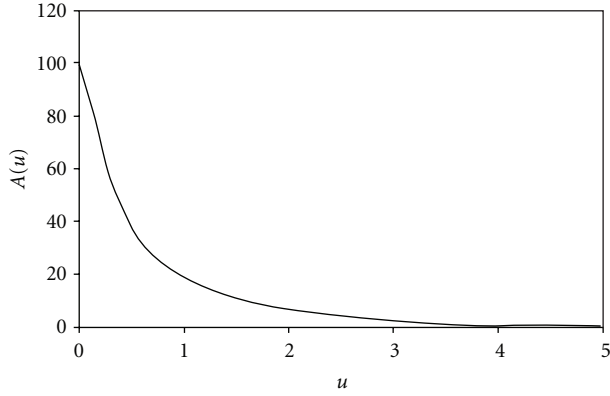


FIGURE 4: The amplitude spectrum of the self-potential anomaly $V(x)$: $b = 1$, $K = 100$, $k = 0.5$.

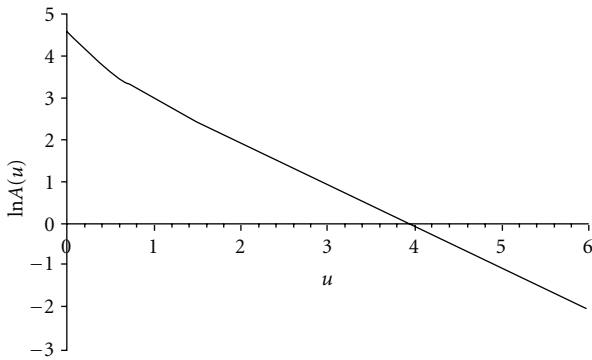


FIGURE 5: The natural logarithm of amplitude A against spatial frequency u .

4. Quantitative Interpretation of the SP Anomaly

In Figure 5, the variation of the natural logarithm of amplitude A against u is presented. It can be seen that as long as u increases, the quantity $\ln A$ tends to present a linear variation with u .

The mathematical expression for this linear variation can be derived by relation (15) if u is big enough so that $k \cdot \exp(-2bu)$ may be neglected, meanwhile $\exp(-bu)$ remains more than zero. In such a case, the natural logarithm of $A(u)$ becomes

$$\ln A(u) \approx \ln|K| - bu. \quad (16)$$

This means that, for relatively high u values, for which $k \cdot \exp(-2bu) \approx 0$, the absolute value of the slope of the straight line $\ln A(u)$ is equal to the depth b of the cylinder. The minimum value u for which relation (16) is valid depends on b and k . In practice, the interpreter has to define the linear part of $\ln A$ against u , by which b may be calculated.

Now let u_t be the u value for which $A(u_t)$ is equal to one tenth of A at null spatial frequency. Such a condition is

expressed by

$$A(u_t) = \frac{A(0)}{10}. \quad (17)$$

According to relation (15), $A(0)$ is given by

$$A(0) = \frac{|K|}{1-k}. \quad (18)$$

Combining relations (15), (17), and (18) and solving for k give

$$k = \frac{10 \cdot \exp(-bu_t) - 1}{10 \cdot \exp(-bu_t) - \exp(-2bu_t)}. \quad (19)$$

The quantity $\exp(-2bu_t)$ is much smaller than $10 \cdot \exp(-bu_t)$ (ten times smaller for $bu_t = 0$ and even more as long as bu_t increases). Neglecting $\exp(-2bu_t)$, relation (19) takes the following simplified form:

$$k \approx 1 - 0.1 \exp(bu_t). \quad (20)$$

Therefore, determining the u_t value for which the amplitude A is equal to $A(0)/10$, it is possible to calculate the reflection coefficient k , by relation (20).

According to the mathematical study of the behavior of the amplitude spectrum, a direct quantitative interpretation method is proposed, which may be executed by the following steps.

- (1) Calculate the amplitude spectrum $A(u)$ of the SP anomaly measured in the field.
- (2) Take the natural logarithm $\ln A$ of A and calculate the slope of the linear part of $\ln A$ against u . The absolute value of the slope is equal to the depth b .
- (3) Find the u_t value for which the amplitude $A(u_t)$ is equal to $A(0)/10$. The reflection coefficient k between the two layers can be calculated by relation (19) or (20).

With this interpretation method it is possible to calculate the depth of the horizontal subsurface flow and the reflection coefficient k between the two layers.

5. Experimentation with a Synthetic Model

In order to test the efficiency of the proposed quantitative interpretation method, a synthetic model was used with $4I\rho_1\rho_2R/[\pi(\rho_1 + \rho_2)] = 5000 \text{ mV.m}$, $b = 50 \text{ m}$, and $k = 0.6$. The SP anomaly $V(x)$ for 256 values of x and a 10 m interval was calculated. The Fourier analysis of $V(x)$ was done, applying the well-known FFT algorithm.

In Figure 6, the amplitude spectrum $A(u)$ of the self-potential anomaly is presented, for u between 0 and 0.07 rad/m. The value u_t for which A becomes equal to $A(0)/10$ may also be noted.

In Figure 7 one can see how $\ln A$ varies with u . The range of u is from zero to the Nyquist frequency. For very low and for very high values of u the variation is not linear.

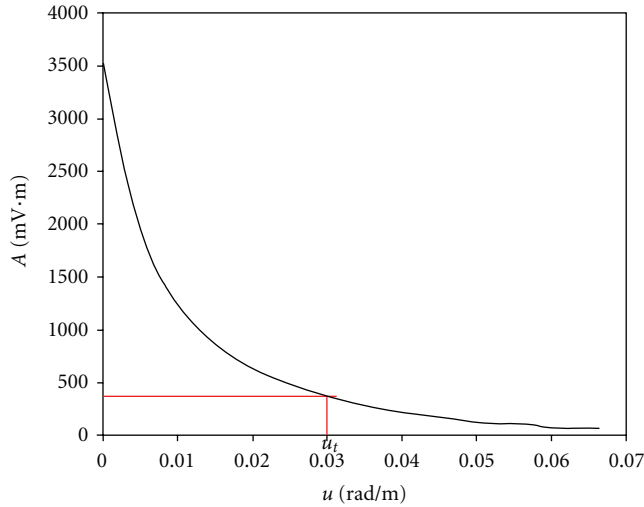


FIGURE 6: The amplitude spectrum of the SP curve of the synthetic model.

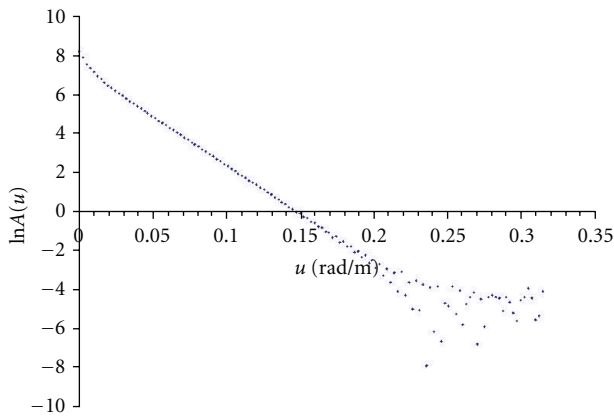


FIGURE 7: The natural logarithm of the amplitude A against spatial frequency u .

The nonlinear behavior for low spatial frequencies is in agreement with the theoretical predictions, as it can be seen in Figure 5. The scattering of $\ln A$ values for very high spatial frequencies is due to numerical errors, which may seriously affect the calculations when $A(u)$ is very small. In a broad part of the spectrum, $\ln A$ varies linearly with u .

In Figure 8, the linear part of the spectrum is presented. The least squares straight line was calculated, and the slope of the line was found to be equal to -50.02 . Thus, the calculated b is equal to 50.02 m, which is very close to the true value of 50.00 m (the relative error is 0.04%).

As it can be seen in Figure 6, $u_t = 0.030$ rad/m. Putting $b = 50.02$ and $u_t = 0.030$ at the right part of relation (20), a value of k equal to 0.55 is calculated. Thus, there is an 8% relative error between the calculated and the true value of k , which is equal to 0.600 . If k is calculated by (19), which is an accurate expression, it takes the value $k = 0.56$ (relative error equal to 7%). Therefore, the approximate formula (20) gives

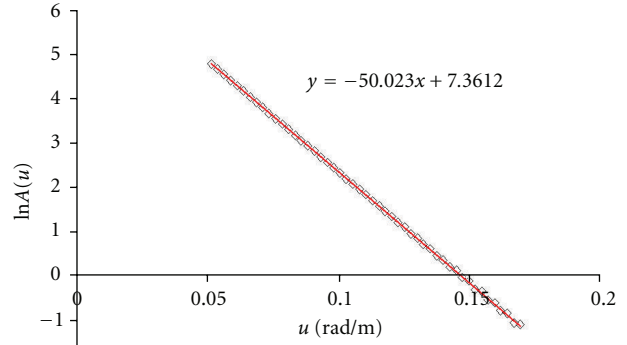


FIGURE 8: The linear part of the variation of $\ln A$ against u , fitted by the least squares line.

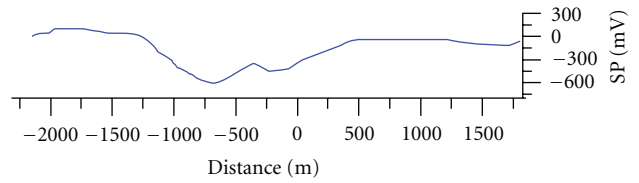


FIGURE 9: A self-potential profile along Waita volcano, Japan (Mauri et al. [4]).

a k value which is very close to that of the exact expression (19).

The experimentation with the synthetic model produced encouraging results as long as the reliability of the proposed quantitative interpretation method is concerned, since the calculated b and k values are very close to the true ones.

6. Application on Real-Field Data

The proposed method was tested on an SP profile along Waita volcano (Japan), where hydrothermal activity is developed (Mauri et al. [4]). The self-potential anomaly is presented in Figure 9. From the mathematical point of view the SP anomaly may be simulated by a polarized cylinder with an upper negative pole and a lower positive pole. The two negative peaks at the centre of the anomaly indicate the possible existence of at least two polarized bodies, but according to the proposed method only one body may be detected. The horizontal projection of the cylinder is estimated to be located at the centre of the anomaly, which means at distance x between -500 m and -300 m (mean value of $x = -400$ m).

The SP anomaly was manually digitized and 128 values were stored (sampling interval equal to 31.25 m). These values were analyzed by an FFT. In Figure 10 the amplitude spectrum $A(u)$ of the anomaly is presented.

It can be observed that because of the “wavy” behaviour of the curve $A(u)$, the value u_t cannot be exactly defined and it is estimated to be between a little more than 0.0045 rad/m and a little less than 0.0090 rad/m. u_t takes the value of the midpoint of this interval, which is $u_t = 0.0068$ rad/m. The

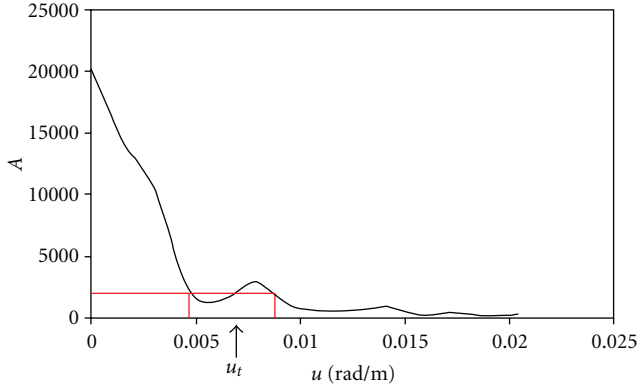


FIGURE 10: The amplitude spectrum of the SP anomaly.

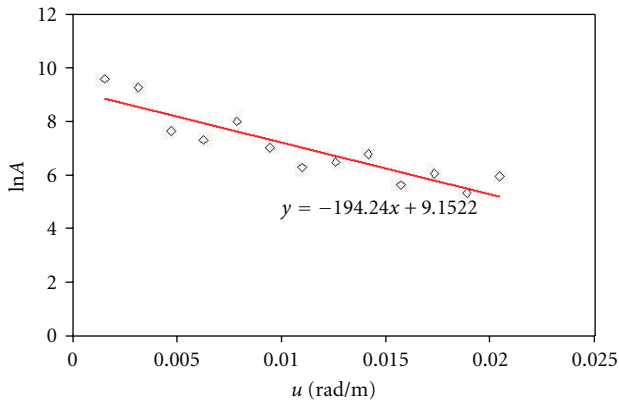


FIGURE 11: The linear part of natural logarithm of the amplitude spectrum against spatial frequency u .

error $\sigma(u_t)$ can be taken equal to half of the uncertainty range between 0.005 and 0.009, which means $\sigma(u_t) = 0.002$ rad/m.

In Figure 11, the linear part of $\ln A$ against u is presented. The inclination of the least squares straight line is equal to -194 ; therefore the depth of the SP source, which is also the depth of the horizontal contact between the two layers, is $b = 194$ m. The standard error in the calculation of the inclination of the least squares line was found to be $\sigma(b) = 27$.

The reflection coefficient k may be calculated by relation (20), putting $b = 194$ and $u_t = 0.0068$, which gives $k = 0.63$. If k is calculated according to relation (19), then $k = 0.64$. The error in k may be calculated by the square root of the sum of the squares of $(\partial k/\partial u_t) \cdot \sigma(u_t)$ and $(\partial k/\partial b) \cdot \sigma(b)$, for $b = 194$, $u_t = 0.0068$, $\sigma(u_t) = 0.002$, and $\sigma(b) = 27$. This error was found to be $\sigma(k) = 0.16$.

The results of the quantitative interpretation may be summarized as follows

$$b = (190 \pm 30)\text{m}, \quad k = 0.6 \pm 0.2. \quad (21)$$

According to relation (5), a reflectance coefficient equal to 0.6 gives a resistivity ratio equal to 4/1 (lower to upper layer).

Mauri et al. [4] interpreted the SP anomaly by a tomography methodology using the wavelet transform. They detected

five SP sources all along the self-potential profile, at depths varying between 30 m and 400 m. More precisely, they found sources at $x = -1850$ m, -1230 m, -400 m, $+365$ m and $+1220$ m, with respective depths $b = 295$ m, 150 m, 400 m, 100 m, and 30 m. The methodology which is proposed in the present paper cannot detect more than one source and the calculated depth has an intermediate value between the five source depths.

On the other hand, Mauri et al. [4] do not report anything about the resistivity distribution of the ground. It would be interesting to compare our prediction about a horizontal layer boundary at 190 m depth and a 4/1 resistivity ratio with data obtained by vertical electric sounding or electrical tomography, if there is any.

7. A Study of the Sensitivity of the Method

The efficiency of the proposed interpretation method is controlled by the ground resistivity distribution and the noise.

The role of ground resistivity may be understood by taking into account relation (8). High values of ρ_1 and ρ_2 produce strong SP anomalies, which help to make a reliable calculation of depth and reflection coefficient. On the other hand, a very low value of ρ_1 or ρ_2 may produce a very weak SP anomaly, which cannot be reliably interpreted. This may happen, for example, if the upper layer is a clay formation. Since clay has an electronic conductivity, its resistivity is very low and this does not favor the development of a strong SP anomaly.

In order to study the sensitivity of the quantitative interpretation method in the presence of noise, the synthetic model of paragraph 5 was used (model parameters: $4I\rho_1\rho_2R/[\pi(\rho_1 + \rho_2)] = 5000$ mV·m, $b = 50$ m, and $k = 0.6$). Random noise was introduced, with a zero mean value and amplitudes between 0% and 40% of the amplitude of the SP anomaly of the synthetic model. Each SP curve, which contained the signal of the polarized body and random noise, was interpreted according to the proposed method. The absolute relative error values $|\Delta b/b|$ and $|\Delta k/k|$ were calculated according to the relations:

$$\left| \frac{\Delta b}{b} \right| = \left| \frac{bc - b}{b} \right|, \quad (22)$$

$$\left| \frac{\Delta k}{k} \right| = \left| \frac{kc - k}{k} \right|, \quad (23)$$

b_c and k_c are the calculated values of depth and reflection coefficient, respectively.

Figure 12 presents the relative absolute error $|\Delta b/b|$ against the noise percentage (ratio of noise amplitude to signal amplitude). It can be observed that up to a 5% noise, the error is null and keeps being small (less than 20%), when the noise percentage is not more than 10%. For higher noise percentages, $|\Delta b/b|$ increases and exceeds 50% for a noise percentage more than 30%.

Figure 13 presents the relative absolute error $|\Delta k/k|$ against the noise percentage. Compared to $|\Delta b/b|$, the error in the calculation of the reflection coefficient is considerably

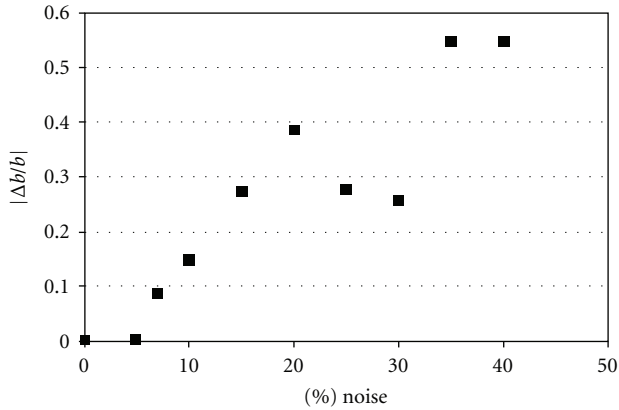


FIGURE 12: Absolute relative error in the calculation of depth against noise percentage.

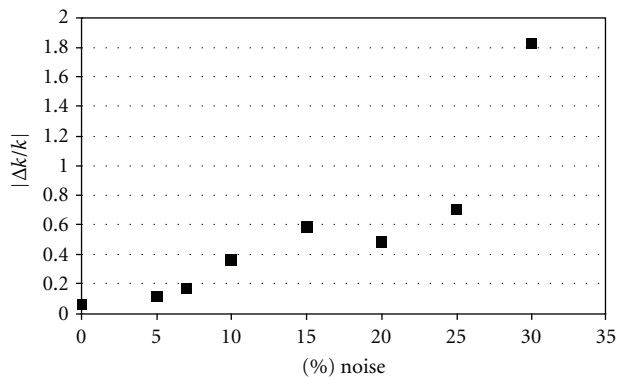


FIGURE 13: Absolute relative error in the calculation of the reflection coefficient against noise percentage.

bigger. For a 5% noise content, it is 15% and for a 30% noise percentage or more the deviations between real and calculated k are so high that it is meaningless to calculate k .

In Figure 12, it can be observed that there is a decrease in the error $|\Delta b/b|$ between 20 and 30% noise. Actually, $|\Delta b/b|$ depends on the exact values of the random noise and, more important, on the exact points of the amplitude spectrum which are considered to follow a straight line. These points were chosen by a visual criterion, according to which the beginning and the end of the line was defined. Such a criterion is inevitably subjective and may produce deviations in the ascending tendency of the error with the noise content. The decrease of $|\Delta k/k|$ in between 15 and 20% noise (see Figure 13) may be partly attributed to the deviation of b and partly to the “wavy” behavior of the curve $A(u)$, because of which there is an uncertainty in the value of u_t .

8. Conclusions

Self-potential measurements at ground surface are often considered as a preliminary exploration method, which has to be followed by other techniques, such as geoelectrical sounding or electrical tomography, in order to form a more

precise picture of the subsurface water flow and the geological formations in which this flow occurs.

On the other hand, it is well known that if ground electrical inhomogeneities are not taken into account, considerable errors in the calculation of the parameters of the SP source may be made.

Applying the quantitative interpretation method which is proposed in the present paper, the depth of the SP source (which is a horizontal subsurface flow) may be reliably calculated since the electrical inhomogeneity is not ignored, although it is not known a priori. Furthermore, it is possible to estimate the ground resistivity contrast by calculating the reflection coefficient, according to relation (19) or to relation (20). The latter is an approximate formula to calculate k ; however, it gives a value which is very close to that of the exact expression (19). Therefore, the SP method gains reliability and provides information about the geological stratification of the ground, which may be taken into account during the application of other exploration techniques.

Experimentation with a synthetic model provided encouraging results long as the reliability of the proposed quantitative interpretation method is concerned. Good estimates of depth b may be done, for an up to 10% noise percentage. The calculation of the reflection coefficient k is considerably more sensitive to noise than the one of b . If the noise content is not more than 5%, the relative error in the calculation of k is less than 20%.

The ground resistivity distribution controls the amplitude of the self-potential anomaly. Weak SP anomalies are expected to be produced over a layer with a very low resistivity, such as a clay formation.

The proposed method was applied to field data obtained at a hydrothermal field with more than one SP sources. The method could calculate only one depth value, which was found to be between the depth values of the sources. Further application on other self-potential anomalies produced by only one source is necessary in order to assess the efficiency of the method. This could be the subject of a future research.

Acknowledgment

This paper is part of a research project funded by the University of Athens, in the context of supporting the research activity of the Faculty of Geology and Geoenvironment.

References

- [1] G.-B. Zhang and M. Aubert, “Quantitative interpretation of self-potential anomalies in hydrogeological exploration of volcanic areas: a new approach,” *New Surface Geophysics*, vol. 1, no. 2, pp. 69–75, 2003.
- [2] A. Finizola, J.-F. Lénat, O. Macedo, D. Ramos, J.-C. Thouret, and F. Sortino, “Fluid circulation and structural discontinuities inside Misti volcano (Peru) inferred from self-potential measurements,” *Journal of Volcanology and Geothermal Research*, vol. 135, no. 4, pp. 343–360, 2004.
- [3] H. Hase, T. Hashimoto, S. Sakanaka, W. Kanda, and Y. Tanaka, “Hydrothermal system beneath Aso volcano as inferred from self-potential mapping and resistivity structure,” *Journal of*

- Volcanology and Geothermal Research*, vol. 143, no. 4, pp. 259–277, 2005.
- [4] G. Mauri, G. Williams-Jones, and G. Saracco, “Depth determinations of shallow hydrothermal systems by self-potential and multi-scale wavelet tomography,” *Journal of Volcanology and Geothermal Research*, vol. 191, no. 3-4, pp. 233–244, 2010.
- [5] A. Jardani, A. Revil, F. Santos, C. Fauchard, and J. P. Dupont, “Detection of preferential infiltration pathways in sinkholes using joint inversion of self-potential and EM-34 conductivity data,” *Geophysical Prospecting*, vol. 55, no. 5, pp. 749–760, 2007.
- [6] R. E. Nimmer and J. L. Osienky, “Direct current and self-potential monitoring of an evolving plume in partially saturated fractured rock,” *Journal of Hydrology*, vol. 267, no. 3-4, pp. 258–272, 2002.
- [7] V. Naudet, M. Lazzari, A. Perrone, A. Loperte, S. Piscitelli, and V. Lapenna, “Integrated geophysical and geomorphological approach to investigate the snowmelt-triggered landslide of Bosco Piccolo village (Basilicata, southern Italy),” *Engineering Geology*, vol. 98, no. 3-4, pp. 156–167, 2008.
- [8] C. Doussan, L. Jouniaux, and J.-L. Thony, “Temporal variations of SP and unsaturated water flow in loam and clay soils: a seasonal field study,” *Journal of Hydrology*, vol. 267, pp. 173–185, 2002.
- [9] A. Maineult, E. Strobach, and J. Renner, “Self-potential signals induced by periodic pumping tests,” *Journal of Geophysical Research*, vol. 113, Article ID B01203, 12 pages, 2008.
- [10] V. Allègre, L. Jouniaux, F. Lehmann, and P. Sailhac, “Streaming potential dependence on water-content in Fontainebleau sand,” *Geophysical Journal International*, vol. 182, no. 3, pp. 1248–1266, 2010.
- [11] L. Jouniaux, A. Maineult, V. Naudet, M. Pessel, and P. Sailhac, “Review of self-potential methods in hydrogeophysics,” *Comptes Rendus Géoscience*, vol. 341, no. 10-11, pp. 928–936, 2009.
- [12] D. Schiavone and R. Quarto, “Self-potential prospecting in the study of water movements,” *Geoexploration*, vol. 22, no. 1, pp. 47–58, 1984.
- [13] B. Nourbehecht, *Irreversible thermodynamic effects in inhomogeneous media and their application in certain geoelectric problems*, Ph.D. thesis, Massachusetts Institute of Technology, Cambridge, Mass, USA, 1963.
- [14] D. V. Fitterman, “Electrokinetic and magnetic anomalies associated with dilatant regions in a layered earth,” *Journal of Geophysical Research*, vol. 83, no. B12, pp. 5923–5928, 1978.
- [15] W. R. Sill, “Self-potential modeling from primary flows,” *Geophysics*, vol. 48, no. 1, pp. 76–86, 1983.
- [16] A. A. Ogilvy, E. J. Ostrovskij, and E. N. Ruderman, “Electrical surveys using the method of the natural potential electrical field; new investigations,” in *Detection of Subsurface Flow Phenomena*, G. P. Merkler, H. Militzer, H. Hötzl, H. Armbruster, and J. Brauns, Eds., pp. 401–462, Springer, Berlin, Germany, 1989.
- [17] B. B. Bhattacharya and N. Roy, “A note on the use of a nomogram for self-potential anomalies,” *Geophysical Prospecting*, vol. 29, no. 1, pp. 102–107, 1981.
- [18] B. V. S. Murty and P. Haricharan, “Nomogram for the complete interpretation of spontaneous potential profiles over sheet-like and cylindrical two-dimensional sources,” *Geophysics*, vol. 50, no. 7, pp. 1127–1135, 1985.
- [19] S. G. Aim, T. D. Papadopoulos, and D. A. Vaiopoulos, “Distortional affects on the self-potential curve over a polarized body,” in *Proceedings of the 2nd Scientific Geophysics Conference*, vol. 2-3, pp. 205–214, Florina, Greece, 1993, (in greek).
- [20] S. G. Aim, T. D. Papadopoulos, and D. A. Vaiopoulos, “Self-potential field over a horizontal polarized cylinder laid in a horizontally layered medium,” in *Proceedings of the 1st Congress of the Balkan Geophysical Society (Extended Abstracts)*, pp. 200–201, Athens, Greece, 1996.
- [21] W. Shi, *Advanced modeling and inversion techniques for three-dimensional geoelectrical surveys*, Ph.D. thesis, Massachusetts Institute of Technology, Cambridge, Mass, USA, 1998.
- [22] B. J. Minsley, J. Sogade, and F. D. Morgan, “Three-dimensional source inversion of self-potential data,” *Journal of Geophysical Research*, vol. 112, Article ID B02202, 13 pages, 2007.
- [23] D. Patella, “Introduction to ground surface self-potential tomography,” *Geophysical Prospecting*, vol. 45, no. 4, pp. 653–681, 1997.
- [24] D. Patella, “Self-potential global tomography including topographic effects,” *Geophysical Prospecting*, vol. 45, no. 5, pp. 843–863, 1997.
- [25] D. Gibert and P. Sailhac, “Comment on “Self-potential signals associated with preferential groundwater flow pathways in sinkholes” by A. Jardani, J. P. Dupont, and A. Revil,” *Journal of Geophysical Research*, vol. 113, no. 3, 2008.
- [26] D. Gibert and M. Pessel, “Identification of sources of potential fields with the continuous wavelet transform: application to self potential profiles,” *Geophysical Research Letters*, vol. 28, no. 9, pp. 1863–1866, 2001.
- [27] G. V. Keller and F. C. Frischknecht, *Electrical Methods in Geophysical Prospecting*, Pergamon Press, Oxford, England, 1966.
- [28] M. R. Spiegel, *Fourier Analysis*, McGraw-Hill, New York, ESPI Athens, 1978.